
Australian National University

# Electrospun Vanadium-based Oxides as Positive Battery Electrodes

Ceilidh Fiona Armer

A thesis submitted for the degree of
DOCTOR OF PHILOSOPHY

The Australian National University

November 2017

I hereby declare that this thesis is my own original work and that, to the best of my knowledge and belief, it contains no material previously published or written by another person nor material which to a substantial extent has been accepted for the award of any other degree or diploma of the university or other institute of higher learning, except where due acknowledgement has been made in the text.

Ceilidh Armer

3 November 2017

*I dedicate this thesis to my parents; Elizabeth and Douglas Armer,*

*Also to Michal Dunski and Wally Mackay,*

*With honourable mentions to Charlie and Calvin.*

# Acknowledgements

First and foremost, I would like to acknowledge and thank the chair of my supervisory panel, Dr Adrian Lowe. I have been very fortunate to have had the opportunity to work with Adrian for both my Honours and PhD projects. Adrian's hands-off approach has allowed me to explore different avenues of investigation under my own volition. His research area, enthusiasm, interest in collaborating with other researchers and an appreciation for a work-life balance made this a worthwhile and enjoyable PhD journey for me.

To Dr Li Xu, my primary supervisor at the Institute of Materials Research and Engineering (IMRE) in Singapore, thank you for being very approachable, for trusting me to work at my own pace, and for always knowing who to direct me to when further assistance was required.

Thanks to the Higher Degree Research program at the Australian National University which funded this PhD project along with the Postgraduate and Research Students Association for providing free Shup Up and Write sessions that were instrumental in supporting me during the completion stages of this project. I acknowledge the Australian Microscopy and Microanalysis Research Facility at the Centre for Advanced Microscopy of the Australian National University for the use of their scanning electron microscopy facilities.

I acknowledge the A*STAR Research Attachment Program for providing me the opportunity to research at IMRE in Singapore from May 2015 to November 2016. The experiences I gained during this time were invaluable and helped me develop a broader perspective and appreciation for research culture.

Many thanks to Mechthild Lübke for being a wonderfully fun collaborator, mentor and friend at IMRE. Meggi was consistently inclusive, encouraging, generous with her time, always interested to learn and refreshingly direct with her approach to research.

Dr M.V. Reddy from the Department of Physics at the National University of Singapore (NUS), was exceptionally generous in allowing me to use his glovebox for lithium ion coin cell

production on multiple occasions during the IMRE relocation and was the source of many helpful discussions. Special thanks to Professor B.V.R. Chowdari, also from the NUS Department of Physics, for the use of his laboratories in processing coin cells during the IMRE relocation.

To Aled Roberts for facilitating a smooth introduction to IMRE and for being entertaining while doing so. Thanks to Wong Siew Yee, Dr Zhang Yu, Dr Zhang Zheng and Dr Ding Ning at IMRE for their assistance and advice in the collection of transmission electron micrographs, X-ray photoelectron spectroscopy data and galvanostatic data during my research attachment.

Thank you to Ian Johnson for his Rietveld refinement skills and interest in all things vanadium oxide. Also, thanks to Jawwad A. Darr from the University College London (UCL), for facilitating the collection of Mo-source X-ray diffraction spectra and transmission electron micrographs. I would like to acknowledge the use of the UCL Legion High Performance Computing Facility (Legion@UCL), and associated support services. I am grateful to Kit McColl and Furio Cora for taking on the theoretical calculations of the materials in Chapter 5 and for showing interest in my work.

Luxmi Devi Narain is thanked for drawing some excellent pictures used in this project.

The Teabugs crew at IMRE: Joanna Pursey, Ulrike Wais, Eleftherios Christos Stathara, Aleksandra Gardecka, Diana Teixeira, Samuel Fishlock, Andrew Breeson, Hamid Khan, William Ambler, William Web, Davide Ansovini, Enock Kyei Assah and Elpiniki Georgiou. Biscuit-Thursdays and group therapy (over a variety of different drinks) was a delightful and necessary reprieve.

It was an absolute pleasure working with Joyce Yeoh during my last year at ANU; her perspectives, approach to research, integrity and curiosity was inspiring and motivating. Thank you to Francesca Maclean, whose ability to inspire confidence in oneself came at a time when it was really needed.

Friends at ANU: Brendan Voss, Tegan McNulty, Kiara Bruggeman, Hamza Bendemra, Michael Roberts, Chris Stokes-Griffin, Alice Bates, Dave Adams, Ehsan Abbasi, Vi Kie Soo, Cameron Summerville, Tom Cochrane, Jess Tsimeris, Alex Rodriguez and Asim Riaz. Another source of group therapy over tea, or alternative beverages, that were a consistent reminder of the importance of the comradery that exists between research students.

To the undergraduate students who worked with me on other vanadium oxide related projects; James Feltrin, Aaron Zegelin, Oscar Tigwell, Samuel Turner and Samuel Palmer, thank you for your interest and enthusiasm to learn.

To my parents; Elizabeth and Doug Armer for their unwavering, never-ending support and love on this journey. My brother Aaron; his music, along with book and TV show recommendations were thoroughly appreciated and enjoyed during my down-time. To my grandfather, Wally Mackay for his stories. And to Michal Dunski, for still being here and for continuing to understand me even when I do not.

This research is supported by an Australian Government Research Training Program (RTP) Scholarship.

# Abstract

Energy storage is an important area of research as demand for reliable, efficient and intermittent energy increases. The development and research of energy storage technologies, in particular lithium ion batteries, is intimately linked to the research of electrode materials. These materials need to be abundant, capable of providing high capacities, possess long cycle life and have good rate retention. Nanosizing of energy storage materials shows promise in addressing these requirements.

This thesis focusses on the synthesis, characterisation and electrochemical properties of electrospun fibrous vanadium-based pentoxides for lithium ion batteries. Vanadium pentoxides ($V_2O_5$) are candidate electrode materials due to their high theoretical capacity and layered structure that can reversibly intercalate lithium ions.

Starting solutions consisting of vanadium oxytripropoxide, poly(vinyl acetate) (PVAc) and ethanol were used for electrospinning the nanostructured hierarchical fibres. Dopant cations were introduced into the electrospinning solution using sodium acetate, barium oxide, aluminium isopropoxide or titanium (IV) isopropoxide. After electrospinning the as-spun materials were converted into fibrous metal oxides through a single step calcination process.

Varying the calcination treatment from of the as-spun fibres showed that crystallite size and fibre morphology were dependant on temperature. Crystallite size and conductivity of the electrospun $V_2O_5$ increased with calcination temperature though electrochemical performances did not correlate. Fibres calcined at 500 °C were shown to provide the best compromise between crystallinity, conductivity and capacity.

Fibre diameter was controllable by varying the amount of PVAc in the electrospinning starting solution while keeping all other parameters constant. Crystallite size increased with a decrease in fibre diameter, however, no trend in electrochemical performance was observed with $V_2O_5$

fibre diameter. Despite this, results indicated that fibrous hierarchical structures are necessary to maintain material integrity and promote higher conductivity during cycling.

The structural stabilisation of $V_2O_5$ during cycling was investigated using redox-inactive dopants $Ti^{4+}$ and $Ba^{2+}$ with loadings of approximately 10 atomic percent (at%). The doped materials improved both rate retention and cycling stability though only $Ti^{4+}$ doped $V_2O_5$ offered improved capacity. The dopants were shown to structurally stabilise $V_2O_5$ *via* phase change prevention.

Further dopant investigation showed that dopant location was an important factor in the overall electrochemical performance of the $V_2O_5$ host material, and that dopant loading, and oxidation state can influence their location as rationalised by atomistic simulations. Interstitial 2 at% $Na^+$ and 3 at% $Ba^{2+}$ in electrospun $V_2O_5$ provided both improved structural and electronic effects on the $V_2O_5$ structure and resulted in improved electrochemical performance. The substitutionally located 3 at% $Al^{3+}$ provided an improved structural effect but decreased electronic conductivity and lowered capacity.

The simplicity of the electrospinning technique combined with the reliability of $V_2O_5$ fibre production shows promise in wider implementation of this alternate electrode material for other metal-ion energy systems. For future research of electrospun $V_2O_5$ it is recommended that a hierarchical fibrous structure be utilised along with the incorporation of an interstitially located dopant metal.

Electrospun $V_2O_5$ shows promise as an electrode material by contributing towards providing an alternative abundant metal oxide for efficient energy storage technologies.

# Contents

# List of Figures

# List of Tables

# List of Abbreviations

| | |
|---|---|
| LIB | Lithium ion battery |
| Li-ion | Lithium ion |
| PVAc | Polyvinyl acetate |
| PVP | poly(vinylpyrrolidone) |
| PXRD | Powder x-ray diffraction |
| XPS | X-ray photoelectron spectroscopy |
| SEM | Scanning electron microscopy |
| TEM | Transmission electron microscopy |
| BET | Brunauer, Emmet and Teller surface area determination |
| TGA | Thermogravimetric analysis |
| CV | Cyclic voltammetry |
| GDC | Galvanostatic lithiation/delithiation |
| ICL | Irreversible capacity loss |
| EIS | Electrical impedance spectroscopy |

# Chapter 1 Literature Review

## 1.1 INTRODUCTION

Chapter 1 of this thesis outlines the relevant literature and background information that supports this project. Initially outlined in Section 1.2 is the motivation for this research project and its relevancy in the broader research community focussed on the development of energy storage materials. The fundamentals of energy storage are presented in Section 1.3 and in Section 1.4, followed by the electrochemistry of lithium ion batteries (LIBs) and the various types of electrode materials with mechanistic explanations for their charge transfer modes in Section 1.5. Metal-ion energy storage systems beyond LIBs are introduced in Section 1.6 though in-depth exploration is omitted as this project focussed on the use of electrospun vanadium pentoxide ($V_2O_5$) as a positive electrode in LIBs. Vanadium oxides are then discussed in Section 1.7 in which the structural and redox-based charge transfer mechanisms of $V_2O_5$ as a positive electrode are explored. Common nanostructured material processing techniques are then introduced in Section 1.8 with detailed descriptions of the electrospinning method highlighting the experimental setup and synthesis parameters. The electrochemical performance of undoped, doped and carbon incorporated electrospun $V_2O_5$ in the literature is presented in Section 1.9. The chapter concludes with a summary of the afore mentioned sections.

## 1.2 MOTIVATION

The increase in energy consumption and the use of its associated sources combined with population growth is a significant driving force for much of the scientific literature published in energy storage related research [1]. The critical, and ultimately inevitable, transition from non-renewable energy sources to renewables has driven the ongoing

development of advanced energy storage technologies. An increased demand for efficient energy conversion creates a necessity for efficient energy storage methods that provide consistent energy reliably. Current challenges associated with the development of these devices are linked to the research of supercapacitors, fuel cells, dye-sensitised solar cells, and batteries [2]. Batteries are currently considered to be the most promising due to their high specific energy and efficiencies.

These clean alternative energy devices represent an important step towards satisfying society's energy demands. Despite this, they are still under development and new break throughs are needed to improve these devices' performance in terms of energy density, power density, conversion efficiency, harvest efficiency, durability, and cost [1]. The need to develop such devices results in the development of new functional materials.

Batteries, in particular LIBs, are widely used as power sources as they are compact with high specific energy, high lithiation voltages, and good cycle performance [3]. They are market leaders in clean energy storage technologies as they can be made from non-toxic materials, have high energy-to-weight ratios and a long cycle life. Research and development breakthroughs with energy storage systems are centred on the active materials in such devices, in particular nanosizing of material dimensions, and their advanced fabrication techniques [4].

$V_2O_5$ and its derivatives are candidate alternative electrode materials for energy storage as they are made up of a consecutively layered crystal structure that provides the means for metal ion intercalation, in addition to good catalytic activity for energy conversion. They are used in numerous technological applications including solar cells, sensors, electrical and optical switching devices, photocatalyst and supercapacitors [5–11]. However, low structural stability with cycling and low ionic and electronic conductivities limits the performance of this promising electroactive material. Consequently, strategies

for improving $V_2O_5$ are necessary in the research and development of alternative energy systems.

Effective nanofabrication methods are under extensive investigation in the energy storage research area as procedures for producing functional nanostructured materials reliably, economically and efficiently are explored. Electrospinning is relatively simple and inexpensive bottom-up nano-fabrication technique for synthesizing one dimensional fibres from sol-gel solutions [12] and is beneficial to LIB development as it is able to vary nanoparticle morphologies [13]. The effectiveness of electrospinning lies with the use of electrostatic forces to draw the sol-gel solution into fibres with diameters on the order of tens of nanometres. Nanostructured fibres are of particular interest in LIB research as they offer large electrolyte/electrode contact areas, facile strain relaxation during cycling, short lithium ion (Li-ion) diffusion distances, and effective electronic transport pathways for higher capacity and improved rate performance [14].

This thesis investigates the effects of varying electrospinning process parameters and the intentional introduction of defects *via* dopants on the $V_2O_5$ morphology and structure along with the resultant electrochemical performance. It focusses on the role dopants play in the stabilisation of the $V_2O_5$ structure with lithium ion (Li-ion) intercalation in addition to the role dopant location plays in $V_2O_5$ conductivity. This project contributes to the development of functional nanostructured materials for energy storage applications by investigating the structural and electrochemical aspects of a nanostructured metal oxide. Furthermore, the research presented shows that electrospun $V_2O_5$ is a viable alternative electrode material with promise for practical implication.

This thesis addresses the following objectives of the project:

- To develop a sol-gel method to serve as a reliable starting solution for the electrospinning process to which dopants can be easily incorporated,

- To investigate the electrospinning process to enable controllable morphology of the $V_2O_5$ fibres and,
- To investigate the stabilisation and conductivity effects of dopants on the electrospun $V_2O_5$.

## 1.3 BASIC ELECTROCHEMISTRY OF ENERGY STORAGE DEVICES

The chemistry of energy storage devices and available energy can be described and quantified using the equations that are introduced in this section. Gibbs energy (*ΔG*, J mol$^{-1}$) (Equation 1) represents the maximum cell potential as the difference in available energy between the reactants and the products of a reaction.

$$\Delta G = -nF\Delta E \quad (1)$$

*ΔE* is the potential difference (V) between the half-cell reactions, *F* is the Faraday constant (96485 C mol$^{-1}$) and *n* is the stoichiometric coefficient of the electrons transferred per mole (mol) [15]. The negative sign indicates that the reaction is spontaneous, or favourable, such as the lithiation sequence in an electrochemical cell. Gibbs energy can also be thermodynamically related to temperature and pressure according to Equation 2.

$$\Delta G = \Delta G^0 + RT\, ln\left(\frac{a_p}{a_R}\right) \quad (2)$$

$\Delta G^o$ is the maximum work, *R* is the gas constant (8.3145 J mol$^{-1}$ K$^{-1}$), *T* is the temperature (K), $a_P$ is the activity of the product and $a_R$ is activity of the reactants. When Equations 1 and 2 are combined the Nernst Equation (Equation 3) is formed.

$$E = E^0 - \frac{RT}{nF}\, ln\left(\frac{a_p}{a_R}\right) \quad (3)$$

The potential, *E* (V), of each half-cell in an electrochemical device can be determined using the Nernst Equation and the reaction is spontaneous if $E > 0$ [15]. $E^o$ (V) is the

standard potential of each material which can be found in the literature. The potential of a full cell (Equation 4) can then be determined when the potential of each half-cell is known.

$$\Delta \boldsymbol{E} = \boldsymbol{E_{cathode}} - \boldsymbol{E_{anode}} \quad (4)$$

The theoretical specific capacity, $Q_{th}$ (mA h $g^{-1}$) of both the electrode materials is an important parameter when determining the energy of a full cell (Equation 5).

$$\boldsymbol{Q_{th}} = \frac{\boldsymbol{zF}}{\boldsymbol{3.6\ M}} \quad (5)$$

A high specific capacity is possible with a low molar mass, $M$ (g $mol^{-1}$), and a high number of transferred electrons, $n$. The theoretical specific energy, $W$ (Wh $kg^{-1}$), can be determined with the product of the cell potential, $\Delta E$, and the theoretical specific capacity, $Q_{th}$, according to Equation 6.

$$\mathbf{W} = \int_{\boldsymbol{q=0}}^{\boldsymbol{Q_{th}}} \boldsymbol{\Delta E\ dq} = \boldsymbol{Q_{th}\ \Delta E} \quad (6)$$

Consequently, an increase in both the cell voltage and the specific capacity results in higher energy densities [16]. These values can be measured using potentiostatic and galvanostatic methods such as those described in Section 2.2.8.

## 1.4 ENERGY STORAGE

Ideal electrochemical conversion and storage devices have high specific energy and power, are environmentally friendly, safe and cost effective. Examples of these systems are batteries, supercapacitors and fuel cells. While the energy storage and conversion mechanisms are different, similarities include the separation of ion and electron transport and the charge transfer processes taking place at the electrolyte/electrode conjunction [16]. Charge transfer processes occur *via* redox reactions for batteries and fuel cells resulting in high energy and medium life cycles (10,000 cycles).

Fuel cells convert hydrogen or hydrogen-rich fuel *via* an electrochemical oxidation reaction into electrical energy. These types of cells require the flow of hydrogen and oxygen which react in the presence of catalysts. Consequently, the catalysts, their supporting substrates and the proton exchange membrane are the most critical components [1]. Delithiation is stored physically at the electrode surface for capacitors and supercapacitors allowing rapid transfer of charge resulting in high power and high life cycles (1,000,000 cycles) [17]. Supercapacitors, also known as electric double-layer capacitors or electrochemical capacitors, are able to charge and discharge rapidly [18]. Due to this ability to rapidly transfer charge, their capacitance is dependent on the surface area of the electrode material that is accessible to the electrolyte. Typically, porous carbons are used in commercially available supercapacitors [19].

Specific power and specific energy and often inversely related which is shown in Figure 1.1. As specific energy increases, specific power typically decreases. Consequently, the development of high specific power devices with high specific energy and high life cycles is a challenge for researchers.

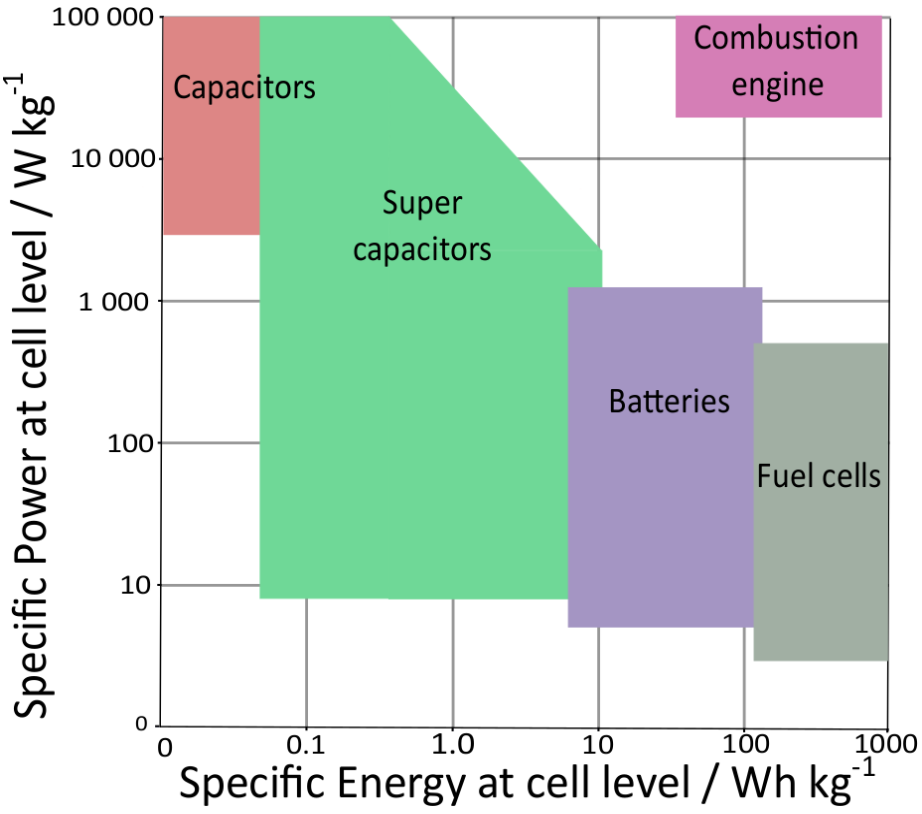


**Figure 1.1: Ragone plot comparing the specific energy and specific power of various electrochemical conversion and storage systems, adapted from [16,20].**

In the past decade, the demand for LIBs has eclipsed all other battery types including nickel-cadmium (NiCd), nickel-metal hydrides (NiMH), zinc, and alkaline batteries due to their higher specific energy. They occupy the majority of the battery market [21] and in 2010 held a market share of 11 billion dollars [22]. Initially lithium (Li) metal was used as a negative electrode material due to its very high specific capacity of 3860 mA h $g^{-1}$, light molecular weight of 6.94 g $mol^{-1}$, and specific gravity of 0.53 g $cm^{-3}$. It was replaced in the late 1970s and early 1980s due to safety and reactivity concerns with dendritic growth. Li metal was substituted with transition metal oxides of the form $LiMO_2$ (M = Co, Ni, Mn), that are capable of the reversible intercalation of Li-ions [21]. Sony commercialized LIBs developed by Asahi Chemical in 1991 with lithiated metal oxides and graphite as the electrode materials [23].

The Ragone plot in Figure 1.2 compares energy density and power density of commercially available batteries and capacitors. This figure shows that LIBs possess the highest energy density of common battery technologies with high power LIBs that are almost comparable to supercapacitors.

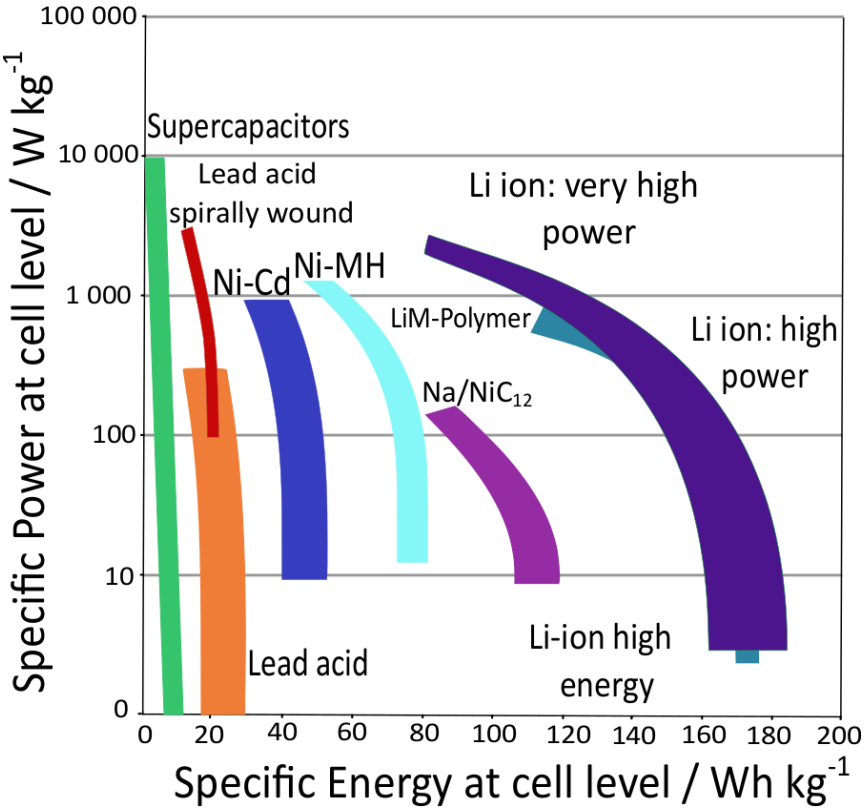


**Figure 1.2: Ragone plot comparing the specific energy and specific power of commercial batteries and capacitors of various chemistries, adapted from [24].**

Developing suitable electrode materials for use in LIBs that are reliable, structurally stable and possess high cycle stability is an important area of research along with the development of reliable and cost-effective processing technologies.

## 1.5 LITHIUM ION BATTERIES

### 1.5.1 Lithium Ion Battery Chemistry

An electrochemical cell is the smallest unit of an electrochemical device which converts chemical energy to electrical energy. It is made up of two electrodes of differing potentials and when immersed in an electrolyte, a potential difference called the open circuit voltage, is created. When discharging, lithiation in the case of LIBs, oxidation occurs at the negative electrode and reduction at the positive electrode with a Li-ion flow from negative to positive electrodes. During charging, or delithiation, reduction occurs at the negative electrode and oxidation at the positive electrode as Li-ions move out of positive electrode. This process is schematically represented in Figure 1.3, with a conventional LIB design, which shows the transfer of electrons in the external circuit while the electrolyte acts as an ionic conductor facilitating Li-ion transport between the electrodes. The lithiation process is represented in the forward reaction of Equation 7, where Li-ions are extracted from a graphitic negative electrode ($Li_xC_y$) and inserted into a lithiated metal oxide positive electrode ($LiMO_2$), with approximately 0.5 Li-ions ($x$) inserted and extracted per unit of $LiMO_2$ [25].

$$\boldsymbol{Li_xC_y + Li_{(1-x)}MO_2 \leftrightarrow C_y + LiMO_2 \qquad x \approx 0.5, y = 6} \tag{7}$$

In a rechargeable cell, the electrochemical reactions are reversible so both oxidative and reductive reactions can occur at the same electrode. Consequently, during delithiation, the roles of the electrodes switch so Li-ions move out of the positive electrode and into the negative electrode, as represented by the back reaction in Equation 7. Though, by convention, the terms remain the same with oxidation occurring at the negative electrode and reduction occurring at the positive electrode during the spontaneous lithiation process [23].

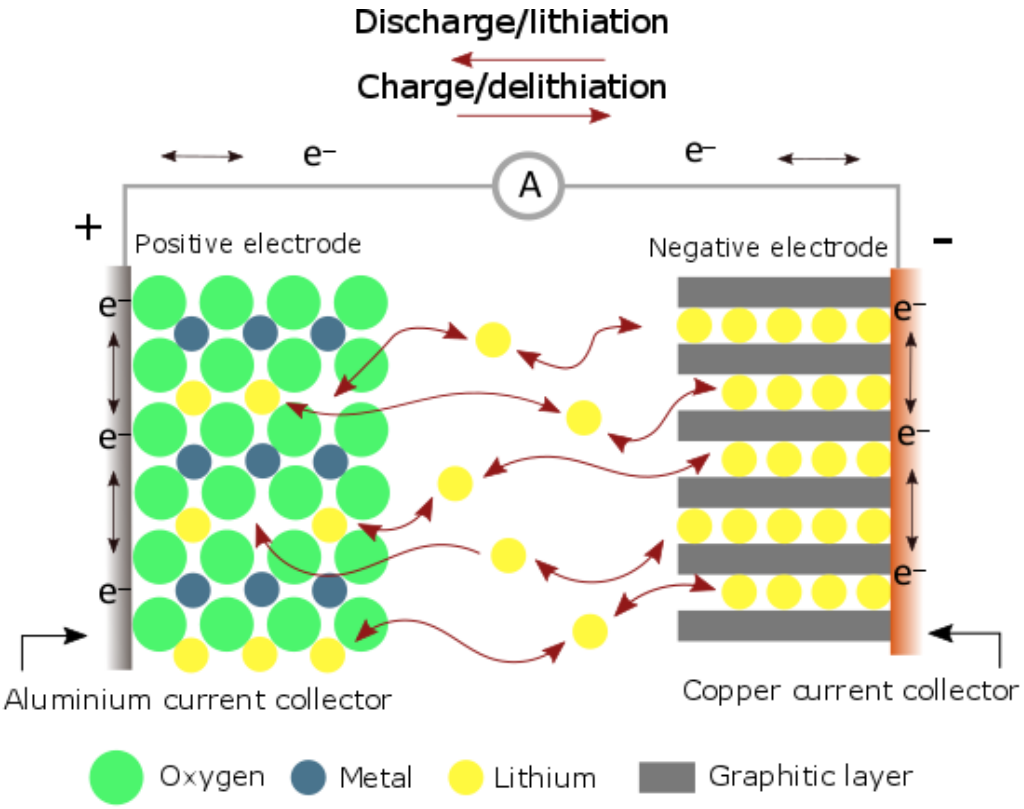


**Figure 1.3: Lithium ion battery components in a conventional design with a copper current collector for the negative electrode an aluminium current collector for the positive electrode, adapted from [4,25].**

A high performing LIB has a high specific energy. This is achieved with a high cell voltage and electrode materials with high specific capacities (Equation 6). This is shown graphically in Figure 1.4, where commercially used and investigated electrode materials for LIBs are grouped into different material types. For a LIB to be high performing, it must also have good cycle stability and rate capability. There are different classes of battery materials that can fulfil these requirements to different extents; these are insertion, conversion and alloying. In general, insertion materials have low theoretical capacities, undergo small structural changes and have high life cycles. Conversion and alloying materials have high theoretical capacities, undergo large structural changes and have low life cycles. These material classes are discussed in more detail in Sections 1.5.2 and 1.5.3.

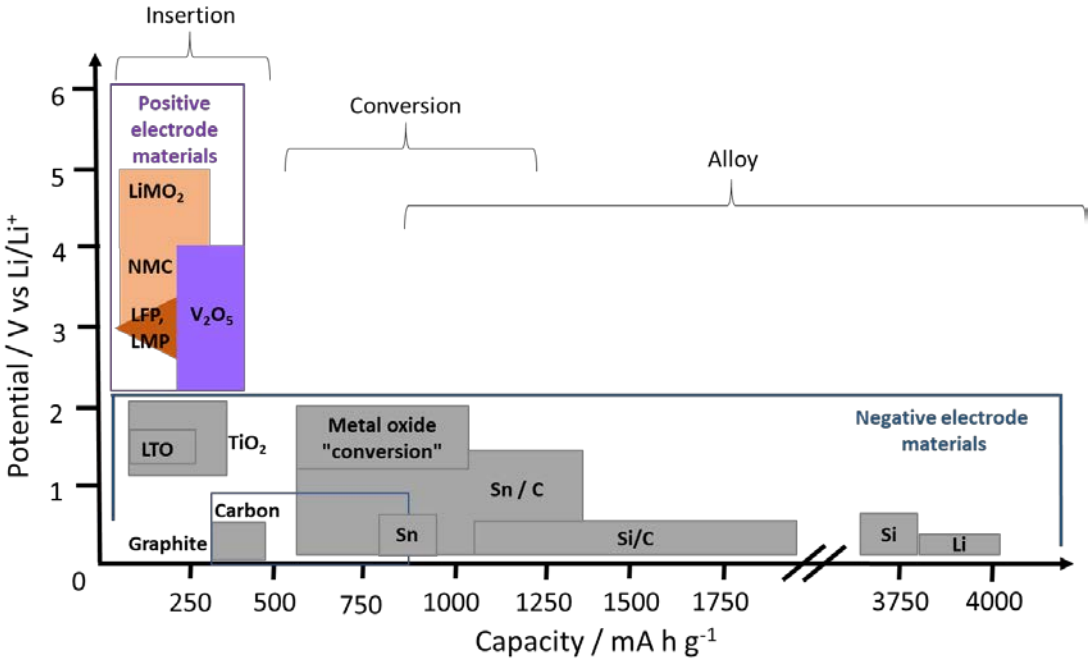


**Figure 1.4: Commercially used and researched electrode materials for LIBs where $LiMO_2$ = $LiCoO_2$, $LiMn_2O_4$, LFP = $LiFePO_4$, LMP = $LiMnPO_4$, NMC = $LiNi_{1/3}Mn_{1/3}Co_{1/3}O_2$ , LTO = $Li_4Ti_5O_{12}$, and Sn = $SnO_2$, adapted from [26].**

### 1.5.2 Insertion Electrode Materials for Lithium Ion Batteries

Insertion materials can reversibly store Li-ions in the host material with limited structure variation. This characteristic makes this class of electrode materials extremely useful for commercial LIBs. The charge transfer mechanism proceeds according to Equation 7. Insertion materials can be further divided into insertion (one dimensional – olivines, $TiO_2$, LFP or three dimensional – LTO, $Li_2MnO_3$) and intercalation materials (two dimensional – $LiCoO_2$, or graphite layers) as seen in Figure 1.5. These defined structures promote Li-ion diffusion in specific orientations. For example, olivines promote Li-ion diffusion in one direction along 1D channels, while spinels allow Li-ion diffusion in multiple directions within its 3D network. Layered intercalation materials promote diffusion within the interlayer space in addition to being ionic/electronic conductors. Ionic transport is enabled within intercalation materials due to the presence of diffusion

pathways offering interstitial sites for Li-ion movement and occupation. Electronic transport is caused by the overlapping of the *d* orbitals on the transition metal.

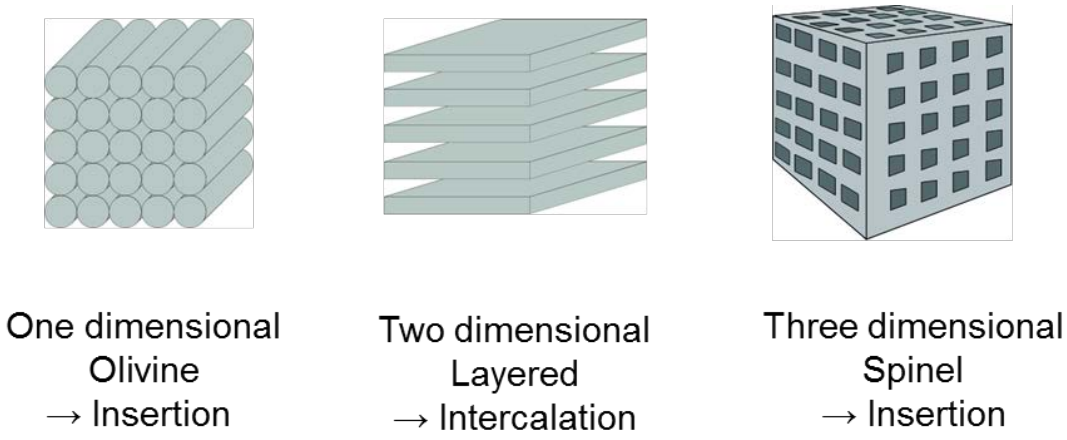


**Figure 1.5: Insertion material structures for one, two and three-dimensional variations.**

Currently used positive electrode materials include variations of the compounds $LiCoO_2$, $LiMnO_2$, and $LiNiO_2$ which have theoretical capacities of approximately 275 mA h $g^{-1}$ [27]. These insertion electrode materials possess high electronic and ionic conductivities, vacant sites in their crystalline structures, high redox potentials, high chemical stability, low specific surface area, and low cost [28]. Despite this, Co is scarce, so an alternate competitive cathode material is required. Additionally, Mn leaches out of $LiMnO_2$ electrodes during cycling [29]. Other notable compounds include spinel $LiMn_2O_4$, which is structurally stable with cycling, and $LiNiO_2$ for which a high degree of Li-ion reversibility can be obtained; although $LiMn_2O_4$ produces low capacity and $LiNiO_2$ is thermally unstable compared to $LiCoO_2$ as $Ni^{3+}$ is more readily reduced than $Co^{3+}$ [30]. Furthermore, positive electrode materials of the formula $LMO_2$ can typically store one Li-ion per unit formula which limits their stored energy and renders them susceptible to kinetic problems that arise from slow ion diffusion and poor electrical conductivity [31]. Graphitic materials are typically used in commercial LIBs as negative electrodes. Carbon-based negative electrodes served as a replacement for Li metal as it was found that the

build-up of Li species, such as LiOH, was somewhat prevented due to the insertion of Li-ions within the graphitic layers. Carbon experiences little structural change upon Li-ion insertion/extraction, with interlayer distance increases of only 10%, and has contributed to the high-energy density and reasonable cycle life of commercial LIBs today [23]. Though carbon electrodes have a high lithiation capacity of 370 mA h $g^{-1}$, they are limited by a low insertion potential. This causes metal Li deposition onto the electrode surface over time, which has a detrimental effect on battery safety and long cycle life [28].

### 1.5.3 Conversion and Alloying Materials for Lithium Ion Batteries

High energy density can also be achieved using conversion and alloying materials as they can store more Li-ions than insertion materials; the insertion material $LiCoO_2$ can only store one Li-ion. Despite this, conversion and alloying materials are susceptible to extreme structural changes during lithiation and have low operational potentials. As such, they are typically negative electrode materials, as seen in Figure 1.4. A conversion material is one where the metal oxide converts to its metallic state during the delithiation process in the forward reaction according to Equation 8.

$$\boldsymbol{M_aX_b + (b \cdot n)Li^+ \leftrightarrow aM + b\,Li_nX} \quad (8)$$

The $M_aX_b$ compound, where $M$ is the metallic cation and $X$ is the anion (S, N, O, P, F), is reduced to its metal form, $aM$, with the lithium compound by-product, $Li_xX$. Examples of candidate conversion materials for LIBs include $Fe_2O_3$ and $Fe_3O_4$ which have theoretical capacities of 1007 mA h $g^{-1}$ and 926 mA h $g^{-1}$, respectively. These materials are non-toxic, abundant, inexpensive and environmentally friendly. Despite this, they suffer substantial capacity fading caused by poor voltage hysteresis [32]. A voltage hysteresis is the shifting of the activation potential from low to high during delithiation

of the negative electrode. This potential shift is the result of large volume variations brought about structural changes experienced during the lithiation/delithiation processes.

Similar to conversion materials, alloying materials show much higher theoretical capacities, such as 993 mA h $g^{-1}$ for Sn and 3572 mA h $g^{-1}$ for Si, compared to 372 mA h $g^{-1}$ for graphite [33]. The high capacities and low operating potentials of these materials (Sn Si, Sb, Al) result in higher energy densities for LIBs. Also, like conversion materials, alloying materials undergo drastic structural changes as up to 15 Li-ions can be incorporated into the material (Equation 9).

$$\boldsymbol{M + zLi^{+} + ze^{-} \leftrightarrow Li_{z}M} \quad (9)$$

Where the metal (*M*) alloys with Li-ions to form the compound $Li_zM$. These structural changes result in drastic irreversible capacity losses which are caused by extreme volume changes, for example, Sn experiences more than 300% volume change during lithiation [34]. Such large volume changes can cause separation of the active material from the negative electrode. This can be mitigated using low active material masses and/or high conductive carbon loadings [33,35]. These are not long-term solutions as they lower the energy density in a full cell.

With the increasing energy demands of LIBs, there is an increase in demand for the use of higher performing electrode materials that have larger gravimetric and volumetric energy densities [36]. Due to the limitations of electrode materials briefly mentioned in this section, alternative materials are required for the advancement of LIBs. Other metal oxide variations are receiving much attention due to their novel properties, in particular 1D nanostructured materials are proving to be a potential solution [37].

### 1.5.4 Nanosizing of Electrode Materials for Lithium Ion Batteries

An issue with the use of nanomaterials is the question of toxicity. The effects of continual exposure to nanosized materials on both humans and the environment are not properly documented and there are concerns [38]. Additionally, issues with synthesis methods of nanomaterials also exist, with difficulties in reproduceable morphologies, size control and cost.

The atoms at the surface of active nanomaterials are less coordinated compared to those in bulk. This can result in differing chemical and physical behaviours, such as catalytic effects and cation dissolution. Due to high surface energy, nanomaterials are often thermodynamically unstable and can self-aggregate within the battery, which reduces the effective contact area and compromises the merits associated with the use of these materials [39] as discussed shortly. Transition metal dissolution resulting in the loss of material contact and degradation is especially a problem with electrodes made up of nanomaterials at higher active mass loadings [40]. Furthermore, a high electrolyte/electrode surface area promotes a high flux of Li-ions to the surface which can provide more opportunity for side reactions which can result in capacity losses [41].

Microscale electrode materials are susceptible to kinetic problems which arise from slow ion diffusion and poor electrical conductivity. Nanomaterials can improve the kinetics, promote higher solid-state ion diffusivity than those on the bulkscale, achieve higher electrical conductivity and minimize path lengths for ion and electron transport due to smaller particle size. Various nanoscale materials, such as metal organic/inorganic frameworks, $LiVPO_4F$, $LiMn_{1.5}Ni_{0.5}O_4$, $LiFePO_4$, and $Li_3V_2(PO_4)_3$ have been widely synthesised and have shown improved electrochemical performance in comparison to the bulk materials [42–46]. Using nanostructured materials in electrodes and electrolytes can help reduce the weight, volume and cost of materials, leading to an improvement in the efficiency and durability of LIBs.

Several studies have shown that materials can become electrochemically active electrode materials when nanosized compared to their bulk scale counterparts [47–49]. Nanomaterials can buffer the volume expansion that alloying and conversion materials are extremely susceptible to. Increased band gap energies can be offered by nanomaterials along with further band quantizing which leads to changes in their electronic behaviour [50]. Furthermore, nanomaterials offer higher power characteristics due to a higher surface-to-volume ratio providing more Li-ion storage sites.

Hierarchical nanostructured materials such as nanotubes, hollow nanospheres, and porous nanostructures can promote large contact areas between the electrode material and the electrolyte [51,52]. Nanofibres are of interest in energy storage development as, in addition to large electrolyte/electrode contact areas, they offer facile strain relaxation during cycling, short Li-ion diffusion distances, and effective electronic transport pathways. These aspects have been shown to improve both capacity and rate performance of energy storage devices [14].

## 1.6 OTHER METAL ION BATTERIES

Research into alternate metal ion battery systems is gaining traction due to the uneven distribution of Li metal and high material cost. Additionally, with increasing concerns regarding energy requirements of renewable energy sources, the expanding electric vehicle market, and high demand of portable devices, much research focus now encompasses alternate energy storage systems [53]. Li metal is the least abundant of the metal ion candidates (Table 1.1) implying that LIBs are not sustainable energy storage devices for the future despite its low oxidation potential and high theoretical capacity.

**Table 1.1: Summary of the energy storage parameters of candidate metal ion negative electrodes [15,54,55].**

| | Lithium | Sodium | Magnesium | Aluminium | Potassium | Calcium |
|---|---|---|---|---|---|---|
| Oxidation state | $Li^+$ | $Na^+$ | $Mg^{2+}$ | $Al^{3+}$ | $K^+$ | $Ca^{2+}$ |
| Atomic Weight [g $mol^{-1}$] | 6.94 | 22.99 | 24.31 | 26.98 | 39.10 | 40.08 |
| Specific Capacity [mA h $g^{-1}$] | 3862 | 1165 | 2205 | 2980 | 685 | 1340 |
| Volumetric Capacity [mA h $cm^{-3}$] | 2000 | 1000 | 3900 | 8000 | 600 | 2000 |
| Standard Potential [V vs SHE] | -3.04 | -2.71 | -2.36 | -1.68 | -2.93 | -2.87 |
| Abundance in crust [ppm] | 18 | 22700 | 23000 | 82000 | 18400 | 41000 |
| Ionic Radius [pm] | 76 | 102 | 72 | 53.5 | 138 | 100 |

Sodium ion batteries (NIBs) are a strong contender for the replacement of Li-based batteries with sodium's oxidation potential, abundance, comparable reaction mechanisms during charge transfer to LIBs, absence of alloying with aluminium, and low cost [56,57]. Despite this, the gravimetric and volumetric densities of NIBs do not exceed LIBs due to the heavier Na-ion and its larger radius (102 pm vs 76 pm). This results in slower kinetics during cycling in addition to its lower reducing potential [57,58]. Consequently, electrode materials for NIBs must possess appropriate structural characteristics to enhance electrochemical activity during sodiation.

In contrast, K-ion is a relatively poor candidate due its low theoretical capacity combined with its monovalent state indicating only one charge transfer per redox reaction like that of Li-ion and Na-ion. Despite this, K-ion does possess a slightly lower redox potential than Na-ion suggesting higher cell voltages along with lower toxicity and moderate abundance making K-ion batteries a viable candidate alternative battery system [59–61].

For Mg-ion, Al-ion, and Ca-ion more than one charge transfer takes place per redox reaction allowing for higher energy densities and specific capacities. For these metal ion systems to be viable, the electrode material must allow ion mobility.

It has been claimed that aluminium ion batteries (AIBs) are the most promising battery technology in development beyond lithium-based energy storage systems [62]. Al is the most abundant of the metal ion candidates and its volumetric capacity, 8046 mA h $mL^{-1}$, is four times higher than that of Li-ion at 2062 mA h $mL^{-1}$. Additionally, Al-ion has a smaller ionic radius than Li (53.5 pm vs 76 pm) and is capable of a three-electron redox reaction *via* the insertion/extraction of the trivalent Al-ion [22,63]. Its gravimetric density is lower than that of Li (2980 vs 3861 mAh $g^{-1}$) though higher than other metals researched for energy storage devices such as Na-ion (1165 mA h $g^{-1}$) and Mg-ion (2205 mA h $g^{-1}$) [62].

Al-based systems are proving to be quite competitive though electrolyte studies have shown that performance is limited in aqueous electrolytes due to the formation of resistive oxide layers on the Al electrode. This leads to polarisation and low cell voltage. The oxide layer on the Al metal electrode can be dissolved using alkaline electrolytes though this can lead to corrosion of the electrode itself. Strategies for overcoming this corrosion include alloying the Al negative electrode, low operational temperatures, increased current density and corrosion inhibitors [22]. Non-aqueous electrolytes, such as inorganic and ionic molten salts, have proven to be more practical offering a wider electrochemical window. In particular, room temperature ionic liquids containing a mixture of aluminium chloride and imidazolium salts have shown high $Al^{3+}$ dissolution and plating efficiencies [64,65].

## 1.7 VANADIUM OXIDE

### 1.7.1 Vanadium Oxide Stoichiometries

The diverse chemistry and catalytic performance of vanadium oxides are the result of a variety of available oxidation states (2+ to 5+) and oxygen coordination geometries. These geometries include octahedral, tetrahedral, pentagonal bipyramids and square pyramids which combine to share edge, faces, and corners in a large variety of structural arrangements [66]. An illustration of edge and face sharing of two generic square pyramids are shown in Figure 1.6(a,b). The vanadium oxide system has up to 13 distinct phases with further variation in stoichiometry and mixed vanadium oxidation states occurring in some structures, making this material family a potential electrode material for energy storage technologies [67]. These structures can be broadly categorized into two families. The first contains structures according to $V_nO_{2n+1}$ which consists of $V_3O_7$, $V_4O_9$, and $V_6O_{13}$. The second contains structures according to $V_nO_{2n-1}$ which is composed of $V_4O_7$, $V_5O_9$, $V_6O_{11}$, $V_7O_{13}$, and $V_8O_{15}$ [68].

To highlight the complexity of the vanadium oxide system, vanadium dioxide ($VO_2$) is a polymorph binary compound with known structures $VO_2$(A), $VO_2$(B), $VO_2$(M) and $VO_2$(R) [69]. A typical thermochromic material; the rutile phase, $VO_2$(R), is the most thermodynamically stable phase and possesses a reversible metal-insulator phase transition to a monoclinic phase, $VO_2$(M), at 68 °C varying the electrical, optical and magnetic properties. This variation in properties accompanying a reversible phase transition makes $VO_2$(R) a potential candidate for applications in gas sensors, optical switching devices and optical data storage. The $VO_2$(A) is metastable though it is absent during the preparation of the $VO_2$ polymorph, as such, it has been less studied. In terms of LIBs, $VO_2$ is a useful material due to its low cost, layered structure allowing for rapid Li-ion intercalation/extraction, and excellent electronic conductivity which is a key

property for high power performance [70,71]. For detailed discussion of the $VO_2$ structure and Li-ion intercalation proportions see the review by Chernova *et al.* where a range of layered vanadium oxides are discussed [72].

### 1.7.2 Vanadium Pentoxide ($V_2O_5$)

$V_2O_5$ possesses mixed valence sates with $V^{5+}$ and some $V^{4+}$ and is the most stable of the vanadium oxide structures preferentially forming when heat treated in air at elevated temperatures [73]. It has an orthorhombic unit cell of space group *Pmmn* No. 59, and is made up of a layered structure consisting of stacks of distorted $VO_5$ square pyramids that share edges to form zigzag double chains, as shown in Figure 1.6(c). These pyramids are arranged in an up-up-down-down configuration. The layers are bonded along the *z*-axis, or the (001) direction, by weak van der Waals bonds between the vanadium and oxygen of neighbouring pyramids in adjacent layers [74,75].

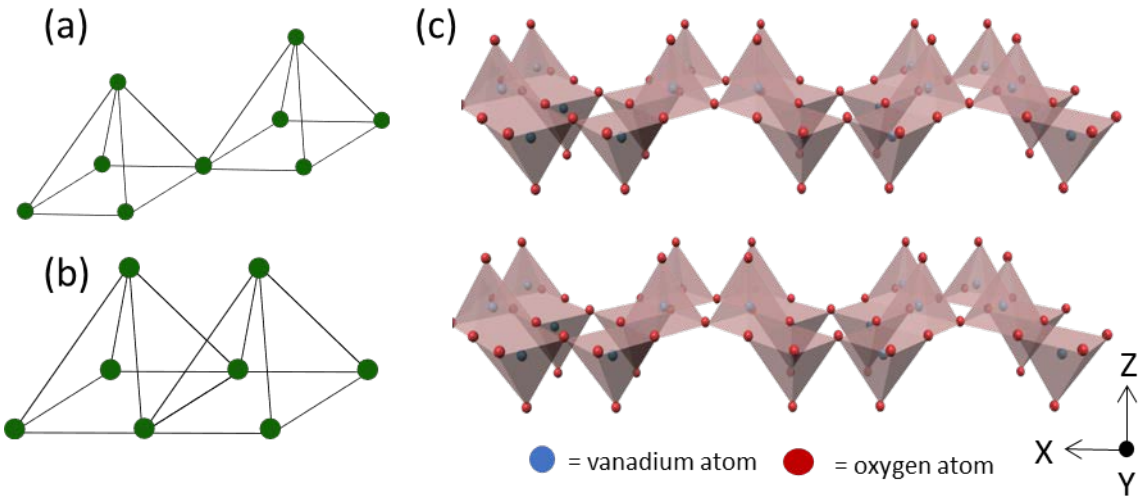


**Figure 1.6: Generic illustrations of (a) corner- and (b) edge-sharing square pyramids, and (c) structural representation of $V_2O_5$, where blue = vanadium atoms and red = oxygen atoms, showing two individual layers consisting of edge and corner sharing $VO_5$ distorted square pyramids.**

Nanostructured $V_2O_5$ is of interest for use in LIBs as it possesses lower polarisation than microstructured $V_2O_5$ due to reduced particle size. Smaller particle size as offered by nanostructuring results in increased contact surface area with the electrode and electrolyte [3,76]. There is also an improvement in the Li-ion intercalation properties due to a decrease in the diffusion distances. The combination of chemical stability, structure, and high energy density makes $V_2O_5$ a desirable material for use in electrochemical devices [77]. Additionally, $V_2O_5$ is capable of intercalating monovalent and multivalent cations making it a candidate for other metal ion battery systems [78].

### 1.7.3 $V_2O_5$ Phase Transitions

$V_2O_5$ is typically examined in the 2.0 – 4.0 V vs $Li/Li^+$ potential window and possesses two pairs of intercalation reactions referring to two Li-ions per cycle. The first Li-ion intercalation/extraction occurs in the range of 3.0 – 4.0 V vs $Li/Li^+$. In some cases, depending on material morphology, there can be strong peak splitting which suggests multiple Li-ion sites of varying energy differences for multi-stepped intercalation/extraction processes which is typical of nanoscale $V_2O_5$ [76]. This Li-ion intercalation event occurs with oxidation reaction(s) in the range of 3.3 – 3.5 V vs $Li/Li^+$ and with reduction reaction(s) in the range of 3.1 – 3.3 V vs $Li/Li^+$ which can be described by Equation 10 and Equation 11 [76,79].

$$\boldsymbol{\alpha - V_2O_5 + 0.5Li^+ + 0.5e^- \leftrightarrow \varepsilon - Li_{0.5}V_2O_5} \quad (10)$$

$$\boldsymbol{\varepsilon - Li_{0.5}V_2O_5 + 0.5Li^+ + 0.5e^- \leftrightarrow \delta - LiV_2O_5} \quad (11)$$

The ε-phase is similar to the non-intercalated α-$V_2O_5$ phase, as shown in Figure 1.7(a), with some distortion of the $V_2O_5$ layers caused by gliding of the $VO_5$ square pyramids. The δ-$LiV_2O_5$ phase is also made up of $V_2O_5$ layers but they are substantially more distorted as the $VO_5$ square pyramids have shifted by half a unit cell parameter along the

*b*-axis causing the *c*-parameter to increase [80]. The effects of this phase change on the $V_2O_5$ structure are shown in Figure 1.7(b) where the distortion in the δ-phase requires little energy so no V-O bonds are broken. Cheah *et al*. conducted a detailed study into the Li-ion intercalation of $V_2O_5$ and observed that the structural transformation of the α/ε and ε/δ phases are reversible during cycling in the range of 2.0 – 4.0 V vs $Li/Li^+$ [81].

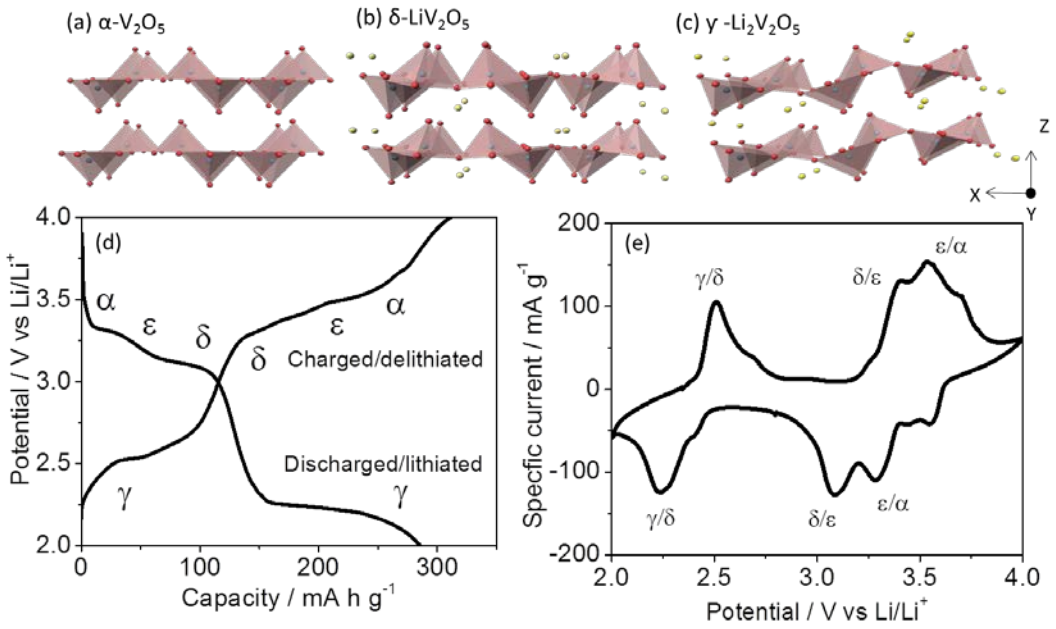


**Figure 1.7: Structural representations of (a) α-$V_2O_5$ the pristine phase, (b) δ-$LiV_2O_5$, (c) y-$Li_2V_2O_5$ showing different degrees of structural variations caused by Li-ion intercalation, (d) galvanostatic profile of $V_2O_5$ in the range 2.0 – 4.0 V vs $Li/Li^+$, and (e) cyclic voltammetry trace of $V_2O_5$ in the range 2.0 – 4.0 V vs $Li/Li^+$ with relevant phases labelled.**

The second Li-ion intercalation/extraction event occurs in the range of 2.2 – 2.5 V vs $Li/Li^+$ according to Equation 12.

$$\boldsymbol{\delta - LiV_2O_5 + 1Li^+ + 1e^- \leftrightarrow \gamma - Li_2V_2O_5} \quad (12)$$

Generally, the δ/γ phase transformation is partially irreversible as V-O bonds must be broken during the conversion from δ-$LiV_2O_5$ to form the new phase and accommodate excessive Li-ion intercalation, resulting in extensive bending and flexing of the $V_2O_5$

layers as seen in Figure 1.7(c). The presence of Li-ions combined with $V^{5+}$ reduction leads to a modification of the positive charge distribution within the oxygen ion array [82]. However, $x$ Li-ions within the stoichiometric range $0 < x < 2$ $0 < x < 2$ can be reversibly cycled in the metastable y-$Li_xV_2O_5$ phase. Once this phase is formed, y-$Li_xV_2O_5$ is retained upon further cycling [83]. These intercalation events described above can be seen with galvanostatic and potentiodynamic methods according to Figure 1.7(d,e). Several studies have compared the electrochemical performance of commercial and nanoscale $V_2O_5$ and observed comparable phase transitions and cyclic voltammogram shape as those described above for both types of $V_2O_5$. In all cases, it was shown that the nanosized $V_2O_5$ possessed lower polarisation and higher peak currents reflecting higher capacities [76,84,85].

When cycled below 2.0 V vs $Li/Li^+$, a third Li-ion is intercalated at *ca*. 1.9 V vs $Li/Li^+$ forming a rock salt structure according to Equation 13.

$$\boldsymbol{\gamma - Li_2V_2O_5 + 1Li^+ + 1e^- \leftrightarrow \omega - Li_3V_2O_5} \quad \textbf{(13)}$$

Ban *et al*. observed the formation of this material when their electrospun $V_2O_5$ was cycled in potential window of 1.75 – 3.75 V vs $Li/Li^+$ which resulted in the loss of potential steps within the capacity versus potential profile [86]. Dewangan *et al.* noted the formation of this structure in the cyclic voltammogram of their $V_2O_5$ with a strong oxidation peak at 1.9 V vs $Li/Li^+$ in the first cycle but no corresponding reduction peaks [87]. The formation of this phase results in significant capacity fading and is irreversible [80].

Due to the tuneable Li-ion intercalation events, schematically represented in Figure 1.8, it is possible to the examine the electrochemical performance of $V_2O_5$ for one Li-ion intercalation [88,89] (2.5 – 4.0 V vs $Li/Li^+$, 147 mA h $g^{-1}$), two Li-ion intercalations [90–92] (2.0 – 4.0 V vs $Li/Li^+$, 294 mA h $g^{-1}$) or three Li-ion intercalations [51,67] (1.5 – 4.0 V vs $Li/Li^+$, 441 mA h $g^{-1}$) with appropriate potential window constraints.

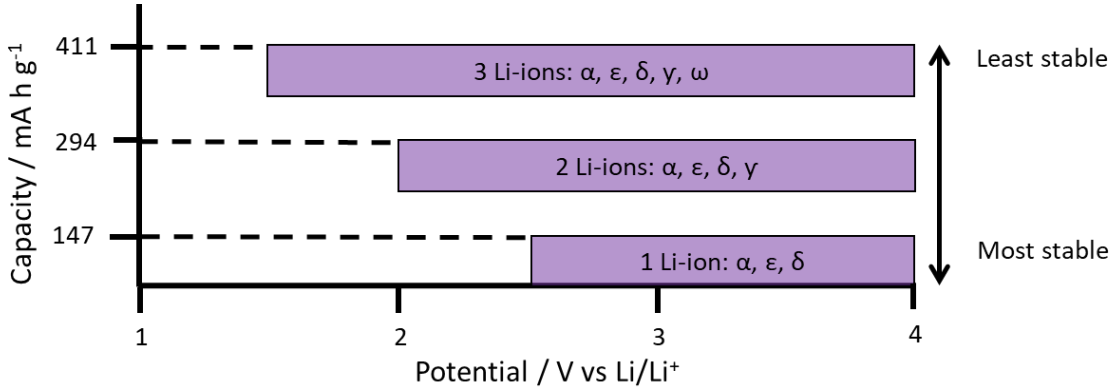


**Figure 1.8: The tuneable Li-ion intercalation events for $V_2O_5$ are dependent on potential window variations with one Li-ion for 2.5 – 4.0 V vs $Li/Li^+$, two Li-ions for 2.0 – 4.0 V vs $Li/Li^+$ and three Li-ions for 1.5 – 4.0 V vs $Li/Li^+$, adapted from [68].**

Despite this versatility, $V_2O_5$ is susceptible to structural variations and slow electrochemical kinetics associated with the intercalation/extraction of Li-ions, resulting in poor cycle stability [93]. In addition, $V_2O_5$ is limited by low electrical conductivity ($10^{-2}$ to $10^{-3}$ S $cm^{-1}$) and low Li-ion diffusion coefficients ($10^{-12}$ to $10^{-15}$ $cm^2$ $s^{-1}$) [3].

### 1.7.4 Structural Effects of Doping $V_2O_5$

While $V_2O_5$ has drawn wide attention as an electrode material, its poor capacity retention and rate performance, caused by its low electronic conductivity and low Li-ion diffusion rate, have hindered the development of this material [94]. Electrochemical properties of $V_2O_5$ can be improved by doping with other metals, which may lead to the expansion of the crystal lattice; this expansion can provide an increased opportunity for Li-ion intercalation [74].

Doping materials with other elements is undertaken to introduce a percentage of other atoms into the crystal structure [95]. This allows for the introduction of mixed-valence states into the material and the modification of the properties of the host crystal lattice leading to improved electron conductivity [8]. The mixed conductivities of the host

material and dopant are necessary for charge neutrality preservation during Li-ion intercalation/extraction. Additionally, oxygen vacancies, brought about by doping, have also been shown to increase conductivity in oxide materials [96]. The presence of increased $V^{4+}$ in $V_2O_5$ is indicative of dislocations and vacancies which may facilitate charge transfer by providing a more open structure and additional dopant energy levels along with improved Li-ion transport [97].

Zhan *et al.* doped $V_2O_5$ with $Cr^{3+}$, prepared *via* a sol-gel method and showed a prevention of an irreversible phase change of $V_2O_5$ with an improvement in cycling performance compared to that of undoped $V_2O_5$ [74]. Dopant amounts require optimisation as the effects on structural variations and phases must be considered in conjunction with the effects on electrochemical performance. For example, Li compounds, such as $Li_2O$, can form within the active electrode materials and cause large volume expansion and material decomposition which results in capacity fading [98].

The incorporation of carbon or other carbonaceous materials with another material is a common doping method which can produce a synergetic effect with the long life cycle of carbon and the defining features of the other additives [99]. Carbon has high electronic conductivity and hence improves the conductance of composite materials [100]. Producing composites of vanadium oxide has been shown to be an effective way to improve its electrochemical performance [10]. The introduction of activated carbon, carbon nanotubes or carbon shells have stabilized vanadium oxide nanostructures [3,101–105]. Graphene-incorporated vanadium oxide-based materials have shown to improve electrochemical conductivity, thermal stability and Li-ion diffusion rates in LIB systems [79,106–109]. In some cases, functionalising graphene oxide is undertaken in order to introduce hydrophilic groups (-COOH, -C=O, -OH) to the surface of the graphene sheets which act as anchoring sites for the vanadium oxide nanostructures [39]. Carbon coating is another effective method for improving electrochemical performance of electrodes by

forming protective layers on the active materials. A coating can also improve structural stability during cycling as carbon can act as a barrier to suppress pulverisation and aggregation of active particles [110].

## 1.8 NANOSTRUCTURED MATERIAL PROCESSING

### 1.8.1 Examples of Processing Techniques

Nanotechnology provides a means to produce very small and finely structured materials and devices. Consequently, processing techniques that reliably fabricate nanostructured materials are required. These techniques should have tuneable parameters to enable the exertion of some control over the resulting morphology and structure. Many nanoprocessing techniques typically make use of "top-down" or "bottom-up" procedures [15]. These procedures are illustrated in Figure 1.9. A "top down" procedure is the decomposition of bulkscale into nanoscale dimension, such as ball-milling, grinding or lithography. A "bottom up" procedure is the synthesis of nanomaterials from atoms or molecules, such as hydrothermal methods.

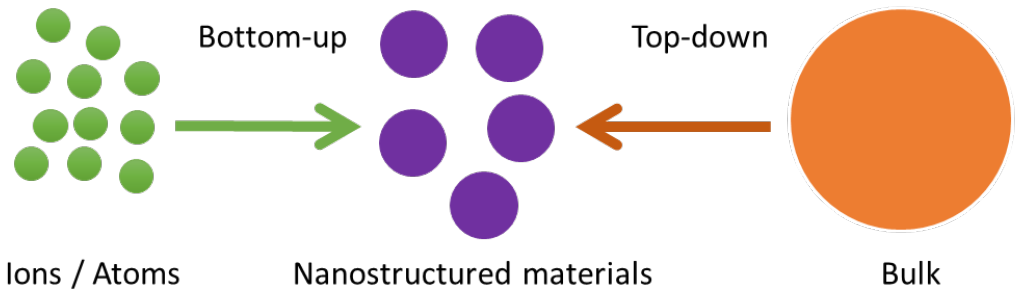


**Figure 1.9: Schematic of "top-down" and "bottom-up" approaches to nanomaterial processing.**

In order for fabrication of nanostructured materials to be convenient and financially viable, production methods need to be practical in terms of pressure and temperature

requirements, simplicity, and safety [111,112]. Liquid state processing technologies, such as electrospinning, co-precipitation, sol-gel methods, micro-emulsions and hydrothermal synthesis are popular for the development of nanoceramics. Co-precipitation is used for producing nanoscale metals, oxides, and organics using a combination of nucleation, particle growth, coarsening and agglomeration processes [113]. Reaction products are typically insoluble and require a metal salt solution, a base, and a stabilizing agent in conjunction with specified temperatures, pH, and reaction times. Micro-emulsions make use of micelles, a thermodynamic stabile and an isotropic dispersion of two non-soluble solutions, such as water and oil. The micelles, stabilized by surfactants, consist of a metal salt and a reducing or precipitation agent and are used for the formation of nanoscale particles after the exchange of the micellar cores [114]. The sol-gel process is a wet-chemical technique consisting of a chemical solution or colloidal particles that produce an integrated network. This network, collectively known as a gel, is formed during a drying process and is the result of condensation and hydrolysis reactions [115]. Hydrothermal and solvothermal methods take place in sealed containers called autoclaves under high pressures and moderate temperatures [116,117]. A range of materials can be produced such as powders, fibres, single crystals, and coatings on metals, polymers, and ceramics. Particle growth within the autoclave is controlled *via* specific temperature and pressures.

### 1.8.2 The Electrospinning Technique

Electrospinning is an effective, scalable, and inexpensive bottom-up nano-fabrication technique for synthesizing one dimensional fibres from solutions [77,118]. Electrospinning of sol-gel solutions allows uniform fibres with nanoscale diameters to be formed without further purification [12].

There are several types of precursor solutions used for preparing oxide- and polymer-based nanofibres with associated advantages and disadvantages. For example, using inorganic sols can result in fibres that are several hundred nanometres in diameter which may be too large for certain applications [119]. Controlling the diameter of electrospun nanofibres requires the precise control of the composition of the precursor solution, generally an alkoxide or salt, and the spinning parameters. The spinnability of the solution is partially dependent on the polymer used and changing the sol-gel precursor enables different types of ceramic oxides to be produced.

During the electrospinning operation, a strong electric field is applied to the tip of a capillary containing the precursor solution which is drawn into a droplet. An electrostatic field is applied between the capillary and a grounded collector such as a flat plate shown in the experimental set up in Figure 1.10. When the electrostatic force at the end of the capillary exceeds the surface tension of the droplet, a continuous fine jet of solution is ejected from the capillary and moves through the electric field to deposit on the collector [120].

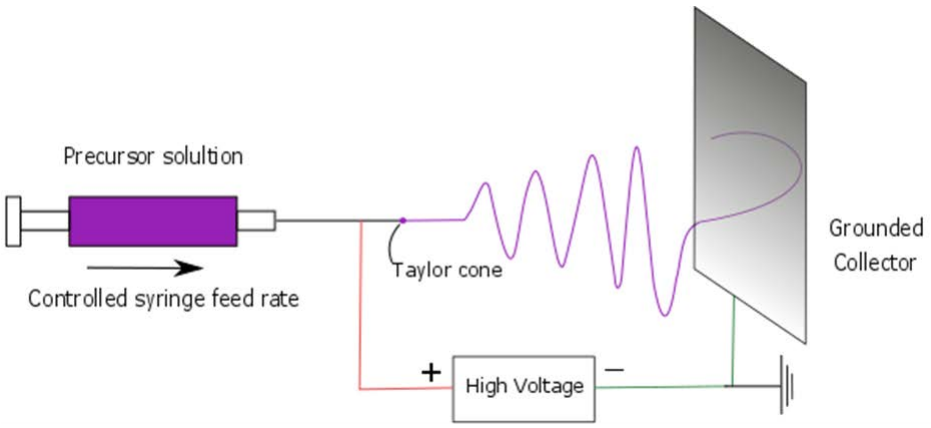


**Figure 1.10: Experimental schematic of typical electrospinning apparatus using a grounded plate collector, adapted from [121].**

Elongation of the charged droplet, called the Taylor cone, expelled from the tip of the needle into a fibre is caused by electrostatic repulsions experienced in the bends of the

lengthening droplet. The elongation and thinning of the fibre creates uniform fibres with nanometre-scale diameters [122]. The surface morphology and diameter of the fibres can be controlled by varying the set-up parameters and sol-gel components [67]. Parameters of the starting solution include viscosity, surface tension, conductivity, polymer molecular mass, dipole moment, and solution permittivity. The simplicity of the sol-gel method and the use of inexpensive equipment are advantageous traits for mass production [123]. Additionally, a standard solution can easily be doped with a secondary metal precursor prior to electrospinning.

The setup parameters include solution feed rate, distance between syringe and collector, electric field density, collector setup, and needle specifications. The environmental influences are humidity and temperature. A combination of these parameters will determine the quantity and quality of electrospun fibres. Berezina *et al.* conducted a study on electrospun vanadium oxide fibres using a theoretical method based on non-stationary electrodynamics [123]. They found that the potential difference, which is specified by the distance between the needle and substrate, is an important factor that can affect the qualitative and quantitative characteristics of the fibres. At high potentials, solution splashing took place where fibres did not reach the collector and there was an increased chance of fibre break-down between the needle and collector. Conversely, at low potentials fibre defects may increase, such as inconsistence diameters or morphologies. Fibre defects are also more likely when the distance between the syringe and collector is small as the fibres do not have enough time to solidify before depositing on the collector. Sol-gels that have high polymer to precursor ratio, resulting in a higher sol viscosity, require larger distances between the syringe and collector for fibre solidification.

After the electrospinning operation, the as-spun material is typically subjected to heat treatment. Figure 1.11 summarises three morphological changes that can occur which are hollow, hierarchical and single crystalline variations. It has been shown that heat

treatment temperature plays an important role in determining fibre morphology and can affect structural characteristics and electrochemical performances of vanadium oxides [88,124–126].

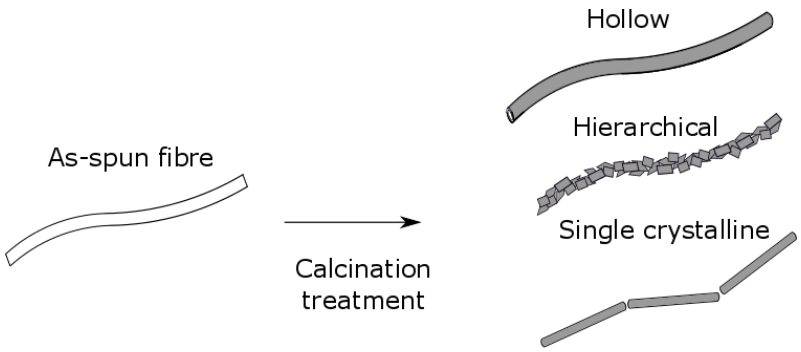


**Figure 1.11: The heat treatment of as-spun material can be used to dictate the resulting morphology to produce hollow fibres, hierarchical fibres or single crystalline rods.**

## 1.9 ELECTROCHEMICAL PERFORMANCE OF ELECTROSPUN $V_2O_5$

Due to the electrochemical nature of $V_2O_5$, it has been extensively studied as a positive electrode material while, in comparison other vanadium oxide phases have received far less attention.

The studies discussed in Section 1.9.1 to Section 1.9.6 relate to electrospun undoped $V_2O_5$ fibres with open or layered structures and controllable morphologies for research as LIB electrode materials. Electrochemical performance details are summarised in Table 1.2 for undoped electrospun $V_2O_5$ and in Table 1.3 for doped and carbon incorporated electrospun $V_2O_5$. The motivation for these studies lies with the advantages of using of fibrous nanostructures in LIBs combined with the simple, cost-effective and versatile production technique electrospinning. Electroactive materials possessing porous, hollow or hierarchical fibres are expected to exhibit the following advantages: efficient one-

dimensional electron transport in the longitudinal direction, increased Li-ion flux at the interface of the electrolyte/electrode, decrease in Li-ion diffusion length which promotes faster charge transfer and improved structural stability against volume expansion thus improving cycling stability.

$V_2O_5$ has been prepared using hydrothermal routes [37,127,128], thermal-decomposition process [76], ball milling [129], and sol-gel processes [85,130]. Table 1.4 provides a select summary of the electrochemical performance of vanadium oxides prepared by synthesis routes other than electrospinning. Comparing Table 1.2 and Table 1.3 to Table 1.4 shows that the electrochemical performance of electrospun vanadium oxides are competitive LIB positive electrodes to those prepared by other synthesis methods. Detailed analysis of Table 1.4 is omitted as it falls outside the scope of this project. For details of electrochemical performances of vanadium oxides prepared by various synthesis methods see the review by Yue and Liang [68].

An investigation of electrospun $V_2O_5$ not tested in a Li-ion coin cell was conducted by Yu *et al.* using a three-electrode cell with an electrolyte made up of 1 M $LiCoO_4$ in propylene carbonate and Pt as the counter electrode [126]. Galvanostatic cycling was conducted at a potential range of -0.5 – 0.1 V vs Ag/AgCl with a high current density of 625 mA $g^{-1}$. The lithiation capacity was initially 372 mA h $g^{-1}$, decreased by 7% in the tenth cycle and remained stable for the remaining 30 cycles. This reversible capacity is significantly higher than the theoretical capacity of 294 mA h $g^{-1}$ for bulk $V_2O_5$ assuming two Li-ion intercalations per moiety of $V_2O_5$. This electrochemical performance was attributed to improved Li-ion intercalation kinetics, high surface area, and short diffusion distances of the $V_2O_5$ fibres. As the galvanostatic testing took place in a three-electrode cell, it is likely that this contributed to the excellent performance as the excess of electrolyte would have ensured a fresh and constant flow of Li-ions to the surface of the electrodes.

**Table 1.2: Summary of electrospun undoped $V_2O_5$ with corresponding electrochemical performance for long term cycling.**

| Reference | Material | Morphology | Lithiation capacity 1st cycle (mA h $g^{-1}$) / rate (mA $g^{-1}$, C) / potential range (V vs $Li/Li^+$) | $N^{th}$ cycle / lithiation capacity (mA h $g^{-1}$) / rate (mA $g^{-1}$, C) / retention % / potential range (V vs $Li/Li^+$) |
|---|---|---|---|---|
| [124] | $V_2O_5$ | Fibres; 1000 nm | N/A | N/A |
| [131] | $H_{0.48}V_4O_{10}$ | Fibres; 250 nm | 120 / 0.1 mA $cm^{-2}$ (1.75 – 3.75 V) | N/A |
| [86] | $V_2O_5$ | Fibres; 40-70 nm, | 350 / 0.1 mA $c^{-2}$ (1.75 – 4 V) | n = 25 / 241 / 0.1 mA $cm^{-2}$ / 69% |
| [51] | $V_2O_5$ (with impurities $V_xO_2$) | Nanowires; 100-200 nm<br>Nanorods; 50-100 nm | 275 / 30 (2 – 4 V),<br>390 / 30 (1.75 – 4 V) | n = 50 / 187 / 30 / 68% (2 – 4 V),<br>n = 50 / 201 / 30 / 51% (1.75 – 4 V) |
| [132] | $V_2O_5$ | Nanowires; 300-80 nm<br>Nanorods; 70-800 nm | 300 / 35 (1.75 – 4 V),<br>230 / 35 (2 – 4 V) | n = 50 / 150 / 35 / 50% (1.75 – 4 V),<br>n = 50 / 170 / 35 / 74% (2 – 4 V) |
| [126] | $V_2O_5.nH_2O$ | Fibres; 350 nm | 377 / 655 (-0.5 – 1 V vs Ag/AgCl) | n = 40 / 340 / 655/ 90% |
| [88] | $V_2O_5$ | Nanotubes; 560 nm<br>Nanofibres; 340 nm<br>Nanobelts; 300 nm | Nanotubes; 131.2 / 2000 (2.5 – 4 V)<br>Nanofibres; 92 / 2000 (2.5 – 4 V)<br>Nanobelts; 95 / 2000 (2 – 4 V) | Nanotubes; n = 250 / 105.6 / 2000 / 80.5%<br>Nanofibres; n = 250 / 78.1 / 2000 / 85.4%<br>Nanobelts; n = 250 / 137.8 / 2000 / 85% |
| [89] | $V_2O_5$ | Nanofibres; 500-800 nm | 140 / 20 (2.5 – 4 V) | n = 30, delithiation: 127 / 20 / 91% (2.5 – 4 V) |
| [90] | T- $V_2O_5$ (template), S- $V_2O_5$ (no template) | Tubular; 1000 nm, | T-$V_2O_5$: 242 / 294, (2 – 4 V)<br>T-$V_2O_5$: 174 / 1175, (2 – 4 V)<br>S-$V_2O_5$: 207 / 294, (2 – 4 V)<br>S-$V_2O_5$: 138 / 1175 (2 – 4 V) | n = 300, T-$V_2O_5$: 218 / 294 / 89%,<br>148 / 1175 / 85%,<br>n = 300, S-$V_2O_5$: 162 / 294 / 78%,<br>77 / 1176 / 56% |
| [91] | $V_2O_5$ | Nanofibres; 200-400 nm | 139.4 / 800 (2 – 4 V) | n = 100 / 133.9 / 800 / 96.05% |
| [133] | $V_2O_5$ | Porous nanofibres; 300-500 nm | $V_2O_5$-15: 150 / 0.2 (1 C = 147 mA $g^{-1}$) (2.5 – 4 V),<br>275.2 / 0.2 C (1 C = 29 mA $g^{-1}$) (2 – 4 V)<br>$V_2O_5$-60: 144 / 0.2 C (I C = 147 mA $g^{-1}$) (2.5 – 4 V) | $V_2O_5$-15: n = 50 / 130.5 / 0.2 C (1 C = 147 mA $g^{-1}$) / 86.9% (2.5 – 4 V),<br>n=50, / 204 / 0.2 C (1 C=294 mA $g^{-1}$) / 73.8% (2 – 4 V)<br>$V_2O_5$-60: no cycling data reported |
| [92] | $V_2O_5$ | Micro/nanorods, 300 nm diameter | $V_2O_5$-550 °C: 418.8 / 50 (2 – 4 V) | n = 50 / 180.5 / 50, 43% |

**Table 1.3: Summary of electrospun doped $V_2O_5$ and carbon incorporated $V_2O_5$ with corresponding electrochemical performance for long term cycling.**

| Reference | Material | Morphology | Lithiation capacity 1st cycle (mA h $g^{-1}$) /rate (mA $g^{-1}$, C), (potential range V vs $Li/Li^+$) | $N^{th}$ cycle / lithiation capacity (mA h $g^{-1}$) / rate (mA $g^{-1}$, C) / retention %, potential range (V vs $Li/Li^+$) |
|---|---|---|---|---|
| [134] | $V_2O_5$, $Al_{0.5}$-$V_2O_5$, $Al_{1.0}$-$V_2O_5$ | Nanofibres: 100-200 nm | Ambient at 0.1 C (1 C = 350 mA $g^{-1}$): $V_2O_5$ 316, $Al_{0.5}V_2O_5$ 250, $Al_{1.0}V_2O_5$ 350.<br>At 55°C at 0.1 C, n = 2: $V_2O_5$ 285, $Al_{0.5}V_2O_5$ 360, $Al_{1.0}V_2O_5$ 350.<br>Ambient at 1C: $V_2O_5$ 114, $Al_{0.5}V_2O_5$ 240, $Al_{1.0}V_2O_5$ 208, (2 – 4 V) | Ambient at 0.1 C: $V_2O_5$ 136 / 43%, $Al_{0.5}V_2O_5$ 158 / 63%, $Al_{1.0}V_2O_5$ 298 /85%<br>At 55°C n =50: $V_2O_5$ 120 /40%, $Al_{0.5}V_2O_5$ 180 /50%, $Al_{1.0}V_2O_5$ 231 / 66%<br>Ambient at 1C: $V_2O_5$ 68 / 60% $Al_{0.5}V_2O_5$ 144 / 60%, $Al_{1.0}V_2O_5$ 146 / 70% |
| [135] | $LiV_3O_8$ | Fibres; 1 μm | 103 / 60, (0.4 – 1.6 V) | n = 50 / 72 / 60 / 70% |
| [136] | ß-$Ag_{0.33}V_2O_5$ | Nanorods; diameter 70 nm | 250 / 20, (2 – 3.6 V)<br>175 / 100, (2 – 3.6 V) | n = 30 / 180 / 20 / 72%,<br>n = 30 / 125 / 100 / 71% |
| [137] | reduced graphene oxide $V_2O_5$ nanowires (GVO) | Nanowires; 100 nm | 225 / 0.2 C (50 mA $g^{-1}$) (2 – 4 V) | N/A |
| [138] | $V_2O_5$/graphitic nanotubes | Graphitic nanotubes encapsulating $V_2O_5$; 150 nm | 224 (reversible capacity) / 150 (2 – 4 V) | n = 200 / 211 / 150 / 91.7% |

**Table 1.4: Summary of $V_2O_5$ prepared by various synthesis methods with corresponding electrochemical performance for long term cycling.**

| Reference | Material | Synthesis Method | Morphology | Lithiation capacity 1st cycle (mA h $g^{-1}$) /rate (mA $g^{-1}$, C) (potential range V vs $Li/Li^+$) | $N^{th}$ cycle / lithiation capacity (mA h $g^{-1}$) / rate (mA $g^{-1}$, C) / retention % / potential range (V vs $Li/Li^+$) |
|---|---|---|---|---|---|
| ref [37] | $V_2O_5$ | Hydrothermal | Nanobelts | 398 / NA (1.5 – 3.75 V) | n = 8 / 284 / N/A / 71% |
| ref [127] | $V_2O_5$ | Hydrothermal | Nanowires | 278 / 50 (2 – 4 V) | n = 50 / 200/ 50 / 72% |
| Ref [128] | $V_2O_5$ | Hydrothermal | Plates | 470 / 17 (1.75 – 4 V) | n = 50 / 260 / 170 / 55% |
| Ref [76] | $V_2O_5$ | Thermal-decomposition | Nanoparticles | 274 / C/20 (2 – 4 V) | n = 30 / 225 / C/20 / 82% |
| Ref [129] | $V_2O_5$ | Ball-milling | Particles | 340 / 10 / (1.5 – 3.5 V) | n = 50 / 260 / 10 / 76% |
| Ref [84] | $V_2O_5$ | Sol-gel | Nanoparticles | 249 / 300 / (2 – 4 V) | n = 50 / 229 / 300 / 92% |
| Ref [130] | $V_2O_5$ | Sol-gel | | 281 / 58 / (2 – 4 V) | n = 100 / 87 / 58 / 31% |

### 1.9.1 Electrospun Undoped $V_2O_5$ – Electrospinning Combined with Hydrothermal

Electrospinning has been used in conjunction with hydrothermal treatments of the as-spun materials by Ban *et al.* in two separate studies. In the first study, single crystalline fibres with diameters of approximately 100 nm produced an initial lithiation capacity at 0.1 mA $cm^{-2}$ in the 1.75 – 3.75 V vs $Li/Li^+$ range of 120 mA h $g^{-1}$ [131]. This capacity faded with subsequent cycling and continuously smoothed galvanostatic capacity versus potential curves were produced suggesting little Li-ion intercalation within the layered structure.

For the second study by Ban *et al.* the calcination temperature after the hydrothermal treatment was increased from 420 °C to 500 °C [86]. $H_{0.48}V_4O_{10}.2H_2O$ with a monoclinic structure was formed after hydrothermal treatment of the as-spun materials and yielded low initial capacity of 110 mA h $g^{-1}$ when delithiated to 1.75 V vs $Li/Li^+$ which decayed rapidly with further cycling. The evolution of the structure on heating was studied and it was shown that $V_2O_5$ was irreversibly formed between 450 °C and 500 °C. Galvanostatic testing of $V_2O_5$ was vastly improved with an initial lithiation capacity of 350 mA h $g^{-1}$ at a current density of 0.1 mA $cm^{-2}$ within 1.75 – 3.75 V vs $Li/Li^+$ with multi-step behaviour which is typical for a crystalline intercalation material. With subsequent galvanostatic cycles the potential steps were lost due to the formation of rock salt ω-$Li_xV_2O_5$ where Li and vanadium ions become randomised due to the formation of this phase. The capacity decreased though it remained reversible above 240 mA h $g^{-1}$ for 25 cycles despite the formation of ω-$Li_xV_2O_5$ observed around the $10^{th}$ cycle. The improved electrochemical performance was attributed to shorter diffusion lengths associated with the nanofibres and greater structural stability which lead to better capacity retention.

### 1.9.2 Electrospun Undoped $V_2O_5$ – Potential Window Variation

Electrospun $V_2O_5$ investigations show an interesting progression in potential window size variations. It was shown that the potential window affects phase change formation and cycle stability [51,88,89,132]. Both Mai *et al.* [51] and Cheah *et al.* [132] showed that cycling between 2.0 – 4.0 V vs $Li/Li^+$ yielded higher cycle stability, 68% and 74%, respectively compared to 1.75 – 4.0 V vs $Li/Li^+$ with retentions of 51% and 50%, respectively. The increased stability was attributed to absence of the irreversible ω-$Li_3V_2O_5$ rock salt phase which is formed at potentials less than 2.0 V vs $Li/Li^+$ as shown previously by Ban *et al.* [86,131].

Structural characterisation of electrospun nanowires by Mai *et al.* showed that hierarchical nanowires were made of vanadium nanorods [Figure 1.12(a)] composed of predominantly $V_2O_5$ with $V_xO_2$ impurities [51]. It was proposed by the authors that this structure kept the contact area of the active materials, conductive additives and electrolyte large allowing high capacities to be reached. The first galvanostatic lithiation and delithiation capacities when cycled within 2.0 – 4.0 V vs $Li/Li^+$ were both 275 mA h $g^{-1}$ indicating no irreversible capacity loss in the first cycle. Conversely, the first galvanostatic lithiation/delithiation capacities when cycled in the 1.75 – 4.0 V vs $Li/Li^+$ range were 361 mA h $g^{-1}$ and 90 mA h $g^{-1}$, respectively. Continued cycling showed that multistep lithiation behaviours which were still present for 2.0 – 4.0 V vs $Li/Li^+$ disappeared when cycled in the 1.75 – 4.0 V vs $Li/Li^+$ range owing to the irreversible formation of ω-$Li_3V_2O_5$. After 50 cycles, the lithiation capacities were 201 mA $g^{-1}$ at 1.75 – 4.0 V vs $Li/Li^+$ and 187 mA h $g^{-1}$ at 2.0 – 4 V.0 vs $Li/Li^+$ [Figure 1.12(b)], with higher efficiencies for the latter range.

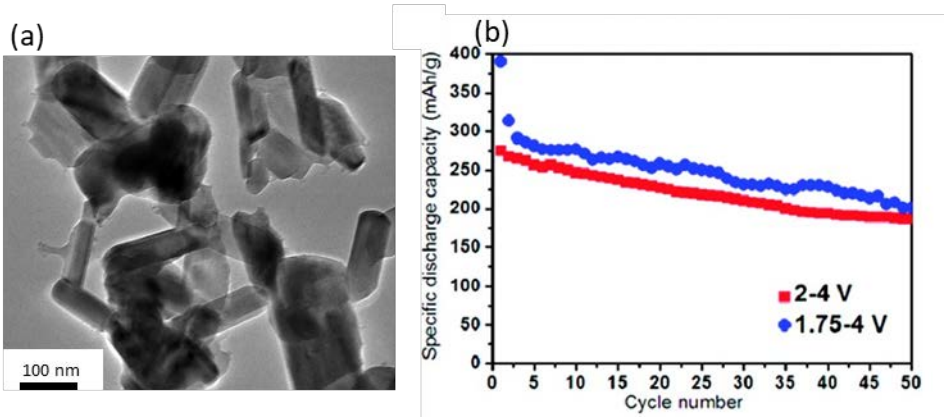


**Figure 1.12: (a) TEM of vanadium oxide nanowires with 100 nm scale bar, (b) galvanostatic cycling at 30 mA $g^{-1}$ at 1.75 – 4.0 V vs $Li/Li^+$ and 2.0 – 4.0 V vs $Li/Li^+$, reprinted and adapted with permission from [51]. Copyright (2010) American Chemical Society.**

Cheah *et al.* produced electrospun single-phase polycrystalline $V_2O_5$ nanowires with an initial lithiation capacity of 230 mA h $g^{-1}$ within 2.0 – 4.0 V vs $Li/Li^+$ and a cycle retention of 55% over 50 cycles at a current density of 35 mA $g^{-1}$ [132]. Electrical impedance spectroscopy analysis showed that the $V_2O_5$ nanowires had the potential to minimize diffusion barriers, and ionic/electronic resistances by decreasing the internal resistance and facilitating electrolyte accessibility in the positive electrode network. The electrospinning process produced single-phase $V_2O_5$ nanofibres with porous and randomly interconnected networks that allowed increased contact with the electrolyte/electrode material and facilitated the movement of Li-ions into and out of the vanadium-based cathode. It should also be noted that a high proportion of conductive agent and binder was used in the preparation of these electrodes with a ratio of 60:20:20. This is likely to have affected cycle performance and capacity retention though this was not quantified in this study.

Cycle stability was improved again by Cheah *et al.* [89] and Wang *et al.* [88] by further reducing the potential range to 2.5 – 4.0 V vs $Li/Li^+$ which prevented the formation of the γ-$Li_xV_2O_5$ phase by limiting the Li-ion insertion to 1 mol per unit formula. Cheah *et al.* presented an interesting analysis of both full- and half-cell results with spinel $Li_4Ti_5O_{12}$ as the negative

electrode with an operating potential of 1.8 V vs $Li/Li^+$. Galvanostatic analysis over 30 cycles at 20 mA $g^{-1}$ revealed capacity retention of 91% with an initial lithiation of 140 mA h $g^{-1}$ [Figure 1.13(a,b)] [89].

Wang *et al.* synthesised electrospun $V_2O_5$ nanostructures with morphologies that were dictated by calcination temperature [88]. The synthesised nanotubes and nanofibres were cycled between 2.5 – 4.0 V vs $Li/Li^+$ at a high current density of 2000 mA $g^{-1}$ over 250 cycles with stabilities of 80.5% and 85.4%, respectively, and final capacities of 106 mA h $g^{-1}$ and 78 mA h $g^{-1}$. Capacity versus potential profiles and galvanic cycling for the nanotubes are presented in Figure 1.13(c,d). However, the electrospun nanobelts were only cycled between 2.0 – 4.0 V vs $Li/Li^+$ and exhibited high cycle stability of 85% over 250 cycles at 2000 mA $g^{-1}$ with a final capacity of 138 mA h $g^{-1}$. This performance was attributed to fibre morphology and advantageous crystal orientation with suppression of the [001] direction which prevented crystal volume fluctuation and electrode aggregation. The reason as to why the nanobelts were not cycled in the reduced 2.5 – 4.0 V $Li/Li^+$ range was not specified.

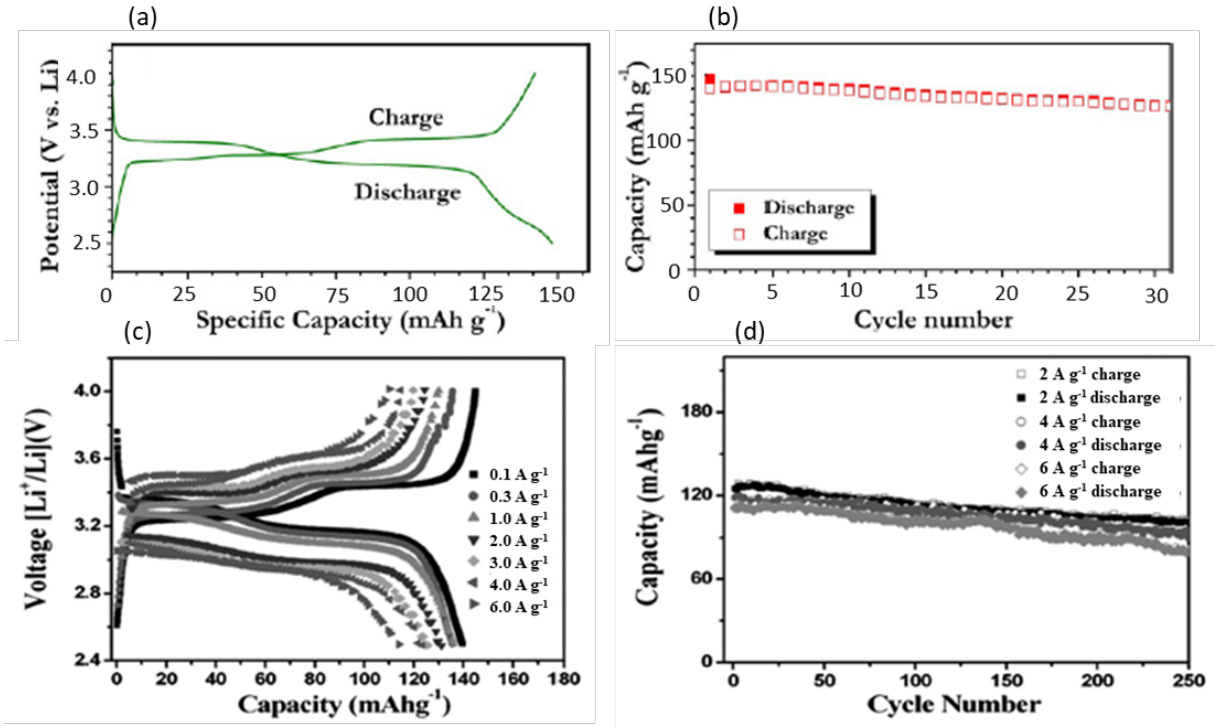


**Figure 1.13: (a) Capacity versus potential profiles of $V_2O_5$ nanofibres over 2.5 – 4.0 V vs $Li/Li^+$ at 20 mA $g^{-1}$, (b) galvanostatic cycling of $V_2O_5$ nanofibres at 20 mA $g^{-1}$ over 250 cycles at various current densities, adapted and reprinted with permission from [89]. Copyright (2013) American Chemical Society. (c) Capacity vs potential profiles and (d) galvanostatic cycling of $V_2O_5$ nanotubes at various current densities over 2.5 – 4.0 V vs $Li/Li^+$, adapted and reproduced from [88] with permission from Wiley.**

Li *et al.* also investigated the potential window variation effects on the electrochemical performance of $V_2O_5$ that was heat treated at 400 °C for either 15 minutes ($V_2O_5$-15) or 60 minutes ($V_2O_5$-60) [133]. The electrochemical performance of $V_2O_5$-15 was investigated more extensively than $V_2O_5$-60 due the superiority of its performance with an initial lithiation capacity of 150 mA h $g^{-1}$ at 0.2 C (1 C = 147 mA $g^{-1}$) over 2.5 – 4.0 V vs $Li/Li^+$ and a capacity retention of 86.9% after 50 cycles. For the 2.0 – 4.0 V vs $Li/Li^+$ range, the initial lithiation capacity was 275 mA h $g^{-1}$ at 0.2 C (1 C = 294 mA $g^{-1}$) with a cycle retention of 73.8% over 50 cycles. $V_2O_5$-60 produced an initial capacity of 144 mA h $g^{-1}$ at 0.2 C for 2.5 – 4.0 V vs $Li/Li^+$. The improvement in electrochemical performance for $V_2O_5$-15 was attributed to residual carbon within the porous nanotubes measured at 0.37 wt% according to XPS analysis. Despite

this, no discussion of morphological changes, such as d-spacing variations or XRD refinements to compare unit cell variations between the samples were presented.

### 1.9.3 Electrospun Undoped $V_2O_5$ – 2.0 – 4.0 V vs $Li/Li^+$

As previously suggested by Yue and Liang, 2.0 – 4.0 V vs $Li/Li^+$ is the most prevalent operational window as it provides a compromise between capacity and stability [68]. The electrospun $V_2O_5$ investigations for LIBs electrodes discussed in this section were conducted over 2.0 – 4.0 V vs $Li/Li^+$.

Electrospun poly(methyl methacrylate) (PMMA) fibres were used as a template by Yu *et al*. to prepare $V_2O_5$ which was removed after heat treating at 400 °C for 6 h [90]. The resulting porous nanostructured fibres were cycled over the 2.0 – 4.0 V vs $Li/Li^+$ potential range for 300 cycles at both 294 mA $g^{-1}$ and 1175 mA $g^{-1}$ current densities with respective capacities of 218 mA h $g^{-1}$ and 162 mA h $g^{-1}$, and corresponding impressive cycle retentions of 89% and 78%. The improvement in electrochemical performance between templated and non-templated fibres indicates the extra structural stability provided by the template is beneficial for Li-ion intercalation kinetics. Despite this improvement, it does introduce another experimental step into the preparation process which may negate the simplicity of the electrospinning method.

Yan *et al.* and Zhu *et al.* added oxalic acid to the precursor solution prior to electrospinning in order to facilitate the dissolution of the vanadium precursor in the starting solution [91,92]. Fibres produced by Yan *et al.* showed impressive cycle stability over 100 cycles, when cycled at 800 mA $g^{-1}$ over 2.0 – 4.0 V vs $Li/Li^+$, with an initial capacity of 139 mA h $g^{-1}$ and cycle retention of 96% at the $100^{th}$ cycle. This performance was attributed to the porous nanostructured fibre that increased the electrolyte/electrode interface and consequently reduced charge transfer resistances. In addition, the reduced particle size, that constituted the porous nanofibres, promoted electrochemical activity and improved Li-ion kinetics.

$V_2O_5$ micro/nanorods electrospun by Zhu *et al.* proved to be very competitive with 419 mA h $g^{-1}$ at a current density of 50 mA $g^{-1}$ over 2.0 – 4.0 V vs $Li/Li^+$ [92]. However, the capacity consistently degraded to 181 mA h $g^{-1}$ with a resulting cycle retention of 43%. No indication of the rate performance was included. The as-spun material was heat treated at 500 °C, 550 °C and 600 °C though it was not clear which temperature the electrochemical performance data was obtained from. It would have been interesting to have all data included to compare energy storage capability as a function of heat treatment.

### 1.9.4 Electrospun Undoped $V_2O_5$ – Heat Treatment Effects

This section highlights the observations made with respect to heat treatment temperature variations of electrospun $V_2O_5$ in studies discussed in Sections 1.9.2 and 1.9.3. Viswanathamurthi *et al*. electrospun $V_2O_5$ and observed that fibres heat treated at 400 °C, possessed smoother surfaces compared to those heat treated at 500 °C [124]. This was attributed to the incomplete combustion of polyvinyl acetate at 400 °C. They showed *via* X-ray diffraction that fibres heat treated at higher temperatures possessed higher degrees of crystallinity and larger particle sizes.

Yu *et al*. found that the incomplete combustion of poly(vinylpyrrolidone), confirmed by thermogravimetric analysis, resulted in a small amount of residual carbon at 0.3 wt% in the electrode material. The competitive performance of the electrospun $V_2O_5$ was attributed to the residual carbon leading to a high performing positive electrode [126].

Wang *et al.* synthesised electrospun $V_2O_5$ with controllable morphologies *via* heat treatment in air which included porous nanotubes, hierarchical nanofibres, and single-crystalline nanobelts at 400, 500 and 600 °C, respectively (Figure 1.14) [88]. The electrochemical performances for these materials were presented in Section 1.9.2.

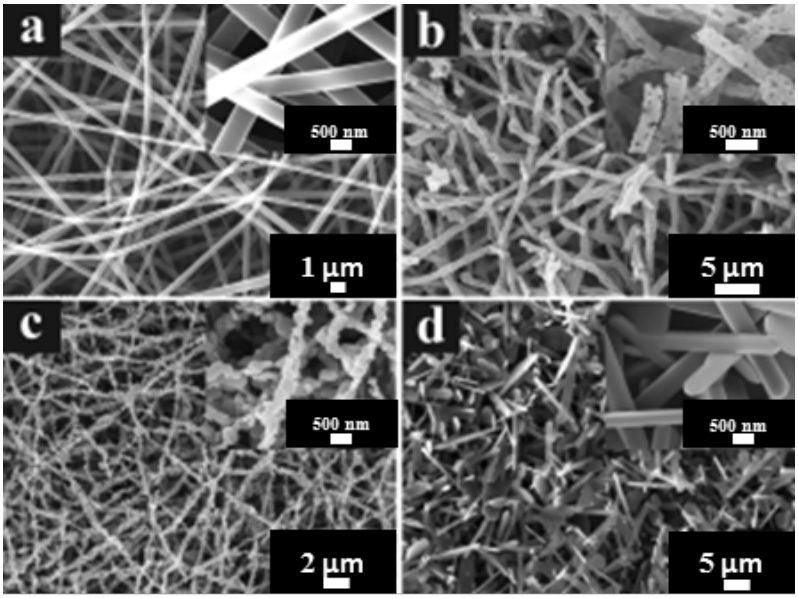


**Figure 1.14: SEM images with inset scales of 500 nm of (a) as-spun fibres, (b) porous nanofibres calcined at 400 °C, (c) hierarchical nanofibres calcined at 500 °C and (d) single crystalline nanofibres calcined at 600 °C, reproduced from [88] with permission from Wiley.**

Li *et al.* varied heat treatment time for their electrospun $V_2O_5$ at 400 °C from 15 minutes to 60 minutes, as discussed in Section 1.9.2. It was suggested that residual carbon from the polymer component of the electrospinning solution after heat treatment was responsible for the improvement in electrochemical performance for the $V_2O_5$. The incomplete combustion resulted in higher carbon content within the fibres which led to an improvement in the delithiation storage capabilities of the positive electrode.

### 1.9.5 Electrospun Doped $V_2O_5$

Doping is easily achieved in electrospinning as the dopant precursor can be added into the electrospinning solution resulting in a homogenously distributed dopant.

Cheah *et al.* continued preparing electrospun vanadium oxide for LIBs in a study that examined the effects of $Al^{3+}$ doped $V_2O_5$ at two different loadings of 20 and 33 at%, with sample names $Al_{0.5}V_2O_5$ and $Al_{1.0}V_2O_5$, on the electrochemical performance when compared to undoped

$V_2O_5$ electrospun fibres [134]. Characterisation showed porous nanofibres and Rietveld refinement revealed an increase in the *c*-parameters between undoped and $Al^{3+}$ doped $V_2O_5$ which was attributed to $Al^{3+}$ residing between the $V_2O_5$ layers. Initial lithiation capacities for undoped $V_2O_5$, $Al_{0.5}V_2O_5$, and $Al_{1.0}V_2O_5$ at 35 mA $g^{-1}$ were 316 mA h $g^{-1}$, 250 mA h $g^{-1}$, and 350 mA h $g^{-1}$ with cycle efficiencies over 50 cycles of 43%, 63%, and 85% respectively [Figure 1.15(a)]. Galvanostatic cycling at 35 mA h $g^{-1}$ over 2.0 – 4.0 V vs $Li/Li^+$ at both room temperature and at 55 °C revealed the highest capacity for $Al_{1.0}V_2O_5$ indicating that $Al^{3+}$ provides thermal stability to $V_2O_5$ [Figure 1.15(b)]. Both dopant loadings of $Al^{3+}$ delivered improved cycle efficiency compared to undoped $V_2O_5$ at current densities 35 mA $g^{-1}$ and 350 mA $g^{-1}$ when cycled at room temperature and 55 °C for 1.75 – 4.0 V vs $Li/Li^+$ as shown in Figure 1.15(c). These results, summarised in Table 1.3, suggests that the $Al^{3+}$ dopant stabilizes the $V_2O_5$ structure in a way that the irreversible phase change to the ω-$Li_xV_2O_5$ rock salt form is prevented or hindered. The electrochemical performance of this $Al^{3+}$ doped electrospun vanadium oxide is quite competitive compared to the other electrospun $V_2O_5$ studies examined in this review, especially considering the wide potential range.

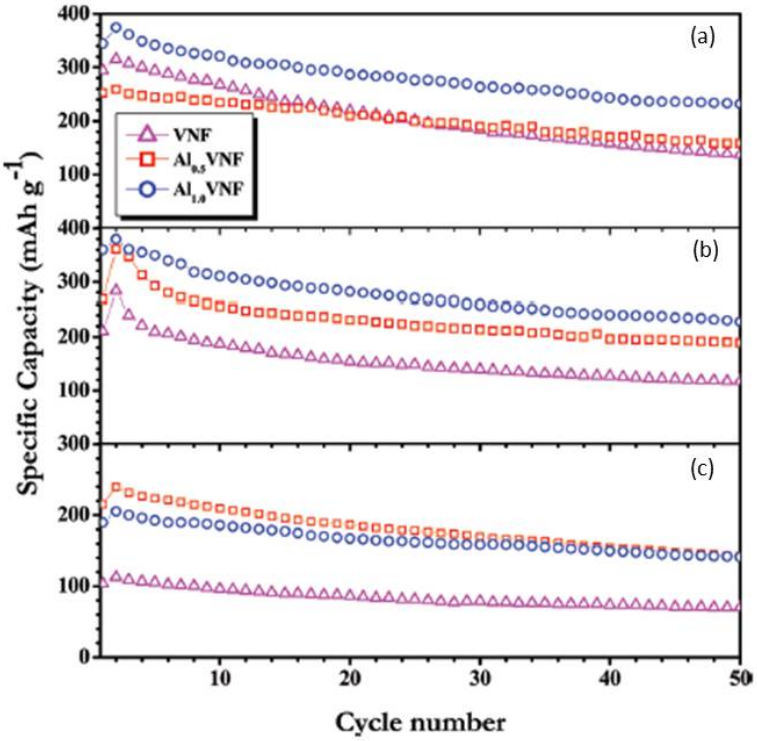


**Figure 1.15: Galvanostatic cycling of $V_2O_5$, $Al_{0.5}V_2O_5$ and $Al_{1.0}V_2O_5$ at (a) 35 mA $g^{-1}$ at room temperature, (b) 35 mA $g^{-1}$ at 55 °C and (c) 350 mA $g^{-1}$ at 55 °C, reprinted with permission from [134]. Copyright (2012) American Chemical Society.**

Wu *et al.* synthesised ß-$Ag_{0.33}V_2O_5$ using as-spun electrospun vanadium oxide for hydrothermal treatment with $AgNO_3$ [136]. Electrospinning before hydrothermal treatment allowed increased contact area between the as-spun fibres and $AgNO_3$ permitting a complete reaction to produce ß-$Ag_{0.33}V_2O_5$ despite adding in an extra experimental step. Galvanostatic analysis showed improved cycle performance compared to other silver doped vanadium oxide nanostructures referenced in their study. At 20 mA $g^{-1}$ and 100 mA $g^{-1}$ the initial capacities were 250 mA h $g^{-1}$ and 175 mA h $g^{-1}$ respectively with cycle efficiencies of 72% and 71% over 30 cycles in the 2.0 – 3.6 V vs $Li/Li^+$ range.

Despite the competitive performance of electrospun doped $V_2O_5$, there is a significant lack of these materials present in the literature. This presents a potential path of investigation for the improvement of $V_2O_5$ as an electrode material *via* electrospinning due to the relative ease of

dopant addition to the starting solution combined with the interesting role that the dopant plays within the $V_2O_5$ structure.

### 1.9.6 Electrospun $V_2O_5$ with Incorporated Carbon-based Materials

Electrospinning of vanadium oxide with subsequent carbon treatment is not particularly prevalent in the literature with only two studies, to the best of the authors' knowledge, in this section.

Pham-Cong *et al.* electrospun $V_2O_5$ nanowires and mixed them with reduced graphene oxide, according to Figure 1.16(a), to create a composite that possessed the advantages of both vanadium oxide and graphene [137]. Electrochemical performance of the composite compared to the undoped $V_2O_5$ nanowires over the 2.0 – 4.0 V vs $Li/Li^+$ range was improved. However, the improvement was not by a significant amount, with the composite experiencing capacity decrease continuously over 30 cycles at 0.2 C. The value associated with 1 C in terms of mA h $g^{-1}$ was not specified. Consequently, it is assumed here that 1 C to equal to the approximate theoretical value of $V_2O_5$ for the intercalation of 2 mol Li-ions which is approximately 300 mA h $g^{-1}$. A rate performance test revealed that the composite did show good rate capability of 25 mA h $g^{-1}$ at 5 C though both samples did not show any electrochemical response at 10 C [Figure 1.16(b)]. Coulombic efficiencies were shown to be very high for the composite, around 98% over the entire rate performance tests which totalled 60 cycles with 95% for the undoped $V_2O_5$ nanowires. Long term galvanostatic cycling was not included in this study. The improvement was attributed to increased conductivity due to the presence of graphene which also facilitated volume control during Li-ion movement in the composite material. This study shows that there is room for improvement of electrospun vanadium oxide and the incorporation of carbon for use in LIBs.

Kong *et al*. also produced a $V_2O_5$ composite using electrospun $V_2O_5$ nanosheets that were encapsulated in chemical vapour deposited graphitic carbon layers [138]. The resultant nanotubes were woven into flexible free-standing sheets and then used directly as positive electrodes for LIBs. A capacity of 224 mA h $g^{-1}$ was obtained at 150 mA $g^{-1}$ (0.5 C) with a Coulombic efficiency of 92%. Cycle retention after 200 cycles was 211 mA h $g^{-1}$ with a cycle stability of 91.7%. Additionally, the composite possessed excellent rate capability with a capacity of 90 mA h $g^{-1}$ obtained at a current density of 30 A $g^{-1}$ (100 C). The good performance was attributed to not only improved conductivity afforded by the graphitic carbon but also due to the absence of the standard electrode components (binder, conductive carbon, current collector foil). This study is an interesting and valid addition to free-standing electrode device development.

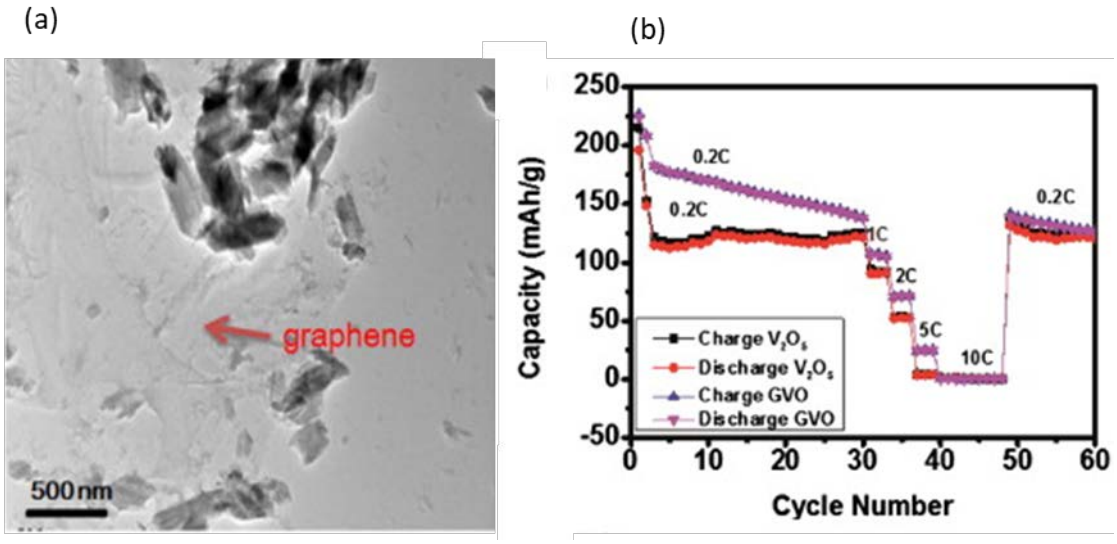


**Figure 1.16: (a) TEM image of graphene covered $V_2O_5$ particles, (b) galvanostatic cycling at 0.2 C followed by C-rate test for $V_2O_5$ fibres and graphene oxide $V_2O_5$ (GVO) from [137] with permission from Elsevier.**

A couple of studies presented in Section 1.9.4 attributed the presence of residual carbon after heat treatment from the polymer component of the electrospinning solution to an improvement in electrochemical performance [126,133]. It is then logical that the incorporation of carbon

into electrospinning is a viable method to achieve improvements in both capacity and cycle stability.

## 1.10 SUMMARY

This chapter started with the motivation for this project and its relevancy by explaining that LIBs have made up a significant portion of the battery market for over a decade due to their long shelf life and high energy density, in Section 1.2. Furthermore, it is vital that effective energy storage technologies be continuously developed to address society's growing energy demand. However, the discussion of the electrochemistry of LIBs and other metal-ion energy storage systems in Sections 1.3, 1.4, 1.5, and 1.6 showed that most positive electrode materials, typically of the formula $LiMO_2$, can only store one Li-ion per unit formula, which drastically limits stored energy and leaves them susceptible to kinetic problems that arise from slow ion diffusion and poor electrical conductivity. Vanadium oxide was introduced as a candidate electrode material in Section 1.7 as it capable of multiple electron transfers within its layered structure. Nanosizing of materials has proven to be a viable way forward in improving electrode performance. Despite this, the use of nanostructured materials often results in increased side reactions during cycling due to high surface areas. Consequently, defined structures are used to enable all advantages of nanostructures. Defined hierarchical structures in the form of fibres can be produced *via* the electrospinning technique as shown in Section 1.8 and has been shown to promote Li-ion transport from the electrolyte to the active material surface, reduce Li-ion diffusion distances and alleviate volume expansion during cycling.

Section 1.9 explored in detail the literature featuring electrospun $V_2O_5$ as an electrode material for LIBs. Undoped electrospun $V_2O_5$ has proven to produce competitive performances by investigating heat treatment temperatures and varying the operational potential window which controls the extent and reversibility of lithiation. The studies analysed in this literature review

presented a range of cases where electrospun vanadium oxide was produced in either a single-step process (i.e. just electrospinning) or a two-step process (i.e. electrospinning and hydrothermal treatment).

The common aspects of these studies relating to electrospun $V_2O_5$ discussed in this chapter were the open particle network produced from the electrospinning process providing increased contact between the positive electrode and a decrease in Li-ion diffusion pathways.

Controlling the number of Li-ions intercalated into the vanadium oxide *via* potential range variations presented an evolution in cycle stability investigations. The two Li-ion intercalation mode (2.0 – 4.0 V vs $Li/Li^+$) is the most adopted mode for electrospun $V_2O_5$-based electrodes.

This thesis first aims to further investigate the effects of process parameter variation, *via* heat treatment temperature and starting solution polymer content on the resultant electrospun $V_2O_5$ fibres in Chapter 3. Despite the competitive performances of electrospun doped $V_2O_5$ discussed in this chapter, there is a significant lack of these materials present in the literature. Consequently, this thesis also aims to address this gap in the literature by studying the structural and electrochemical properties of various doped $V_2O_5$ fibres for LIBs, with emphasis on the structural stabilisation and electronic conductivity effects brought about by the addition of a dopant material. In Chapter 4 the structural and energy storage properties of electrospun $V_2O_5$ are compared to approximately 10 at% $Ba^{2+}$ and $Ti^{4+}$ doped equivalents. The investigation behind the effects and roles that dopants play on electrospun $V_2O_5$ continues in Chapter 5using 2 at% $Na^+$, $Ba^{2+}$ and $Al^{3+}$ dopants.

# Chapter 2 Experimental Methods

## 2.1 INTRODUCTION

This chapter introduces the experimental methodology used in this project. Experimental parameters and equipment specifications are included to emphasise the consistency of results gathering between the materials discussed in Chapter 3, Chapter 4 and Chapter 5. Where there is variation in experimental parameters between materials in the afore mentioned chapters, justification is outlined herein where appropriate.

The synthesis methodology is outlined first and includes the preparation of the electrospinning solution, details of the electrospinning setup and calcination parameters. The characterisation of the electrospun fibres are divided into the structural and electrochemical techniques. Structural characterisation included Powder X-ray Diffraction, X-ray Photoelectron Spectroscopy, Scanning Electron Microscopy, Transmission Electron Microscopy, Energy Dispersive X-ray Spectroscopy, Brunauer, Emmet and Teller Surface Area Determination, Thermogravimetric Analysis, and Pair Potential Calculations. The electrochemcial charaterisation section starts with the process undertaken for electrode preparation with relevant parameters. The electrochemical techniques employed were Cylic Voltammetry, Galvanostatic Cycling and Electrical Impedance Spectroscopy. The chapter concludes with a summary outlining the order of charaterisation undertaken in the relevant experimental chapter.

## 2.2 SYNTHESIS METHODOLOGY

The nanostructured vanadium oxides fabricated in this project were produced *via* electrospinning with a series of changing system variables to produce a range of vanadium-

based oxides. This technique, while simple and cost-effective, is capable of producing nanoscale particles within a fibrous hierarchical structure [119].

### 2.2.1 Electrospinning solution preparation

The sol-gel (referred to as the starting solution from here on) for the electrospinning process consisted of a solvent, an organometallic precursor and a polymer. For doped systems, there was a secondary organometallic precursor. The synthesis method used is unique in its simplicity with few experimental steps required. Forced hydrolysis of the vanadium precursor was avoided, by limiting its exposure to air and water, and heating of the sol-gel to promote precursor dissolution could also be omitted [90].

All chemicals were received and used without further purification. A standard undoped starting solution in all chapters consisted of 1 g of a vanadium precursor, vanadium oxytripropoxide (Sigma-Aldrich, 98%), 1 g of ethanol (Chem-Supply, 96%) and 0.3 g of polyvinyl acetate (PVAc) (Mw 140,00 g $cm^{-3}$, Sigma-Aldrich) which was prepared by stirring for *ca*. 3 h or until the PVAc was completely dissolved to form an orange transparent viscous solution. The PVAc provided a template for the formation of the fibres. Unwanted hydrolysis of the vanadium oxytripropoxide was suppressed by limiting exposure to air and eliminating the addition of water. This was achieved by layering the vanadium precursor under the ethanol prior to stirring. Consequently, prolonged stirring was not necessary.

Stoichiometric calculations were used to determine the correct amount of dopant precursor, as an atomic percentage (at%), to add to the starting solution according to Equation 14.

$$\boldsymbol{m_d = at\,\% \times m_v \times \frac{M_d}{M_v}} \tag{14}$$

Where $m_d$ is the mass (g) of the dopant precursor, *at %* is the atomic percentage written as a decimal, $m_v$ is the mass (g) of the vanadium precursor, $M_d$ is the molecular weight (g $mol^{-1}$) of

the dopant precursor material and $M_v$ is the molecular weight (g $mol^{-1}$) of the vanadium precursor.

For the 10 at% doped materials featured in Chapter 4, 0.116 g of titanium (IV) isopropoxide (Sigma-Aldrich, 97%) or 0.126 g of barium oxide (AJAX Chemicals, 90%,) were added to the standard vanadium oxide starting solution and stirred to obtain a homogeneous mixture. The $Ti^{4+}$ starting solution was transparent and dark orange in appearance while the $Ba^{2+}$ starting solution was a cloudy and yellow suspension.

For the 2 at% dopant materials featured in Chapter 5, 0.0067 g of sodium acetate (Sigma-Aldrich, > 98%) was added to the vanadium oxide sol-gel and stirred to obtain a homogeneous mixture. For a 3 at% dopant amount, 0.0126 g of barium oxide (AJAX Chemicals, 90%,) or 0.017 g of aluminium isopropoxide (Sigma-Aldrich, 98%) were added. The $Na^{+}$ solution was transparent and dark orange in appearance while the $Ba^{2+}$ and $Al^{3+}$ solutions were cloudy yellow suspensions.

### 2.2.2 Electrospinning Setup

A schematic of the electrospinning set up is shown in Figure 2.1(a) which shows a syringe and needle containing the starting solution, aluminium foil-coated drum and a high-voltage DC power supply. A photo of the experimental set up is shown in Figure 2.1(b) which contains a syringe pump (KD Scientific 78-9100 KDS-100-CE) loaded with a syringe (5 cc) and a needle (Terumo 23 Gauge). The starting solution was fed through the needle at a predetermined rate of 2 mL $h^{-1}$, which was controlled by the syringe pump. The positive (red) electrode of the power supply (Gamma High Voltage Research Inc.) was connected to the needle and the earthed electrode to the collector drum, which were approximately 10 cm from each other, to produce a strong electric field of 22 kV between them.

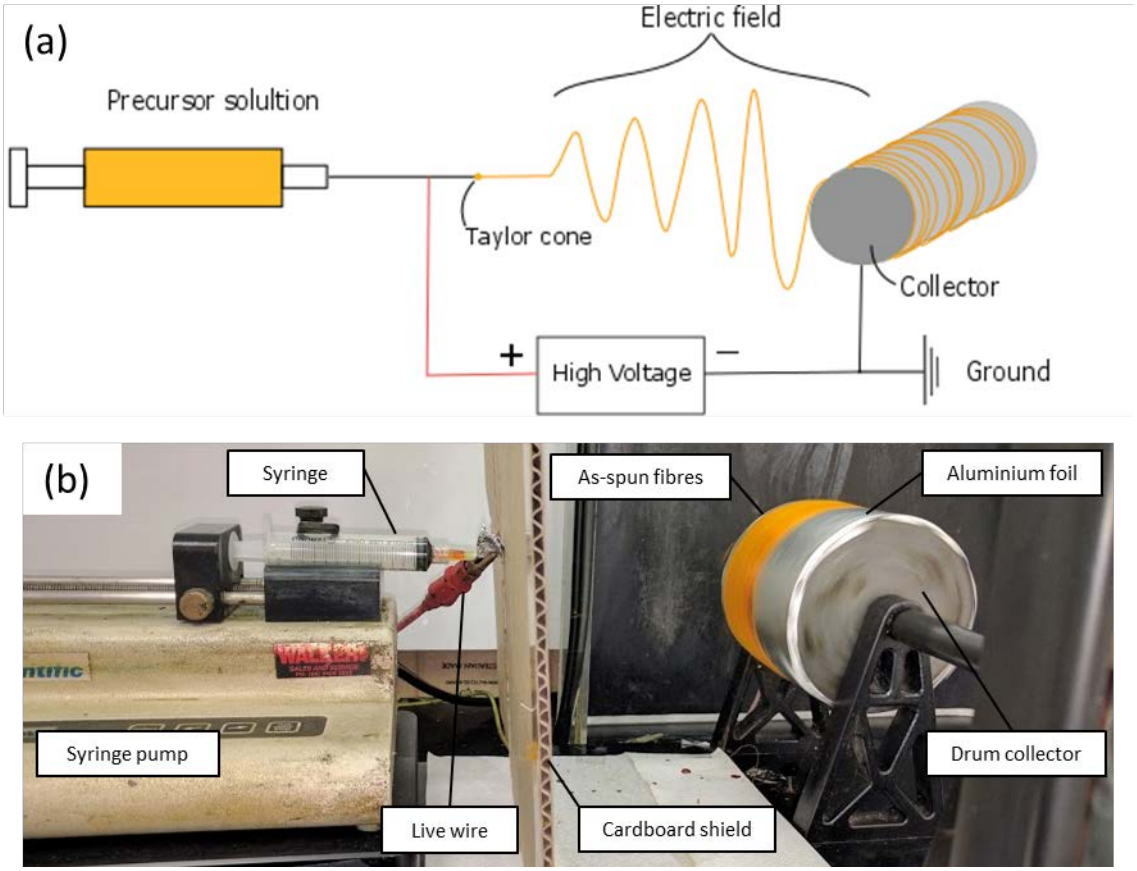


**Figure 2.1: (a) Experimental schematic of the electrospinning procedure where the starting solution in the syringe was ejected at a constant rate over approximately 10 cm through the electric field and deposited on an aluminium foil-coated rotating drum collector. (b) A photo of the electrospinning experimental set up with the major components labelled which also included a cardboard shield between the syringe and the collector to assist in insulating the syringe pump.**

After the electrospinning process was complete, the as-spun fibres were gently scraped from the aluminium foil-coated drum with a spatula. The aluminium foil was used to assist in the collection of as-spun fibres. Alignment of as-spun fibres could be facilitated to a certain extent with the rotating collector though complete alignment of fibres was limited due to the nature of the electric field which caused random orientation of the fibres as they whipped through it. Despite this, alignment of the fibres was not the primary goal in this project, rather a rotating drum served as an effective collection method. Others have shown the merits of aligning electrospun fibres, especially in tissue biotechnology research [139–141] though in this project

it was deemed unnecessary as the fibres were later vigorously mixed to separate them during the electrode fabrication step.

### 2.2.3 Calcination Procedure

The as-spun fibres were calcined after collection. During calcination, a material is subjected to high temperatures to remove volatile substances *via* combustion, and to convert it to an oxide equivalent without melting the material. Calcination of the as-spun fibres was undertaken to remove the polymeric and organic substances from the sol-gel polymer network to form a metal oxide network. Calcination time, temperature and atmosphere can heavily influence the structural characteristics and hence alter the electrochemical characteristics.

Typically, throughout this project, as-spun fibres were collected and calcined in air in a single pyrolysis step at 500 °C for 2 h at a heating rate of 3 °C $min^{-1}$ (furnace: SEM, SA Pty Ltd Cat No 1022). However, in Chapter 3.1, the structural and electrochemical properties of electrospun $V_2O_5$ were investigated *via* variation of the calcination temperature from 500 °C to either 450 °C or 550 °C. All other calcination parameters were kept constant.

## 2.3 STRUCTURAL CHARACTERISATION

### 2.3.1 Powder X-ray Diffraction

Powder X-ray Diffraction (PXRD) provides information about the molecular and atomic arrangements of the material under inspection [142]. Diffraction occurs when an incoming x-ray beam passes through a material and encounters a series of regularly spaced crystal planes which causes the beam to scatter. If scattering occurs, then the material possesses interplanar spacings that are comparable to the phase and magnitude of the x-ray beam. X-rays have high

energy and short wavelengths that are on the order of the atomic spacings for solids. The necessary conditions for diffraction are described by Bragg's Law detailed in Equation 15.

$$\boldsymbol{n\lambda = 2d\,sin\theta} \tag{15}$$

Where *n* is the order of diffraction as an integer, $\lambda$ is the wavelength (Å) of the incoming x-rays, *d* is the interplanar spacing (Å) and θ is the angle (°) between the planes. If these conditions are not satisfied, then a low intensity diffracted beam will be registered by the collector which reveals destructive interference. Bragg's Law is schematically represented in Figure 2.2 which shows that reflection only occurs at defined angles for constant wavelength and known lattice plan *d*.

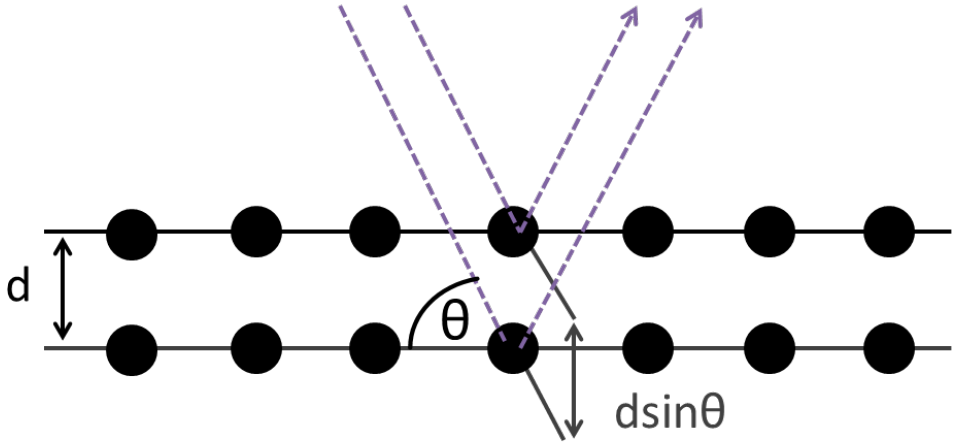


**Figure 2.2: A schematic of Bragg's Law schematic representing the conditions necessary for diffraction.**

Crystallite size (D) can be determined using the width of a diffraction peak in an XRD pattern according to the equation developed by Scherrer [143] (Equation 16):

$$\boldsymbol{D = \frac{k\lambda}{\beta cos\theta}} \tag{16}$$

Where D is the apparent crystallite size (nm), $\lambda$ is the wavelength (nm) of the incoming x-rays, *b* is the broadening of the peak (°) at full-width at half-maximum (FWHM) and θ is the Bragg angle. The Scherrer constant (*k*) is a shape factor that acts as a dimensionless constant based on the shape of the crystals and focal properties of the equipment. Crystallite sizes calculated in

this project used a shape factor 0.9. Typical *k* values are 0.89 for spherical crystallites, 0.98 for cubic crystallites or, if crystallite size is unknown, 0.9 is appropriate to use [144]. For a more comprehensive explanation of the PXRD method see [145].

Reference XRD data for $V_2O_5$ were obtained from the Inorganic Crystal Structures Database (ICSD) with collection code 60767. The space group was *Pmmn* with unit cell parameters of *a* = 11.512 Å, *b* = 3.564 Å, *c* = 4.368 Å. Unit cell parameters of the nanostructured fibres were determined *via* le Bail refinement in Chapter 3 and Chapter 4 using the Jana2006 crystallography program (version 25/10/2015) with the space group and unit cell parameters mentioned above as baselines. In Chapter 5, cell parameters were determined *via* Rietveld refinement using MAUD software [146]. For both refinement methods, optimisation of the unit cell was performed to improve the goodness of fit (GOF) and reduce the residual factors $R_P$ and $R_{WP}$, which indicate how well the refined structure matches the experimental data. $R_P$ is the profile factor that relates to the residual error which is directly calculated from the difference between the structural model of the PXRD and the experimental data. $R_{WP}$ is the weighted profile factor which increases the weight of a particular location within the fitted model based on $R_P$ [147].

Le Bail and Rietveld refinements are similar methods used to determine unit cell parameters in this thesis where phase information is available and reflection intensities are derived from the unit cell and space group. For le Bail refinement no crystal structure data is available and peak intensities are not refined. Rietveld refinement can be used quantitative analysis, such as determining the amount of an impurity phase, as is the case in Chapter 5.

PXRD spectra of the electrospun fibres in Chapter 3 were collected using a Bruker D8 with Cu-Kα radiation (λ = 1.54 Å), a step size of 0.02 ° and step time of 1 s for scattering angles (2θ) of 10-80 °. PXRD electrospun fibres in Chapter 4 and Chapter 5 was performed using a STOE StadiP diffractometer using Mo-Kα radiation (λ = 0.71 Å) over the 2θ range of 5 to 40° with a step size of 0.5 ° and step time of 30 s. Different x-ray sources were used for the chapters

featuring doped materials to produce a clearer spectra which allowed easier identification of any impurity phases present.

### 2.3.2 X-ray Photoelectron Spectroscopy

X-ray Photoelectron Spectroscopy (XPS) measures the chemical composition of a material's surface and is used to determine the elemental composition, empirical formula, chemical state and oxidation state of the elements present at the surface. The kinetic energy of the reflected electron signals are obtained from depths of 10 – 100 Å and includes contributions from both photoelectron and Auger electron lines [148]. For a more comprehensive explanation of the XPS technique see [149].

Surface composition measurements and the oxidation state of the elements featured in Chapter 4 and Chapter 5 were carried out using a Thermo Scientific$^{TM}$ K-Alpha$^{TM+}$ X-ray photoelectron spectrometer with a monochromatic Al-Kα source. Results were then fitted using Avantage software [Chapter 4] or CasaXPS$^{TM}$ software (version 2.3.16) [Chapter 5]. The binding energy scales were calibrated using the adventitious C 1s peak (285.0 eV), which represents the thin layer of carbonaceous material present on the surface of material samples, or to O 1s (530.0 eV) for $V_2O_5$ and to vanadium (517.4 eV) for the doped samples. The elemental peaks were fitted using Gaussian/Lorentzian line shapes and the relative elemental concentrations were calculated using peak area determination with the appropriate shape factor.

### 2.3.3 Scanning Electron Microscopy

During Scanning Electron Microscopy (SEM) a focussed beam of electrons, called primary electrons, is scanned over the surface of material to gain information about the surface topography and morphology. The interaction of the electron beam with the surfaces causes high energy backscattered electrons and low energy secondary electrons to be emitted from the

material surface [142]. Secondary electrons are produced from inelastic collisions though the scattering of loosely bound surface electrons. As the secondary electrons escape, the detection intensity determines whether there are many electrons detected, producing a light greyscale image, or few electrons detected, producing a darker greyscale image as illustrated in Figure 2.3. Secondary electrons have a low field of depth and shallow interaction with the surface due to their low energy which results in high sensitivity to topography characteristics [150].

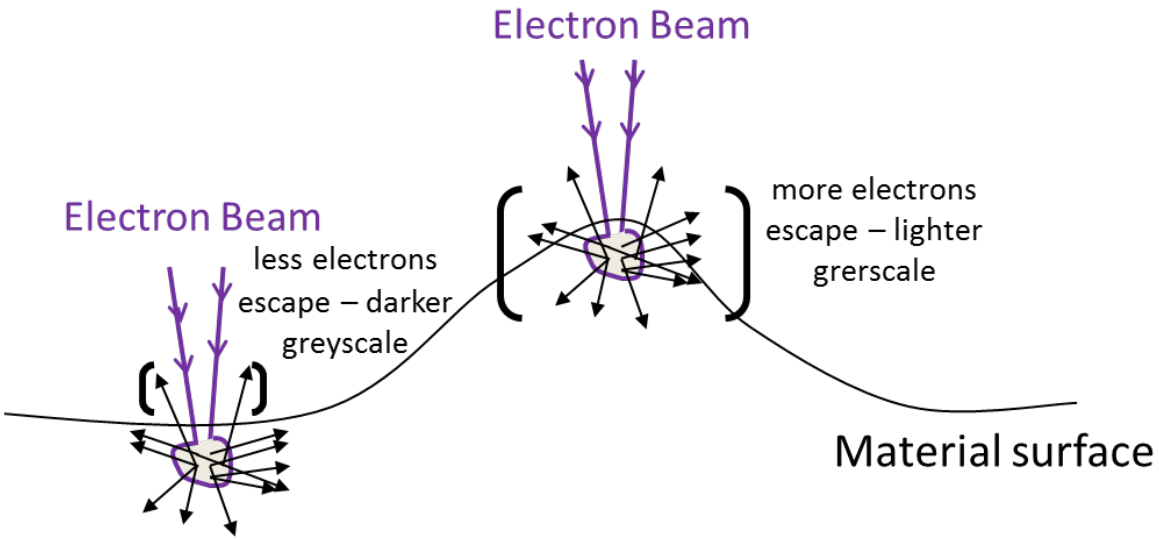


**Figure 2.3: A schematic representing the variations in detected greyscale intensities produced during SEM analysis where the number of secondary electrons originating from the material surface is dependent on topography allowing for variations in morphology to be determined.**

SEM images, in Chapter 3 and Chapter 4, of the fibres were taken with a Zeiss UltraPlus Field Emission EM, to study the extent of the morphology, fibrosity, and grain structure. In Chapter 5 the SEM images were taken with a JOEL FESEM JSM6700F. Reported dimensions of the fibres in this project were determined using ImageJ *via* pixel counting using the scale bar for distance determination.

### 2.3.4 Transmission electron microscopy

Transmission Electron Microscopy (TEM) allows for extremely fine imaging within the order of 0.3 μm to 0.1 nm using a focussed beam of electrons for viewing of lattice planes [151]. Electron microscopes can image a sample in real space with high resolution and provide information in reciprocal space of the same sample with electron diffraction patterns. The electron source is located at the top of the microscope column and is maintained under a high voltage and vacuum to ensure that a focussed beam of fast moving electrons can be directed through the sample as illustrated in Figure 2.4. The investigated sample must be carefully prepared and be of low concentration on a conductive surface to allow electron transmission through the material.

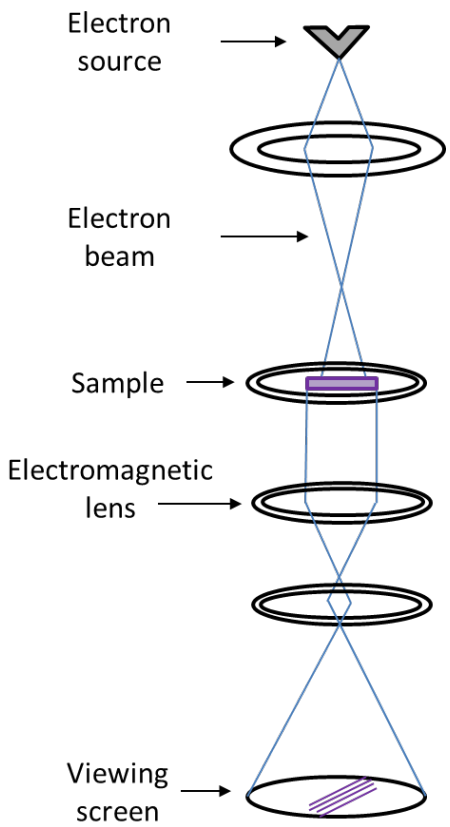


**Figure 2.4: An illustration of the TEM column with the electron source at the top that is focussed with electromagnetic lenses through the sample towards the viewing screen.**

The size and morphology of the crystallites in Chapter 4 and Chapter 5 were determined by transmission electron microscopy (TEM) using a JEOL JEM 2100 – $LaB_6$ filament. Images were taken with a Gatan Orius digital camera. Samples were prepared by dispersing in methanol followed by brief sonication and pipetting several droplets on a 300 mesh copper film grid (Agar Scientific). Reported dimensions of the fibres, particles size and lattice plane distances of TEM images were determined using ImageJ *via* pixel counting using the scale bar for distance determination.

### 2.3.5 Energy Dispersive X-ray Spectroscopy

Energy Dispersive X-ray Spectroscopy (EDS) is a simple technique that analyses the X-ray spectrum emitted from a sample that has been bombarded with focussed a beam of electrons. Analysis of the intensities of the X-ray lines allows for the identification and quantification of the elements present. Elemental mapping and point analysis is used to determine element dispersion in the sample. EDS is typically retrofitted with a SEM or TEM.

EDS point analysis was conducted on a JOEL FESEM JSM6700F to determine dopant amounts in Chapter 4 and Chapter 5.

### 2.3.6 Brunauer, Emmet and Teller Surface Area Determination

Brunauer, Emmet and Teller (BET) surface area determination is a common technique used to define surface pore distribution and specific surface area of a material *via* gas adsorption. However, it is possible that internal porosity can be misrepresented with this technique. Physical adsorption, or physisorption, describes the adherence of gas molecules to a surface to form weak bonds at pressures below the vapour pressure [152]. The measurements are calculated using an adsorption isotherm which represents the amount of gas ($N_2$) adsorbed over

a range of adsorptive pressures at a constant temperature (-196 °C for liquid $N_2$). The desorption isotherm is calculated using the removal of gas over a reduction in pressure.

Surface area measurements in Chapter 4 and Chapter 5 were determined using BET measurements with $N_2$ in a micrometrics Tri Star II 3012 analyser. Before measurements were the taken the powders were degassed at 120 °C for 12 h under vacuum.

### 2.3.7 Thermogravimetric Analysis

Thermogravimetric Analysis (TGA) is analytical method used to determine mass variations and heat flow of a sample under an applied temperature over time. The sample environment is controlled by the purge gas which can be reactive or unreactive. The TGA method is used to analyse the chemical reactions a sample undergoes with heating in a given gaseous environment by monitoring the sample mass.

A Pyris 1 (Perkin Elmer) was used for TGA analysis in Section 3.1 with a $N_2$ flow rate of 20 mL $min^{-1}$ over 40 to 500 °C with a heating rate of 3 °C $min^{-1}$ to analyse mass variations experienced by the fibres.

### 2.3.8 Pair Potential Calculations

The atomistic simulations investigating the incorporation energetics for substitutional and interstitial $Na^+$, $Ba^{2+}$ and $Al^{3+}$ ions in Chapter 5 were conducted using empirically-fitted pair-potential methods. These methods are well established for the investigation of dopants in positive electrode materials, and their details are discussed in detail elsewhere [153,154]. All calculations were performed using the General Utility Lattice Program (GULP) [155].

Briefly, all systems are described as ionic crystalline solids, and ion-ion interactions are described by a combination of long-range Coulombic and short-range interactions. The short-

range interactions for the materials in Chapter 5 are predominantly described by Buckingham potentials in Table 2.1 in the form of Equation 17 [156].

$$\boldsymbol{\phi_{ij}(r_{ij}) = A_{ij}\exp\left(\frac{-r_{ij}}{\rho_{ij}}\right) - \left(\frac{C_{ij}}{r^6}\right)} \quad (17)$$

Where $r$ is the inter-ion distance, A, $\rho$ and C are constants and $i$ and $j$ are indices of the interacting ions. Additionally, a short-range Morse potential for the vanadyl bond in $V_2O_5$, in Table 2.2, takes form according to Equation 18 [157–159].

$$\boldsymbol{\phi_{ij}(r_{ij}) = D_o(\{1 - exp[\alpha(r - r_0)]\}^2 - 1)} \quad (18)$$

Where $D_0$, $\alpha$ and $r_0$ are constants. The Morse potential is used to reproduce the short V-O1 'vanadyl' bond in $V_2O_5$, with a maximum cutoff length of 1.99 Å. The remaining equatorial V-O bonds in $V_2O_5$ are described by a Buckingham potential, whilst the V-O1 interlayer distance is reproduced using a highly repulsive Buckingham potential with a minimum $r$ of 1.9 Å. The V-O and O-O potentials have been used successfully to represent the structure of $V_2O_5$ [160] whilst the Al-, Ba- and Na-O potentials have been used to investigate a range of transition metal oxides [161]. Ion polarizability is described using the core-shell model of Dick and Overhauser [162] and the parameters used are shown in Table 2.3. Defect calculations are implemented using the Mott-Littleton scheme using region I and region II sizes of 10.0 and 25.0 Å respectively [163]. All calculations were performed in the GULP program [155].

**Table 2.1: Buckingham potentials and cutoffs used in the potential pair calculations.**

| Interaction | A (eV) | $\rho$ (Å) | C (eV Å$^6$) | $r_{min}$ (Å) | $r_{max}$ (Å) |
|---|---|---|---|---|---|
| $V^{V}$–$O_{equatorial}$ | 5312.99 | 0.26797 | 0.0 | 0.0 | 10.0 |
| $V^{V}$···$O1_{interlayer}$ | 2549.73 | 0.34115 | 0.0 | 1.99 | 10.0 |
| $V^{IV}$–O | 1260.56 | 0.34039 | 0.0 | 0.0 | 10.0 |
| O–O | 22764.30 | 0.1490 | 23.0 | 0.0 | 10.0 |
| Al–O | 2409.505 | 0.2649 | 0.0 | 0.0 | 10.0 |
| Ba–O | 4818.416 | 0.3067 | 0.0 | 0.0 | 10.0 |
| Na–O | 1271.504 | 0.300 | 0.0 | 0.0 | 10.0 |

**Table 2.2: Morse potential parameters and cutoff used in the potential pair calculations.**

| Interaction | $D_0$ (eV) | $\alpha$ (Å$^{-1}$) | $r_0$ (Å) | $r_{min}$ (Å) | $r_{max}$ (Å) |
|---|---|---|---|---|---|
| $V^{V}$–$O1_{vanadyl}$ | 10.0 | 2.302170 | 1.584 | 0.0 | 1.99 |

**Table 2.3: Core-shell model parameters and spring constants used in the potential pair calculations.**

| Species | $q_{core}$ (\|e\|) | $q_{shell}$ (\|e\|) | k (eV Å$^2$) |
|---|---|---|---|
| $V^{V}$ | 0.0 | 5.0 | 9999.9 |
| $V^{IV}$ | 0.0 | 4.0 | 9999.9 |
| O | 0.717 | -2.717 | 54.952 |
| Al | 0.043 | 2.957 | 403.98 |
| Ba | 0.169 | 1.831 | 34.05 |
| Na | 1.0 | - | - |

## 2.4 ELECTROCHEMICAL CHARACTERISATION

There are a range of electroanalytical techniques that are useful for the evaluation electrochemical properties and determining the effectiveness of energy storage devices [164]. Electrochemical techniques can be broadly divided into steady-state and non-steady-state techniques.

The basis for all electrochemical techniques involves keeping the quantities which describe the state of the interface, such as temperature, pressure and area, steady while the response of one of the electrical quantities, current or potential, is observed as the other is changed. There are two domains that are fundamental in studying the relationship between current and potential. The cathodic current domain is caused by reduction of the active species in a solvent while the anodic region results from the oxidation of the active species. The anodic domain, where metal dissolution occurs, is positive while the cathodic domain, where metal deposition occurs, is negative. The processes that lead to charge transfer are known as Faradaic processes which occur *via* redox reactions and are best studied under steady-state conditions, such as cyclic voltammetry [165].

Non-steady-state techniques involve the analysis of the electrochemical system's behaviour in response to the application of either large or small amplitude perturbations. These perturbations may be either continuous such as a sine wave, or transient in a stepwise fashion. Subsequent analysis is related to the relaxation of the perturbed system returning to an equilibrium state. Relaxation times and responses of the electrochemical of the electrochemical system vary at different rates for different processes of which the mechanisms can be analysed. Small signal analysis using a sine wave leads to the impedance of an electrochemical system. These tests are instrumental is determining charge transfer mechanisms, charge storage capability and material conductivity of an electrode within an electrochemical cell.

### 2.4.1 Electrode fabrication

The materials were tested against Li metal as this battery system is well-established and most of the cell characteristics are understood and well explained in the literature. This thesis focussed on material characterisation of the working electrode. Consequently, there was little focus on device engineering aspects which would require significantly more consideration in other metal ion battery systems.

To test materials in Li-ion coin cells the working electrode must be prepared using materials that ensure the active material can interact with the Li-ions. A conductive additive, such as carbon black, and a binding agent, such as polyvinylidene fluoride (PVDF), polytetrafluoroethylene (Teflon) or styrene-butadiene-rubber (SBR) is combined with the active material before doctor blading onto a current collector. To ensure that the electrochemical performance is reflective of the active material, electrode components must be adequately and homogenously mixed. Cu and Al foils are typically used as current collectors to minimise cost. Cu oxidises above 3.6 V vs $Li/Li^+$ while Al forms an alloy with Li below 0.6 V vs $Li/Li^+$, implying that Cu is used for low potential negative electrodes while Al for high potential positive electrodes. Alternate current collectors for the positive electrode are graphene fabrics and for the negative side, alternatives are nickel-based foams and foils [21].

After electrode preparation is complete, electrochemical investigations against Li metal are undertaken in a coin cell which is assembled in a glove box under argon according to the scheme in Figure 2.5.

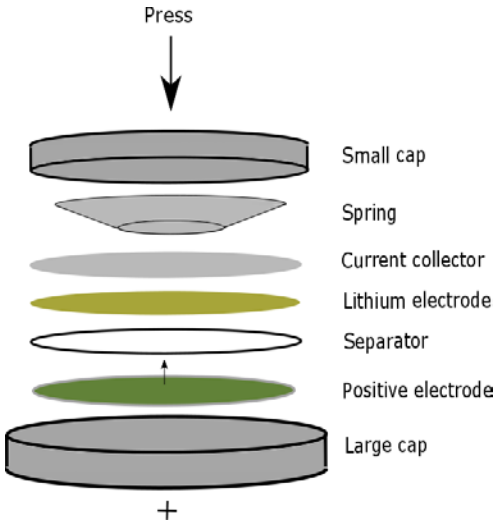


**Figure 2.5: Coin cell components aligned in assembly configuration so that no contact is made between the positive and negative electrodes.**

For the vanadium oxides in Section 3.1, the fibres were processed into positive electrodes and incorporated into coin cells for electrochemical testing. The working electrode consisted of 80 wt% active material, 10 wt% conductive agent (carbon black, Super P004, MMM Carbon), and 10 wt% PVDF (Kynar 761) in N-methyl pyrrolidinone (NMP, Sigma Aldrich). After vigorous mixing using a mortar and pestle, the mixture was doctor-bladed onto Al foil. After drying in the vacuum furnace at 120 °C, the dried doctor bladed mixtures were pressed through a roller and then 16 mm working electrode discs were cut and dried at 70 °C overnight. The electrodes were assembled into CR2016 coin cells in an argon glove box (MBraun) with oxygen and water levels below 3 ppm. Lithium foil (Hohsen Corp) made up the counter electrode with separators (glass microfibre filters, Whatman®,GF/B) saturated in 1 M $LiPF_6$ dissolved in a 1:1 v/v ratio of ethylene carbonate/dimethyl carbonate (EC/DMC) (1:1 v/v, Merck Selectipur LP40) as the electrolyte. The active mass loadings ranged from 1.0 to 2.0 mg $cm^{-2}$.

The vanadium-based positive electrodes in Section 3.2 and Chapter 4 were made up of the same mixture as those in Section 3.1 though the PVDF was stirred in NMP overnight to ensure complete dissolution followed by addition of the active material and conductive agent. After ball-milling for 30 min at 500 rpm, the mixture was cast onto aluminium foil and dried for

approximately 1 h at 70 °C. Working electrode discs were punched with 14 mm diameters, pressed with 1 ton of force for 30 s and once again dried overnight at 70 °C. Prepared electrodes were assembled into CR2032-type coin cells and all other assembly parameters were constant. The active material mass loadings were 1.0 – 2.0 mg $cm^{-2}$ for Section 3.2 and 0.9±0.1 mg $cm^{-1}$ for Chapter 4.

The vanadium-based positive electrodes in Chapter 5 were prepared using the same method as those in Section 3.1. The prepared electrodes were assembled into CR2032-type coin cells and all other assembly parameters were constant. The active mass loadings were 3.4 ± 0.2 mg $cm^{-2}$. The coin cell components used in this thesis were kept as consistent as possible and no consideration was given to varying the Li-ion coin cells or their configuration, as the investigations in following experimental chapters were focussed on the electroactive positive electrode material.

### 2.4.2 Cyclic Voltammetry

Cyclic Voltammetry (CV) is a potentiodynamic electrochemical technique commonly used in electrochemical characterisation of ion insertion electrodes made of nanostructured materials [166]. This technique gives qualitative information about the nature of the charge transfer process and the reversibility of the reactions of the investigated material. The stability and presence of phase transformations during lithiation/delithiation can be studied for crystalline materials which present as sharp peaks. Additionally, the active potential range of the working electrode can be determined.

During CV testing, the potential of the working electrode is varied linearly between two vertices, $E_1$ and $E_2$, as an input [Figure 2.6(a)] and the current response is plotted as a function of potential on a voltammogram [Figure 2.6(b)]. The shape of the voltammogram is determined by the mass transport which is influenced by equilibrium effects, such as diffusion, at the

surface. The potential distance between the peaks ($\Delta E_p$) is a measure of reversibility and Li-ion kinetics which provides an indication of the repeatability of the charge transfer process along with the ease of Li-ion movement [85].

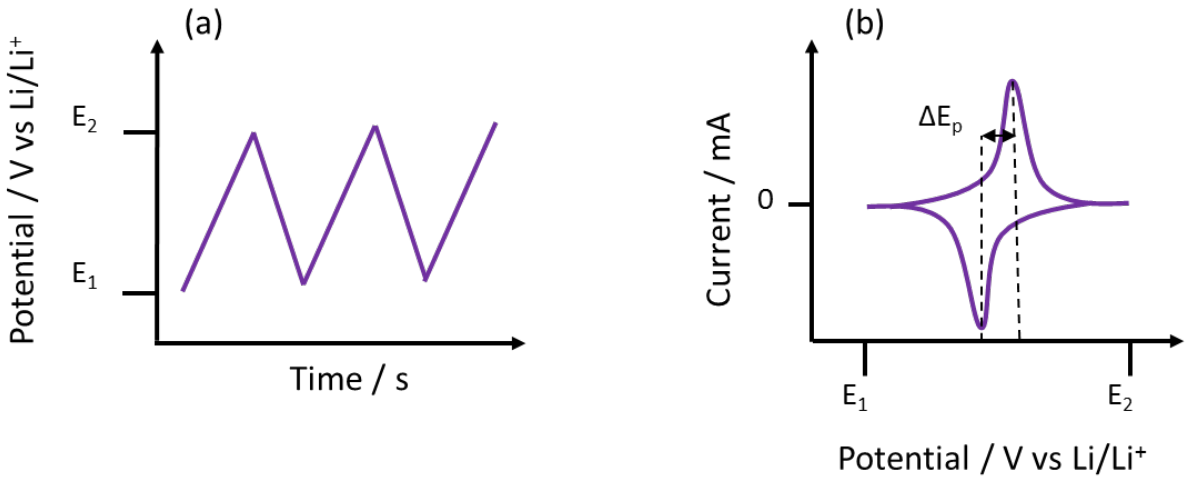


**Figure 2.6: Schematic representing the CV method where (a) an applied scan rate (mV $s^{-1}$) is inputted and cycled between two vertex potentials, $E_1$ and $E_2$, and (b) the resultant current (mA) is detected in the output.**

Cyclic voltammetry was conducted on a potentiostat (PGSTAT302, AUTO-LAB, Metrohm) over a potential range of 2.0 – 4.0 V vs $Li/Li^+$ at a scan rate of 0.15 m $Vs^{-1}$ in Chapter 3 and 0.1 mV $s^{-1}$ in Chapter 4 and Chapter 5 over two cycles.

### 2.4.3 Galvanostatic Cycling

Galvanostatic techniques are used to determine cycle stability and rate capability *via* discharge/charge tests. During a galvanostatic discharge/charge (GDC) test, a constant current is applied with respect to the working electrode's active mass between two vertex potentials [Figure 2.7(a)]. C-rate tests are used to determine the rate capability of an electroactive material by varying the current density. This test can provide information about a material's high-power

characteristics which is indicative of surface charge storage. Long-term cycling is conducted at one current density over many cycles to determine the cycle stability of an electroactive material. Capacity versus potential profiles in Figure 2.7(b) can be produced for each lithiation/delithiation sequence. The resultant shape and gradient changes in these profiles provide information about phase changes. These gradient changes are called potential steps in this thesis.

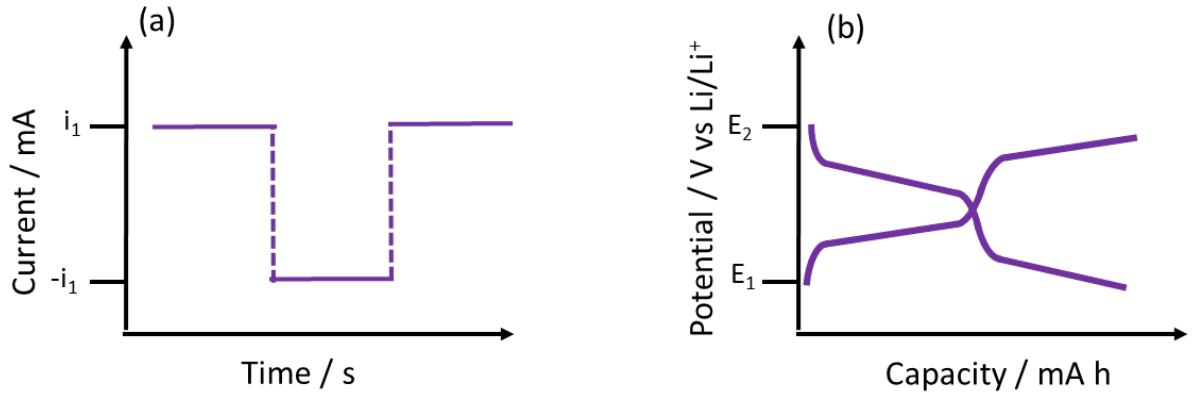


**Figure 2.7: Schematic representing the galvanostatic discharge/charge cycling method where (a) a constant current (mA) is applied between two potential vertexes, E1 and E2, and (b) the resultant capacity (mA h) is measured for each lithiation/delithiation sequence.**

An important factor in ascertaining the cyclability of the working electrode is the Coulombic efficiency, η, which describes the proportion of the capacity ($Q_{delithiation}/Q_{lithiation}$) lost during lithiation compared to delithiation. The higher the value, the more effective the energy storage material and can be determined according to Equation 19.

$$\boldsymbol{\eta}\,[\%] = \frac{\boldsymbol{Q_{lithiation}[mA\,h\,g^{-1}]}}{\boldsymbol{Q_{delithiation}\,[mA\,h\,g^{-1}]}} \times \mathbf{100} \qquad (19)$$

In Chapter 3 the C-rate tests were analysed in the potential range 2.0 – 4.0 V vs $Li/Li^+$, using a NEWARE battery tester at 50 mA $g^{-1}$ for 16 cycles followed by the proceeding current densities 100, 300, 600, 300, 100 and 50 mA $g^{-1}$ at ten cycles each. In Chapter 4 and Chapter 5, the C-

rate tests and long-term cycling performance of the cells were analysed using a MACCOR battery tester (Model 4200) for 10 cycles at 50, 100, 300, 600, and 50 mA $g^{-1}$ within a potential range of 2.0 to 4.0 V vs $Li/Li^+$. Reducing the current density to 50 mA $g^{-1}$ was included to provide an indication of capacity recovery after cycling at 600 mA $g^{-1}$. When Li-free materials were used as positive electrodes, such as those in this thesis, they were discharged first in order to lithiate the $V_2O_5$ [90].

### 2.4.4 Electrical Impedance Spectroscopy

Electrochemical Impedance Spectroscopy (EIS) is a computational technique used to obtain and analyse kinetic information regarding electrode structure, electrode surface and solution resistances of the electrolyte along with lithiation/delithiation properties. EIS is a non-destructive method as the amplitude of the perturbating alternating current (AC) signal is very small resulting in a polarisation of the electrode in a linear potential region [164]. Impedance represents the ability of a circuit, or an electrochemical system, to resist an electrical current though it is not limited by Ohm's law and is dependent on frequency. Ohm's law is defined as the ratio of voltage (*U(t)*) and current (*I(t)*) (Equation 20) which is representative as the ideal resistor with one circuit element.

$$\boldsymbol{R = \frac{U(t)}{I(t)}} \tag{20}$$

An ideal resistor is independent of frequency and obeys Ohm's law for all voltages and currents while remaining in phase. The impedance of a real resistor is frequency (*f*) dependent and can be presented using both voltage and current where the AC potential (*U(t)*) is dependent on time (*t*), $U_o$ is the amplitude of the signal and $\omega$ is the radial frequency ($\omega = 2\pi f$) while the current (*I(t)*) is shifted by $\varphi$ according to Equation 21 and Equation 22.

$$\boldsymbol{U(t) = U_0 \, sin(\omega t)} \tag{21}$$

$$\boldsymbol{I(t) = I_0 \, sin(\omega t + \phi)} \tag{22}$$

By combining Equations 20, 21 and 22 the impedance (*Z*) can be expressed as Equation 23.

$$\boldsymbol{Z = \frac{U(t)}{I(t)} = \frac{U_0 sin(\omega t)}{I_0 sin(\omega t + \phi)} = Z_0 \frac{sin(\omega t)}{sin(\omega t + \phi)}} \quad (23)$$

The impedance can be expressed as a complex function using Euler's equation, Equation 24.

$$\boldsymbol{exp(i\phi) = cos(\phi) + isin(\phi)} \quad (24)$$

Equation 24 combined with transformation of Equations 21 and 22 into exponential relationships result in the complex function ($Z(\omega)$) according to 25.

$$\boldsymbol{Z(\omega) = \frac{U(t)}{I(t)} = Z_0\, exp(i\phi) = Z_0(cos(\phi) + i\, sin(\phi))} \quad (25)$$

Equation 25 is made up of a real (*Z'*) and imaginary part (*Z''*) which can be represented as a Nyquist plot according to Figure 2.8. Figure 2.8(a) represents an ideal resistor, $R_b$, and its relevant electrical equivalents circuit element (inset), which is representative of the electrolyte in an ideal electrochemical device such as an electric double layer capacitor (EDLC).

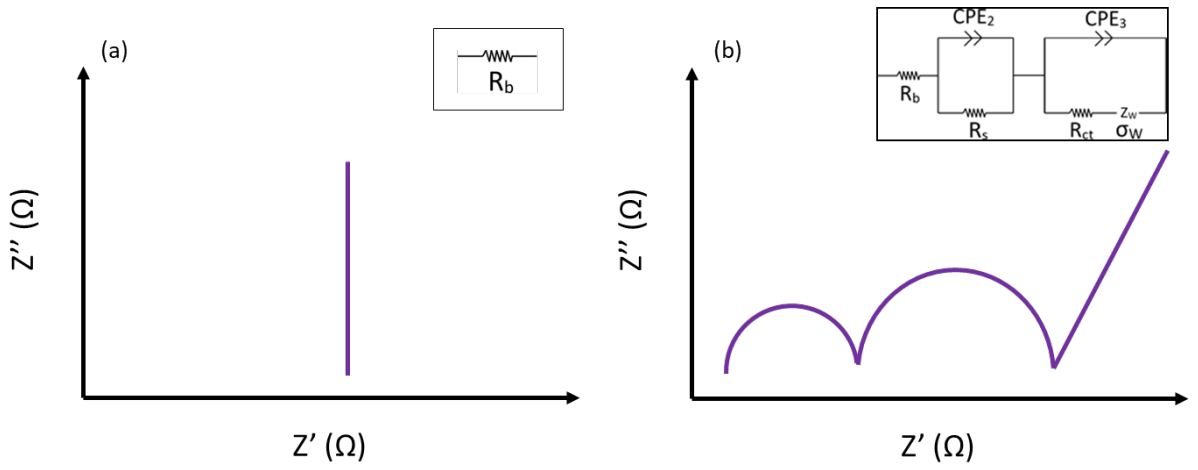


**Figure 2.8: (a) Nyquist Plot showing real part (Z') on the *x*-axis and imaginary part (Z") on the *y*-axis with (inset) relevant electrical equivalent circuit for an ideal resistor $R_1$ and (b) Nyquist plot with two time constants and a Warburg impedance tail with the relevant electrical equivalent circuit (inset).**

In a non-ideal scenario, other components of the electrochemical cell impact the impedance; these components include resistances between the electrolyte and electrode, contact between

the active material and current collectors and grain boundary resistances between the active material particles. Due to this, two interfaces within the tested coin cells in this project were considered in the analysis of the impedance data: the first corresponds to the electrolyte/electrode interface and the second is defined by the grain boundaries between the nanostructured crystallites of the electrode material. These phenomena are observed in the distorted semicircle caused by an overlap of two time constants which are representative of charge transfer processes in Figure 2.8(b) [167,168].

EIS analysis in Chapter 3 and Chapter 5 was performed on a Bio-Logic VMP3 potentiostat over 100 kHz – 100 mHz at the open circuit voltage (≈ 3.4 V vs $Li/Li^+$) with an AC amplitude of 20 mV on pristine coin cells. Nyquist plots and equivalent circuit determination were derived using the Zfit curve fitting function available in EC-Lab® V10.33 software. The electrical equivalent circuit in Figure 2.8(b) (inset) was used to represent the faradaic impedances which consisted of three resistances, two constant phase elements (*CPE*) and a Warburg impedance component ($\sigma_W$). The bulk resistance ($R_b$) in the high frequency region corresponds to the ohmic resistance in the electrolyte and coin cell components [169]. The surface layer resistance (*Rs*) and $CPE_2$ in parallel represent Li-ion transport from the active material particle surface. $R_s$ represents the resistance of Li-ion diffusion through the surface film layer of the electrode [170]. $CPE_2$ models the surface layer capacitance in the material structure. The charge transfer resistance ($R_{ct}$) and $CPE_3$ in parallel represent the electron transport properties of the electrochemical process and $CPE_3$ is the non-ideal capacitance of the double layer [79]. The upturn of the data in the low frequency region on the Nyquist plot [Figure 2.8(b)] is the beginnings of a straight line corresponding to Li-ion transport within the active material of the electrode and is represented by $\sigma_W$ [167]. *CPE*s were chosen to represent non ideal scenarios such as inhomogeneous surfaces [171].

The EIS investigations were conducted to compare the different electrode material resistances and conductivities within the respective chapter. It should be noted that direct comparison

between the experimental chapters in this thesis is unadvised as coin cells were used when testing these materials. There are differences in the contact between the separator and electrodes, variations in active material masses, and variations in electrode synthesis conditions. Consequently, EIS results should be used for qualitative comparison rather than quantitative.

## 2.5 EXPERIMENTAL METHODOLOGY

The characterisation techniques introduced in this chapter are summarised in Figure 2.9 as a flow chart. After fibre synthesis, summarised in steps 1-3, initial material characterisation in step 4 took place for all materials with PXRD and SEM. Only the materials in Section 3.1 underwent TGA analysis. Electrode preparation, CV and GDC tests, summarised in steps 5 and 6, followed the initial material characterisation for all materials. Only the materials in Chapter 3 and Chapter 5 underwent EIS analysis. To gain a greater understanding of dopant loading and resulting material structures, further material characterisation *via* BET, XPS and TEM was undertaken for materials in Chapter 4 and Chapter 5 (Figure 2.9, step 7). This structural characterisation was only undertaken for doped materials as further investigations were necessary to ascertain the structural effect of the dopant and to determine exact at% loading.

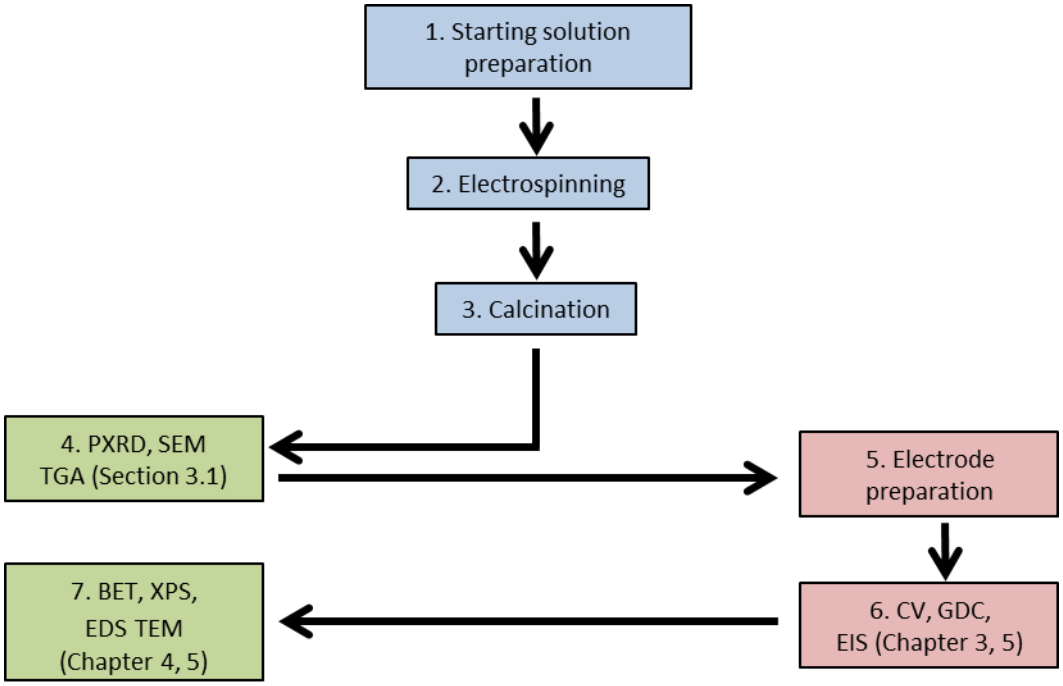


**Figure 2.9: Flow chart summarising the characterisation techniques used in this thesis where the blue boxes correspond to material synthesis (steps 1, 2 and 3), green boxes for structural characterisation (steps 4 and 7) and red boxes for electrochemical characterisation (steps 5 and 6).**

## 2.6 SUMMARY

Chapter 2 outlined the experimental methodology undertaken in this project. This chapter contained three sections; the synthesis methodology, structural characterization techniques, and electrochemical characterisation techniques. Relevant parameters and technique specifications were included to provide consistency across the project and to align the experimental processes and electrochemical investigations with those of the energy storage research community.

In Chapter 3, the synthesis and resultant structural aspects of electrospun undoped $V_2O_5$ are investigated *via* calcination temperature variation of the fibres and variation of the fibre diameter for use as positive electrodes in LIBs.

# Chapter 3 Synthesis and Structural Investigations of Electrospun Undoped $V_2O_5$

## 3.1 Structural and Electrochemical Investigations of Electrospun Undoped $V_2O_5$ with Varying Calcination Temperature

### 3.1.1 Introduction

In this section, single-phase crystalline $V_2O_5$ nanostructured fibres were electrospun from starting solution components described in Chapter 2 followed by calcination in air at either 450 °C, 500 °C or 550 °C for 2 h. Changing the calcination temperature was undertaken to determine whether a variation in structure and electrochemical performance could be induced and controlled to mitigate the limitations of this promising ceramic oxide.

### 3.1.2 Results and Discussion – Calcination Temperature Variation

The resultant samples were named according to the calcination temperature under which they were treated. For example, the $V_2O_5$ sample that was calcined at 450 °C is called $V_2O_5$-450 °C. As the heating rate for the calcination treatment was set at 3 °C $min^{-1}$, each of the samples experienced different lengths of time during the heating sequence despite all of them undergoing a 2 h hold at their specified temperature. This heating rate was used to prevent energetic combustion of any volatile substances contained in the organic material of the as-spun fibres. Assuming a starting temperature of 20 °C, it took 143 minutes to reach 450 °C, 160 minutes to reach 500 °C and 177 minutes to reach 550 °C. This variation in time spent under temperature along with the holding temperature, has shown to affect both the resultant morphology and particle characteristics of the materials shown in the following analysis.

Powder XRD (PXRD) patterns in Figure 3.1(a), clearly show that for each calcination temperature (450 °C, 500 °C and 550 °C) the as-spun fibres preferentially converted to $V_2O_5$ which is typical when vanadium-based oxides are calcined in air to a high-enough temperature [73]. The reflections have been labelled according to orthorhombic $V_2O_5$ [172]. While $V_2O_5$ is exclusively formed, $V_2O_5$-450 °C possessed broader reflections, as seen in Figure 3.1(b), than both $V_2O_5$-500 °C and $V_2O_5$-550 °C implying smaller individual crystallites and lower degree of crystallinity [76,173]. Additionally, Figure 3.1(b) also shows a variation in reflection intensity with $V_2O_5$-550 °C possessing the sharpest peaks, followed by $V_2O_5$-500 °C and $V_2O_5$-450 °C. This implies that there is a progressive increase in crystallinity and particle size with increasing temperature and is in agreement with a number of other studies [85,92,124,125].

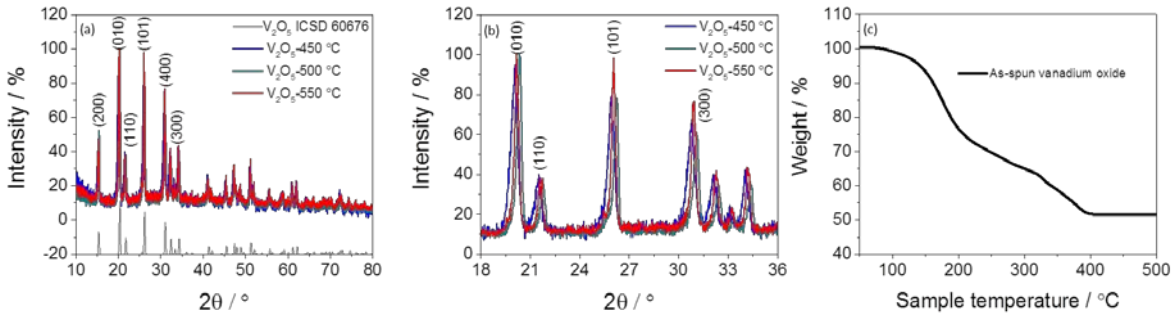


**Figure 3.1: (a) XRD patterns for $V_2O_5$-450 °C, $V_2O_5$-500 °C and $V_2O_5$-550 °C with ICSD Reference Code: 60767 for orthorhombic $V_2O_5$, (b) 18° < 2θ < 36° range showing variation in reflection intensity and placement and (c) TGA profile showing complete removal of the polymer constituents at 400 °C.**

D-spacings were calculated using Bragg's Law for the (010) peak and produced a non-linear trend with temperature, according to Table 3.1, with 4.42, 4.37, 4.40 Å for $V_2O_5$-450 °C, $V_2O_5$-500 °C and $V_2O_5$-550 °C respectively. The interlayer spacing for $V_2O_5$-450 °C was larger than $V_2O_5$-500 °C which was likely due to less time under temperature for $V_2O_5$ layer rearrangement. $V_2O_5$-550 °C had a larger interlayer spacing than $V_2O_5$-500 °C and was more crystalline indicating that the layers became more separated in the presence of higher

temperatures. Scherrer crystal sizes, summarised in Table 3.1, were calculated using the (200), (010), (101) and (400) peaks with averages of 16.07, 22.55, and 23.59 nm for $V_2O_5$-450 °C, $V_2O_5$-500 °C and $V_2O_5$-550 °C respectively, confirming a progressive increase in crystallinity with particle size.

**Table 3.1: PXRD characterisation summary of the electrospun $V_2O_5$-450 °C, $V_2O_5$-500 °C and $V_2O_5$-550 °C where D-spacings were calculated *via* Bragg's law and crystallite size was determined *via* the Scherrer equation.**

| Sample | D-spacings for (010) (Å) | Crystallite size (nm) |
|---|---|---|
| $V_2O_5$-450 °C | 4.42 | 16.07 |
| $V_2O_5$-500 °C | 4.37 | 22.55 |
| $V_2O_5$-550 °C | 4.40 | 23.59 |

TGA analysis was undertaken to ascertain whether the crystal structure was affected by the presence of any residual carbon resulting from an incomplete combustion of the polymer constituents from the starting solution. Figure 3.1(c) shows the TGA results and it indicates that at 400 °C the weight change plateaus implying that all organics and polymer components had been removed with an approximate 49 wt% loss. D-spacing calculations and crystallite size variations in conjunction with TGA results imply that while the mass of the material does not appear to change from 400 °C, the materials still underwent structural rearrangements with crystallite size and interlayer space variations according to Table 3.1.

Le Bail refinement in Table 3.2 shows that lattice parameters increased between $V_2O_5$-450 °C and $V_2O_5$-500 °C while $V_2O_5$-550 °C possessed the smallest lattice parameters and the smallest unit cell volume. It has been shown that an increase in calcination temperature results in an increase in lattice parameters, which is observed between V2O5-450 °C and V2O5-500 °C [174,175]. However, it has been observed that contraction of the unit cell is caused by a difference in bond length [176]. This suggests, considering analysis above, that a prolonged time in the furnace allowed the V2O5-550 °C to become more ordered producing smaller lattice

parameters due to variations in bond length while allowing larger nanostructured particles to grow.

**Table 3.2: Lattice parameters from le Bail refinement for $V_2O_5$ calcined at 450 °C, 500 °C, and 550 °C.**

| Sample | a (Å) | b (Å) | c (Å) | Volume (Å$^3$) | $R_{wp}$ | $\chi 2$ |
|---|---|---|---|---|---|---|
| $V_2O_5$-450 °C | 11.534(1) | 3.5745(5) | 4.3873(8) | 180.885(84) | 9.90 | 1.28 |
| $V_2O_5$-500 °C | 11.544(1) | 3.5769(4) | 4.3929(6) | 181.395(67) | 10.09 | 1.27 |
| $V_2O_5$-550 °C | 11.530(1) | 3.5714(3) | 4.3827(5) | 180.467(50) | 9.98 | 1.29 |

The analysis so far shows that the higher calcination temperature of 550 °C does not imply increased lattice parameters and unit cell volume despite the increase in crystallinity. Rather, it likely symbolises a prolonged opportunity for reordering of the structure when more total time was spent under heat treatment.

SEM images in Figure 3.2(a,b) show that calcination in air for 2 h at 450 °C produced particles with rounded edges in hierarchical microscale fibres. The smaller crystallite size indicated by both PXRD and the Scherrer calculation are observed in the SEM images of $V_2O_5$-450 °C. The nanoscale particles had diameters and lengths *ca*. 100 nm and *ca*. 300 nm, respectively, while fibre diameters ranged in size from 1 to 5 µm. Calcination at 500 °C produced fibres with diameter ranges from 0.7 to 2.3 µm that were made up of nanoparticles with well-defined boundaries as seen in Figure 3.2(c,d). Figure 3.2(e,f) shows $V_2O_5$-550 °C fibres with longer grains suggesting higher directionality associated with their growth and a higher degree of crystallinity than those of $V_2O_5$-450 °C and $V_2O_5$-500 °C. The larger and greater definition associated with the $V_2O_5$-550 °C fibres was likely to due to longer time spent in the furnace during the 3 °C min$^{-1}$ temperature increase which allowed for larger particles to grow. Particle diameters ranged from 120 to 160 nm and lengths of *ca.* 230 to 760 nm which were significantly larger than that of $V_2O_5$-450 °C and $V_2O_5$-500 °C. The fibre diameter range, while large, was similar to $V_2O_5$-450 °C fibres with 0.5 to 4.5 µm. A similar observation in minimal diameter variation between $V_2O_5$ calcined at 400 °C and 500 °C was made by Viswanathamurthi *et al*.,

who reported that when polymer and organic constituents are removed, fibre diameters undergo little change [124]. The non-uniformity of the fibre diameters in all three samples may be evidence of uncontrolled hydrolysis or gelation rates [119]. This was minimized by monitoring humidity readings in the laboratory. The vanadium precursor starting solution is moisture sensitive, so hydrolysis rates were likely to be higher when the electrospinning experiment is conducted in air with higher humidity. There is evidence of this in Figure 3.2(b) for $V_2O_5$-450 °C and in Figure 3.2(f) for $V_2O_5$-550 °C where some of the fibres appear to be fused together.

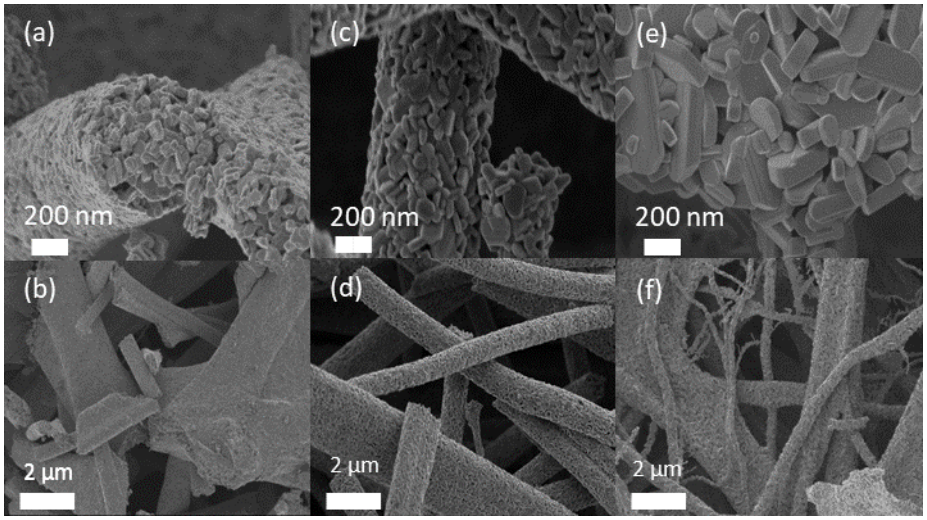


**Figure 3.2: High resolution and low resolution SEM images emphasising both the hierarchical nature of the fibres and variation in particle definition of (a,b) $V_2O_5$-450 °C, (c,d) $V_2O_5$-500 °C, and (e,f) $V_2O_5$-550 °C.**

The trend observed in the PXRD [Figure 3.1] with reflection width and intensity increase with calcination temperature also matches the particle definition in the SEM images (Figure 3.2) indicating that the crystallinity was affected by calcination temperature. In particular, SEM images of $V_2O_5$-550 °C show well defined nanoparticles and PXRD showed narrower reflections indicating a higher degree in crystallinity.

The cyclic voltammograms in Figure 3.3 revealed a series of phase transitions which corresponded to α-$V_2O_5$, ε-$Li_{0.5}V_2O_5$, δ-$LiV_2O_5$ and y̓-$Li_2V_2O_5$ as described in Section 1.7.3. This indicated that the capacity of the tested materials resulted primarily from oxidation and reduction reactions that were associated with redox mechanisms *via* changes in oxidation state [177]. The lack of symmetry between the positive and negative current regions shows that the redox species was only partially recovered and that charge transfer was diffusion controlled which would eventually lead to a loss of redox activity [178,179]. The lack of rectangular current response shows that the redox reactions possessed little double-layer capacitive properties.

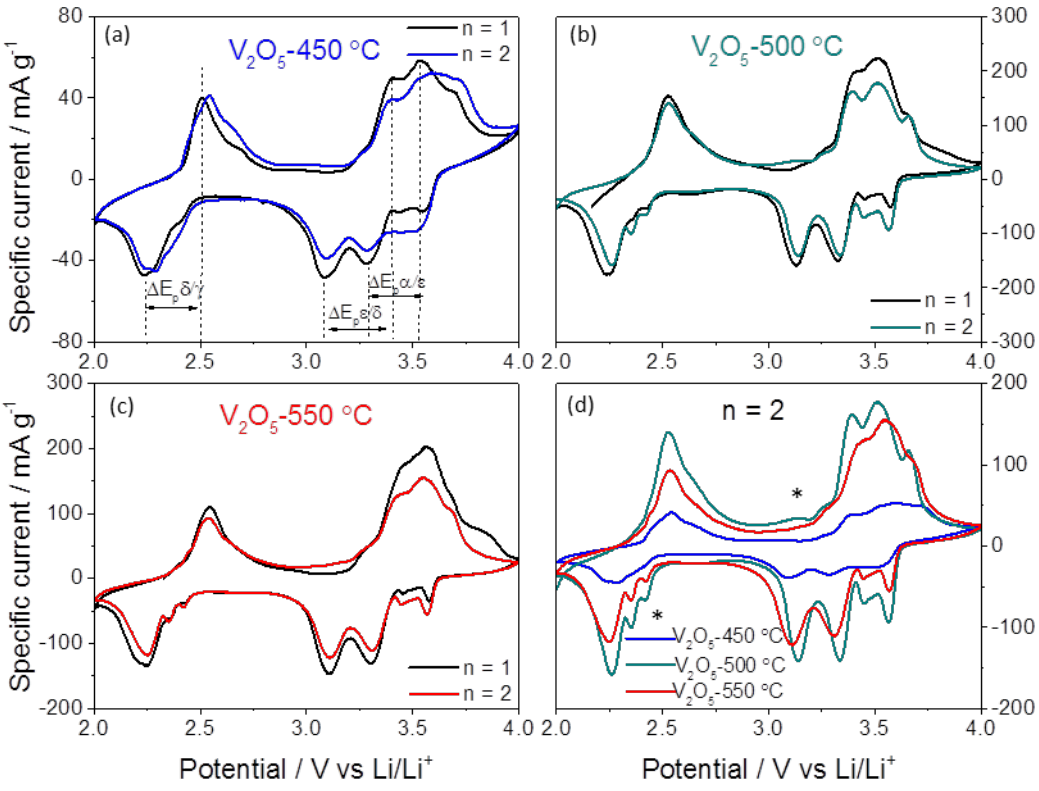


**Figure 3.3: Cyclic voltammograms at 0.15 mV $s^{-1}$ over 2 cycles clearly show a series of phases changes brought about by redox reactions at defined potentials for (a) $V_2O_5$-450 °C with $\Delta E_P$ labelled for the α/ε, ε/δ, and δ/y̓transitions, (b) $V_2O_5$-500 °C, (c) $V_2O_5$-550 °C and (d) voltammograms for each material over cycle 2 emphasising the variation in redox peak definition.**

There was quite strong peak splitting observed in all three samples, especially in the reduction peak at *ca.* 3.0 – 3.5 V vs. $Li/Li^+$. This suggests that there were multiple Li-ion sites of varying energy differences for multi-stepped intercalation/extraction processes [180]. Additionally, the redox reduction peak at *ca*. 3.6 V vs $Li/Li^+$ and the oxidation shoulder peak at *ca*. 3.7 V vs $Li/Li^+$ has been attributed to the irreversible phase transition of the y/y' system [91,181]. The metastable y-$Li_xV_2O_5$ phase formed within the 2.2 – 2.5 V vs $Li/Li^+$ potential range is reversible if cycled within $0 \leq x \leq 2$ [83]. Once this phase is formed there was a loss of redox capacity observed for α/ε phase change in the form of a decrease in peak current in the second CV cycle which was observable for each material. Comparison of oxidation and reduction peak current outputs show that reduction in the cathode domain was favoured for the δ/y phase change while oxidation in the anode domain was favoured for the α/ε phase change. This high degree of redox imbalance is likely to lead to irreversibilities.

The peak separations ($\Delta E_p$) evident in all samples reflect polarisation in the relevant electrochemical reaction and low reversibility [3]. The values are summarised in Table 3.3 and show that $V_2O_5$-450 °C experienced the lowest polarisation for the δ/γ phase followed by $V_2O_5$-500 °C and $V_2O_5$-550 °C. Conversely, $V_2O_5$-450 °C experienced the largest polarisation variation between cycles 1 and 2 for the α/ε phase change compared to $V_2O_5$-500 °C and $V_2O_5$-550 °C. These redox peak splits could be reduced with the introduction of dopants which would act to facilitate or prevent these phase transitions [74]. Most of these peak separations are smaller than that of those analysed by Yan *et al*. who compared the redox peak separations between micro- and nanoscale $V_2O_5$ [91]. Their CV analysis clearly showed an improvement in the electrochemical activity and Li-ion insertion capability of nanofibrous $V_2O_5$ compared to the bulkscale counterpart which was attributed to improved Li-ion kinetics during charge transfer processes.

**Table 3.3: Redox peak separations ($\Delta E_p$) from the cyclic voltammetry analysis for the δ/γ and α/ε phase for $V_2O_5$-450 °C, $V_2O_5$-500 °C and $V_2O_5$-550 °C.**

| Sample | Cycle | $\Delta E_p$δ/γ (V vs $Li/Li^+$) | Cycle | $\Delta E_p$α/ε (V vs $Li/Li^+$) |
|---|---|---|---|---|
| $V_2O_5$-450 °C | 1 | 0.27 | 1 | 0.25 |
| | 2 | 0.25 | 2 | 0.31 |
| $V_2O_5$-500 °C | 1 | 0.29 | 1 | 0.18 |
| | 2 | 0.27 | 2 | 0.18 |
| $V_2O_5$-550 °C | 1 | 0.30 | 1 | 0.27 |
| | 2 | 0.29 | 2 | 0.23 |

Figure 3.3(d) shows a comparison of CV traces between the samples. $V_2O_5$-500 °C and $V_2O_5$-550 °C had significantly higher curve areas and higher redox peak currents compared to $V_2O_5$-450 °C which suggest higher capacity and faster Li-ion insertion/extraction kinetics [91]. Additionally, the presence of an extra oxidation/reduction peak in the form of small shoulders for all samples labelled with a star (*), has been identified as evidence of a well-defined crystalline micro-nanostructured material [76,79]. This observation was confirmed with the well-defined nanoparticle constituents of the microfibres observed in the SEM images and sharp reflection intensities in the PXRD.

A C-rate test was conducted to investigate the rate capability of the materials with cycling at 50 mA $g^{-1}$ for 16 cycles followed by 100, 300, 600, 300, 100, and 50 mA $g^{-1}$ for 10 cycles each as shown in Figure 3.4.

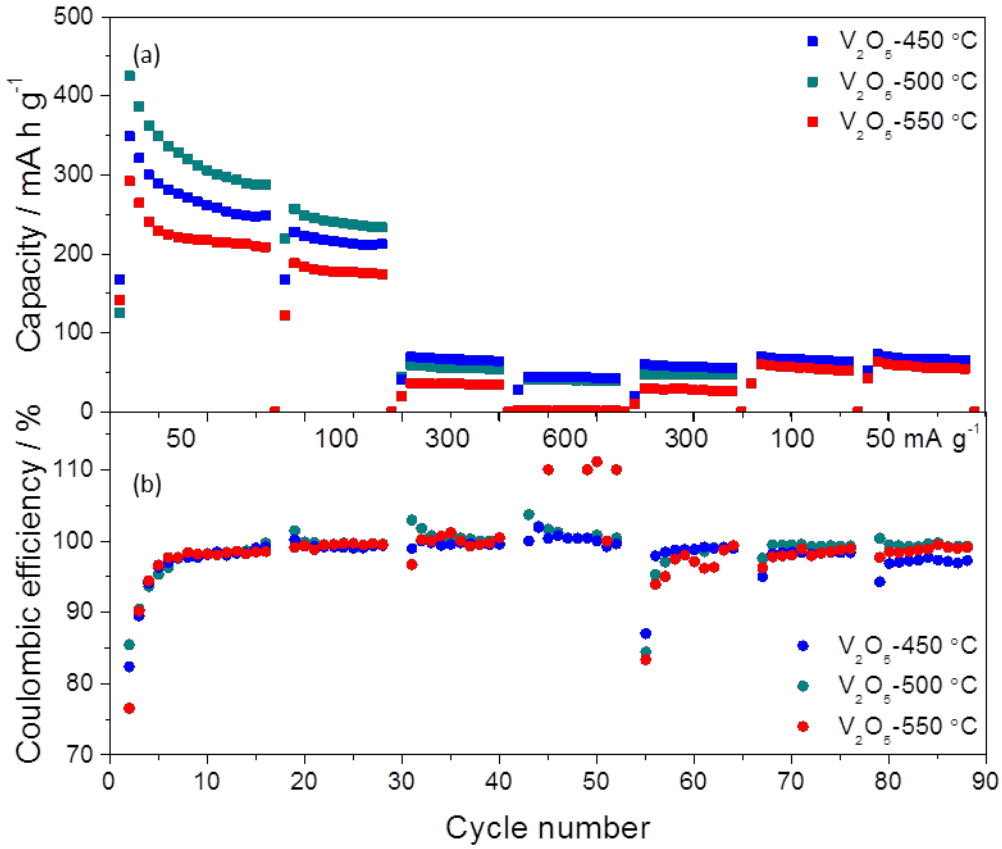


**Figure 3.4: (a) C-rate test at the following current densities: 50 mA $g^{-1}$ for 16 cycles followed by 100, 300, and 600, 300, 100, 50 mA $g^{-1}$ for 10 cycles each and the (b) associated Coulombic efficiencies during C-rate test for $V_2O_5$-450 °C, $V_2O_5$-500 °C and $V_2O_5$-550 °C electrospun fibres from starting solutions containing 0.3 g of polymer.**

Cycle stability was quite low in the first 16 cycles at 50 mA $g^{-1}$ [Figure 3.4(a)] with capacities and stabilities of 349 mA h $g^{-1}$ at cycle 2 (n = 2) and 71% for $V_2O_5$-450 °C, 425 mA h $g^{-1}$ (n = 2) and 68% for $V_2O_5$-500 °C, 292 mA h $g^{-1}$ (n = 2) and 71% for $V_2O_5$-550 °C. This variation in cycle stabilities over these initial cycles was not large suggesting that calcination temperature, over the range investigated in this chapter, does not play a significant role in improving stability. Additionally, the sharp decrease in capacity during the initial cycles has been seen previously by others which was caused by phase transitions that $V_2O_5$ is susceptible to over the 2.0 – 4.0 V vs $Li/Li^+$ range [57–59]. Improvement in stability can be clearly seen at each current density after the first 16 cycles at 50 mA $g^{-1}$ which was likely due to a reduction

in side reactions [130]. The irreversible capacity loss (ICL) is high with 256 mA h $g^{-1}$ for $V_2O_5$-450 °C, 372 mA h $g^{-1}$ for $V_2O_5$-500 °C and 417 mA h $g^{-1}$ for $V_2O_5$-550 °C. These high values indicate that there was substantial interfacial storage across the electrode/electrolyte interface [134].

All materials showed poor rate capability when changing current densities with $V_2O_5$-450 °C performing only slightly better than the other two materials. This poor rate capability was likely due to large fibre diameters as seen in SEM images in Figure 3.2. Fibres with large diameters do not have the advantages associated with large surface areas and short diffusion distances seen in nanostructures [184]. At 600 mA $g^{-1}$, there was little capacity recorded, especially for $V_2O_5$-550 °C which is indicative of little interaction between the materials' surface and the Li-ions. This implies that these materials were high energy rather than high power materials. This is characteristic of $V_2O_5$ and could be improved with the incorporation of a dopant or a carbon-based material.

A review of vanadium oxides and their electrochemical performance in LIBs by Yue and Liang found that statistically, the optimal current density range is 30 – 500 mA $g^{-1}$ [68]. Consequently, it is unsurprising to see poor capacity retention at 600 mA $g^{-1}$ which indicated that the performance of the electrospun $V_2O_5$ in this study was comparable to the literature. There was little capacity recovery after cycling at 600 mA $g^{-1}$ which was likely due to the stepwise decrease in current density back to 50 mA $g^{-1}$. As the materials showed poor rate retention during current density increase, it is then reasonable to observe low capacity recovery as current density was decreased to 300 mA $g^{-1}$, 100 mA $g^{-1}$ and 50 mA $g^{-1}$. This indicates that the ionic pathways created during initial cycling were destroyed with significant Li-ion trapping resulting in permanent structural damage [185].

The average Coulombic efficiencies over the investigated C-rate cycles were determined and revealed to be 98% for both $V_2O_5$-450 °C and $V_2O_5$-500 °C and 97% for $V_2O_5$-550 °C. These Coulombic efficiencies are quite competitive and overall there was little variation between

samples suggesting that calcination temperature does not play a significant role in dictating efficiency. This is likely due to the small variation in crystallite size between the materials. The Coulombic efficiencies achieved during the initial cycling at 50 mA $g^{-1}$ for all samples is low suggesting that overcharging occurred. This implies that at a lower current density of 50 mA $g^{-1}$ the positive electrode became over-oxidised due to side reactions with the electrolyte [86]. The over-oxidised state of the positive electrode indicated that the $V_2O_5$ was fully delithiated with each cycle which was likely contributing to large volume expansions and hence decreased cycle stability and low coulombic efficiency. Low Coulombic efficiencies are also caused by Li-ion trapping which occurs during phase transitions [185]. This combination of over-oxidation and Li-ion trapping likely caused the erratic Coulombic efficiencies for $V_2O_5$-550 °C during 600 mA $g^{-1}$, which did not fit the scale shown in Figure 3.4(b).

Impedance measurements were undertaken to compare the relative conductivities and resistances of the electrospun materials with resultant Nyquist plots in Figure 3.5(a). All Nyquist plots were composed of a distorted semicircle in the high-to-moderate frequency range with a small upturning in the low frequency range.

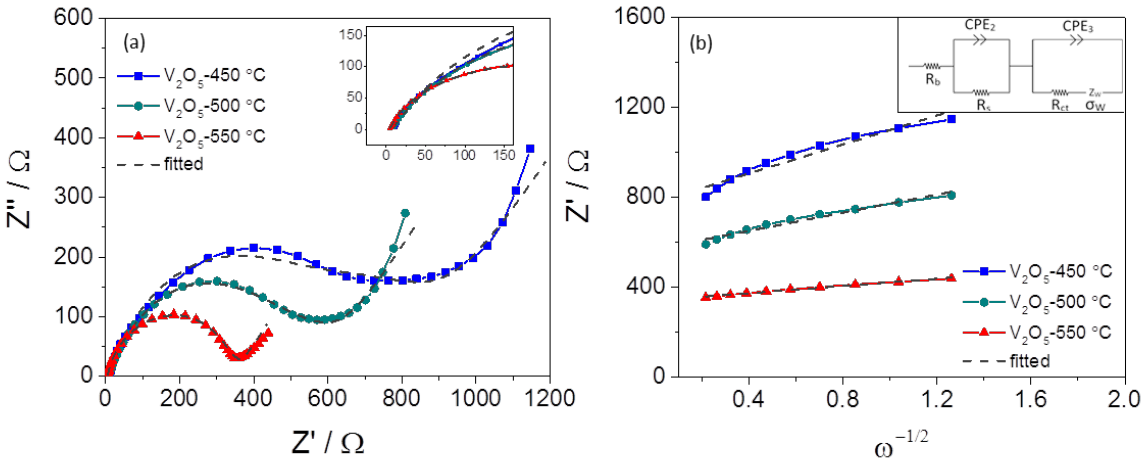


**Figure 3.5: (a) Nyquist plots of pristine cells for $V_2O_5$ calcined at 450 °C, 550 °C and 550 °C with an enlargement of the high frequency region (inset) and (b) linear curves of $\omega^{-1/2}$ vs Z' in the low frequency region with the electrical equivalent circuit (inset).**

The resistances were quantified using the electrical equivalent circuit in Figure 3.5(b) (inset) with relevant explanation of electrical equivalent circuit components in Section 2.3.4. Briefly, $R_b$, $R_s$ and $R_{ct}$ are the bulk, solution and charge transfer resistances, respectively, $CPE_2$ and $CPE_3$ are the constant phase elements representing charge storage and $\sigma_w$ is the Warburg impedance coefficient. The resistance values are summarised in Table 3.4, where the surface layer resistance, $R_s$, and charge transfer resistance, $R_{ct}$, decreased with increasing calcination temperature implying an improvement in cycling efficiency and electronic conductivity [186,187]. A higher calcination temperature has been shown by others to lower charge transfer resistances [127,188].

**Table 3.4: Curve fitted resistance values, $\chi^2$ goodness of fit and the Warburg impedance coefficient ($\sigma_w$).**

| Sample | $R_b$ - electrolyte (Ω) | $R_s$ – surface layer (Ω) | $R_{ct}$ – charge transfer (Ω) | $\chi^2$ | $\sigma_w$ (Ω cm$^2$ s$^{-1/2}$) |
|---|---|---|---|---|---|
| $V_2O_5$-450 °C | 9 | 318 | 530 | 0.06852 | 322.74 |
| $V_2O_5$-500 °C | 8 | 134 | 465 | 0.00608 | 201.75 |
| $V_2O_5$-550 °C | 4 | 109 | 237 | 0.00436 | 80.44 |

The Warburg impedance, $\sigma_w$, was determined by calculating the slope of $\omega^{-1/2}$ vs Z' in Figure 3.5(b) and is inversely related the Li-ion diffusion coefficient, $D_{Li}$. A decrease in $\sigma_w$ (Table 3.4) implies an increase in $D_{Li}$ [3,186]. This trend also matches calcination temperature.

Interestingly, $V_2O_5$-550 °C showed favourable impedance results in the pristine state, which is likely due to its high degree of crystallinity in facilitating Li-ion movement into the $V_2O_5$ structure. Despite this, the highly crystalline nature of $V_2O_5$-550 °C, along with its large crystallites, resulted in the lowest capacities during the C-rate test. $V_2O_5$-450 °C in comparison did not show favourable impedance results but this material produced the lowest ICL and the

best rate retention of the investigated materials. Electrochemical analysis of $V_2O_5$-500 °C showed that the combination of moderate polarisation, reversibility and impedance results, compared to $V_2O_5$-450 °C and $V_2O_5$-550 °C, and produced the highest capacities in the C-rate test. After analysis of these results, the compromise in structural characteristics and electrochemical performance offered by calcination of the electrospun fibres at 500 °C was considered to be the most effective heat treatment temperature to use in further investigations of this material. These results indicate that varying the calcination temperature was a necessary investigation towards understanding how the calcination process parameters affect structural and electrochemical characteristics of this electrospun $V_2O_5$ system.

### 3.1.3 Conclusion – Varying Calcination Temperature

The results showed that improving crystallinity did improve conductivity, as seen with $V_2O_5$-550 °C in the EIS analysis but did not necessarily lead to an improvement in capacity. A highly crystalline material promotes Li-ion intercalation/extraction but is more susceptible to material degradation. Furthermore, CV tests indicated that calcination temperature has an moderately appreciable impact on phase changes and kinetics of the insertion capability of Li-ions. C-rate results showed poor rate capability which was attributed to large fibre diameters. Consequently, it is assumed that a reduction in fibre diameter would decrease Li-ion diffusion distances and improve rate capability.

## 3.2 STRUCTURAL AND ELECTROCHEMICAL INVESTIGATIONS OF ELECTROSPUN UNDOPED $V_2O_5$ WITH VARYING FIBRE DIAMETERS

### 3.2.1 Introduction

$V_2O_5$ fibres made with the standard sol-gel components and amounts, used in the previous section, ranged from 1 to 5 µm in diameter indicating that they are nanostructured microfibres

rather than nanofibres. Fibres with large diameters do not have the advantages associated with large surface area and short diffusion distances of nanostructures [184]. Rather, small fibre diameters haven been shown to decrease Li-ion diffusion distances and hence increase capacity in lithiation/delithiation tests by allowing high contact areas between the electrolyte and electrode [67,86].

The diameters of electrospun fibres with circular cross sections can be controlled by varying the concentration of the polymer, the conductivity of the electrospinning solution, electric field potential and the feed rate [189]. Li and Xia showed that by varying the amount of poly(vinyl pyrrolidone) (PVP)-to-alkoxide precursor ratio in their starting solution, the resulting diameter of their $TiO_2$ fibres could be controlled [190].

This section investigates the synthesis of electrospun $V_2O_5$ from starting solutions containing varying amounts of the polymer poly(vinyl acetate) (PVAc) to determine whether the fibre diameter was controllable. This was achieved by systematically decreasing the polymer content while all other parameters were kept constant. Subsequent structural analysis of the resultant electrospun fibres was undertaken to ascertain whether fibre diameter decrease was accomplished and what effects on electrochemical properties were imparted.

### 3.2.2 Materials and Methods

The standard $V_2O_5$ starting solution as introduced in Section 2.1.1 was used though the amount of PVAc was progressively decreased according to Table 3.5.

**Table 3.5: Starting solution variation summary indicating amount of PVAc variation.**

| PVAc amount (g) | PVAc (%) | Sample name |
|---|---|---|
| 0.30 | 100 | PVAc-0.30 g |
| 0.24 | 80.0 | PVAc-0.24 g |
| 0.20 | 66.7 | PVAc-0.20 g |
| 0.16 | 53.3 | PVAc-0.16 g |

| | | |
|---|---|---|
| 0.12 | 40.0 | PVAc-0.12 g |
| 0.08 | 26.7 | PVAc-0.08 g |

### 3.2.3 Results and Discussion – Varying Polymer Amount

A summary of PXRD patterns with varying polymer amount is shown in Figure 3.6 with reflections assigned to orthorhombic $V_2O_5$ [172]. This stoichiometry was preferentially formed when calcined in air regardless of the amount of polymer used in the electrospinning starting solution.

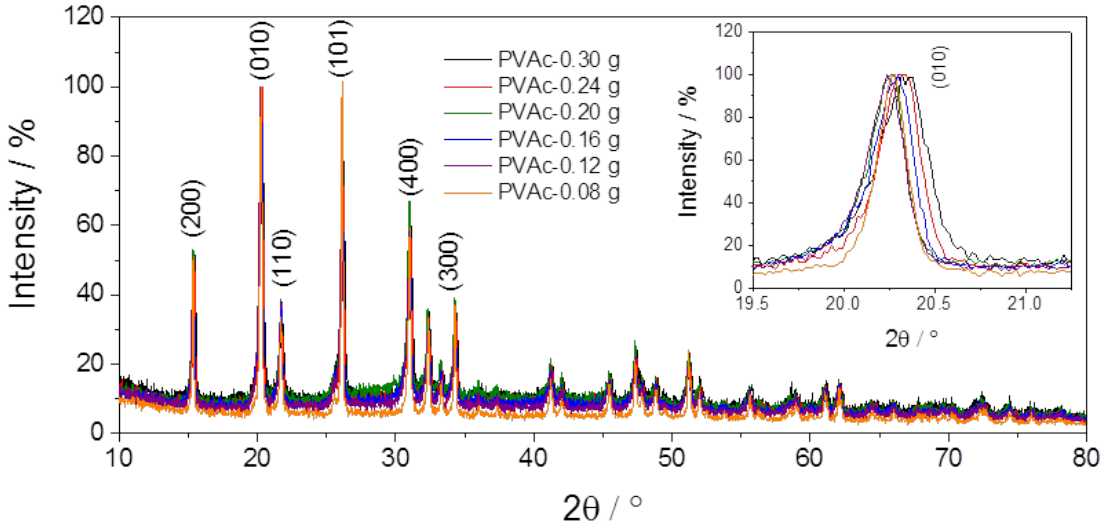


**Figure 3.6: PXRD for $V_2O_5$ with varying polymer amount and (inset) enlarged region of 19.5° < 2θ < 21.25° emphasizing minimal peak shift.**

D-spacings were calculated using Bragg's Law for the (010) peak and according to Table 3.6 (a) there was no substantial variation in the interlayer spacing with decreasing polymer content. This was also observable in the minimal shifting in the (010) peak to lower 2θ values in Figure 3.6 (inset).

**Table 3.6: Structural data summary for $V_2O_5$ with varying polymer amount with (a) D-spacings, (b) Scherrer crystal sizes and (c) fibre diameters determined from pixel counting of the SEM images.**

| Sample | (a) D-spacing (010) (Å) | (b) Scherrer crystal size (010) (nm) | (c) Fibre dimeters |
|---|---|---|---|
| PVAc-0.30 g | 4.37 | 23.73 | 0.74 – 2.3 μm |
| PVAc-0.24 g | 4.37 | 28.21 | 600 – 700 nm |
| PVAc-0.20 g | 4.38 | 30.33 | *ca.* 600 nm |
| PVAc-0.16 g | 4.37 | 30.33 | *ca.* 700 nm |
| PVAc-0.12 g | 4.38 | 31.51 | 300 – 500 nm |
| PVAc-0.08 g | 4.37 | 40.74 | N/A |

Scherrer crystal sizes were determined and averaged using the (200), (010), (101) and (400) reflections with results according to Table 3.6 (b). There is an overall increase in crystal size with decrease in polymer content of the starting solution. This suggests that if there was less organic material within the as-spun material, then there was more room and opportunity for crystal growth during the calcination treatment. The results of the le Bail refinement of the PXRD patterns are shown in Table 3.7. Overall, there was a decrease in the unit cell volumes with decrease in polymer amount. This suggests improved packing efficiency of the vanadium and oxygen atoms when there were less polymer constituents to remove during calcination.

**Table 3.7: Lattice parameters from le Bail refinement for $V_2O_5$ with varying polymer content showing an overall decrease in unit cell volumes.**

| Sample | a (Å) | b (Å) | c (Å) | Volume ($Å^3$) | $R_{wp}$ | $\chi 2$ |
|---|---|---|---|---|---|---|
| PVAc-0.30 g | 11.544(1) | 3.5769(4) | 4.3929(6) | 181.395(67) | 10.09 | 1.27 |
| PVAc-0.24 g | 11.534(1) | 3.5730(3) | 4.3862(5) | 180.762(54) | 10.05 | 1.28 |
| PVAc-0.20 g | 11.531(1) | 3.5713(3) | 4.3829(5) | 180.496(50) | 10.18 | 1.27 |
| PVAc-0.16 g | 11.535(1) | 3.5724(3) | 4.3842(5) | 180.666(57) | 10.73 | 1.29 |
| PVAc-0.12 g | 11.531(1) | 3.5711(3) | 4.3820(4) | 180.437(47) | 10.68 | 1.27 |
| PVAc-0.08 g | 11.520(1) | 3.56712(2) | 4.3772(3) | 179.864(27) | 10.11 | 1.28 |

SEM images are presented in Figure 3.7 with approximate fibre dimensions recorded in Table 3.6(c). The as-spun fibres made from a starting solution containing 0.3 g of polymer (not pictured), possessed diameters of 1 – 3.390 µm with featureless surfaces. Calcination of PVAc-0.30 g in air for 2 h at 500 °C produced fibres with diameters of 0.7 – 2.3 µm and were made up of interconnected nanoparticles with well-defined boundaries as seen in Figure 3.7 (a,b). Fibre shrinkage after heat treatment was caused by the decomposition of the PVAc resulting in the development of interlinked nanocrystals of metal oxides [67].

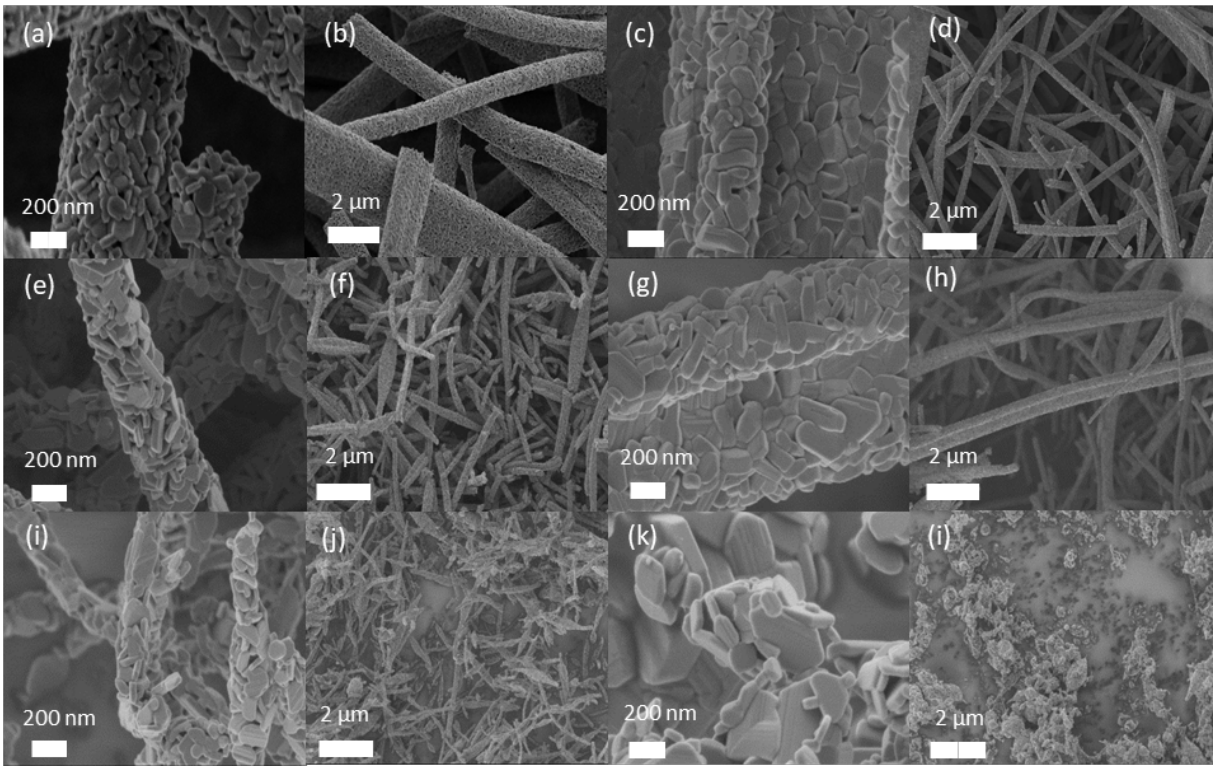


**Figure 3.7: High resolution and low resolution SEM images emphasizing both the hierarchical nature of the fibres and variation in fibre morphology of (a,b) PVAc-0.30 g, (c,d) PVAc-0.24 g, (e,f) PVAc-0.20 g, (g,h) PVAc-0.16 g, (i,j) PVAc-0.12 g, and (k, l) PVAc-0.08 g.**

Figure 3.7(c,d) shows a mix of fibre morphologies for PVAc-0.24 g with thin fibres possessing diameters of 600 – 700 nm and microscale ribbons of thicknesses *ca*. 2.8 – 3.3 µm. It has been

suggested that a ribbon morphology can be formed when the solvent rapidly evaporates on the surface of the spinning fibres resulting in the collapse in the circular cross section of the fibres [191–193].

PVAc-0.20 g in Figure 3.7(e,f) shows particles that were elongated and two dimensional in nature with inconsistent fibre diameters of *ca*. 600 nm along their length. For Figure 3.7(g,h) the PVAc-0.16 g fibres were consistently formed and with consistent diameters of *ca*. 700 nm. Fibre diameters were inconsistent for PVAc-0.12 g in Figure 3.7(i,j) with dimensions ranging from 300 to 500 nm and decreased fibre lengths. There is very little fibre formation evident for PVAc-0.08 g in Figure 3.7(k,l) and the 3D hierarchical nanostructures do not appear to be of consistent shapes. These clusters of nanoparticles are likely to be evidence of electrospraying implying that with little polymer in solution, no consistent templating was available for fibre formation.

SEM analysis showed that fibre diameter was controlled by polymer content in the starting solution. As polymers are used as a template for fibre formation, it is reasonable then that a decrease in PVAc provided less opportunity for long fibres to form as seen in Figure 3.7(i,j) for PVAc-0.12 g. Additionally, reduction of polymer content resulted in the elongation of the particles suggesting that with less polymer there was less organic material to be removed during calcination. From this, the $V_2O_5$ layers can stack more effectively, as suggested by unit cell refinement in Table 3.7, which resulted in the increased two-dimensional nature of the particles. The increased crystallite size shown in Table 3.6(b) can be visually observed in the SEM images where particle size increased with decreasing polymer content.

Capacity versus potential profiles for cycles 1 and 5 of the C-rate test are plotted for each sample in Figure 3.8. The potential steps in Figure 3.8 can be easily assigned to α-$V_2O_5$, ε-$Li_{0.5}V_2O_5$, δ-$LiV_2O_5$ and γ-$Li_2V_2O_5$ as outlined in Section 1.7.3. Figure 3.8(b) shows that the $V_2O_5$ phases were still present along with an improvement in the conductivity, observed in a decreased overpotential, with cycling.

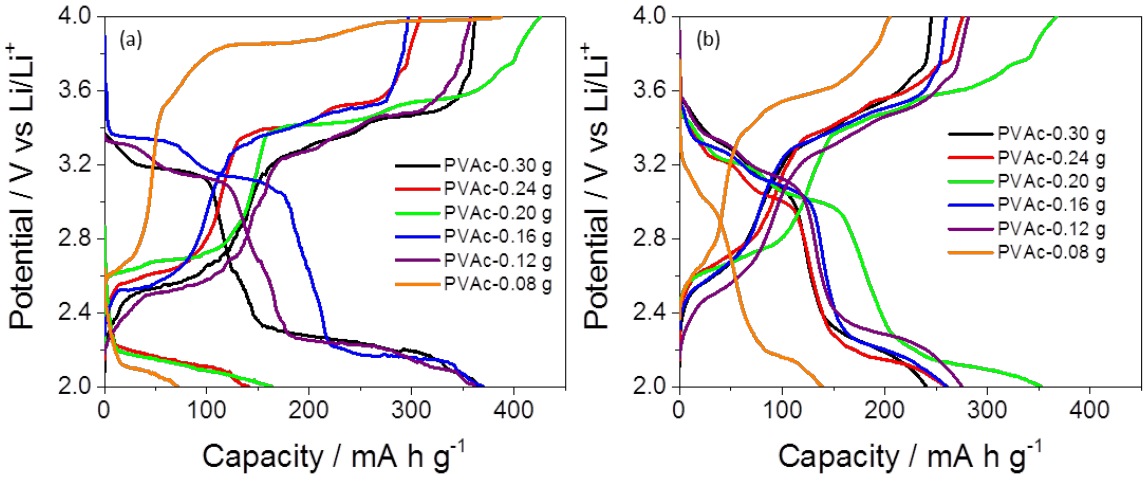


**Figure 3.8: Capacity versus potential profiles for $V_2O_5$ with varying polymer content during the C-rate test for (a) the first cycle and (b) the fifth cycle at 50 mA $g^{-1}$.**

Initial lithiation capacities for the materials are summarised in Table 3.8 and show that PVAc-0.3 g, PVAc-0.16 g, and PVAc-0.08 g achieved capacities above the theoretical capacity for $V_2O_5$, assuming 2 mol Li intercalation over 2.0 – 4.0 V vs $Li/Li^+$ which is 294 mA h $g^{-1}$. Achieving a capacity over the theoretical value highlights common issues with the use of nanostructured materials for battery applications. This is typically the result of side reactions between the less coordinated surface atoms and the electrolyte. While this phenomenon produces higher capacities, it is difficult to control and predict. The capacities and stabilities shown in Table 3.8 do not display a trend with polymer content and fibre diameter.

**Table 3.8: GDC results summaries for $V_2O_5$ with varying polymer content with initial lithiation capacities and cycle stabilities for 2 < n < 10 at 50 mA $g^{-1}$.**

| Sample | Initial lithiation capacities (mA h $g^{-1}$) | Cycle stabilities for 2 < n < 10 at 50 mA $g^{-1}$ (%) |
|---|---|---|
| PVAc-0.30 g | 366 | 73 |
| PVAc-0.24 g | 141 | 79 |
| PVAc-0.20 g | 164 | 87 |
| PVAc-0.16 g | 370 | 65 |
| PVAc-0.12 g | 361 | 84 |
| PVAc-0.08 g | 71 | 60 |

The capacity versus potential profiles in Figure 3.8 also clearly show the variations in the irreversible capacity losses (ICLs) which correlate to the difference in obtained capacities for the first lithiation and first delithiation sequences. When the first delithiation capacity is higher than the first lithiation it indicates that the excess capacity was due to interfacial storage across the electrolyte/electrode interface [134]. This is evident for PVAc-0.24 g and -0.2 g which have large ICLs of 168 and 262 mA h $g^{-1}$ respectively.

The capacity versus potential profile for PVAc-0.08 g suggested a very large overpotential which indicated low conductivity for the material [194]. This may be related to the morphology of this sample [Figure 3.7(k,l)] which did possess nanostructured particles, though there is no defined hierarchical structure. Without a hierarchical structure, there was likely decreased contact between the particles resulting in lower conductivity.

The results of the C-rate test at 50, 100, 300, 600 and back to 50 mA $g^{-1}$ over 10 cycles at each current density along with associated Coulombic efficiencies are presented Figure 3.9(a) and Figure 3.9 (b), respectively.

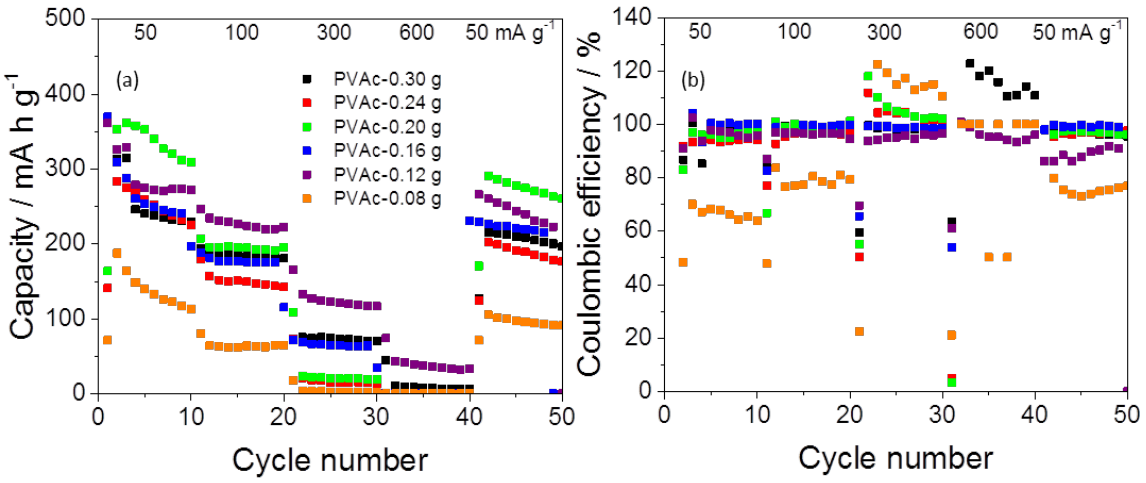


**Figure 3.9: (a) C-rate test at the following current densities: 50, 100, 300, 600 mA $g^{-1}$ and 50 mA $g^{-1}$ for 10 cycles each and (b) associated Coulombic efficiencies during the C-rate test for $V_2O_5$ with varying polymer content.**

Cycle stability is variable for all materials which is clear in the first 10 cycles at 50 mA $g^{-1}$ in Figure 3.9(a), with stabilities summarised in Table 3.8. There is an improvement in cycle stability for these initial cycles for PVAc-0.24 g, PVAc-0.20 g, and PVAc-0.12 g though there was still considerable capacity fading which was likely due to the agglomeration of nanoscale particles [195,196]. These cycle stabilities were similar to those obtained in Section 3.1.2. The increased cycle stability at higher currents was visibly observable in the C-rate and is due to a decrease in side reactions within the cells [130].

Table 3.9 summarises the capacity decreases between differing current densities and it shows that PVAc-0.12 g experienced the lowest capacity decreases indicating the highest capacity retention of the investigated samples. Interestingly, there appears to be no trend with fibre diameter and C-rate performance with the highest to lowest rate retention performer occurring in the following order: PVAc-0.12 g, PVAc-0.30 g, PVAc-0.16 g, PVAc-0.48 g, PVAc-0.20 g, PVAc-0.08 g.

**Table 3.9: A summary of capacity decreases, as percentages, between differing current densities for $V_2O_5$ with varying polymer content for (a) 100 mA $g^{-1}$ to 50 mA $g^{-1}$, (b) 300 mA $g^{-1}$ to 100 mA $g^{-1}$, (c) 600 mA $g^{-1}$ to 300 mA $g^{-1}$ and (d) the recovery in capacity as a percentage between n = 42 at 50 mA $g^{-1}$ after cycling at 600 mA $g^{-1}$ and n = 10 at 50 mA $g^{-1}$.**

| Sample | (a) % drop between n = 15 (100 mA $g^{-1}$) and n = 5 (50 mA $g^{-1}$) | (b) % drop between n = 25 (300 mA $g^{-1}$) and n = 15 (100 mA $g^{-1}$) | (c) % drop between n = 35 (600 mA $g^{-1}$) and n = 25 (300 mA $g^{-1}$) | (d) % recovery between n = 42 (600 mA $g^{-1}$) and n = 10 (50 mA $g^{-1}$) |
|---|---|---|---|---|
| PVAc-0.30 g | 22.8 | 59.8 | 89.3 | 94.0 |
| PVAc-0.24 g | 42.0 | 90.4 | 96.6 | 89.9 |
| PVAc-0.20 g | 44.6 | 89.2 | 97.6 | 94.3 |
| PVAc-0.16 g | 31.9 | 63.0 | 98.7 | 95.1 |
| PVAc-0.12 g | 17.6 | 46.0 | 69.2 | 95.4 |
| PVAc-0.08 g | 55.8 | 95.8 | 93.5 | 93.0 |

All materials performed poorly at 600 mA $g^{-1}$ indicating that these materials do not fall under the category of high power materials which is unsurprising as $V_2O_5$ is susceptible to low electronic conductivity and low Li-ion diffusion rates [94]. The low capacities at 600 mA $g^{-1}$ are likely caused by a diffusion effect implying that there was no Li-ion interaction with the surface of these materials [197]. Despite this, all materials made an almost complete recovery when cycling returned to 50 mA $g^{-1}$ in Figure 3.9(a) according to Table 3.9(d). This recovery was not observed for $V_2O_5$-450 °C, $V_2O_5$-500 °C and $V_2O_5$-550 °C in Figure 3.4 which was likely due to large diameters of fibres combined with the stepwise decrease in current density (600 mA $g^{-1}$ to 300 mA $g^{-1}$ to 100 mA $g^{-1}$ to 50 mA $g^{-1}$) which reflected low rate retention. In this section the current density variation from 600 mA $g^{-1}$ to 50 mA $g^{-1}$ was undertaken to

determine how well the materials could retain their capacity with large a large variation in current density (600 mA $g^{-1}$ to 50 mA $g^{-1}$).

PVAc-0.08 g had the lowest rate retention, lowest capacities and highest overpotential. This was the only sample that did not clearly possess a fibrous morphology, implying that a defined hierarchical structure is beneficial to prevent agglomeration and volume expansion [91,198]. The particles in PVAc-0.08 g also appeared to be quite plate-like and two dimensional in nature with a large average crystal size and pronounced PXRD reflection intensities. The results suggest that highly crystalline $V_2O_5$ is not beneficial for efficient charge transfer. This is also seen in the erratic Coulombic efficiencies which is indicative of Li-ion trapping. A similar result was shown in the Section 3.1 for $V_2O_5$-550 °C which was more crystalline in nature compared to the samples treated at lower temperatures. Additionally, Yue and Liang observed in their review that vanadium oxide electrode materials consisting of hierarchical structures produced higher capacities [68].

Impedance measurements were undertaken to compare the relative conductivities of the electrospun materials with resultant Nyquist plots presented in Figure 3.10(a). All Nyquist plots were composed of a distorted semicircle in the high-to-moderate frequency range with a small upturning in the low frequency range.

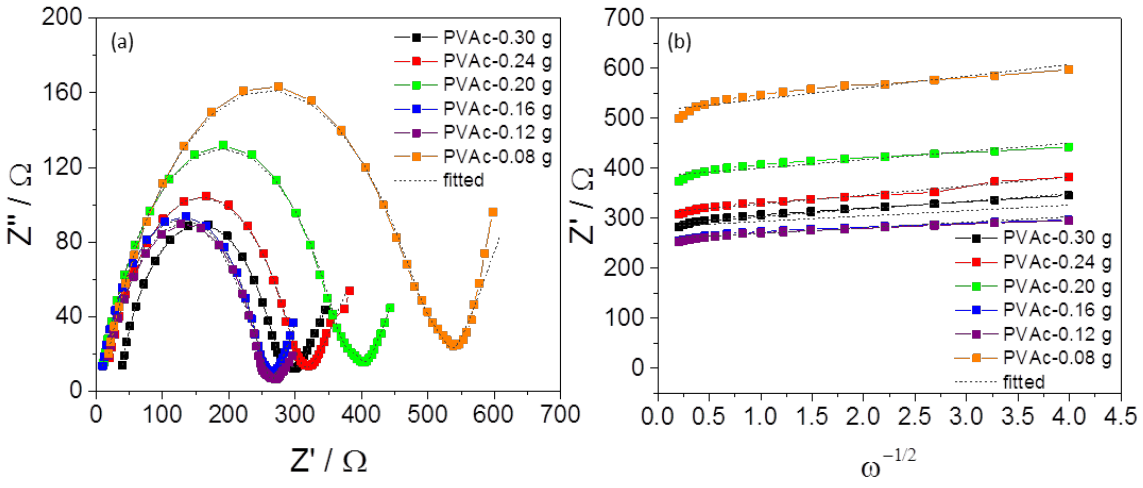


**Figure 3.10: (a) Nyquist plots of pristine cells for $V_2O_5$ with varying polymer content and (b) linear curves of $\omega^{-1/2}$ vs Z' in the low frequency region.**

The electrical equivalent circuit in Figure 3.5 of Section 3.1 was in the analysis of these Nyquist plots in Figure 3.10. The resultant resistant values are summarised in Table 3.10.

**Table 3.10: Curve fitted resistance values, $\chi^2$ goodness of fit and the Warburg impedance coefficient ($\sigma_w$) for varying polymer samples.**

| Sample | $R_b$ electrolyte (Ω) | $R_s$ surface layer (Ω) | $R_{ct}$ charge transfer (Ω) | $\chi^2$ | $\sigma_w$ ($\Omega\ cm^2\ s^{-1/2}$) | Σ R (Ω) |
|---|---|---|---|---|---|---|
| PVAc-0.30 g | 34.31 | 26.12 | 238.30 | 0.0004 | 15.3 | 264.42 |
| PVAc-0.24 g | 7.01 | 58.87 | 269.10 | 0.0016 | 17.99 | 328.00 |
| PVAc-0.20 g | 5.18 | 26.72 | 366.70 | 0.0013 | 16.48 | 393.42 |
| PVAc-0.16 g | 4.92 | 248.2 | 11.34 | 0.0013 | 11.09 | 259.54 |
| PVAc-0.12 g | 3.73 | 152.8 | 10.69 | 0.0081 | 10.7 | 259.70 |
| PVAc-0.08 g | 8.28 | 497.9 | 19.17 | 0.0022 | 23.04 | 517.07 |

Overall, it can be observed that there was an increase in the surface layer resistance ($R_s$) with an overall decrease in charge transfer resistance ($R_{ct}$) with lower polymer content. It should be noted that the impedance results in Table 3.10 suggest that some resistance values must be examined together, rather than separately, as the Nyquist plots and electrical equivalent circuit indicate that there were two overlapping time constants which was seen in the distorted semicircle. Therefore, it is reasonable that $R_s$ and $R_{ct}$ are examined in conjunction with one another [199,200].

The summation of resistances indicates that there was little to no trend with fibre diameter except for PVAc-0.08 g which has the largest semicircle in the Nyquist plot implying low conductivity. This sample also had poor rate capability with high overpotential. The results support the observation that a defined hierarchical structure promotes contact between the nanoparticles and reduces charge transfer resistances [91].

The Warburg impedance is smaller for samples (PVAc-0.16 g and PVAc-0.12 g) that have noticeably smaller fibre diameters than PVAc-0.30 g, though this trend is not exclusively observed for all samples with smaller diameters such as for PVAc-0.24 g and PVAc-0.20 g.

Despite PVAc-0.12 g showing the best electrochemical performance in terms of rate retention and capacities which is likely due to its small fibre diameter range of 300 – 500 nm, PVAc-0.30 g proved to be nearly as competitive. This polymer content was used in the previous section for $V_2O_5$-450 °C, $V_2O_5$-500 °C and $V_2O_5$-550 °C. Consequently, the polymer content was used to electrospin the doped vanadium-based oxide fibres in the following chapters.

### 3.2.4 Conclusion – Varying Polymer Amount

Results showed that fibre diameter can be controlled *via* electrospinning with polymer variation in the starting solution. Despite this, a clear trend was not present in the electrochemical performance, with no trend in the ICLs, rate retention or impedance analysis. These results do

show that a defined hierarchical structure is beneficial for these electrospun $V_2O_5$ fibres which likely prevented particle agglomeration and promoted improved conductivity. This was clearly shown with PVAc-0.08 g which possessed the lowest polymer content and consequently no fibrous morphology. Additionally, a fibrous morphology is likely to provide increased contact between the particles of the material, which improved conductivity and may have alleviated volume expansion.

## 3.3 SUMMARY

This chapter focussed on the structural and electrochemical investigations of electrospun $V_2O_5$ calcined at 450 °C, 500 °C, and 500 °C, in Section 3.1, and that of $V_2O_5$ electrospun from starting solutions of varying polymer content, in Section 3.2.

Both sections showed that crystallite size, d-spacings, fibre diameters, and Faradaic impedances could be controlled by varying either calcination temperature treatment or polymer content in the starting solution. Despite this, the electrospun $V_2O_5$ remained susceptible to substantial capacity decay and poor rate capability. Investigations as positive electrode materials in Li-ion coin cells showed that a compromise with capacity, stability and crystallinity of the nanostructured particles must be considered during material suitability evaluation for energy storage. The systematic investigation of the electrospun undoped vanadium oxide in Chapter 3 was unique and showed that another strategy is required to improve the performance of this promising electrode material. This chapter showed that calcination at 500 °C and a polymer content of 0.3 g gave promising results and was deemed acceptable for further analysis of electrospun vanadium-based oxides for LIBs.

This was a worthwhile investigation as several studies have emphasised the importance of the crystalline nature of the $V_2O_5$ with the resultant electrochemical performance [88,92,130]. Meanwhile others have focussed on improving $V_2O_5$ electrochemical performances by

introducing defects into the structure [91]. The intentional introduction of defects has gained traction recently as a potential path of investigation in the development of amorphous vanadium oxides, such as the introduction of dopants.

# Chapter 4 Electrospun $V_2O_5$, barium-doped and titanium-doped $V_2O_5$ as positive electrodes for lithium ion batteries

### 4.1.1 Introduction

Redox-inactive dopants (for which there is no additional redox charge transfer reactions upon lithiation/delithiation) are often used for positive electrode materials in LIBs. Lithium iron phosphate (LFP) is a very stable high-power electrode material and many redox-inactive dopants have been shown to improve the cycling performance, e.g. $Nb^{5+}$ [201], $Ti^{4+}$ [202], and $Al^{3+}$ [203]. The occupying site of the dopant depends on the cation and has been often shown to improve the electronic and/or ionic conductivity [203]. For lithiated transition metal oxides, one main issue is the stability upon cycling, which can be improved by using redox-inactive cations such as $Mn^{4+}$ or $Al^{3+}$. NCA ($LiNi_{0.8}Co_{0.15}Al_{0.05}O_2$) is one such example where a small amount of the redox inactive dopant $Al^{3+}$ has been shown to improve electrochemical performance and reduce cell impedance, resulting in a stabilisation of both the material structure and surface reactivity [204]. The use of the $Al^{3+}$ dopant combined with the reduction of cationic disorder caused by the partial substitution of Ni with Co [205], as $Co^{3+}$ is not as readily reduced as $Ni^{3+}$ [30], results in NCA having a high lithiation capacity of approximately 200 mA h $g^{-1}$, long storage life and reduced cost compared to undoped Co-based positive electrodes [27].

In terms of $V_2O_5$, redox-inactive dopants include, but are not limited to $Cr^{3+}$ [74,206], $Ag^{+}$ [136,207], $Cu^{2+}$ [182], $Al^{3+}$ [134,207,208], $Nb^{5+}$ [171], $Na^{+}$ [209], and $Fe^{3+}$ [210] when studied within or near to the 2.0 – 4.0 V vs $Li/Li^{+}$ range. The use of $Ti^{4+}$ as a dopant for vanadium oxides has shown to improve electronic conductivity when used as electrode materials for supercapacitors [211]. $Ti^{4+}$ is a useful potential dopant as it has valence states of 4+ and 3+ and its diameter is comparable to $V^{5+}$ with a coordination number of six [184]. Like many of the previously mentioned dopants, alkaline earth metals, such as $Ba^{2+}$ and $Ca^{2+}$ are redox-inactive,

meaning they do not show additional redox charge transfer during lithiation/delithiation between 2.0 to 4.0 V vs $Li/Li^+$. They have been used because they have shown to improve the cycling performance in materials such as tin oxide [212,213]. Zhan *et al.* reported that $Cr^{3+}$ doped vanadium oxide, $Cr_{0.1}V_2O_{5.15}$, prepared *via* a sol-gel method, partially prevented irreversible phase transitions of the $V_2O_5$ structure using a cyclic voltammetry analysis [74]. This was made apparent with irreversible redox peaks present in the $V_2O_5$ voltammogram plot while reversible redox peaks were seen in the $Cr_{0.1}V_2O_{5.15}$ voltammogram. Also observed was an improvement in cycling performance compared to that of undoped $V_2O_5$. Li-ion diffusion has been shown to increase *via* the use of dopants [184]. Liang *et al.* showed that $Na^+$ doped $V_2O_5$ formed ß-$Na_{0.33}V_2O_5$ and resulted in improved Li-ion diffusion caused by a mesoporous flake-like structure produced *via* the introduction of the $Na^+$ dopant [209].

In this chapter, redox-inactive $Ti^{4+}$ and $Ba^{2+}$ were homogeneously mixed with a vanadium-based oxide starting solution and electrospun to produce continuous microscale nanostructured fibres. $Ti^{4+}$ was chosen to explore the effects of introducing a redox-inactive dopant that is similar in size to $V^{5+}$. $Ba^{2+}$ was used to determine the structural and electrochemical effects of incorporating a redox-inactive large ion into the electrospun $V_2O_5$. The structural variations created due to the introduction of both dopants were investigated along with the electrochemical properties. It was observed that 10 at% $Ti^{4+}$ doping made significant improvements on electrochemical performance and that phase changes that occurred during cycling were noticeably different between undoped $V_2O_5$ and doped $V_2O_5$.

## 4.2 RESULTS AND DISCUSSION

### 4.2.1 Morphology and Structure

XPS and EDS analysis were used to confirm the amount of $Ba^{2+}$ and $Ti^{4+}$ doped into electrospun $V_2O_5$. The results from these techniques, which will be discussed in greater detail later in this section, indicate that the formulas for the doped materials are $V_{1.79}Ba_{0.21}O_5$ and $V_{1.81}Ti_{0.19}O_5$. The PXRD patterns comparing undoped $V_2O_5$ to $V_{1.79}Ba_{0.21}O_5$ and $V_{1.81}Ti_{0.19}O_5$ obtained through electrospinning are shown in Figure 4.1(a) showing that orthorhombic α-$V_2O_5$ was produced corresponding to the space group *Pmmn* (ICSD 60767) with appropriate reflection labelling [172]. The slight impurity detected in the PXRD for $V_{1.79}Ba_{0.21}O_5$, highlighted with an asterisk in Figure 4.1(a,b), is tentatively attributed to a phase separated compound of $Ba_3(VO_4)_2$ [214]. The PXRD pattern of $V_{1.81}Ti_{0.19}O_5$ sample shows no impurity reflections indicating that a stable single phase solid solution was formed [215]. The materials were of varying colours according to Figure 4.1(a) (inset) in which undoped $V_2O_5$ was bright yellow, $V_{1.79}Ba_{0.21}O_5$ material appeared orange and $V_{1.81}Ti_{0.19}O_5$ was dark yellow.

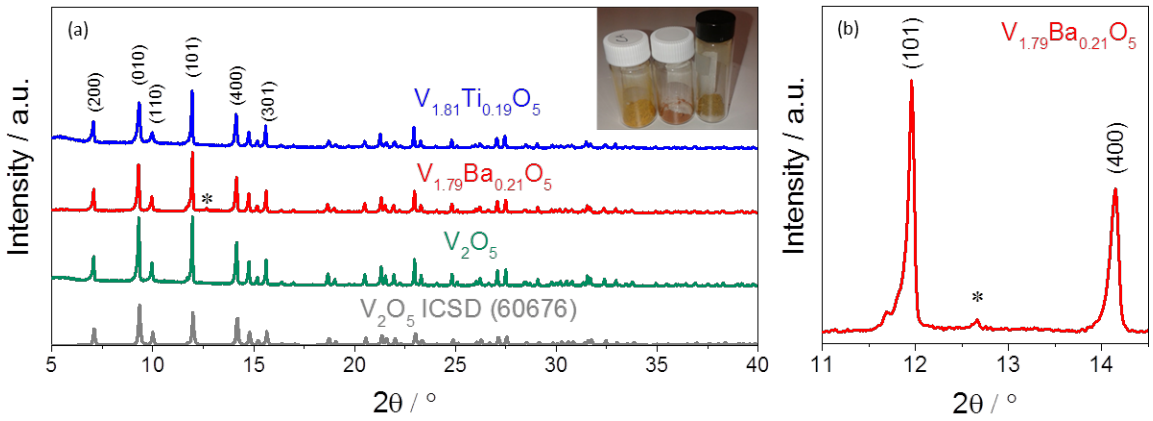


**Figure 4.1: (a) PXRD patterns for $V_2O_5$, $V_{1.79}Ba_{0.21}O_5$, and $V_{1.81}Ti_{0.19}O_5$ with a slight impurity highlighted with an asterisk at 2θ = 12.7° for $V_{1.79}Ba_{0.21}O_5$ and (inset) a photo emphasizing the colour variations caused by the introduction of a dopant from bright yellow (undoped $V_2O_5$) to orange ($Ba^{2+}$) and dark yellow ($Ti^{4+}$). (b) Enlarged region of impurity for $V_{1.79}Ba_{0.21}O_5$.**

Le Bail refinement results are shown in Table 4.1. Refinement of the PXRD patterns revealed increased *a*- and *b*-directions for the doped samples compared to undoped $V_2O_5$. The *c*-direction increased for $V_{1.79}Ba_{0.21}O_5$ and decreased for $V_{1.81}Ti_{0.19}O_5$ when respectively compared to the undoped $V_2O_5$. Overall $V_{1.81}Ti_{0.19}O_5$ had a smaller unit cell than the undoped sample while the $V_{1.79}Ba_{0.21}O_5$ had a larger unit cell.

**Table 4.1: Le Bail refinements of lattice parameters with the resultant unit cell volumes of $V_2O_5$, $V_{1.79}Ba_{0.21}O_5$, and $V_{1.81}Ti_{0.19}O_5$.**

| Sample | a (Å) | b (Å) | c (Å) | Volume ($Å^3$) | $R_{wp}$ (%) | $X^2$ |
|---|---|---|---|---|---|---|
| $V_2O_5$ | 11.544(1) | 3.5769(4) | 4.3929(6) | 181.395(67) | 10.09 | 1.27 |
| $V_{1.79}Ba_{0.21}O_5$ | 11.589(3) | 3.587(1) | 4.417(1) | 183.63(17) | 10.24 | 1.26 |
| $V_{1.81}Ti_{0.19}O_5$ | 11.581(3) | 3.578(1) | 4.365(1) | 180.86(13) | 10.17 | 1.26 |

The same progression observed in the unit cell volumes was also seen in the d-spacings which were calculated using the (010) peak and Bragg's law with 4.08, 4.37, and 4.38 Å for $V_{1.81}Ti_{0.19}O_5$, $V_2O_5$, and $V_{1.79}Ba_{0.21}O_5$ respectively. A decreased interlayer spacing for $V_{1.81}Ti_{0.19}O_5$ can be attributed to a reduction in the electrostatic repulsion between the $V_2O_5$ layers caused by the $Ti^{4+}$ shielding the negative charge associated with the apical oxygen atoms on the $VO_5$ pyramids [207,216,217]. This is a reasonable conclusion as the ionic radius of $Ti^{4+}$ is larger (0.51 Å, CN = 5) than $V^{5+}$ (0.46 Å, CN = 5) and hence could have provided increased shielding. $Ba^{2+}$ (1.35 Å, CN = 6) is significantly larger than $V^{5+}$ which was reflected in an increased unit cell volume and likely distortion of the $V_2O_5$ layers.

XPS analysis for the materials in this chapter, which were later processed into electrodes for this study, are shown in Figure 4.2. Figure 4.2(a) showed a $V^{4+}$:$V^{5+}$ ratio of 0.06:0.94 for undoped $V_2O_5$. XPS analysis of $V_{1.79}Ba_{0.21}O_5$ in Figure 4.2(b) revealed a $V^{4+}$:$V^{5+}$ ratio of 0.05:0.95 and a $Ba^{2+}$:V atomic ratio of 10.5:89.5 which was slightly higher than 8:92 suggested by EDS. XPS analysis of $V_{1.81}Ti_{0.19}O_5$ in Figure 4.2 (c) revealed a $V^{4+}$:$V^{5+}$ ratio of 0.06:0.94

and a $Ti^{4+}$:V atomic ratio of 9.5:90.5 which was in good agreement with 10:90 as suggested by EDS. The variation in atomic ratios for $V_{1.79}Ba_{0.21}O_5$ was likely due to the precursor falling out of suspension during the electrospinning process as the $Ba^{2+}$ precursor, BaO, was less compatible with the ethanol solvent. Despite this, very little precursor was seen to fall out of the suspension, consequently the electrospinning process was allowed to continue. As the solubility limit of the starting solution was surpassed, as evidenced by the suspension, it is likely that there was a slightly higher concentration of $Ba^{2+}$ at the surface of the microfibres.

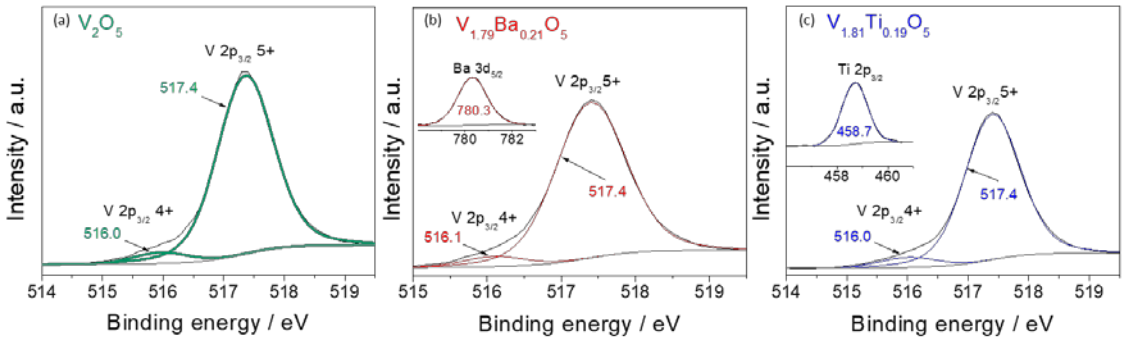


**Figure 4.2: XPS elemental scans of the (a) V2p$_{3/2}$ peak for $V_2O_5$. (b) V2p$_{3/2}$ peak and the Ba3d$_{5/2}$ peak (inset) for $V_{1.79}Ba_{0.21}O_5$. (c) V2p$_{3/2}$ peak and the Ti2p$_{3/2}$ peak (inset) for $V_{1.81}Ti_{0.19}O_5$.**

The SEM images presented in Figure 4.3 reveal microscale fibres made up of nanoscale particles in a hierarchical structure. The fibres possess diameters of *ca.* 1100 nm for $V_2O_5$ fibres [Figure 4.3(a,b)], a range of 700 – 1000 nm for $V_{1.79}Ba_{0.21}O_5$ [Figure 4.3(c,d)] and *ca.* 1660 nm for $V_{1.81}Ti_{0.19}O_5$ [Figure 4.3(e,f)]. The $V_2O_5$ fibres, as shown in Figure 4.3(a,b), were not consistent with the $V_2O_5$ fibres in Chapter 3 which had a large fibre diameter range of 0.7-2.3 μm compared to *ca.* 1100 nm. This was likely due to the electrospinning operation undertaken in lower humidity.

In some cases, it appeared that some of fibres had adhered during the electrospinning operation. The larger diameter fibres in Figure 4.3(d) for $V_{1.79}Ba_{0.21}O_5$ and in Figure 4.3(f) for

$V_{1.81}Ti_{0.19}O_5$ are approximately 1500 nm in size. This may have been caused by inconsistencies in the electrospinning operation such as blockage of the needle, inhomogeneous sol-gel, slow solvent evaporation or elevated humidity [218,219]. The optimisation of the starting solution components for these materials along with the electrospinning environment would produce fibres which are more consistent in diameter. This was not undertaken in this thesis as the electrospinning parameters and starting solution components were kept constant during this investigation of doped $V_2O_5$. Vreize *et al.* found that an increase in humidity resulted in an increase in fibre diameters of their electrospun cellulose acetate and PVP [218]. Furthermore, they observed that with starting solutions containing ethanol, an increase in humidity led to absorption of water by the fibres making them solidify slower.

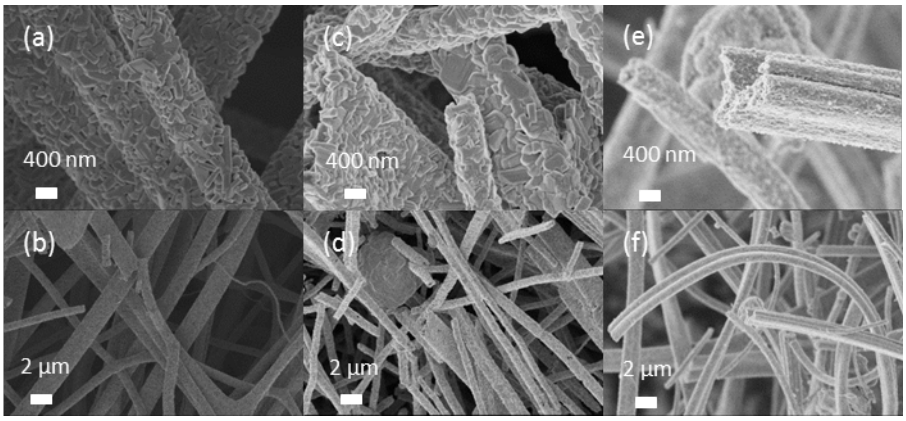


**Figure 4.3: SEM images of (a,b) undoped $V_2O_5$, (c,d) $V_{1.79}Ba_{0.21}O_5$., (e,f) $V_{1.81}Ti_{0.19}O_5$ highlighting the nanostructured microfibres produced *via* electrospinning.**

Particle morphology of the microfibres was examined using TEM and was seen to substantially vary between materials, suggesting that particle growth and morphology was heavily influenced by the addition of a dopant material, as seen in Figure 4.4. The undoped $V_2O_5$ fibres and particles [Figure 4.4(a,b,c)] were large and angular in appearance suggesting directional growth of the $V_2O_5$ layers with lengths of 240 – 260 nm and widths of 150 – 180 nm. The $V_{1.79}Ba_{0.21}O_5$ particles as seen in Figure 4.4(e) were needle-like in appearance and upon closer inspection

possessed widths of approximately 10 nm and lengths up to 1 µm [Figure 4.4(f,g)]. $V_{1.81}Ti_{0.19}O_5$ particles showed a similar shape to those of undoped $V_2O_5$ though smaller and less directional with dimensions of 130 – 230 nm [Figure 4.4(j)]. The porous particle surface suggested in Figure 4.4(h) was also observed in Figure 4.4(k) for $V_{1.81}Ti_{0.19}O_5$. In addition, lattice spacings were less defined in the $V_{1.79}Ba_{0.21}O_5$ material [Figure 4.4(h)] compared to $V_2O_5$ [Figure 4.4(d)] and $V_{1.81}Ti_{0.19}O_5$ [Figure 4.4(i)] with detected lattice spacings of 0.57 nm and 0.33 nm corresponding to the (200) and (101) plane for $V_2O_5$ and $V_{1.81}Ti_{0.19}O_5$, respectively. The lack of lattice space definition for $V_{1.79}Ba_{0.21}O_5$ may be due to a combination of the large $Ba^{2+}$ dopant and the small amount of $Ba_3(VO_4)_2$ impurity resulting in a slightly defective structure and marked variations in particle morphology between the samples with doping [220–222].

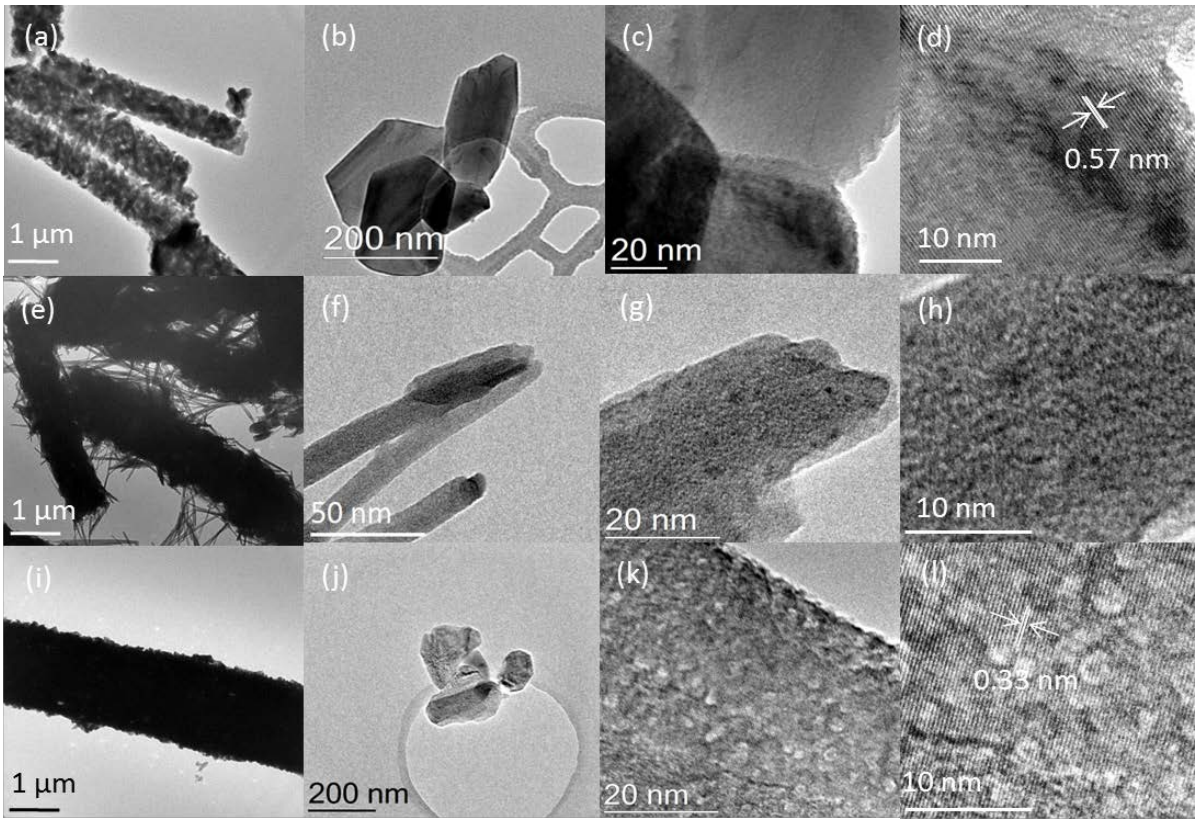


**Figure 4.4: TEM images of (a) $V_2O_5$ microfibres, (b,c) $V_2O_5$ particles, (d) high resolution image of the $V_2O_5$ particle surface with lattice spacings highlighted, (e) $V_{1.79}Ba_{0.21}O_5$ microfibres, (f,g) $V_{1.79}Ba_{0.21}O_5$ particles, (h) high resolution image of $V_{1.79}Ba_{0.21}O_5$ particle surface showing an absence of defined lattice**

**spacings, (i) $V_{1.81}Ti_{0.19}O_5$ microfibres, (j,k) $V_{1.81}Ti_{0.19}O_5$ particles, (l) high resolution image of $V_{1.81}Ti_{0.19}O_5$ particle surface with lattice spacings highlighted.**

BET specific surface area measurements for undoped $V_2O_5$, $V_{1.79}Ba_{0.21}O_5$ and $V_{1.81}Ti_{0.19}O_5$ were 9.0, 12.8, and 19.3 $m^2\ g^{-1}$ respectively. While the variation between samples was not that great, it has been suggested that as crystallinity increases the surface area decreases [127]. This is reflected in the preceding structural analysis.

### 4.2.2 Electrochemical Performance

Figure 4.5 details the cyclic voltammograms for the three materials and shows that the undoped and doped materials possessed oxidation and reduction peaks. This implies that the charge transfer mechanisms are predominantly redox-based with phase transitions that match α-$V_2O_5$, ε-$Li_{0.5}V_2O_5$, δ-$LiV_2O_5$, and γ-$Li_2V_2O_5$ using Figure 1.7 and the literature [76,79]. The voltammogram for $V_2O_5$ in Figure 4.5(a) is similar to that of $V_2O_5$-500 °C in Figure 3.3(a) which showed that the fibre diameter variation observed between Figure 4.3(a,b) for $V_2O_5$ in this chapter and Figure 3.2(a,b) for $V_2O_5$-500 °C does not overly affects CV test results.

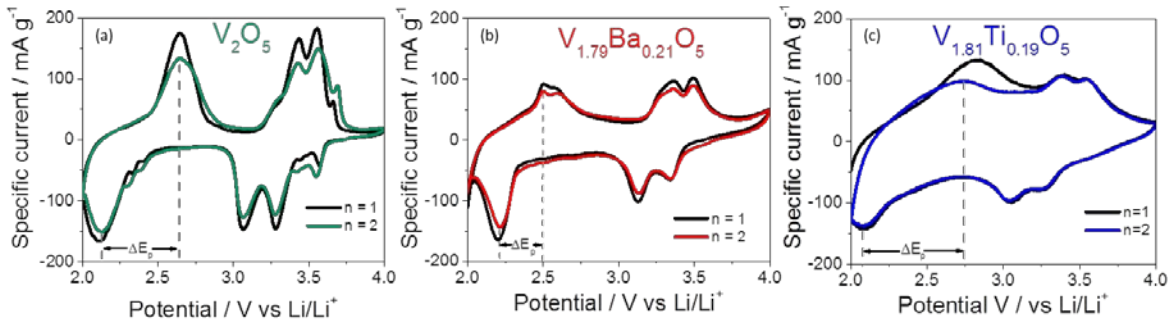


**Figure 4.5: Cyclic voltammograms at 0.1 mV $s^{-1}$ over 2 cycles with $\Delta E_p$ labelled for the δ/γ transition for (a) $V_2O_5$, (b) $V_{1.79}Ba_{0.21}O_5$ and (c) $V_{1.81}Ti_{0.19}O_5$.**

Redox peak separations ($\Delta E_p$) for the δ/γ transition, which are highlighted on the appropriate voltammogram, are 0.54, 0.30 and 0.65 V vs $Li/Li^+$ for $V_2O_5$, $V_{1.79}Ba_{0.21}O_5$, $V_{1.81}Ti_{0.19}O_5$, respectively. The larger $\Delta E_p$ value for $V_{1.81}Ti_{0.19}O_5$ suggests that the electrochemical reversibility of the δ/γ transition was lower for this material, compared to $V_2O_5$ and $V_{1.79}Ba_{0.21}O_5$, implying that the $Ti^{4+}$ dopant may have been hindering this phase transition [206,223,224]. There is also a reduction in $\Delta E_p$ for the α/ε and ε/δ transitions in the doped materials compared to $V_2O_5$ indicating that Li-ion kinetics were improved for the doped materials along with reduced polarisation and higher reversibility [3]. The shoulder peaks on the undoped $V_2O_5$ voltammogram at *ca.* 3.5 V vs $Li/Li^+$ indicate that the undoped sample offered multiple Li-ion active sites for multi-stepped intercalation/extraction processes [180] and had a higher degree of crystallinity compared to the doped counterparts [76,79]. The absence of these shoulder peaks for both $V_{1.79}Ba_{0.21}O_5$ and $V_{1.81}Ti_{0.19}O_5$ indicated that the complex structural changes occurring for $V_2O_5$ were reduced for both doped counterparts [134]. Moreover, the $V_{1.81}Ti_{0.19}O_5$ voltammogram occupied a greater area than either $V_2O_5$ or $V_{1.79}Ba_{0.21}O_5$ which suggested that in addition to diffusion controlled processes *via* Li-ion insertion there may be non-diffusion-controlled processes which occurred resulting in increased storage capability [102].

Capacity versus potential profiles for cycles 1, 5, 15 and 25 of the C-rate test are plotted for each sample in Figure 4.6. The initial lithiation capacities seen in Figure 4.6(a) were 146 mA h $g^{-1}$ for $V_2O_5$, 87 mA h $g^{-1}$ for $V_{1.79}Ba_{0.21}O_5$, and 215 mA h $g^{-1}$ for $V_{1.81}Ti_{0.19}O_5$. These capacities improved to 231 mA h $g^{-1}$ for $V_2O_5$, 142 mA h $g^{-1}$ for $V_{1.79}Ba_{0.21}O_5$, and 237 mA h $g^{-1}$ for $V_{1.81}Ti_{0.19}O_5$ for cycle 5 in Figure 4.6(b) as ionic pathways were established [179].

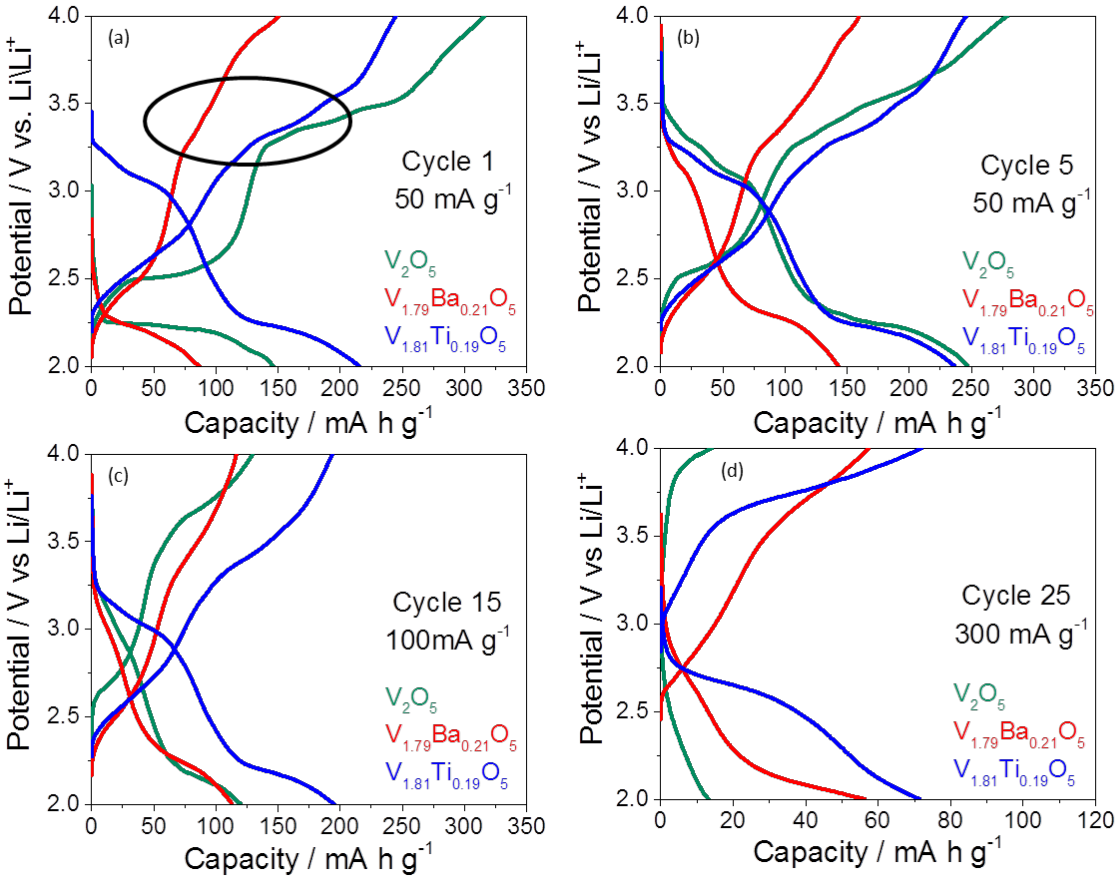


**Figure 4.6: Capacity versus potential profiles for all materials during the C-rate test for (a) cycle 1 at 50 mA $g^{-1}$ with a circle emphasising the range of potential step definition, (b) cycle 4 at 50 mA $g^{-1}$, (c) cycle 15 at 100 m $Ag^{-1}$, and (d) cycle 25 at 300 mA $g^{-1}$.**

The phase transitions in $V_2O_5$ were quite distinct and could be assigned to α-$V_2O_5$, ε-$Li_{0.5}V_2O_5$, δ-$LiV_2O_5$, and γ -$Li_2V_2O_5$ referring to Figure 1.7. However, these phase transitions, observed as potential steps, were less defined for the doped counterparts, though arguably still present, as shown in Figure 4.6(a) within the circle. This is likely due to a dispersion of strain caused by the lithiation/delithiation process [225].

Irreversible capacity loss (ICL) is variable for all materials where $V_2O_5$ experienced the largest ICL of 169 mA h $g^{-1}$ followed by $V_{1.79}Ba_{0.21}O_5$ at 64 mA h $g^{-1}$ and $V_{1.81}Ti_{0.19}O_5$ with 29 mA h $g^{-1}$. This indicated that there was a large layer built up between the $V_2O_5$ and electrolyte which appeared to be significantly reduced for both doped samples. A large ICL of

111 mA h $g^{-1}$ was observed by Yu *et al.* for undoped $V_2O_5$ thin films compared to 36 mA h $g^{-1}$ for $Mn^{2+}$ doped $V_2O_5$ films [225]. The authors attributed this improvement in Li-ion intercalation/extraction of the $Mn^{2+}$ doped film to the amorphisity of the films and increased oxygen vacancies providing nucleation centres for phase transitions. The capacity versus potential profiles also showed that as current density increased, the overpotential remains lower for $V_{1.79}Ba_{0.21}O_5$ and $V_{1.81}Ti_{0.19}O_5$ compared to the undoped $V_2O_5$ which implied higher electronic conductivity for the doped materials in this chapter [194].

The C-rate tests for the three materials are presented in Figure 4.7(a). Undoped $V_2O_5$ underwent high capacity losses over the initial 10 cycles at 50 mA $g^{-1}$ with 285 mA h $g^{-1}$ (n=2) which decreases to 185 mA $g^{-1}$ (n=10) equating to a 35% loss. Conversely, $V_{1.79}Ba_{0.21}O_5$ and $V_{1.81}Ti_{0.19}O_5$ experienced no such capacity loss over the initial 10 cycles at 50 mA $g^{-1}$ implying increased stabilisation brought about by the dopants.

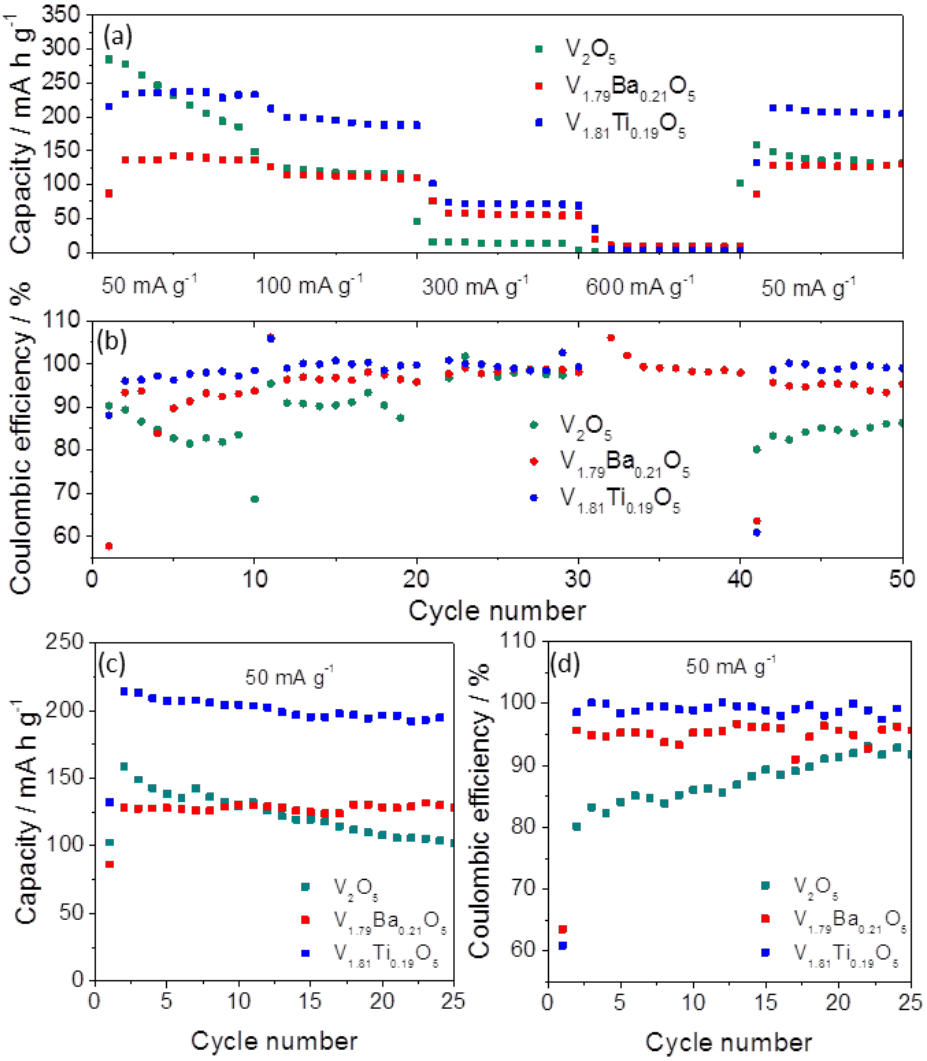


**Figure 4.7: (a) C-rate test at various current rates with (b) the relevant Coulombic efficiencies. (c) Cycling at 50 mA $g^{-1}$ after the C-rate test detailed in (a) and (d) relevant Coulombic efficiencies.**

Rate retention was variable between samples with a noticeable improvement between both doped samples and undoped $V_2O_5$ [Figure 4.7(a)]. Table 4.2 summarises this rate retention variety and confirmed that the dopants improved the rate capability of $V_2O_5$. This variation in rate capability followed the same trend as the resultant surface areas with undoped $V_2O_5$ showing the poorest rate performance and smallest surface area (9.0 $m^2g^{-1}$). Additionally, $V_{1.81}Ti_{0.19}O_5$ showed the best rate performance of the three samples with the highest surface area (19.3 $m^2g^{-1}$) suggesting more surface reactivity. This was also observed in the cyclic voltammogram for $V_{1.81}Ti_{0.19}O_5$ in Figure 4.5 which possessed less defined redox peaks.

**Table 4.2: A summary of capacity decreases as percentages between differing current densities for $V_2O_5$, $V_{1.79}Ba_{0.21}O_5$ and $V_{1.81}Ti_{0.19}O_5$ for (a) 100 mA $g^{-1}$ to 50 mA $g^{-1}$, (b) 300 mA $g^{-1}$ to 100 mA $g^{-1}$, (c) 600 mA $g^{-1}$ to 300 mA $g^{-1}$ and (d) the recovery in capacity as a percentage between n = 42 at 50 mA $g^{-1}$ after cycling at 600 mA $g^{-1}$ and n = 10 at 50 mA $g^{-1}$.**

| Sample | (a) % drop between n = 15 (100 mA $g^{-1}$) and n = 5 (50 mA $g^{-1}$) | (b) % drop between n = 25 (300 mA $g^{-1}$) and n = 15 (100 mA $g^{-1}$) | (c) % drop between n = 35 (600 mA $g^{-1}$) and n = 25 (300 mA $g^{-1}$) | (d) % recovery between n = 42 (600 mA $g^{-1}$) and n = 10 (50 mA $g^{-1}$) |
|---|---|---|---|---|
| $V_2O_5$ | 50 | 90 | 97 | 85 |
| $V_{1.79}Ba_{0.21}O_5$ | 20 | 50 | 84 | 94 |
| $V_{1.81}Ti_{0.19}O_5$ | 18 | 64 | 96 | 91 |

After the C-rate tests, the samples were further cycled at a current density of 50 mA $g^{-1}$ for 25 cycles [Figure 4.7(c)]. Undoped $V_2O_5$ retained 65% capacity from 158 mA h $g^{-1}$ (n=2) to 102 mA h $g^{-1}$ (n=25). $V_{1.79}Ba_{0.21}O_5$ experienced no overall capacity loss with 128 mA h $g^{-1}$ obtained at n=2 and n=25. $V_{1.81}Ti_{0.19}O_5$ retained 91% capacity from 213 mA h $g^{-1}$ (n=2) to 194 mA h $g^{-1}$ (n=25). Average Coulombic efficiencies of samples over these cycles were 87% for $V_2O_5$, 95% for $V_{1.79}Ba_{0.21}O_5$ and 99% for $V_{1.81}Ti_{0.19}O_5$. Clearly $V_{1.79}Ba_{0.21}O_5$ and $V_{1.81}Ti_{0.19}O_5$ behaved much more efficiently than $V_2O_5$ as characterized by nearly 100% capacity retention compared to $V_2O_5$ in Figure 4.7(d).

The variation in obtained capacities was larger for the undoped $V_2O_5$ and had a higher initial capacity than that of the doped materials. This is expected as $V_2O_5$ is susceptible to substantial structural variations resulting in high capacity fading as more Li-ions can intercalate into the structure and cause more profound structural changes. This significant loss of capacity seen in the $V_2O_5$ material in the initial cycles of Figure 4.7(a) has been confirmed by others [182,210]. Conversely, neither of the doped samples experienced capacity losses over these initial 10 cycles indicating that the dopants provided a role in stabilizing the $V_2O_5$ structure. There is

also an improvement in cycle stability for the doped materials compared to undoped across all current rates. This was also observed to some extent in the voltammograms in Figure 4.5 as there is a greater overlap between cycles 1 and 2 for $V_{1.79}Ba_{0.21}O_5$ and $V_{1.81}Ti_{0.19}O_5$ compared to undoped $V_2O_5$.

All materials performed poorly at a current rate of 600 mA $g^{-1}$ which was reflected in virtually no capacity response at this current density, clearly showing that these materials did not perform well under high rates. The poor capacity retention at 600 mA $g^{-1}$ was likely due to a diffusion effect which implying that there was little to no interaction with the surface of the material at higher current densities. $V_2O_5$ has drawn wide attention as an electrode material, though its poor capacity retention and rate performance is caused by its low electronic conductivity and low Li-ion diffusion rate [94] which was clearly seen at 600 mA $g^{-1}$. Due to the poor capacity response at 600 mA $g^{-1}$ for undoped $V_2O_5$ and $V_{1.81}Ti_{0.19}O_5$ their Coulombic efficiencies have not been included in Figure 4.7(b).

Additionally, Coulombic efficiency was variable for all materials though noticeably improved for the doped materials in both the C-rate and cycling data, implying that there was a prevention of Li-ion trapping in the $V_{1.79}Ba_{0.21}O_5$ and $V_{1.81}Ti_{0.19}O_5$ materials. Despite this, the Coulombic efficiencies were still quite variable at lower rates, such as 50 mA $g^{-1}$, which was likely caused by increased side reactions.

To closely examine what occurred during the first cycling process, ex-situ XRDs were obtained after the first lithiation to 2.0 V vs $Li/Li^+$ and the first delithiation to 4.0 V vs $Li/Li^+$ for each of the investigated materials in Figure 4.8. The coin cells were dismantled in an argon-filled glovebox and the electrodes were rinsed with dimethyl carbonate (DMC) before ex-situ XRD was undertaken.

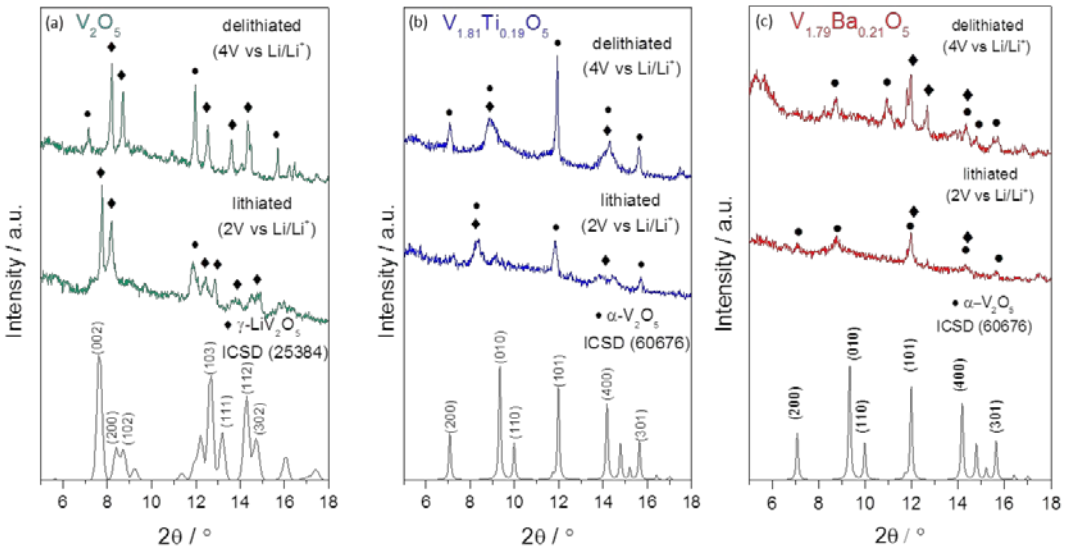


**Figure 4.8: Ex-situ XRD of the lithiated (2 V vs Li/Li$^+$) and delithiated (4 V vs Li/Li$^+$) states showing a higher proportion of (a) γ-$LiV_2O_5$ (♦) for $V_2O_5$ and a higher proportion of α-$V_2O_5$ (●) for both (b) $V_{1.81}Ti_{0.19}O_5$ and (c) $V_{1.79}Ba_{0.21}O_5$.**

All materials had lower reflection intensities at both 2.0 V vs Li/Li$^+$ and 4.0V vs Li/Li$^+$ compared to the pristine powder which was indicative of a decrease in crystallite size [48,226]. Reflection shift variation between the lithiated and delithiated states was largest for $V_2O_5$ indicating a significant shift in the $V_2O_5$ layers as seen in an interlayer distance reduction after extraction of Li-ions from the material. $V_{1.81}Ti_{0.19}O_5$ and $V_{1.79}Ba_{0.21}O_5$ had smaller reflection variations implying that the doped materials experienced increased structural stabilisation [90] which was observed in both the C-rate and cycling results, detailed in Figure 4.7(a,c).

The (200) peak at 2θ = 7° disappeared at the lithiated (2.0 V vs Li/Li$^+$) stage and then returned at the delithiated (4.0 V vs Li/Li$^+$) stage for undoped $V_2O_5$ and $V_{1.81}Ti_{0.19}O_5$ which was an indication of disordering of the $V_2O_5$ structure during lithiation and reordering during delithiation caused by the intercalation/extraction of Li-ions.

The PXRDs for the lithiated (2.0 V vs Li/Li$^+$) and delithiated (4.0 V vs Li/Li$^+$) states of $V_2O_5$ clearly show a mix of both α-$V_2O_5$, the orthorhombic unintercalated phase, and γ-$LiV_2O_5$ with

a space group of *Pnma* [227] that has been known to irreversibly form in the 2.0 – 2.7 V vs $Li/Li^+$ range resulting in capacity fading. Conversely, the reflections of $V_{1.81}Ti_{0.19}O_5$ and $V_{1.79}Ba_{0.21}O_5$ at the lithiated (2.0 V vs $Li/Li^+$) and delithiated (4.0 V vs $Li/Li^+$) states can be attributed to a higher proportion of orthorhombic $V_2O_5$ than that of the γ-$LiV_2O_5$, indicating that both the $Ti^{4+}$ and $Ba^{2+}$ dopants provided increased stabilisation and promoted higher degree of reversibility in the facilitation of phase changes. The absence of ε-$Li_{0.5}V_2O_5$ and δ-$LiV_2O_5$ suggested that these intermediate phases were reversibly formed and that a complete conversion of them occurred during the first lithiation at 2.0 V vs $Li/Li^+$ and the first delithiation at 4.0 V vs $Li/Li^+$.

The large $\Delta E_P$ value for the δ/γ transition for $V_{1.81}Ti_{0.19}O_5$ [Figure 4.5(c)] not only suggests that this transition was not favoured but was also in agreement with the ex-situ XRD [Figure 4.8(b)] that possess a smaller proportion of γ-$LiV_2O_5$ compared to α-$V_2O_5$. Moreover, the large irreversible capacity loss observed for undoped $V_2O_5$ in the capacity versus potential profiles (Figure 4.6) was most likely a result of the high proportion of γ-$LiV_2O_5$ formed in this material and large structural variations which resulted from the build-up of Li-ions at the electrode/electrolyte interface.

Reflection intensities for $V_{1.79}Ba_{0.21}O_5$ at the delithiated state (4.0 V vs $Li/Li^+$) were much lower than that of undoped $V_2O_5$ and $V_{1.81}Ti_{0.19}O_5$ indicating a lower degree of crystallinity. This agrees with the high-resolution TEM image in Figure 4.4(h) which did not clearly show defined lattice planes, suggesting a distorted structure. This was likely caused by the large $Ba^{2+}$ dopant combined with the high dopant loading of 10 at% causing blockages of active sites.

## 4.3 CONCLUSION AND SUMMARY

In this chapter, the structural and energy storage properties of electrospun $V_2O_5$ were compared to approximately 10 at% $Ba^{2+}$ and $Ti^{4+}$ doped equivalents. $V_2O_5$, $V_{1.79}Ba_{0.21}O_5$ and

$V_{1.81}Ti_{0.19}O_5$ were produced *via* the electrospinning process followed by a single pyrolysis step and were investigated as positive electrodes for Li-ion coin cells (vs Li metal). $V_2O_5$ was doped to improve its electrochemical performance and to investigate the effects of intentionally introduced defects. X-ray diffraction analysis showed that each dopant had a critical effect on lattice distortions whilst showing no influence in the overall crystal structure, which was unusual for such large dopant amounts. Both dopant materials offered increased stabilisation of the $V_2O_5$ and rendered the $V_2O_5$ structure less susceptible to distortion caused by the intercalation/extraction of the Li-ions. This was observed in an improvement in cycle stabilities and Coulombic efficiencies. $Ti^{4+}$ was shown to be a suitable redox-inactive dopant providing increased structural stabilisation with cycling *via* phase change prevention. Ex-situ X-ray diffraction measurements showed detrimental phase changes within undoped $V_2O_5$ whereas the $Ba^{2+}$ and $Ti^{4+}$ doped $V_2O_5$ predominantly remained as α-$V_2O_5$ after the first cycle. The improved electrochemical performance of the $Ti^{4+}$ doped sample could be found in the suppressed irreversible phase transformation towards γ-$LiV_2O_5$ as shown by both the ex-situ PXRDs and CV cycling data. This shows that focussing on the improvement of material performance *via* use of dopants for structural stabilisation is a worthwhile path of investigation.

# Chapter 5 Electrochemical stabilisation of electrospun $V_2O_5$ using dopants with progressive oxidation states

## 5.1 INTRODUCTION

Dopants have been demonstrated to modify $V_2O_5$ properties, however determining the precise location of a dopant is often challenging. Incorporation between the layers is generally stated as the likely location as inferred from changes in interlayer spacing [97,228] Giorgetti *et al.* used X-ray Absorption Spectroscopy to investigate the position of dopants in $V_2O_5$ aerogels, finding that dopants can occupy the space between the $V_2O_5$ bilayers or sit close to a single layer [229]. It has been suggested that the dopants that sit between the bilayers block active sites for Li-ion interaction and hence do not contribute to a higher capacity. Conversely, dopants that sit closer to one of the single layers still allow movement of Li-ions while simultaneously offering improved structural stability and improved capacities. In $V_2O_5$ materials exhibiting conventional interlayer d-spacing, dopants will be able to occupy either interstitial sites, between the layers, or substitutional sites, replacing $V^{5+}$.

Determining the location of dopants is challenging experimentally, consequently atomistic simulations can provide key energetic insights. An empirically-fitted pair-potential computational technique has been used in this chapter to investigate the energetics for substitutional and interstitial $Na^+$, $Ba^{2+}$ and $Al^{3+}$ to determine their likely positions in the $V_2O_5$ lattice and help rationalize the experimental electronic conductivity and electrochemical behavior of the doped systems. The dopant loading was decreased to 2-3 at% to determine whether a lower dopant level would result in electronical conductivity variations rather than pure structural effects. The dopants were selected with the intent to systemically vary the oxidation state hence producing a range of ionic radii variations incorporated in the $V_2O_5$ whilst providing opportunity for electronic mis-match between dopant and host material.

This chapter explores in the role these dopants play on the vanadium oxide structure *via* an investigation of oxidation state effects on the electrical and ionic conductivities and the role of $V^{4+}$ on the electrochemical properties.

## 5.2 RESULTS AND DISCUSSION

### 5.2.1 Morphology and Structure

XPS and EDS analysis were used to confirm the amount of $Na^+$, $Ba^{2+}$ and $Al^{3+}$ doped into electrospun $V_2O_5$. The results from these techniques, which will be discussed in greater detail later in this section, indicate that the formulas for the doped materials are $V_{1.96}Na_{0.04}O_5$, $V_{1.94}Ba_{0.06}O_5$ and $V_{1.94}Al_{0.06}O_5$ respectively.

The PXRD patterns in Figure 5.1(a) show that α-$V_2O_5$ was formed *via* the electrospinning process with the space group P*mmn* (ICSD collection code 60767) and reflection labelling for orthorhombic $V_2O_5$ according to Shklover *et al.* [172]. There are multiple impurity peaks detected in the PXRD pattern for $V_{1.96}Na_{0.04}O_5$, highlighted with asterisks that are attributed to $NaV_6O_{15}$ [230]. Rietveld refinement indicated that the volume ratio of $V_2O_5$:$NaV_6O_{15}$ was 83:17. This was converted into a molar ratio according to Equation 26.

$$\frac{V_{ratio\_V2O5} \times \rho_{V2O5}}{MW_{V2O5}} : \frac{V_{ratio\_NaV6O15} \times \rho_{NaV6O15}}{MW_{NaV6O15}} \quad (26)$$

Where the density of $V_2O_5$ ($\rho_{V2O5}$) is 3.36 g cm$^3$, the molecular weight of $V_2O_5$ ($MW_{V2O5}$) is 181.83 g mol$^{-1}$, the density of $NaV_6O_{15}$ ($\rho_{NaV6O15}$) is 3.57 g cm$^3$, and the molecular weight of $NaV_6O_{15}$ ($MW_{NaV6O15}$) is 587.39 g mol$^{-1}$. It is reasonable to expect that the impurity will affect the electrochemical performance.

The PXRD patterns for $V_{1.94}Ba_{0.06}O_5$ and $V_{1.94}Al_{0.06}O_5$ showed no impurity peaks indicating that a stable solid solution was formed at this doping level [215]. Additionally, there was a variation in material colour where undoped $V_2O_5$ was yellow, $V_{1.96}Na_{0.04}O_5$ appeared dark

green/yellow, $V_{1.94}Ba_{0.06}O_5$ was orange and $V_{1.94}Al_{0.06}O_5$ was a bright yellow according to Figure 5.1(a) inset. Figure 5.1(b,c) shows that there is little peak shifting and broadening between the XRD data of the different samples

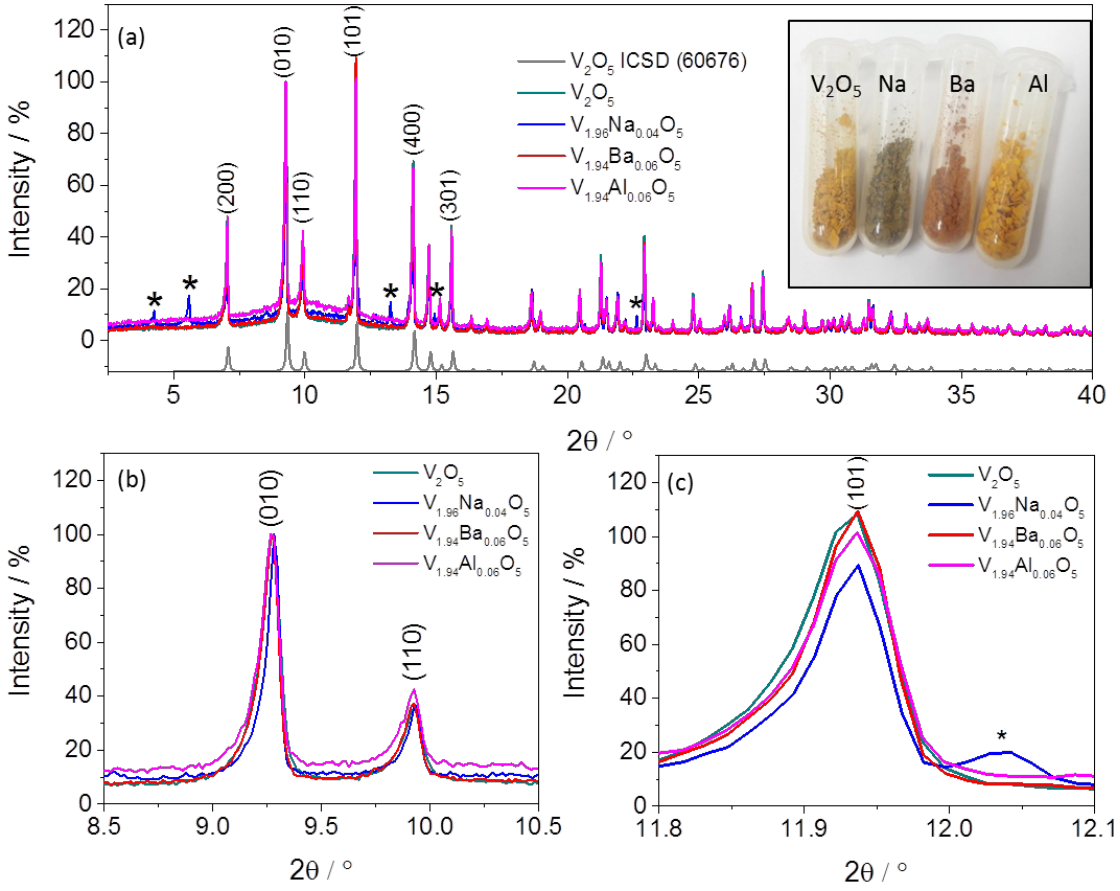


**Figure 5.1: (a) PXRD patterns for $V_2O_5$, $V_{1.96}Na_{0.04}O_5$, $V_{0.94}Ba_{0.06}O_5$, and $V_{1.94}Al_{0.06}O_5$ with impurity peaks highlighted with asterisks for $NaV_6O_{15}$ and (inset) a photo showing the colour of the calcined powder was affected by dopant type. Enlarged region of (b) 8.5° < 2θ < 10.5° and (c) 11.8° < 2θ < 12.1° emphasising intensity variation and the lack of peak shift.**

Table 5.1(a) summarises the Rietveld refined unit cell parameters and resultant unit cell volumes for each material. The unit cell volumes between samples are not particularly varied which was likely to due to the low doping level. The unit cell volume for $V_{1.96}Na_{0.04}O_5$ is the smallest which may be related to the impurity producing a breakdown or altering of the $V_2O_5$ unit cell. Conversely, $V_{1.94}Ba_{0.06}O_5$ had the largest unit cell volume, which was likely due to

both the size and location of the $Ba^{2+}$ atom as it is significantly larger than that of any of the other dopants [with an ionic radius of 1.35 Å for a coordination number (CN) of 6 compared to 1.00 Å for CN = 5 for $Na^+$, 0.48 Å for CN = 5 for $Al^{3+}$ and 0.46 Å for CN = 5 for $V^{5+}$]. This will be discussed in greater detail in Section 5.2.3. Additionally, the *c* parameter was the largest out of the investigated materials implying that large $Ba^{2+}$ dopant distorted the $V_2O_5$ unit cell. This trend with $V_{1.94}Ba_{0.06}O_5$ possessing the large unit cell volume was also observed in Section 4.2.1 for $V_{1.79}Ba_{0.21}O_5$ which showed a significantly larger volume of 183.63 $Å^3$, which is reasonable given the approximate loading of 10 at% compared to 3 at% in this Chapter. Cheah *et al.* observed an increase in the *a* and *c* parameters of $Al^{3+}$ incorporated into $V_2O_5$ [134], whereas $V_{1.94}Al_{0.06}O_5$ in this chapter displayed increased *c*- and reduced *a*- parameters suggesting a different $Al^{3+}$ dopant location in this sample.

**Table 5.1: Characterisation summary: (a) Rietveld refinements of lattice parameters with resultant unit cell volumes, (b) crystallite size determined *via* the Scherrer equation, (c) the vanadium oxidation state ratios $V^{4+}$:$V^{5+}$ identified *via* XPS measurements, (d) specific surface area determined *via* BET surface area measurements.**

| | a | | | | | | b | c | d |
|---|---|---|---|---|---|---|---|---|---|
| Sample | *a* (Å) | *b* (Å) | *c* (Å) | V ($Å^3$) | $R_{wp}$ (%) | $\chi^2$ | Crystallite size (nm) | $V^{4+}$:$V^{5+}$ ratio | Surface area ($m^2$ $g^{-1}$) |
| $V_2O_5$ | 11.5210(3) | 3.56773(9) | 4.37694(12) | 179.909(14) | 9.59 | 1.48 | 36.1 | 0.08:0.92 | 8.70 |
| $V_{1.96}Na_{0.04}O_5$ | 11.5223(2) | 3.56754(7) | 4.37513(9) | 178.846(10) | 7.53 | 1.05 | 47.9 | 0.11:0.89 | 11.80 |
| $V_{1.94}Ba_{0.06}O_5$ | 11.5205(3) | 3.56719(8) | 4.37950(11) | 179.979(13) | 8.81 | 1.32 | 42.1 | 0.09:0.91 | 14.30 |
| $V_{1.94}Al_{0.06}O_5$ | 11.5197(3) | 3.56687(1) | 4.37905(14) | 179.932(16) | 8.45 | 1.17 | 36.5 | 0.02:0.98 | 22.18 |

The Scherrer equation was used to calculate apparent crystallite size from the average of the (200), (010), (101) and (400) peaks with estimates of 36.1 nm for undoped $V_2O_5$, 47.9 nm for $V_{1.96}Na_{0.04}O_5$, 42.1 nm for $V_{1.94}Ba_{0.06}O_5$ and 36.5 nm for $V_{1.94}Al_{0.06}O_5$ as summarised in Table 5.1(b). The crystal sizes are likely to be influenced by the dopant ion affecting crystal growth.

The oxidation states of the dopants were assigned in Figure 5.2 using the Na 1s [230], Ba $3d_{5/2}$ [231] and Al 2p peaks [232], whilst the ratio of the oxidation states for the vanadium was assigned using the V $2p_{3/2}$ peak. Analysis of the vanadium XPS data in Figure 5.2 showed a $V^{4+}$:$V^{5+}$ ratio of 0.08:0.92 for $V_2O_5$, 0.11:0.89 for $V_{1.96}Na_{0.04}O_5$, 0.09:0.91 for $V_{1.94}Ba_{0.06}O_5$ and 0.02:0.98 for $V_{1.94}Al_{0.06}O_5$, also seen in Table 5.1(c). The presence of $V^{4+}$ in the $V_2O_5$ indicates an intrinsic n-type semiconducting nature, where an equilibrium is created between oxygen vacancies and reduced vanadium ions. The incorporation of the dopants had a clear effect on the ratio of $V^{4+}$:$V^{5+}$, and may also have modified the oxygen vacancy concentrations, which will be discussed in greater detail later. The reduction of $V^{5+}$ ($d^0$) to $V^{4+}$ ($d^1$) has been linked to improved electronic conductivity, as the $d^1$ electrons can 'hop' between vanadium atoms [233]. The increased $V^{4+}$ proportion in $V_{1.96}Na_{0.04}O_5$, $V_{1.94}Ba_{0.06}O_5$ may therefore be expected to contribute to improved electronic conductivity, whilst the lower $V^{4+}$ content in $V_{1.94}Al_{0.06}O_5$ was expected to reduce electronic conductivity and may degrade electrochemical performance. The $Na^+$:V atomic ratio according to the XPS analysis for $V_{1.96}Na_{0.04}O_5$ was 2:98 which agreed reasonably well with 3:97 suggested by EDS. For $V_{1.94}Ba_{0.06}O_5$ the $Ba^{2+}$:V ratio was 3:97 (EDS indicated 2:98) and $V_{1.94}Al_{0.06}O_5$ the $Al^{3+}$:V ratio was 2.5:97.5 (EDS indicated 3:97).

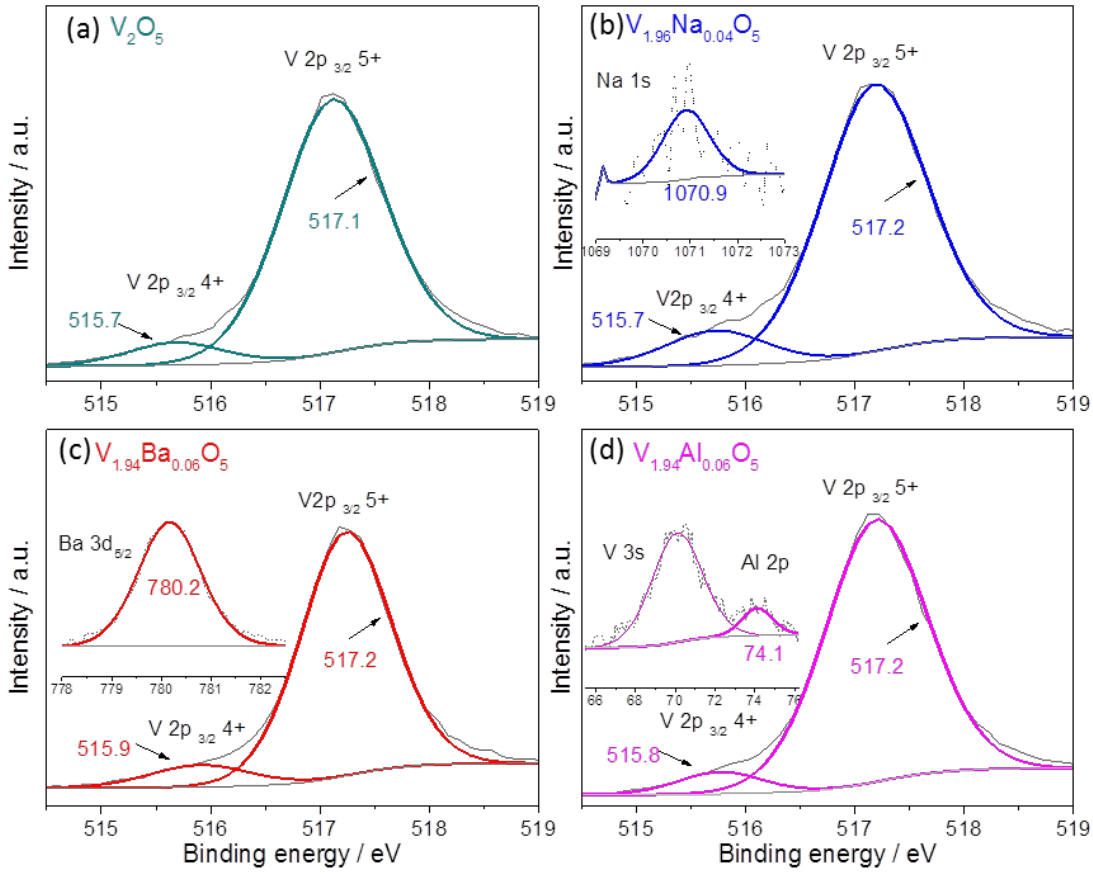


**Figure 5.2: XPS elemental scans of the (a) V $2p_{3/2}$ peak for undoped $V_2O_5$, (b) V $2p_{3/2}$ peak and the Na 1s peak (inset) for $V_{1.96}Na_{0.04}O_5$, (c) V $2p_{3/2}$ peak and the Ba $3d_{5/2}$ peak (inset) for $V_{1.94}Ba_{0.06}O_5$ and (d) the V $2p_{3/2}$ peak and the Al 2p peak (inset) for $V_{1.94}Al_{0.06}O_5$.**

The SEM images in Figure 5.3 revealed that the electrospun fibres in this study were of consistent diameters and were made up of nanostructured particles which formed hierarchical structures. The diameters of the undoped $V_2O_5$ [Figure 5.3(a)], $V_{1.96}Na_{0.04}O_5$ [Figure 5.3(b)], $V_{1.94}Ba_{0.06}O_5$ [Figure 5.3(c)] and $V_{1.94}Al_{0.06}O_5$ [Figure 5.3(d)] were approximately 0.63 – 0.72 µm, 0.88 – 1.25 µm, 1.11 – 1.40 µm, and 1.44 – 1.68 µm, respectively. $V_{1.94}Al_{0.06}O_5$ appeared to have clusters stuck on the side on the fibres in Figure 5.3(d) which could be indicative of an inconsistent electrospinning operation produced by a small imbalance within the starting solution in the ratio between polymer to solvent.

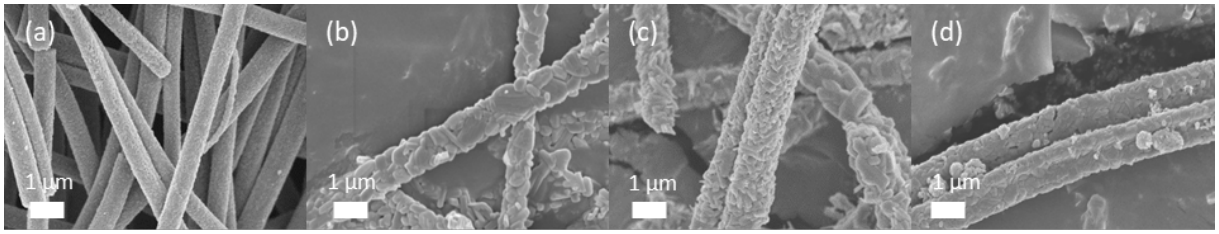


**Figure 5.3: SEM images of (a) $V_2O_5$, (b) $V_{1.96}Na_{0.04}O_5$, (c) $V_{1.94}Ba_{0.06}O_5$, and (d) $V_{1.94}Al_{0.06}O_5$ showing the nanostructured microfibers produced *via* electrospinning.**

TEM images in Figure 5.4 showed that the electrospun fibres were made up of nanoscale particles that were of high crystallinity as evidenced by detectable lattice spacings. Figure 5.4(a-c) and Figure 5.4(d-f) showed similar morphologies for $V_2O_5$ and $V_{1.96}Na_{0.04}O_5$, respectively. These particles were elongated with lengths *ca.* 400 nm for $V_2O_5$ and up to several hundred nanometres for $V_{1.96}Na_{0.04}O_5$ suggesting directional growth during particle formation. They possessed well-defined lattice spacings of approximately 0.34 nm corresponding to (101) for $V_2O_5$ [Figure 5.4(c)] and 0.44 nm for (010) in $V_{1.96}Na_{0.04}O_5$ [Figure 5.4(f)]. The $V_{1.96}Na_{0.04}O_5$ material had particularly well-defined lattice spacings. The addition of $Al^{3+}$ or $Ba^{2+}$ resulted in differing morphologies with rounder particles possessing diameters of *ca.* 400 nm for $V_{1.94}Ba_{0.06}O_5$ and *ca.* 120 nm for $V_{1.94}Al_{0.06}O_5$ Additionally, the materials had less defined lattice spacings of approximately 0.34 nm for (101) in $V_{1.94}Ba_{0.06}O_5$ and in $V_{1.94}Al_{0.06}O_5$. The interplanar spacings were well matched to the relevant XRD reflections. The decrease in lattice space definition suggested that there was a distortion of the $V_2O_5$ layers with the $Al^{3+}$ and $Ba^{2+}$ dopants. Furthermore, the differing lattice spacings observed in the TEM images suggested that these particles were not single-crystalline. A similar observation was previously made in Section 4.2.1.

BET surface area measurements, according to Table 5.1(d), showed that for undoped $V_2O_5$, $V_{1.96}Na_{0.04}O_5$, $V_{1.94}Ba_{0.06}O_5$ and $V_{1.94}Al_{0.06}O_5$ the resultant surface areas were 8.70, 11.80, 14.30 and 22.18 $m^2\ g^{-1}$, respectively, indicating that the presence of a dopant influenced not only the structural characteristics as seen in the XRD refinements but also the surface area. The

doped materials seem to favour particle nucleation rather than Ostwald ripening and growth which resulted in higher surfaces areas. As previously suggested by Huang *et. al.*, crystallinity increases with a decrease in surface area [127], which was especially valid for $V_{1.94}Al_{0.06}O_5$ possessing the smallest particles of the investigated materials herein.

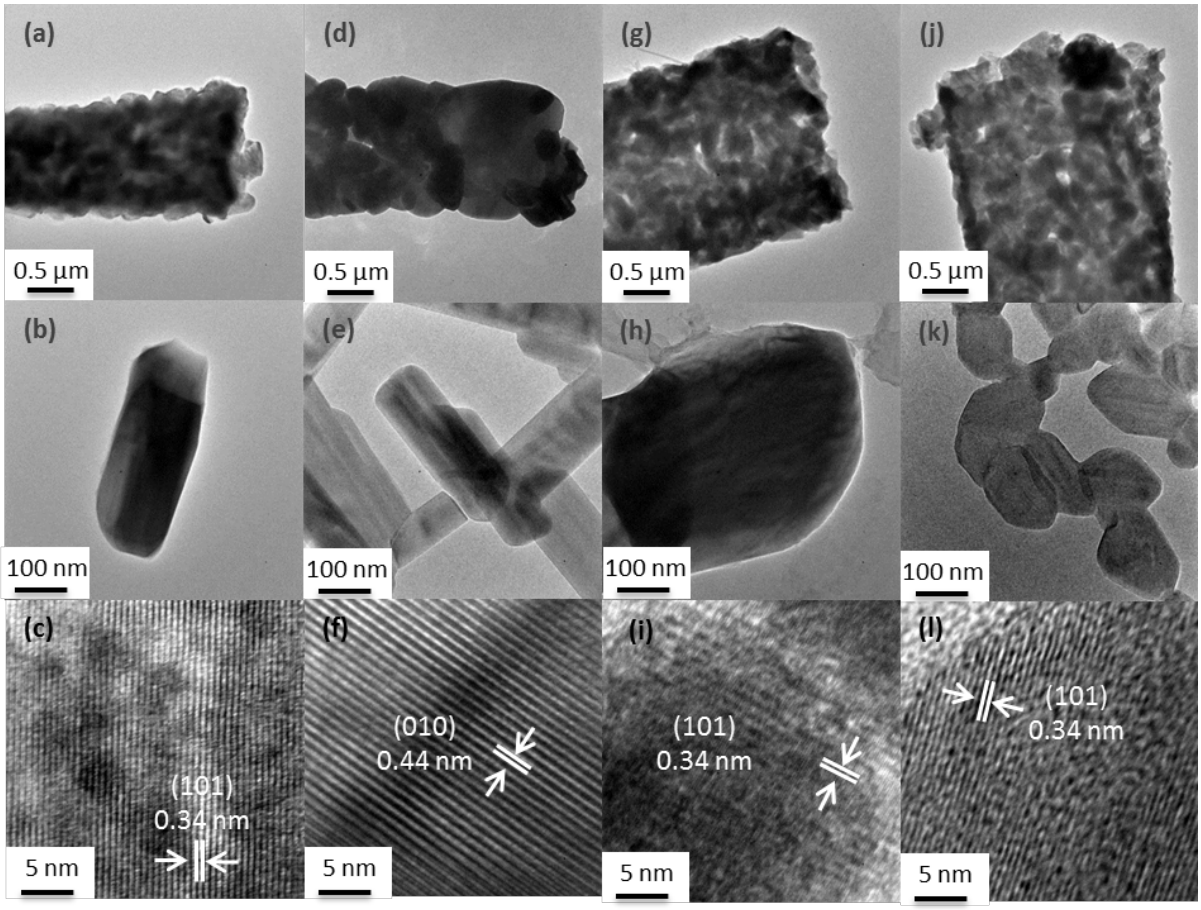


**Figure 5.4: TEM images showing the microfiber in the first row, single particles in the second and lattice spacings *via* HRTEM in the third for (a-c) undoped $V_2O_5$, (d-f) $V_{1.96}Na_{0.04}O_5$, (g-i) $V_{1.94}Ba_{0.06}O_5$ and (j-l) $V_{1.94}Al_{0.06}O_5$, respectively.**

### 5.2.2 Electrochemical Performance

The CV results presented in Figure 5.5 clearly showed defined redox peaks indicating intercalation which corresponded to two Li-ions for each material as explained in Section 1.7.3. In brief, one Li-ion intercalation occurred at *ca.* 3.0 – 3.5 V vs $Li/Li^+$ which corresponded to

the formation of δ-$LiV_2O_5$ from the unintercalated phase α-$V_2O_5$ *via* the intermediate ε-$Li_{0.5}V_2O_5$. The second Li-ion intercalation occurred at 2.1 – 2.5 V vs $Li/Li^+$ which corresponded to the irreversible formation of γ-$Li_2V_2O_5$ [76,79].

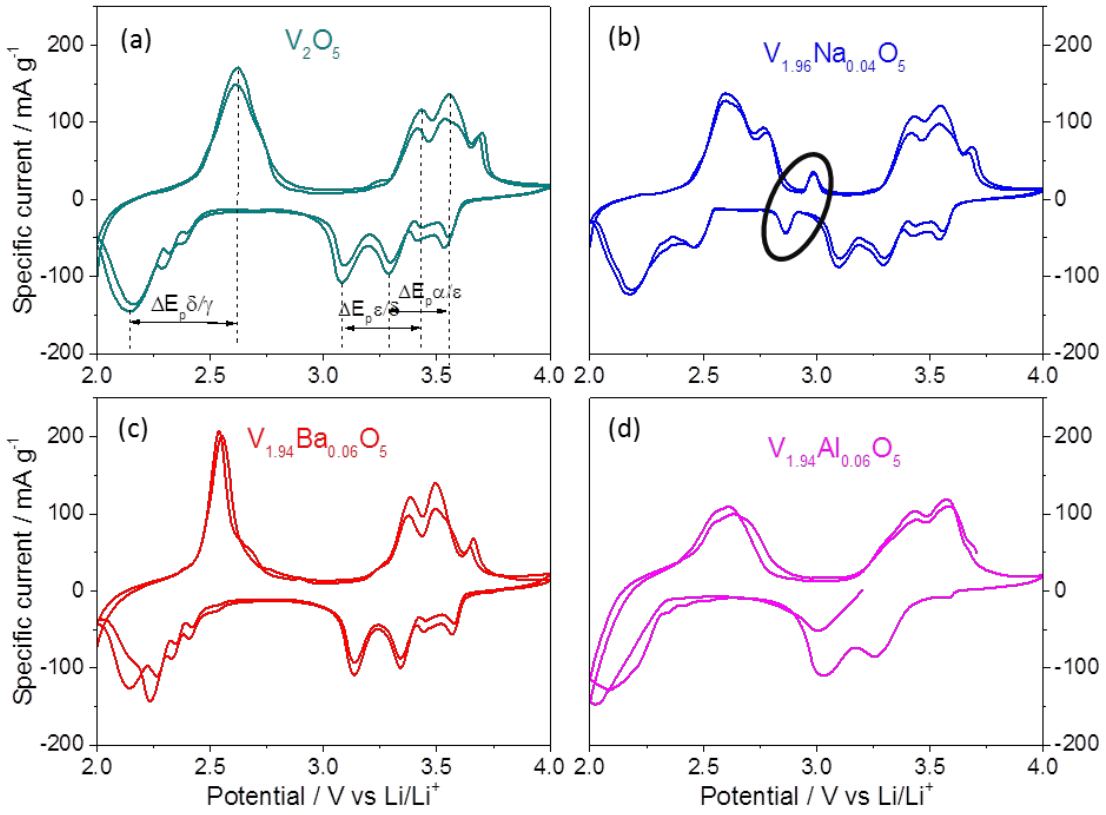


**Figure 5.5: Cyclic voltammograms at 0.1 mV $s^{-1}$ over 2 cycles for (a) $V_2O_5$ with $\Delta E_P$ labelled for the α/ε, ε/δ, and δ/γ transitions, (b) $V_{1.96}Na_{0.04}O_5$ with a circle around the extra redox pair, (c) $V_{1.94}Ba_{0.06}O_5$ and (d) $V_{1.94}Al_{0.06}O_5$.**

The first phase change at *ca.* 3.0 – 3.5 V vs $Li/Li^+$ (α/ε and ε/δ) appeared to be of similar shape for all tested materials implying that the structural variations that occurred during this phase change were similar. Redox peak separations ($\Delta E_p$) for the α/ε, ε/δ, and δ/γ transitions were calculated for each sample. The smallest peak separations were 0.15, 0.24 and 0.24 V vs $Li/Li^+$ for $V_{1.94}Ba_{0.06}O_5$ while the largest at 0.31, 0.40, and 0.53 V vs $Li/Li^+$ corresponded to $V_{1.94}Al_{0.06}O_5$ for the α/ε, ε/δ, and δ/γ transitions, respectively. Additionally, $V_{1.94}Ba_{0.06}O_5$

possessed quite sharp peaks, especially the delithiation peak at 2.6 V vs $Li/Li^+$ indicating improved ionic diffusion. Peak separations for undoped $V_2O_5$ and $V_{1.96}Na_{0.04}O_5$ were similar at 0.24, 0.33 and 0.46 V vs $Li/Li^+$ and 0.24, 0.32 and 0.41 V vs $Li/Li^+$, respectively, for the α/ε, ε/δ, and δ/ɣ transitions. This shows that polarisation decreased and reversibility increased for the $V_{1.94}Ba_{0.06}O_5$ and $V_{1.96}Na_{0.04}O_5$ [3]. The opposite effect is seen for the $Al^{3+}$ dopant, which might be due to the low $V^{4+}$ content limiting Li-ion mobility and electronic conductivity. Additionally, the small shoulder peaks at *ca.* 3.5 – 3.7 V vs $Li/Li^+$ for $V_2O_5$ and $V_{1.94}Ba_{0.06}O_5$ indicated the availability of multiple Li-ion active sites for multi-stepped lithiation/delithiation processes [180].

The extra redox peaks in Figure 5.5(b) within the circle for $V_{1.96}Na_{0.04}O_5$ at 2.85 V vs $Li/Li^+$ (lithiation) and 2.98 V vs $Li/Li^+$ (delithiation) has been previously attributed to the presence of electrochemically active vanadium oxides with significant amounts of lower oxidation state $V^{4+}$ [51,92]. This observation does not seem to be relevant here given that a comparable $V^{4+}$ content was determined for $V_2O_5$, $V_{1.96}Na_{0.04}O_5$ and $V_{1.94}Ba_{0.06}O_5$ at 1.6%, 2.2% and 1.8%, respectively. These peaks were also present in the CV of Na-preinserted $V_2O_5$ by Li *et al.* though it was not explained in any detail as to why they were present [147]. As there was a significant proportion of $NaV_6O_{15}$ impurity present in $V_{1.96}Na_{0.04}O_5$ it was more likely that these extra redox peaks were the result of Li-ion interaction with this phase rather than the $V^{4+}$ content. This will be discussed in more detail later. There were also strong shoulder peaks associated with the δ/γ transition for $V_{1.96}Na_{0.04}O_5$ at 2.45 V vs $Li/Li^+$ (lithiation) and 2.78 V vs $Li/Li^+$ (delithiation). Liu *et al.* attributed lithiation peaks in a similar region in their CV to a multistep Li-ion insertion process with $NaV_6O_{15}$ [147].

Capacity versus potential profiles for the materials cycled at 50 mA $g^{-1}$ are shown in Figure 5.6(a,b) for the 1st and 5th cycles, respectively. The potential steps at *ca.* 2.2 V vs $Li/Li^+$ and above 3.1 V vs $Li/Li^+$ predictably corresponded to the phase transitions of ε-$Li_{0.5}V_2O_5$, δ-$LiV_2O_5$, and ɣ-$Li_2V_2O_5$ which match well with the redox peaks in the Figure 5.5. The reduced

presence of the first potential step for $V_2O_5$, $V_{1.96}Na_{0.04}O_5$ and $V_{1.94}Ba_{0.06}O_5$ is likely due to the higher $V^{4+}$ content facilitating the α/ε phase change.

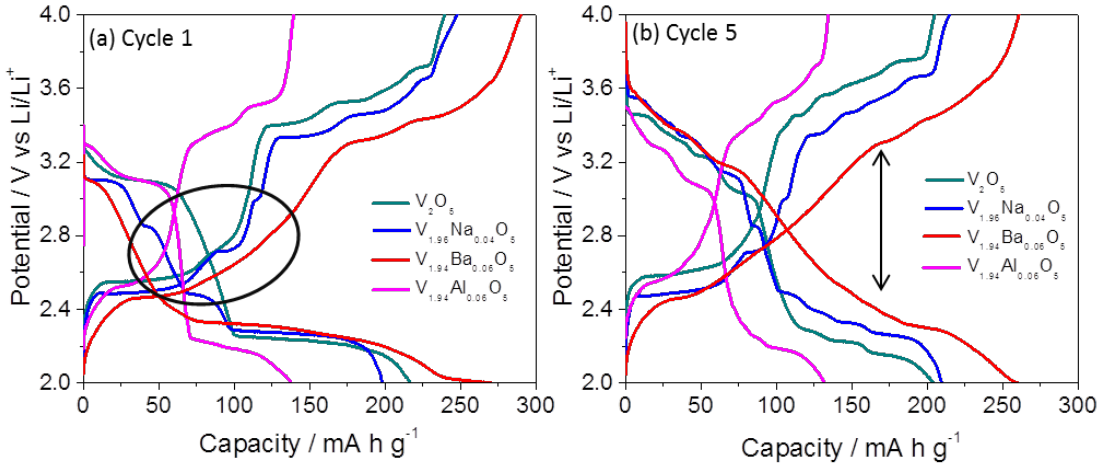


**Figure 5.6: Capacity versus potential profiles of $V_2O_5$, $V_{1.96}Na_{0.04}O_5$, $V_{1.94}Ba_{0.06}O_5$ and $V_{1.94}Al_{0.06}O_5$ at 50 mA $g^{-1}$ for (a) cycle 1 with a circle around the extra potential steps in $V_{1.96}Na_{0.04}O_5$ and (b) cycle 5 from the C-rate test with a black arrow emphasising the decrease in overpotential for $V_{1.96}Na_{0.04}O_5$ and $V_{1.94}Ba_{0.06}O_5$.**

The extra redox peaks for $V_{1.96}Na_{0.04}O_5$ observed in the CV in Figure 5.5(b) are clearly observed in Figure 5.6(a) within the circle as potential steps located at 2.85 V vs $Li/Li^+$ (lithiation) and 3.0 V vs $Li/Li^+$ (delithiation). The potential steps at 2.48 V vs $Li/Li^+$ (lithiation) and 2.72 V vs $Li/Li^+$ (delithiation), also within the circle, match the strong shoulder redox peaks from Figure 5.5. These extra potential steps have been previously observed in lithiation capacity vs potential profiles for $NaV_6O_{15}$ nanorods [147]. They were attributed to the formation of $LiNaV_6O_{15}$ in the range of 2.85 – 3.5 V vs $Li/Li^+$ and $Li_2NaV_6O_{15}$ within 2.5 – 2.8 V vs $Li/Li^+$. Similarly placed redox peaks and potential steps were also attributed to the extraction of $Na^+$ from the host material in $NaV_6O_{15}$ by Hu *et al.* allowing more Li-ions to be inserted thus maintaining high capacities [234]. These extra redox peaks and potential steps were also observed by Zhu *et al.* [92] and Mai *et al.* [51] which were attributed to other active vanadium

oxides of lower valences. Both studies cited a review on layered vanadium oxides by Chernova *et al.* [235]. $V_{1.94}Ba_{0.06}O_5$ possessed a similar $V^{4+}$ content (9%) as $V_{1.96}Na_{0.04}O_5$ (11%) and $V_2O_5$ (8%) though no potential steps at *ca.* 2.9 V vs $Li/Li^+$ and 2.5 V vs $Li/Li^+$ are observed. This leads to the conclusion that the $V^{4+}$ content is not responsible for these extra redox peaks [Figure 5.5(b)] and potential steps [Figure 5.6(b)] as it is more likely that the $NaV_6O_{15}$ impurity is the reason.

The ICL from cycle 1 in Figure 5.6(a) are representative of delithiation storage across a Li-ion layer build up. According to Table 5.2(a), ICLs for $V_2O_5$, $V_{1.96}Na_{0.04}O_5$, $V_{1.94}Ba_{0.06}O_5$ and $V_{1.94}Al_{0.06}O_5$ were 23.2, 49.6, 19.4 and 1.4 mA h $g^{-1}$, respectively. This implied that there was a large build-up of excess Li-ions on the working electrode for $V_{1.96}Na_{0.04}O_5$ and less so for $V_2O_5$, $V_{1.94}Ba_{0.06}O_5$ and $V_{1.94}Al_{0.06}O_5$. The high ICL for the samples highlights common issues with the use of nanostructured materials for battery applications, as discussed in Section 1.5.4, such as side reactions between the less-coordinated surface atoms and the electrolyte. Additionally, $V_2O_5$ is a good catalyst which promotes unpredictable surface reactions with potential cation dissolution. The potential steps for $V_{1.94}Ba_{0.06}O_5$ appeared to be smoother and less defined than the others especially in Figure 5.6(b) suggesting that the $Ba^{2+}$ dopant caused a dispersion of the strain caused by the lithiation/delithiation process [225].

The results of a C-rate test at 50 mA $g^{-1}$, 100 mA $g^{-1}$, 300 mA $g^{-1}$, and 600 mA $g^{-1}$ over 10 cycles at each current density immediately followed by cycling test at 50 mA $g^{-1}$ for a further 60 cycles is presented in Figure 5.7(a). Cycle stability was improved for the doped materials which is clear in the first 10 cycles at 50 mA $g^{-1}$ (Figure 5.7(a)) with capacities and stabilities of 226 mA h $g^{-1}$ (n = 2) and 81% for $V_2O_5$, 230 mA h $g^{-1}$ (n = 2) and 85% for $V_{1.96}Na_{0.04}O_5$, 268 mA h $g^{-1}$ (n = 2) and 90% for $V_{1.94}Ba_{0.06}O_5$, and 138 mA h $g^{-1}$ (n = 2) and 94% for $V_{1.94}Al_{0.06}O_5$. The increased cycle stability at higher currents was visibly observable in the C-rate test and was due to decreased side reactions within the cells [236]. Capacity retention with

varying current density, summarised in Table 5.2(b), was improved for the doped samples compared to the undoped, especially for $V_{1.94}Ba_{0.06}O_5$. Both $V_2O_5$ and $V_{1.94}Al_{0.06}O_5$ had negligible capacities at 600 mA $g^{-1}$ while rate retention noticeably improved for $V_{1.96}Na_{0.04}O_5$ and $V_{1.94}Ba_{0.06}O_5$. Despite the poor performance at 600 mA $g^{-1}$, all materials recovered well when cycling returned to 50 mA $g^{-1}$. The Coulombic efficiencies for the C-rate test in Figure 5.7(b) were much more consistent for $V_{1.96}Na_{0.04}O_5$ and $V_{1.94}Ba_{0.06}O_5$ with respect to current density changes compared to $V_2O_5$ and $V_{1.94}Al_{0.06}O_5$, especially at 300 mA $g^{-1}$. Coulombic efficiencies were particularly erratic for undoped $V_2O_5$ and $V_{1.94}Al_{0.06}O_5$ at 600 mA $g^{-1}$ due to the extremely small capacities obtained at this current density so they have not been included. The capacity, capacity retention and Coulombic efficiencies for the 60 cycles at 50 mA $g^{-1}$ after the C-rate test is summarised in Table 5.2(c). The efficiencies of $V_{1.96}Na_{0.04}O_5$ and $V_{1.94}Ba_{0.06}O_5$ were lower than that of undoped $V_2O_5$ and $V_{0.94}Al_{0.06}O_5$ which contrasts the rate capability performance.

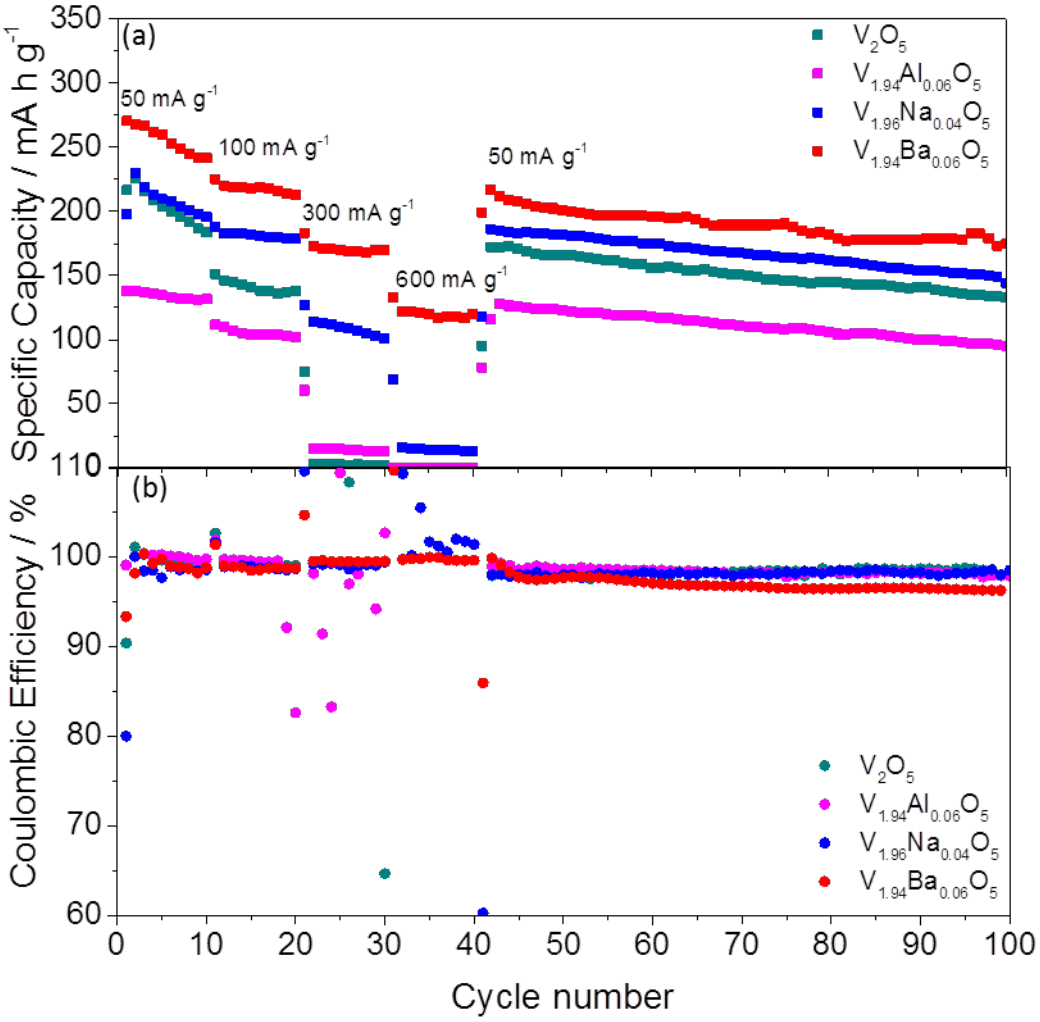


**Figure 5.7: (a) C-rate test at the following current densities: 50 mA $g^{-1}$, 100 mA $g^{-1}$, 300 mA $g^{-1}$, and 600 mA $g^{-1}$ mA $g^{-1}$ for 10 cycles each followed by cycling at 50 mA $g^{-1}$ over 50 cycles after the C-rate test, (b) associated Coulombic efficiencies from the C-rate test for $V_2O_5$, $V_{1.96}Na_{0.04}O_5$, $V_{1.94}Ba_{0.06}O_5$ and $V_{1.94}Al_{0.06}O_5$.**

When considering the effect of surface area on rate capability, undoped $V_2O_5$ possessed both the lowest surface area (8.7 $m^2$ $g^{-1}$) and lowest rate capabilities. Interestingly, $V_{1.94}Al_{0.06}O_5$, despite having the largest surface area (22.18 $m^2$ $g^{-1}$) of the materials examined in this study, did not result in substantial rate capability improvement. This suggests that the surface area is not the most significant factor in rate capability improvement for these materials and that some other aspects, such as dopant location or conductivity variations are more responsible [127,187,237].

**Table 5.2: Cycling data (a) for irreversible capacity loss at n = 1, (b) capacities at n = 5, 15, 25, 35 at each current density in mAh $g^{-1}$, (c) cycling stability after C-rate at 50 mA $g^{-1}$ (42 < n < 100) for for $V_2O_5$, $V_{1.96}Na_{0.04}O_5$, $V_{1.94}Ba_{0.06}O_5$ and $V_{1.94}Al_{0.06}O_5$.**

| | a | b | | | | c | | |
|---|---|---|---|---|---|---|---|---|
| Sample | ICL (mA h $g^{-1}$) | n = 5 at 50 mA $g^{-1}$ | n = 15 at 100 mA $g^{-1}$ | n = 25 at 300 mA $g^{-1}$ | n = 35 at 600 mA $g^{-1}$ | n = 42 (mA h $g^{-1}$) | Capacity retention (%) | Coulombic efficiencies (%) |
| $V_2O_5$ | 23.2 | 204 | 141 | 3 | N/A | 166 | 80 | 98 |
| $V_{1.96}Na_{0.04}O_5$ | 49.6 | 210 | 182 | 110 | 14 | 182 | 82 | 97 |
| $V_{1.94}Ba_{0.06}O_5$ | 19.4 | 260 | 218 | 170 | 120 | 216 | 83 | 98 |
| $V_{1.94}Al_{0.06}O_5$ | 1.4 | 135 | 104 | 15 | N/A | 124 | 74 | 97 |

$V_{1.94}Al_{0.06}O_5$ capacities were particularly low which is unexpected as other studies have reported superior performance of $Al^{3+}$ doped materials [134,228]. The results in this chapter suggest that the low $V^{4+}$ content and amount of oxygen vacancies for $V_{1.94}Al_{0.06}O_5$ (as estimated by XPS) played a significant role in decreasing the electronic conductivity and Li-ion transport and thus limiting the electrochemical performance.

Impedance measurements were undertaken to compare the relative conductivities of the electrospun materials with resultant Nyquist plots in Figure 5.8(a). All Nyquist plots are composed of a distorted depressed semicircle in the high-to-moderate frequency range with a small upturning in the low frequency range.

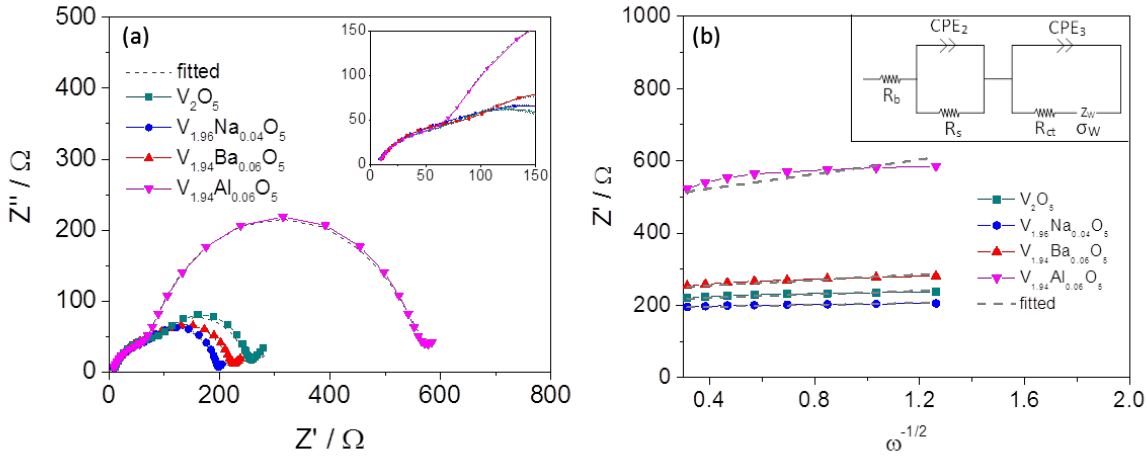


**Figure 5.8: (a) Nyquist plots of pristine cells for $V_2O_5$, $V_{1.96}Na_{0.04}O_5$, $V_{1.94}Ba_{0.06}O_5$ and $V_{1.94}Al_{0.06}O_5$ with an enlargement of the high frequency region (inset) and (b) linear curves of $\omega^{-1/2}$ vs Z' in the low frequency region with the electrical equivalent circuit (inset).**

The electrical equivalent circuit in Figure 5.8(b) (inset) used to represent the Faradaic impedances, consisted of three resistances, two constant phase elements (CPE) and a Warburg impedance component ($\sigma_W$). The relevant descriptions of the circuit components are in Section 2.3.4 and the resistance values of are summarised in Table 5.3.

**Table 5.3: Curve fitted resistance values, $\chi^2$ goodness of fit and the Warburg impedance coefficient ($\sigma_w$) for $V_2O_5$, $V_{1.96}Na_{0.04}O_5$, $V_{1.94}Ba_{0.06}O_5$ and $V_{1.94}Al_{0.06}O_5$**

| Sample | $R_b$ - electrolyte (Ω) | $R_s$ – surface layer (Ω) | $R_{ct}$ – charge transfer (Ω) | $\chi^2$ | $\sigma_w$ (Ω cm$^2$ s$^{-1/2}$) |
|---|---|---|---|---|---|
| $V_2O_5$ | 7.58 | 138.60 | 99.89 | 0.0125 | 38.44 |
| $V_{1.96}Na_{0.04}O_5$ | 6.32 | 71.40 | 116.10 | 0.0039 | 13.81 |
| $V_{1.94}Ba_{0.06}O_5$ | 4.90 | 112.30 | 102.70 | 0.0190 | 23.82 |
| $V_{1.94}Al_{0.06}O_5$ | 7.69 | 262.20 | 73.54 | 0.0326 | 100.16 |

Figure 5.8(b) details the linear relationship between Z' and the inverse squared angular frequency ($\omega^{-1/2}$) in the low frequency region. The slope of this curve is the Warburg impedance coefficient ($\sigma_W$), summarised in Table 5.3, which can be used to determine the Li-ion diffusion coefficient ($D_{Li}$). An indication of Li-ion diffusion can be inferred from the inverse proportional

relationship of $D_{Li}$ and $\sigma_W$ [186]. Therefore, it can be reasoned that the Li-ion diffusion was improved for $V_{1.96}Na_{0.04}O_5$ and $V_{1.94}Ba_{0.06}O_5$ while the opposite was seen for $V_{1.94}Al_{0.06}O_5$. $R_b$ was reasonably consistent for the samples while the smaller $R_s$ values for $V_{1.96}Na_{0.04}O_5$ and $V_{1.94}Ba_{0.06}O_5$ supported the cyclic voltammetry results [Figure 5.5] showing that there was improved current flow through these electrode surfaces resulting in more effective Li-ion diffusion [168]. The opposite was seen for $R_{ct}$ with $V_{1.96}Na_{0.04}O_5$ and $V_{1.94}Ba_{0.06}O_5$ possessing the largest resistances (116.10 Ω and 102.70 Ω, respectively) and $V_{1.94}Al_{0.06}O_5$ showing the lowest with 73.54 Ω. It has been shown that a decrease in $R_{ct}$ represents higher intrinsic conductivity resulting in improved electrochemical performance [186,187,238]. Additionally, increased oxygen vacancies result in decreased charge transfer resistances [147,187]. The opposite effect was seen in this study with $V_{1.96}Na_{0.04}O_5$ and $V_{1.94}Ba_{0.06}O_5$ possessing higher proportions of $V^{4+}$ and oxygen vacancies and superior electrochemical performances despite the higher $R_{ct}$ values. The impedance results in Table 5.3 suggests that $R_s$ and $R_{ct}$ be examined together rather than separately as the Nyquist plots indicate that there were two overlapping time constants which was seen in the distorted semicircle [199,200]. Despite the low $R_{ct}$ for $V_{1.94}Al_{0.06}O_5$, $R_s$ is significantly higher implying hindered Li-ion movement through the surface layer. Additionally, $\sigma_W$ is drastically higher for $V_{1.94}Al_{0.06}O_5$ indicating that despite a low $R_{ct}$, overall conductivity is not improved for this material which has been shown throughout the presented analysis. This suggested that the $Al^{3+}$ dopant was blocking Li-ion movement and lowering kinetics [147,186]. Conversely, $V_{1.96}Na_{0.04}O_5$ and $V_{1.94}Ba_{0.06}O_5$ $R_s$ values implied that these dopants are facilitating the movement of Li-ion through the surface layer of the electrodes.

### 5.2.3 Potential Pair Calculations

The calculated $V_2O_5$ lattice parameters and interatomic distances are reported in Table 5.4(a) and Table 5.4(b), respectively, and are in good agreement when compared to the $V_2O_5$ XRD reference pattern (ICSD code 60676).

**Table 5.4: (a) Comparison of $V_2O_5$ XRD ICSD reference pattern (code 60676) and (b) GULP calculated lattice parameters of bulk $V_2O_5$.**

| a | | | b | | |
|---|---|---|---|---|---|
| Unit cell parameter | ICSD | GULP calculated | Interatomic distance | ICSD | GULP calculated |
| a (Å) | 3.564 | 3.565 (+0.0 %) | V-O1 (vanadyl) (Å) | 1.576 | 1.575 (-0.1%) |
| b (Å) | 11.512 | 11.374 (-1.1 %) | V-O2 (Å) | 1.778 | 1.843 (+3.7%) |
| c (Å) | 4.368 | 4.366 (+0.0 %) | V-O3 (Å) | 1.878 | 1.936 (+3.0%) |
| Vol ($Å^3$) | 179.213 | 177.034 (-1.2 %) | V-O3' (Å) | 2.017 | 1.975 (-2.1%) |
| | | | V-O1 (interlayer) (Å) | 2.793 | 2.790 (-0.1%) |

To rationalise the conductivity and electrochemical changes produced by the different dopants, their locations in the $V_2O_5$ structure were investigated using atomistic simulations. Dopants can be incorporated either substitutionally or interstitially into $V_2O_5$, with different delithiation compensating effects as a result. Substitutional replacement of $V^{5+}$ by the relevant cations can be compensated by the formation of oxygen vacancies, which in Kroger-Vink notation is expressed according to Equation 27, Equation 28 and Equation 29.

$$\frac{1}{2}Al_2O_3 + VO_{VO}^{X} \leftrightarrows Al_{VO}^{X} + \frac{1}{2}V_2O_5 \quad (27)$$

$$BaO + VO_{VO}^{X} + \frac{1}{2}O_O^{X} \leftrightarrows Ba'_{VO} + \frac{1}{2}\square_O^{\bullet\bullet} + \frac{1}{2}V_2O_5 \quad (28)$$

$$\frac{1}{2}Na_2O + VO_{VO}^{X} + O_O^{X} \leftrightarrows Na''_{VO} + \square_O^{\bullet\bullet} + \frac{1}{2}V_2O_5 \quad (29)$$

Where $VO_{VO}^{X}$ indicates a V-O vanadyl group in the $V_2O_5$ lattice, $Al_{VO}^{X}$ indicates an $Al^{3+}$ replacing a V-O vanadyl group with neutral delithiation, $Ba_{VO}'$ and $Na_{VO}''$ are $Ba^{2+}$ and $Na^{+}$ replacing a V-O vanadyl group without neutral charge, and $\square_O^{\bullet\bullet}$ indicates a vacancy on an isolated oxygen site with a net positive delithiation of +2. The simultaneous 'clustered' replacement of a V-O vanadyl group with a cation has a lower formation energy than isolated vanadium and oxygen ($M_V + \square_O^{\bullet\bullet}$) defects and is therefore considered as the main scheme for forming oxygen vacancies due to substitutional doping. Interstitial incorporation of the cations can be accompanied by oxide interstitials ($\mathbf{O_i''}$) for $Al^{3+}$, $Ba^{2+}$ and $Na^{+}$ as summarised in Equation 30, Equation 31 and Equation 32, respectively.

$$\mathbf{\frac{1}{2}Al_2O_3 \leftrightarrows Al_i^{\bullet\bullet\bullet} + \frac{3}{2}O_i''} \quad (30)$$

$$\mathbf{BaO \leftrightarrows Ba_i^{\bullet\bullet} + O_i''} \quad (31)$$

$$\mathbf{\frac{1}{2}Na_2O \leftrightarrows Na_i^{\bullet} + \frac{1}{2}O_i''} \quad (32)$$

Alternatively, interstitial incorporation of the cations can create vanadium vacancies (Equation 33, Equation 34 and Equation 35).

$$\mathbf{\frac{1}{2}Al_2O_3 \leftrightarrows Al_i^{\bullet\bullet\bullet} + \frac{3}{5}\square_V'''' + \frac{3}{10}V_2O_5} \quad (33)$$

$$\mathbf{BaO \leftrightarrows Ba_i^{\bullet\bullet} + \frac{2}{5}\square_V'''' + \frac{1}{5}V_2O_5} \quad (34)$$

$$\mathbf{\frac{1}{2}Na_2O \leftrightarrows Na_i^{\bullet} + \frac{1}{5}\square_V'''' + \frac{1}{10}V_2O_5} \quad (35)$$

Where $Al_i^{\bullet\bullet\bullet}$ represents $Al^{3+}$, $Ba_i^{\bullet\bullet}$ is $Ba^{2+}$, $Na_i^{\bullet}$ is $Na^{+}$ and $\square_V''''$ are vanadium vacancies.

The calculated defect formation energies are reported in Table 5.5. The interstitial cation defects, compensated by vanadium vacancies have high formation energies and are thus not likely to occur. The $Al^{3+}$ substitutional defect is lower in energy than the interstitial defect by 2 eV, therefore it is likely that $Al^{3+}$ will predominantly occupy substitutional sites. However, the energy difference of 2 eV between substitutional and interstitial sites means that it may be

possible for $Al^{3+}$ to occupy interstitial sites under some conditions. In contrast, $Ba^{2+}$ and $Na^{+}$, the interstitial cation defects with oxygen interstitials are significantly lower in energy than the substitutional sites by 8.6 eV and 14.4 eV, respectively. Due to the greater energy difference between the substitutional and interstitial sites, it can be predicted that these cations will only occupy interstitial sites.

**Table 5.5: Calculated defect formation energies determined *via* pair potential calculations.**

| Defect site | Delithiation compensation | Species | Defect energy (eV) | Equation |
|---|---|---|---|---|
| Substitutional | Oxygen vacancies | $Al^{3+}$ | 0.66 | 27 |
| | | $Ba^{2+}$ | 5.61 | 28 |
| | | $Na^{+}$ | 9.80 | 29 |
| Interstitial | Oxide interstitial | $Al^{3+}$ | 2.64 | 30 |
| | | $Ba^{2+}$ | -2.96 | 31 |
| | | $Na^{+}$ | -4.58 | 32 |
| | Vanadium vacancy | $Al^{3+}$ | 23.57 | 33 |
| | | $Ba^{2+}$ | 11.26 | 34 |
| | | $Na^{+}$ | 2.84 | 35 |

As discussed earlier, $V_2O_5$ is oxygen deficient and shows intrinsic n-type semiconducting behaviour, displaying an equilibrium between oxygen vacancies and the partial reduction of $V^{5+}$ ($d^0$) to $V^{4+}$ ($d^1$), which keeps the bulk material electronically neutral which is represented by Equation 36.

$$\mathbf{V_V^X + O_O^X \leftrightarrows 2V_V' + \square_O^{\bullet\bullet} + \frac{1}{2}O_2} \quad (36)$$

In Equation 37, an equilibrium reaction constant ($K_{int}$) is applied to the products of Equation 36.

$$\mathbf{K_{int} = [\square_O^{\bullet\bullet}][V_V']^2 \cdot pO_2^{\frac{1}{2}}} \quad (37)$$

The concentration of oxygen vacancies $[\square_O^{\bullet\bullet}]$ is approximately equivalent to half the concentration of $V^{4+}$ ($[V_V']$) according to Equation 38.

$$\mathbf{[\square_O^{\bullet\bullet}] \approx \frac{1}{2}[V_V']} \quad (38)$$

The introduction of interstitial $Ba^{2+}$ (Equation 39) or $Na^{+}$ (Equation 40) will modify the equilibrium between oxygen vacancies and $V^{4+}$.

$$\left[\square_{\mathbf{O}}^{\bullet\bullet}\right] + \left[\mathbf{Ba}_{\mathbf{i}}^{\bullet\bullet}\right] \approx \frac{\mathbf{1}}{\mathbf{2}}\left[\mathbf{V}_{\mathbf{V}}'\right] \quad (39)$$

$$\left[\square_{\mathbf{O}}^{\bullet\bullet}\right] + \left[\mathbf{Na}_{\mathbf{i}}^{\bullet}\right] \approx \frac{\mathbf{1}}{\mathbf{2}}\left[\mathbf{V}_{\mathbf{V}}'\right] \quad (40)$$

This will likely lower the concentration of oxygen vacancies, whilst increasing the concentration of $V^{4+}$. Also relevant to the concentration equilibria will be the formation of oxygen Frenkel defects ($K_{O-Frenkel}$) in Equation 41, which will have a low equilibrium constant, due to the preference for oxygen deficiency.

$$\mathbf{K_{O-Frenkel}} = \left[\square_{\mathbf{O}}^{\bullet\bullet}\right]\left[\mathbf{O}_{\mathbf{i}}''\right] \quad (41)$$

The concentration of oxygen vacancies exceeds the concentration of oxide interstitials for the following condition in Equation 42.

$$\left[\square_{\mathbf{O}}^{\bullet\bullet}\right] = \boldsymbol{x}\left[\mathbf{O}_{\mathbf{i}}''\right] \;, \boldsymbol{x} \gg \mathbf{1} \quad (42)$$

The introduction of interstitial $Ba^{2+}$ or $Na^{+}$ and associated interstitial oxide ions will push the equilibrium towards lower oxygen vacancy concentrations. This may explain the slightly increased $V^{4+}$ concentrations in the $Na^{+}$ and $Ba^{2+}$ doped samples compared to undoped $V_2O_5$ as indicated by the XPS results. The reduction of $V^{5+}$ to $V^{4+}$ produced by oxygen vacancy formation will tend to result in $d^1$ electrons localised on the V atoms neighbouring the oxygen vacancy. In contrast, if the oxygen vacancy concentration is suppressed, the $d^1$ electrons may be delocalised to a greater extent throughout the material, and this higher mobility may result in the increased conductivity observed for the $Na^{+}$ and $Ba^{2+}$ doped materials.

### 5.2.4 Comparison of experimental and computational results

The experimental results for $V_{1.96}Na_{0.04}O_5$ support the pair potential calculations in Section 5.2.3 and showed improved capacities along with decreased overpotential [Figure 5.6].

Additionally, Li *et al.* suggested that an increase in $V^{4+}$ content, brought about by the introduction of $Na^+$, caused the reduction of $V^{5+}$ rather than the substitution of vanadium [147]. With the presence of 6 at% $NaV_6O_{15}$ impurity, as determined by Rietveld refinement, the extra redox peaks and potential steps observed in Figure 5.5 and Figure 5.6, respectively, was caused by partial substitution of $Na^+$ for Li-ions with this impurity phase [239]. The $NaV_6O_{15}$ impurity may also have contributed to the improved capacity of $V_{1.96}Na_{0.04}O_5$ given its tunnel-like structure.

A low at% loading of $Ba^{2+}$ in this chapter shows that dopant amount played an important role in both structural stability and electron conductivity. $V_{1.94}Ba_{0.06}O_5$ not only showed improved rate capability and cycle stability but also improved diffusion according to the EIS analysis. There was an electron conductivity contribution, suggested by the calculations, as evidenced by a higher $V^{4+}$ content compared to that of the undoped $V_2O_5$ along with the reduced overpotentials in the capacity versus potential profiles.

The introduction of substitutional $Al^{3+}$ ions will modify the equilibrium between oxygen vacancies and $V^{4+}$ in the material, by producing a different effect to the interstitial ions according to Equation 43.

$$\left[\square_{\mathbf{O}}^{\bullet\bullet}\right] = \frac{\mathbf{1}}{\mathbf{2}}\left[\mathbf{V}_{\mathbf{V}}'\right] + \left[\mathbf{Al}_{\mathbf{V}}''\right] \tag{43}$$

If it is assumed that the total concentration of oxygen vacancies remains approximately constant and does not significantly decrease, since each $Al^{3+}$ dopant will be associated with a 'vanadyl' O1 oxygen vacancy, then the concentration of $V^{4+}$ will be reduced by the incorporation of $Al^{3+}$. These predictions correlate with the observed reduction in $V^{4+}$ concentration (2%) for the $Al^{3+}$ doped materials with respect to the undoped $V_2O_5$ (8%) in the XPS analysis. The reduction in $V^{4+}$ concentration will tend to reduce electronic conductivity in $V_2O_5$. Experimentally, this was observed in the C-rate test, CV and impedance results. $V_{1.94}Al_{0.06}O_5$ did however offer improved cycle stability during the C-rate test though structural stability was not improved

during cycling at 50 mA $g^{-1-}$ after the C-rate test [Figure 5.8(a)]. The low $V^{4+}$ content in $V_{1.94}Al_{0.06}O_5$, along with large redox pair variation [Figure 5.5(d)] and large overpotentials [Figure 5.6] suggested fewer nucleation centres for phase transitions during lithiation/delithiation [225].

$Al^{3+}$ doped materials have received positive attention in the literature, though the $V_{1.94}Al_{0.06}O_5$ presented in this study did not perform to the expectations presented by others [134,228,240]. Zhan *et al.* used a soft-chemical method with $V_2O_5$ powder and aluminium nitrate assisted by oxalic acid followed by heat treatment at 350 °C to obtain $V_2O_5$ nanoparticles with 9 at% loading of $Al^{3+}$ [228]. Zhu *et al.* also used a soft chemical method with the same components and reduced graphene oxide to produce $V_2O_5$ and $V_2O_5$ incorporated reduce graphene oxide both with 7 at% loadings of $Al^{3+}$ [240]. Cheah *et al*. electrospun their 20 at% $Al^{3+}$ doped $V_2O_5$ and 33 at% $Al^{3+}$ doped $V_2O_5$ fibres from a solution of vanadyl acetylacetonate, aluminium nitrate and PVP followed by heat treatment at 400 °C [134]. All studies showed an increased in $V^{4+}$ for the $Al^{3+}$ doped $V_2O_5$ *via* XPS measurements and an increase in the *a*-parameter, though for the *c*-parameter, Zhan *et al*. showed a decrease while Zhu *et al.* and Cheah *et al*. reported an increase.

It is likely that the combination of different starting materials, higher heat treatment temperature, which produces nucleation variations, and lower $Al^{3+}$ loading used in this study are responsible for the substitutional $Al^{3+}$ dopant location and low $V^{4+}$ content which resulted in poor performance. The energetics of $Al^{3+}$ incorporation shows that substitutional sites are favoured, but interstitial sites were only 2 eV higher in energy, so they may be accessible under some conditions. Whilst Cheah *et al.* also used electrospinning, the higher loading (20% and 33%) may tend to favour interstitial $Al^{3+}$ sites, or a mix of substitutional and interstitial. These variations in synthesis methods, indicates the important role starting materials play along with fabrication method on the resultant $V^{4+}$ content.

## 5.3 CONCLUSION AND SUMMARY

Electrospinning was used to produce microscale fibres which consisted of nanostructured $V_2O_5$ particles. $Na^+$, $Ba^{2+}$, $Al^{3+}$ were systematically incorporated into $V_2O_5$ to produce $V_{1.96}Na_{0.04}O_5$, $V_{1.94}Ba_{0.06}O_5$, and $V_{1.94}Al_{0.06}O_5$, respectively. $Ba^{2+}$ was investigated again to determine whether the dopant loading was responsible for negatively impacting the capacity. All dopants offered improved rate capability but only $V_{1.96}Na_{0.04}O_5$ and $V_{1.94}Ba_{0.06}O_5$ showed improved cycle stability and improved capacities indicating that an increase in structural stability, afforded by the dopants, and an increase in electrical conductivity is necessary for overall enhanced electrochemical performance. Another key parameter that dictated the performance of these materials was the $V^{4+}$ content where $V_{1.94}Al_{0.06}O_5$ possessed the lowest $V^{4+}$ concentration along with the poorest electrochemical performance. The location of the dopants, $V^{4+}$ content and electronic conductivity were rationalised by atomistic simulations, from which it could be inferred that interstitial dopants are important to improved electrochemical performance. After examination of the literature, it is suggested that synthesis methods of nanomaterials require careful consideration to optimise oxidation state concentrations.

The results presented in Chapter 5 showed that the interstitial $Na^+$ and $Ba^{2+}$ dopants in electrospun $V_2O_5$ provided both improved structural and electronic effects for the $V_2O_5$ structure and resulted in improved electrochemical performance, while substitutional $Al^{3+}$ provided an improved structural effect, but decreased electronic conductivity. This indicates that dopant location is important in affecting the overall electrochemical performance of the host material, and dopant loading and oxidation state can influence where dopants are located.

# Chapter 6 Conclusions and Future Work

## 6.1 CONCLUSIONS

This thesis examines the synthesis, characterisation and electrochemical properties of fibrous vanadium-based oxides as positive electrodes for LIBs. The research and development of alternative electrode materials for energy storage devices, such as LIBs, is necessary in order to meet society's growing energy needs. $V_2O_5$ is a potential candidate as an electrode material on account of its structure, theoretical capacity and abundance. The use of $V_2O_5$ in energy storage devices, while promising, is limited by its low structural stability and slow electrochemical kinetics associated with Li-ion intercalation which results in poor cycle stability. The incorporation of dopant materials into $V_2O_5$ is an important avenue for improving its electrochemical performance. To produce nanostructured undoped and doped $V_2O_5$, the electrospinning technique was used. Electrospinning is a simple and versatile liquid-state processing technique that can form fibrous nanostructured oxides. The vanadium-based oxide fibres in this thesis were made up nanostructured particles in a hierarchical fibrous structure. A starting solution of vanadium oxytripropoxide, PVAc and ethanol was used to produce the undoped $V_2O_5$ studied in this thesis followed by a calcination temperature of 500 °C of the as-spun fibres.

Effect of the process parameters calcination temperature and polymer content were investigated to determine whether this route of investigation could address the electrochemical limitations of $V_2O_5$ as a positive electrode material. Varying the calcination temperature to 450 °C and 550 °C affected the crystallinity of the $V_2O_5$ particles and the morphology of the fibres with larger crystallites produced by higher calcination temperatures. This was shown *via* XRD and SEM analysis. Electrochemical analysis *via* CV and GDC showed that the materials underwent the expected $V_2O_5$ phase changes over 2.0 – 4.0 V vs $Li/Li^+$ though displayed poor rate

retention with varying current density despite producing competitive initial capacities. Impedance measurements showed an improvement in conductivity with an increase in calcination temperature. Overall fibres calcined at 500 °C produced the highest capacities indicating that a compromise between structural characteristics and electrochemical performance must be considered in optimisation investigations of electrode materials.

Varying the polymer content of the starting solution from the standard 0.3 g of PVAc to lower amounts prior to electrospinning indicated, *via* SEM analysis, that fibre diameter could be controlled. XRD analysis showed an overall increase with crystallite size which was likely caused by less organic constituents in the starting solution which allowed more opportunity for particle growth. Despite this, no trends in the electrochemical performance and impedance measurements were observed except for the sample with the lowest polymer content, PVAc-0.08 g. PVAc-0.08 g did not possess a defined fibrous morphology. Varying the polymer content showed that a hierarchical fibrous structure was beneficial for Li-ion intercalation. These results indicated that the polymer amount of 0.3 g used in the varying calcination investigation was suitable for further use. The electrochemical analysis *via* CV, GDC and EIS still showed poor rate capability for the $V_2O_5$ fibres. To address this, dopants were incorporated into $V_2O_5$. This was achieved *via* the addition of a dopant precursor into the starting solution. The polymer content of these starting solutions was 0.3 g of PVAc and the as-spun fibres were calcined at 500 °C.

A high dopant amount of approximately 10 at% of $Ba^{2+}$ and $Ti^{4+}$ was incorporated into $V_2O_5$. It was shown that a high dopant loading did not guarantee an improvement in capacity despite offering significant improvement in the cycle stability. Structural characterisation analyses showed that each dopant had a critical effect on lattice distortions whilst showing little influence in the overall crystal structure as the $V_2O_5$ remained the dominate phase, which is unusual for such large dopant amounts. The doped materials showed better cycle stability and higher efficiencies than the undoped equivalent in the CV and GDC analyses. Ex-situ XRD

measurements clearly showed detrimental phase changes within undoped $V_2O_5$ whereas the $Ti^{4+}$ doped $V_2O_5$ predominantly remained as α-$V_2O_5$ after the first cycle. This investigation clearly showed that dopant can prevent phase changes, which was the mechanistic reason behind improved structural stability observed for these materials.

The dopant investigation continued with the structural and electrochemical investigation of electrospun $V_2O_5$ with selected redox-inactive dopants possessing varying oxidation states, namely 3 at% $Na^+$, 3 at% $Ba^{2+}$, and 2 at% $Al^{3+}$. Structural characterisations showed that there was marked variation in the $V^{4+}/V^{5+}$ ratio which was affected by dopant occupying sites within $V_2O_5$ as suggested by atomistic simulations. Electrochemical investigations using CV, GDC and EIS showed that electrochemical performance was dependent on $V^{4+}$ concentration which influenced electronic conductivity. $Na^+$ and $Ba^{2+}$ doped $V_2O_5$ offered improved conductivities and lithium ion diffusion characteristics while $Al^{3+}$ doped $V_2O_5$ at 3 at% was shown to be detrimental to these properties.

## 6.2 FUTURE WORK

The development of new functional materials requires not only consideration of the efficiency and capacity characteristics, but also cost effectiveness for production. Due to this, it is important that optimisation of nanomaterial fabrication methods continue. Further optimisation of the electrospinning technique *via* examination of the starting solution components or experimental parameters, such as solution feed rate or electric field, could produce fibres with more consistent diameters and with higher structural integrity. This would prove to be beneficial to the electrochemical properties, as varying the polymer content in the starting solution in this thesis emphasised the importance of a fibrous morphology for $V_2O_5$ during Li-ion intercalation. SEM analysis of the 10 at% $Ti^{4+}$ doped $V_2O_5$ showed that some fibres had fused together which suggested inappropriate humidity levels during the electrospinning operation. Additionally, 2

at% $Al^{3+}$ doped $V_2O_5$ possessed particle clusters along the fibre length indicating that there was an imbalance between the polymer and solvent ratios.

Chapter 4 and Chapter 5 showed that the incorporation of dopants produced varied effects in terms of their location, loading and oxidation state, on both the stabilization of the host $V_2O_5$ structure and on electronic conductivity. Given this series of variables, a general conclusion about valence state alone cannot be provided. The analysis in this project suggests that dopants with low valence state are electronically and structurally favourable, however, dopant loading must also be considered. An avenue of investigation could involve the systematic doping of $V_2O_5$ at a low loading with low valence state materials to ascertain the effect of 1+ and 2+ oxidates states on the electrochemical properties.

Comparing the performance of 2 at% $Al^{3+}$ doped $V_2O_5$ in Chapter 5 to the literature, notable differences included the fabrication technique, $Al^{3+}$ loading and the heat treatment temperature. At this stage, it is difficult to ascertain which aspect was the main contributor of the poor performance of electrospun $Al^{3+}$ doped $V_2O_5$ in Chapter 5. Consequently, it may be worthwhile to investigate the $V^{4+}$ content variation in $V_2O_5$ with heat treatment temperature and/or systematically vary the $Al^{3+}$ concentration. Varying the $Al^{3+}$ would require revisiting the electrospinning technique as the spinnability of the starting solutions would need to be continually reassessed with each dopant level, to ensure that fibrous materials were produced. The dopants introduced into $V_2O_5$ in this thesis were redox-inactive in order to study the stabilisation and conductivity effects on the $V_2O_5$ structure provided by the dopant. To expand the dopant investigation, incorporating $V_2O_5$ with conversion/alloying elements, such as $Sn^{4+}$ or $Fe^{2+}/Fe^{3+}$, could combine the stability of the intercalation host $V_2O_5$ and the high capacity of the dopant. This would only be useful if the active range of the dopant overlapped with the active range of $V_2O_5$ for two Li-ion intercalations per formula unit, within 2.0 to 4.0 V vs $Li/Li^+$. Alternatively, expanding the potential window to near 1.5 V vs $Li/Li^+$ to allow for three Li-ion intercalations per unit formula could prove useful if the dopant provided not only a

conductivity effect, but also a structural stabilisation effect. Dopant amount would require optimisation as conversion/alloying elements are susceptible to substantial structural variations which have severe impacts on the cycle stability.

Incorporation of a carbonaceous material into $V_2O_5$, either directly into the starting solution or as a post-electrospinning treatment, would help address the rate capability issues that this material showed in this thesis. Carbon coating is an effective method for improving electrochemical performance of electrodes by forming protective layers on the active materials. These protection layers could improve structural stability during cycling as carbon can act as a barrier to suppress pulverisation, aggregation or agglomeration of active particles. Additionally, graphitic materials have high electronic conductivities and it hence can offer improved conductivity to the entire composite material.

The low abundance and availability of Li metal implies that alternate metal ion systems, such Na- and Al-based, will undoubtedly become more commonplace in the battery market. Consequently, broadening the investigation of the electrospun vanadium oxide system in this thesis into other metal ion systems would be beneficial and relevant. The study of these materials within Li-ion half-cells in this thesis was necessary as this battery system is well understood on a device level. There is little literature featuring the development and research of electrospun vanadium oxides in alternate metal ion battery systems.

Vanadium oxides have shown and will continue to show promise as an electrode material in both LIBs and in alternate metal ion systems. The investigation of nanostructured materials produced *via* electrospinning will continue to impact the research and development of energy storage and conversion systems into the future.

# List of Publications

**C.F. Armer**, M. Lübke, M.V. Reddy, J.A. Darr, X. Li, A. Lowe, Phase change effect on the structural and electrochemical behaviour of undoped and doped vanadium pentoxide as positive electrodes for lithium ion batteries, J. Power Sources. 353 (2017) 40-50.

**C.F. Armer**, J.S. Yeoh, X. Li, A. Lowe, Electrospun Vanadium-based Oxides as Electrode Materials, J. Power Sources. *In review*

**C.F. Armer**, M. Lübke, I. Johnson, J.S. Yeoh, K. McColl, F. Cora, M.V. Reddy, J.A. Darr, X. Li, A. Lowe, Enhanced electrochemical performance of electrospun $V_2O_5$ fibres doped with redox-inactive metals, Solid State Electrochemistry. *To be submitted*

M. Lübke, D. Howard, **C.F. Armer**, A. J. Gardecka, A. Lowe, M.V. Reddy, Zhaolin Liu, J.A. Darr, High energy lithium ion battery electrode materials; enhanced delithiation storage via both alloying and insertion processes, Electrochimica Acta. 231 (2017) 247-254.

M. Lübke, D. Ning, **C.F. Armer**, D. Howard, D. L.J. Brett, Zhaolin Liu, J.A. Darr, Evaluating the Potential Benefits of Metal Ion Doping in $SnO_2$ Negative Electrodes for Lithium Ion Batteries, Electrochimica Acta. 242 (2017) 4000-407.

M. Lübke, A. Sumboja, L. McCafferty, **C.F. Armer**, A.D. Handoko, Y. Du, K. McColl, F. Cora, D. Brett, Z. Liu, J.A. Darr, High performance bifunctional oxygen reduction and evolution α-$MnO_2$ catalysts. ChemistrySelect. 3 (2018) 2613-2622.

J.S. Yeoh, **C.F. Armer**, A. Lowe, Transition Metal Oxalates as Energy Storage Materials. A Review, Materials Today Energy. *In review*

A. J. Gardecka, M. Lübke, **C.F. Armer**, D. Ning, M.V. Reddy, Alan S. Williams, A. Lowe, Z. Liu, I. P. Parkin, J. A. Darr, Nb-doped Rutile $TiO_2$ Nanorods for Lithium-ion Batteries, Solid State Sciences. *In review*

# References


[1] Z. Dong, S.J. Kennedy, Y. Wu, Electrospinning materials for energy-related applications and devices, J. Power Sources. 196 (2011) 4886–4904. doi:10.1016/j.jpowsour.2011.01.090.

[2] S. Cavaliere, S. Subianto, I. Savych, D.J. Jones, J. Roziere, Electrospinning: designed architectures for energy conversion and storage devices, Energy Environ. Sci. 4 (2011) 4761–4785. doi:10.1039/C1EE02201F.

[3] M. Qin, J. Liu, S. Liang, Q. Zhang, X. Li, Y. Liu, M. Lin, Facile synthesis of multiwalled carbon nanotube–V2O5 nanocomposites as cathode materials for Li-ion batteries, J. Solid State Electrochem. 18 (2014) 2841–2846. doi:10.1007/s10008-014-2543-7.

[4] S. Holmberg, A. Perebikovsky, L. Kulinsky, M. Madou, 3-D Micro and Nano Technologies for Improvements in Electrochemical Power Devices, Micromachines. 5 (2014) 171–203. doi:10.3390/mi5020171.

[5] J.-S. Huang, C.-Y. Chou, M.-Y. Liu, K.-H. Tsai, W.-H. Lin, C.-F. Lin, Solution-processed vanadium oxide as an anode interlayer for inverted polymer solar cells hybridized with ZnO nanorods, Org. Electron. 10 (2009) 1060–1065. doi:10.1016/j.orgel.2009.05.017.

[6] M. Benmoussa, A. Outzourhit, A. Bennouna, E.. Ameziane, Electrochromism in sputtered V2O5 thin films: structural and optical studies, Thin Solid Films. 405 (2002) 11–16. doi:10.1016/S0040-6090(01)01734-5.

[7] A. Jin, W. Chen, Q. Zhu, Z. Jian, Multi-electrochromism behavior and electrochromic mechanism of electrodeposited molybdenum doped vanadium pentoxide films, Electrochimica Acta. 55 (2010) 6408–6414. doi:10.1016/j.electacta.2010.06.047.

[8] Z. Zhang, C. Shao, L. Zhang, X. Li, Y. Liu, Electrospun nanofibers of V-doped TiO2 with high photocatalytic activity, J. Colloid Interface Sci. 351 (2010) 57–62. doi:10.1016/j.jcis.2010.05.067.

[9] B.-H. Kim, C.H. Kim, K.S. Yang, A. Rahy, D.J. Yang, Electrospun vanadium pentoxide/carbon nanofiber composites for supercapacitor electrodes, Electrochimica Acta. 83 (2012) 335–340. doi:10.1016/j.electacta.2012.07.093.

[10] X. Chen, B. Zhao, Y. Cai, M.O. Tadé, Z. Shao, Amorphous V–O–C composite nanofibers electrospun from solution precursors as binder- and conductive additive-free electrodes for supercapacitors with outstanding performance, Nanoscale. 5 (2013) 12589. doi:10.1039/c3nr04484j.

[11] S. Li, Y. Li, K. Qian, S. Ji, H. Luo, Y. Gao, P. Jin, Functional Fiber Mats with Tunable Diffuse Reflectance Composed of Electrospun VO2/PVP Composite Fibers, ACS Appl. Mater. Interfaces. 6 (2014) 9–13. doi:10.1021/am405006g.

[12] V. Modafferi, S. Trocino, A. Donato, G. Panzera, G. Neri, Electrospun V2O5 composite fibers: Synthesis, characterization and ammonia sensing properties, Thin Solid Films. 548 (2013) 689–694. doi:10.1016/j.tsf.2013.03.137.

[13] P. Zhu, Y. Wu, M.V. Reddy, A. Sreekumaran Nair, B.V.R. Chowdari, S. Ramakrishna, Long term cycling studies of electrospun TiO2 nanostructures and their composites with MWCNTs for rechargeable Li-ion batteries, RSC Adv. 2 (2012) 531–537. doi:10.1039/C1RA00514F.

[14] Liqiang Mai, Qiulong Wei, Xiaocong Tian, Yunlong Zhao, Qinyou An, Electrochemical Nanowire Devices for Energy Storage, IEEE Trans. Nanotechnol. 13 (2014) 10–15. doi:10.1109/TNANO.2013.2276524.

[15] P. Atkins, T. Overton, J. Rourke, M. Weller, F. Armstrong, Inorganic Chemistry, 4th ed., Oxford University Press, Oxford, 2006.

[16] M. Winter, R.J. Brodd, What Are Batteries, Fuel Cells, and Supercapacitors?, Chem. Rev. 104 (2004) 4245–4270. doi:10.1021/cr020730k.

[17] J.-M. Tarascon, M. Armand, Issues and challenges facing rechargeable lithium batteries, Nature. 414 (2001) 359–367. doi:10.1038/35104644.
[18] A. González, E. Goikolea, J.A. Barrena, R. Mysyk, Review on supercapacitors: Technologies and materials, Renew. Sustain. Energy Rev. 58 (2016) 1189–1206. doi:10.1016/j.rser.2015.12.249.
[19] A.G. Pandolfo, A.F. Hollenkamp, Carbon properties and their role in supercapacitors, J. Power Sources. 157 (2006) 11–27. doi:10.1016/j.jpowsour.2006.02.065.
[20] Y. Zhang, H. Feng, X. Wu, L. Wang, A. Zhang, T. Xia, H. Dong, X. Li, L. Zhang, Progress of electrochemical capacitor electrode materials: A review, 2nd Int. Workshop Hydrog. 34 (2009) 4889–4899. doi:10.1016/j.ijhydene.2009.04.005.
[21] A. Vlad, N. Singh, C. Galande, P.M. Ajayan, Design Considerations for Unconventional Electrochemical Energy Storage Architectures, Adv. Energy Mater. 5 (2015) 1402115. doi:10.1002/aenm.201402115.
[22] L. Fu, N. Li, Y. Liu, W. Wang, Y. Zhu, Y. Wu, Advances of Aluminum Based Energy Storage Systems, Chin. J. Chem. 35 (2017) 13–20. doi:10.1002/cjoc.201600655.
[23] J.-K. Park, Principles and Applications of Lithium Secondary Batteries, WILEY-VCH Verlag GmbH & Co. KGaA, Weinheim, Germany, n.d.
[24] International Energy Agency, Technology Roadmap: Electric and plug-in hybrid electric vehicles, International Energy Agency, Paris, 2011.
[25] B. Scrosati, J. Garche, Lithium batteries: Status, prospects and future, J. Power Sources. 195 (2010) 2419–2430. doi:10.1016/j.jpowsour.2009.11.048.
[26] R. Marom, S.F. Amalraj, N. Leifer, D. Jacob, D. Aurbach, A review of advanced and practical lithium battery materials, J Mater Chem. 21 (2011) 9938–9954. doi:10.1039/C0JM04225K.
[27] N. Nitta, F. Wu, J.T. Lee, G. Yushin, Li-ion battery materials: present and future, Mater. Today. 18 (2015) 252–264. doi:10.1016/j.mattod.2014.10.040.
[28] J. Garcia-Martinez, Nanotechnology for the Energy Challenge, WILEY-VCH Verlag GmbH & Co. KGaA, Weinheim, Padstow, 2010.
[29] J. Tu, X.B. Zhao, G.S. Cao, D.G. Zhuang, T.J. Zhu, J.P. Tu, Enhanced cycling stability of LiMn2O4 by surface modification with melting impregnation method, Electrochimica Acta. 51 (2006) 6456–6462. doi:10.1016/j.electacta.2006.04.031.
[30] H. Arai, S. Okada, Y. Sakurai, J. Yamaki, Thermal behavior of Li1−yNiO2 and the decomposition mechanism, Solid State Ion. 109 (1998) 295–302. doi:10.1016/S0167-2738(98)00075-7.
[31] M.V. Reddy, G.V. Subba Rao, B.V.R. Chowdari, Metal Oxides and Oxysalts as Anode Materials for Li Ion Batteries, Am. Chem. Soc. 113 (2013) 5364–5457.
[32] M.R. Palacin, Recent advances in rechargeable battery materials: a chemist's perspective, Chem Soc Rev. 38 (2009) 2565–2575. doi:10.1039/B820555H.
[33] W.-J. Zhang, A review of the electrochemical performance of alloy anodes for lithium-ion batteries, J. Power Sources. 196 (2011) 13–24. doi:10.1016/j.jpowsour.2010.07.020.
[34] S. Goriparti, E. Miele, F. De Angelis, E. Di Fabrizio, R. Proietti Zaccaria, C. Capiglia, Review on recent progress of nanostructured anode materials for Li-ion batteries, J. Power Sources. 257 (2014) 421–443. doi:10.1016/j.jpowsour.2013.11.103.
[35] L. Ji, Z. Lin, M. Alcoutlabi, X. Zhang, Recent developments in nanostructured anode materials for rechargeable lithium-ion batteries, Energy Env. Sci. 4 (2011) 2682–2699. doi:10.1039/C0EE00699H.
[36] M.A. Reddy, M.S. Kishore, V. Pralong, V. Caignaert, U.V. Varadaraju, B. Raveau, Electrochemical performance of VOMoO4 as negative electrode material for Li ion batteries, J. Power Sources. 168 (2007) 509–512. doi:10.1016/j.jpowsour.2007.02.089.

[37] C.V.S. Reddy, J. Wei, Z. Quan-Yao, D. Zhi-Rong, C. Wen, S. Mho, R.R. Kalluru, Cathodic performance of (V2O5+PEG) nanobelts for Li ion rechargeable battery, J. Power Sources. 166 (2007) 244–249. doi:10.1016/j.jpowsour.2007.01.010.
[38] C. Buzea, I.I. Pacheco, K. Robbie, Nanomaterials and nanoparticles: Sources and toxicity, Biointerphases. 2 (2007) MR17–MR71. doi:10.1116/1.2815690.
[39] V.S. Reddy Channu, D. Ravichandran, B. Rambabu, R. Holze, Carbon and functionalized graphene oxide coated vanadium oxide electrodes for lithium ion batteries, Appl. Surf. Sci. 305 (2014) 596–602. doi:10.1016/j.apsusc.2014.03.140.
[40] S. Ramdon, B. Bhushan, Nanomechanical characterization and mechanical integrity of unaged and aged Li-ion battery cathodes, J. Power Sources. 246 (2014) 219–224. doi:10.1016/j.jpowsour.2013.07.078.
[41] A.S. Arico, P. Bruce, B. Scrosati, J.-M. Tarascon, W. van Schalkwijk, Nanostructured materials for advanced energy conversion and storage devices, Nat Mater. 4 (2005) 366–377. doi:10.1038/nmat1368.
[42] A.S. Hameed, M.V. Reddy, M. Nagarathinam, T. Runčevski, R.E. Dinnebier, S. Adams, B.V.R. Chowdari, J.J. Vittal, Room temperature large-scale synthesis of layered frameworks as low-cost 4 V cathode materials for lithium ion batteries, Sci. Rep. 5 (2015) 16270.
[43] M.V. Reddy, G.V. Subba Rao, B.V.R. Chowdari, Long-term cycling studies on 4 V-cathode, lithium vanadium fluorophosphate, J. Power Sources. 195 (2010) 5768–5774. doi:10.1016/j.jpowsour.2010.03.032.
[44] D. Liu, J. Han, J.B. Goodenough, Structure, morphology, and cathode performance of Li1−x[Ni0.5Mn1.5]O4 prepared by coprecipitation with oxalic acid, J. Power Sources. 195 (2010) 2918–2923. doi:10.1016/j.jpowsour.2009.11.024.
[45] S. Kraas, A. Vijn, M. Falk, B. Ufer, B. Luerßen, J. Janek, M. Fröba, Nanostructured and nanoporous LiFePO4 and LiNi0.5Mn1.5O4-δ as cathode materials for lithium-ion batteries, Funct. Mater. Anal. High Perform. Lithium Ion Batter. 42 (2014) 218–241. doi:10.1016/j.progsolidstchem.2014.04.014.
[46] B. Pei, Z. Jiang, W. Zhang, Z. Yang, A. Manthiram, Nanostructured Li3V2(PO4)3 cathode supported on reduced graphene oxide for lithium-ion batteries, J. Power Sources. 239 (2013) 475–482. doi:10.1016/j.jpowsour.2013.03.171.
[47] F. Jiao, P.G. Bruce, Mesoporous Crystalline β-MnO2—a Reversible Positive Electrode for Rechargeable Lithium Batteries, Adv. Mater. 19 (2007) 657–660. doi:10.1002/adma.200602499.
[48] Y.-S. Hu, L. Kienle, Y.-G. Guo, J. Maier, High Lithium Electroactivity of Nanometer-Sized Rutile TiO2, Adv. Mater. 18 (2006) 1421–1426. doi:10.1002/adma.200502723.
[49] E. Baudrin, S. Cassaignon, M. Koelsch, J.-P. Jolivet, L. Dupont, J.-M. Tarascon, Structural evolution during the reaction of Li with nano-sized rutile type TiO2 at room temperature, Electrochem. Commun. 9 (2007) 337–342. doi:10.1016/j.elecom.2006.09.022.
[50] Y. Gogotsi, What Nano Can Do for Energy Storage, ACS Nano. 8 (2014) 5369–5371. doi:10.1021/nn503164x.
[51] L. Mai, L. Xu, C. Han, X. Xu, Y. Luo, S. Zhao, Y. Zhao, Electrospun Ultralong Hierarchical Vanadium Oxide Nanowires with High Performance for Lithium Ion Batteries, Nano Lett. 10 (2010) 4750–4755. doi:10.1021/nl103343w.
[52] H.-E. Wang, D.-S. Chen, Y. Cai, R.-L. Zhang, J.-M. Xu, Z. Deng, X.-F. Zheng, Y. Li, I. Bello, B.-L. Su, Facile synthesis of hierarchical and porous V2O5 microspheres as cathode materials for lithium ion batteries, J. Colloid Interface Sci. 418 (2014) 74–80. doi:10.1016/j.jcis.2013.12.011.
[53] F. Ambroz, T.J. Macdonald, T. Nann, Trends in Aluminium-Based Intercalation Batteries, Adv. Energy Mater. (2017) 1602093-n/a. doi:10.1002/aenm.201602093.

[54] W.J. Rankin, Minerals, Metals and Sustainability: Meeting Future Material Needs, CRC Press, 2011.
[55] B. Sahoo, N. Charan, A. Samantaray, P. Kumar, Inorganic Chemistry, PHI Learning, 2012.
[56] D. Hamani, M. Ati, J.-M. Tarascon, P. Rozier, NaxVO2 as possible electrode for Na-ion batteries, Electrochem. Commun. 13 (2011) 938–941. doi:10.1016/j.elecom.2011.06.005.
[57] L. Weihan, Z. Linchao, W. Ying, Y. Yan, Nanostructured electrode materials for lithium-ion and sodium-ion batteries via electrospinning, Sci. CHINA Mater. 59 (2016) 287–321. doi:https://doi.org/10.1007/s40843-016-5039-6.
[58] H.-G. Wang, S. Yuan, D.-L. Ma, X.-B. Zhang, J.-M. Yan, Electrospun materials for lithium and sodium rechargeable batteries: from structure evolution to electrochemical performance, Energy Env. Sci. 8 (2015) 1660–1681. doi:10.1039/C4EE03912B.
[59] Z. Jian, W. Luo, X. Ji, Carbon Electrodes for K-Ion Batteries, J. Am. Chem. Soc. 137 (2015) 11566–11569. doi:10.1021/jacs.5b06809.
[60] S. Komaba, T. Hasegawa, M. Dahbi, K. Kubota, Potassium intercalation into graphite to realize high-voltage/high-power potassium-ion batteries and potassium-ion capacitors, Electrochem. Commun. 60 (2015) 172–175. doi:10.1016/j.elecom.2015.09.002.
[61] K. Beltrop, S. Beuker, A. Heckmann, M. Winter, T. Placke, Alternative electrochemical energy storage: potassium-based dual-graphite batteries, Energy Environ. Sci. (2017). doi:10.1039/C7EE01535F.
[62] Z.A. Zafar, S. Imtiaz, R. Razaq, S. Ji, T. Huang, Z. Zhang, Y. Huang, J.A. Anderson, Cathode materials for rechargeable aluminum batteries: current status and progress, J. Mater. Chem. A. 5 (2017) 5646–5660. doi:10.1039/C7TA00282C.
[63] W. Wang, B. Jiang, W. Xiong, H. Sun, Z. Lin, L. Hu, J. Tu, J. Hou, H. Zhu, S. Jiao, A new cathode material for super-valent battery based on aluminium ion intercalation and deintercalation, Sci. Rep. 3 (2013) 3383.
[64] S. Xia, X.-M. Zhang, K. Huang, Y.-L. Chen, Y.-T. Wu, Ionic liquid electrolytes for aluminium secondary battery: Influence of organic solvents, J. Electroanal. Chem. 757 (2015) 167–175. doi:10.1016/j.jelechem.2015.09.022.
[65] H. Wang, S. Gu, Y. Bai, S. Chen, F. Wu, C. Wu, High-Voltage and Noncorrosive Ionic Liquid Electrolyte Used in Rechargeable Aluminum Battery, ACS Appl. Mater. Interfaces. 8 (2016) 27444–27448. doi:10.1021/acsami.6b10579.
[66] S. Surnev, M.. Ramsey, F.. Netzer, Vanadium oxide surface studies, Prog. Surf. Sci. 73 (2003) 117–165. doi:10.1016/j.progsurf.2003.09.001.
[67] Y.L. Cheah, N. Gupta, S.S. Pramana, V. Aravindan, G. Wee, M. Srinivasan, Morphology, structure and electrochemical properties of single phase electrospun vanadium pentoxide nanofibers for lithium ion batteries, J. Power Sources. 196 (2011) 6465–6472. doi:10.1016/j.jpowsour.2011.03.039.
[68] Y. Yue, H. Liang, Micro- and Nano-Structured Vanadium Pentoxide (V2O5) for Electrodes of Lithium-Ion Batteries, Adv. Energy Mater. 7 (2017) 1602545-n/a. doi:10.1002/aenm.201602545.
[69] J. Hou, J. Zhang, Z. Wang, Z. Zhang, Z. Ding, Structural transition of VO2 (A) nanorods studied by vibrational spectroscopies, RSC Adv. 4 (2014) 18055. doi:10.1039/c4ra00585f.
[70] C. Niu, J. Meng, C. Han, K. Zhao, M. Yan, L. Mai, VO2 Nanowires Assembled into Hollow Microspheres for High-Rate and Long-Life Lithium Batteries, Nano Lett. 14 (2014) 2873–2878. doi:10.1021/nl500915b.
[71] M. Lübke, N. Ding, M.J. Powell, D.J.L. Brett, P.R. Shearing, Z. Liu, J.A. Darr, VO2 nano-sheet negative electrodes for lithium-ion batteries, Electrochem. Commun. 64 (2016) 56–60. doi:10.1016/j.elecom.2016.01.013.

[72] N.A. Chernova, M. Roppolo, A.C. Dillon, M.S. Whittingham, Layered vanadium and molybdenum oxides: batteries and electrochromics, J. Mater. Chem. 19 (2009) 2526–2552. doi:10.1039/B819629J.
[73] C. Wu, H. Wei, B. Ning, Y. Xie, New Vanadium Oxide Nanostructures: Controlled Synthesis and Their Smart Electrical Switching Properties, Adv. Mater. 22 (2010) 1972–1976. doi:10.1002/adma.200903890.
[74] S.Y. Zhan, C.Z. Wang, K. Nikolowski, H. Ehrenberg, G. Chen, Y.J. Wei, Electrochemical properties of Cr doped V2O5 between 3.8 V and 2.0 V, Solid State Ion. 180 (2009) 1198–1203. doi:10.1016/j.ssi.2009.05.020.
[75] T. Zhai, H. Liu, H. Li, X. Fang, M. Liao, L. Li, H. Zhou, Y. Koide, Y. Bando, D. Golberg, Centimeter-Long V2O5 Nanowires: From Synthesis to Field-Emission, Electrochemical, Electrical Transport, and Photoconductive Properties, Adv. Mater. 22 (2010) 2547–2552. doi:10.1002/adma.200903586.
[76] A. Pan, J.-G. Zhang, Z. Nie, G. Cao, B.W. Arey, G. Li, S. Liang, J. Liu, Facile synthesized nanorod structured vanadium pentoxide for high-rate lithium batteries, J. Mater. Chem. 20 (2010) 9193. doi:10.1039/c0jm01306d.
[77] N.L. Lala, R. Jose, M.M. Yusoff, S. Ramakrishna, Continuous tubular nanofibers of vanadium pentoxide by electrospinning for energy storage devices, J. Nanoparticle Res. 14 (2012). doi:10.1007/s11051-012-1201-1.
[78] A. Moretti, S. Passerini, Bilayered Nanostructured V2O5·nH2O for Metal Batteries, Adv. Energy Mater. 6 (2016) 1600868-n/a. doi:10.1002/aenm.201600868.
[79] H. Zhao, L. Pan, S. Xing, J. Luo, J. Xu, Vanadium oxides–reduced graphene oxide composite for lithium-ion batteries and supercapacitors with improved electrochemical performance, J. Power Sources. 222 (2013) 21–31. doi:10.1016/j.jpowsour.2012.08.036.
[80] C. Delmas, H. Cognac-Auradou, J.M. Cocciantelli, M. Ménétrier, J.P. Doumerc, The LixV2O5 system: An overview of the structure modifications induced by the lithium intercalation, Solid State Ion. 69 (1994) 257–264. doi:10.1016/0167-2738(94)90414-6.
[81] Yan L. Cheah, V. Aravindan, Srinivasan Madhavi, Chemical Lithiation Studies on Combustion Synthesized V2O5 Cathodes with Full Cell Application for Lithium Ion Batteries, J. Electrochem. Soc. 160 (2013) A1016–A1024. doi:10.1149/2.015308jes.
[82] X. Li, W. Li, H. Ma, J. Chen, Electrochemical Lithium Intercalation/Deintercalation of Single-Crystalline V2O5 Nanowires, J. Electrochem. Soc. 154 (2007) A39–A42.
[83] M. Winter, J.O. Besenhard, M.E. Spahr, P. Novak, Insertion Electrode Materials for Rechargeable Lithium Batteries, Adv. Mater. 10 (1998).
[84] K. Zhu, Y. Meng, H. Qiu, Y. Gao, C. Wang, F. Du, Y. Wei, G. Chen, C. Wang, G. Chen, Facile synthesis of V2O5 nanoparticles as a capable cathode for high energy lithium-ion batteries, J. Alloys Compd. 650 (2015) 370–373. doi:10.1016/j.jallcom.2015.07.122.
[85] S. Liang, M. Qin, Y. Tang, Q. Zhang, X. Li, X. Tan, A. Pan, Facile synthesis of nanosheet-structured V2O5 with enhanced electrochemical performance for high energy lithium-ion batteries, Met. Mater. Int. 20 (2014) 983–988. doi:10.1007/s12540-014-5025-7.
[86] C. Ban, N.A. Chernova, M.S. Whittingham, Electrospun nano-vanadium pentoxide cathode, Electrochem. Commun. 11 (2009) 522–525. doi:10.1016/j.elecom.2008.11.051.
[87] K. Dewangan, N.N. Sinha, P.G. Chavan, P.K. Sharma, A.C. Pandey, M.A. More, D.S. Joag, N. Munichandraiah, N.S. Gajbhiye, Synthesis and characterization of self-assembled nanofiber-bundles of V2O5: their electrochemical and field emission properties, Nanoscale. 4 (2012) 645–651. doi:10.1039/C1NR11444A.
[88] H. Wang, D. Ma, Y. Huang, X. Zhang, Electrospun V2O5 Nanostructures with Controllable Morphology as High-Performance Cathode Materials for Lithium-Ion Batteries, Chem. - Eur. J. 18 (2012) 8987–8993. doi:10.1002/chem.201200434.

[89] Y.L. Cheah, V. Aravindan, S. Madhavi, Synthesis and Enhanced Lithium Storage Properties of Electrospun V2O5 Nanofibers in Full-Cell Assembly with a Spinel Li4Ti5O12 Anode, ACS Appl. Mater. Interfaces. 5 (2013) 3475–3480. doi:10.1021/am400666n.
[90] J.J. Yu, J. Yang, W.B. Nie, Z.H. Li, E.H. Liu, G.T. Lei, Q.Z. Xiao, A porous vanadium pentoxide nanomaterial as cathode material for rechargeable lithium batteries, Electrochimica Acta. 89 (2013) 292–299. doi:10.1016/j.electacta.2012.11.032.
[91] B. Yan, X. Li, Z. Bai, M. Li, L. Dong, D. Xiong, D. Li, Superior lithium storage performance of hierarchical porous vanadium pentoxide nanofibers for lithium ion battery cathodes, J. Alloys Compd. 634 (2015) 50–57. doi:10.1016/j.jallcom.2015.01.292.
[92] C. Zhu, J. Shu, X. Wu, P. Li, X. Li, Electrospun V2O5 micro/nanorods as cathode materials for lithium ion battery, J. Electroanal. Chem. (n.d.). doi:10.1016/j.jelechem.2015.11.013.
[93] D. McNulty, D.N. Buckley, C. O'Dwyer, Synthesis and electrochemical properties of vanadium oxide materials and structures as Li-ion battery positive electrodes, J. Power Sources. 267 (2014) 831–873. doi:10.1016/j.jpowsour.2014.05.115.
[94] S.H. Choi, Y.C. Kang, Uniform Decoration of Vanadium Oxide Nanocrystals on Reduced Graphene-Oxide Balls by an Aerosol Process for Lithium-Ion Battery Cathode Material, Chem. - Eur. J. 20 (2014) 6294–6299. doi:10.1002/chem.201400134.
[95] G. Liu, S. Liu, Q. Lu, H. Sun, Z. Xiu, Synthesis and characterization of Bi(VO4)1-m(PO4)m nanofibers by electrospinning process with enhanced photocatalytic activity under visible light, RSC Adv. 4 (2014) 33695–33701. doi:10.1039/C4RA04107K.
[96] E. Uchaker, G. Cao, The Role of Intentionally Introduced Defects on Electrode Materials for Alkali-Ion Batteries, Chem.- Asian J. 10 (2015) 1608–1617. doi:10.1002/asia.201500401.
[97] H. Zeng, D. Liu, Y. Zhang, K.A. See, Y.-S. Jun, G. Wu, J.A. Gerbec, X. Ji, G.D. Stucky, Nanostructured Mn-Doped V2O5 Cathode Material Fabricated from Layered Vanadium Jarosite, Chem. Mater. 27 (2015) 7331–7336. doi:10.1021/acs.chemmater.5b02840.
[98] L. Huang, Q. Wei, R. Sun, L. Mai, Nanowire Electrodes for Advanced Lithium Batteries, Front. Energy Res. 2 (2014). doi:10.3389/fenrg.2014.00043.
[99] L. Zhang, A. Aboagye, A. Kelkar, C. Lai, H. Fong, A review: carbon nanofibers from electrospun polyacrylonitrile and their applications, J. Mater. Sci. 49 (2014) 463–480. doi:10.1007/s10853-013-7705-y.
[100] G. Zhou, J. Ma, L. Chen, Selective Carbon Coating Techniques for Improving Electrochemical Properties of NiO Nanosheets, Electrochimica Acta. 133 (2014) 93–99. doi:10.1016/j.electacta.2014.03.161.
[101] L. Zhi, D. Kong, Y. Zhang, X. Li, X. Hai, B. Wang, X. Qiu, qi song, Q.H. Yang, Encapsulating V2O5 into Carbon Nanotube Enables Flexible High-Performance Lithium Ion Batteries, Energy Environ. Sci. (2016). doi:10.1039/C5EE03345D.
[102] M. Sathiya, A.S. Prakash, K. Ramesha, J. Tarascon, A.K. Shukla, V2O5-Anchored Carbon Nanotubes for Enhanced Electrochemical Energy Storage, J. Am. Chem. Soc. 133 (2011) 16291–16299. doi:10.1021/ja207285b.
[103] X. Jia, L. Zhang, R. Zhang, Y. Lu, F. Wei, Carbon nanotube-penetrated mesoporous V2O5 microspheres as high-performance cathode materials for lithium-ion batteries, RSC Adv. 4 (2014) 21018. doi:10.1039/c4ra01316f.
[104] Q. Li, Y. Chen, J. He, F. Fu, F. Qi, J. Lin, W. Zhang, Carbon Nanotube Modified $V_2O_5$ Porous Microspheres as Cathodes for High-Performance Lithium-Ion Batteries, Energy Technol. (2017). doi:10.1002/ente.201600435.
[105] J. Cheng, G. Gu, Q. Guan, J.M. Razal, Z. Wang, X. Li, B. Wang, Synthesis of a porous sheet-like V2O5-CNT nanocomposite using an ice-templating "bricks-and-mortar"

assembly approach as a high-capacity, long cyclelife cathode material for lithium-ion batteries, J Mater Chem A. 4 (2016) 2729–2737. doi:10.1039/C5TA10414A.
[106] R. Raccichini, A. Varzi, S. Passerini, B. Scrosati, The role of graphene for electrochemical energy storage, Nat Mater. 14 (2015) 271–279.
[107] G. Du, K.H. Seng, Z. Guo, J. Liu, W. Li, D. Jia, C. Cook, Z. Liu, H. Liu, Graphene-V2O5[middle dot]nH2O xerogel composite cathodes for lithium ion batteries, RSC Adv. 1 (2011) 690–697. doi:10.1039/C1RA00258A.
[108] Z.-F. Li, H. Zhang, Q. Liu, Y. Liu, L. Stanciu, J. Xie, Hierarchical Nanocomposites of Vanadium Oxide Thin Film Anchored on Graphene as High-Performance Cathodes in Li-Ion Batteries, ACS Appl. Mater. Interfaces. 6 (2014) 18894–18900. doi:10.1021/am5047262.
[109] D. Chen, H. Quan, S. Luo, X. Luo, F. Deng, H. Jiang, Reduced graphene oxide enwrapped vanadium pentoxide nanorods as cathode materials for lithium-ion batteries, Phys. E Low-Dimens. Syst. Nanostructures. 56 (2014) 231–237. doi:10.1016/j.physe.2013.09.009.
[110] T. Kim, H. Kim, T.-S. You, J. Kim, Carbon-coated V2O5 nanoparticles derived from metal-organic frameworks as a cathode material for rechargeable lithium-ion batteries, J. Alloys Compd. (2017). doi:10.1016/j.jallcom.2017.08.179.
[111] B. Yan, L. Liao, Y. You, X. Xu, Z. Zheng, Z. Shen, Single-Crystalline V2O5 Ultralong Nanoribbon Waveguides, 21 (2009) 2436–40.
[112] S. Ramakrishna, R. Jose, P.S. Archana, A.S. Nair, R. Balamurugan, J. Venugopal, W.E. Teo, Science and engineering of electrospun nanofibers for advances in clean energy, water filtration, and regenerative medicine, J. Mater. Sci. 45 (2010) 6283–6312. doi:10.1007/s10853-010-4509-1.
[113] A.H. Lu, E.E.. Salabas, Schüth, Magnetic nanoparticles: synthesis, protection, functionalization, and application, n.d.
[114] J.A. López Pérez, M.A. López Quintela, J. Mira, J. Rivas, S.W. Charles, Advances in the Preparation of Magnetic Nanoparticles by the Microemulsion Method, J. Phys. Chem. B. 101 (1997) 8045–8047. doi:10.1021/jp972046t.
[115] I.A. Rahman, V. Padavettan, Synthesis of silica nanoparticles by sol-gel: size-dependent properties, surface modification, and applications in silica-polymer nanocomposites—a review, J. Nanomater. 2012 (2012) 8.
[116] G. Demazeau, Solvothermal processes: a route to the stabilization of new materials, J. Mater. Chem. 9 (1999) 15–18. doi:10.1039/A805536J.
[117] A. Rabenau, The Role of Hydrothermal Synthesis in Preparative Chemistry, Angew. Chem. Int. Ed. Engl. 24 (1985) 1026–1040. doi:10.1002/anie.198510261.
[118] W.-E. Teo, R. Inai, S. Ramakrishna, Technological advances in electrospinning of nanofibers, Sci. Technol. Adv. Mater. 12 (2011) 013002.
[119] D. Li, J.T. McCann, Y. Xia, M. Marquez, Electrospinning: A Simple and Versatile Technique for Producing Ceramic Nanofibers and Nanotubes, J. Am. Ceram. Soc. 89 (2006) 1861–1869. doi:10.1111/j.1551-2916.2006.00989.x.
[120] J.E. Panels, Y.L. Joo, Incorporation of Vanadium Oxide in Silica Nanofiber Mats via Electrospinning and Sol-Gel Synthesis, J. Nanomater. 2006 (2006) 1–10. doi:10.1155/JNM/2006/41327.
[121] E.S. Pampal, E. Stojanovska, B. Simon, A. Kilic, A review of nanofibrous structures in lithium ion batteries, J. Power Sources. 300 (2015) 199–215. doi:10.1016/j.jpowsour.2015.09.059.
[122] S. Beke, A review of the growth of V2O5 films from 1885 to 2010, Thin Solid Films. 519 (2011) 1761–1771. doi:10.1016/j.tsf.2010.11.001.

[123] O.Y. Berezina, D.A. Kirienko, N.P. Markova, A.L. Pergament, Synthesis of vanadium pentoxide micro- and nanofibers by electrospinning, Tech. Phys. 60 (2015) 1361–1366. doi:10.1134/S1063784215090054.
[124] P. Viswanathamurthi, Vanadium pentoxide nanofibers by electrospinning, Scr. Mater. 49 (2003) 577–581. doi:10.1016/S1359-6462(03)00333-6.
[125] H. Liu, D. Tang, Synthesis of ZnV2O6 powder and its cathodic performance for lithium secondary battery, Mater. Chem. Phys. 114 (2009) 656–659. doi:10.1016/j.matchemphys.2008.10.055.
[126] D. Yu, C. Chen, S. Xie, Y. Liu, K. Park, X. Zhou, Q. Zhang, J. Li, G. Cao, Mesoporous vanadium pentoxide nanofibers with significantly enhanced Li-ion storage properties by electrospinning, Energy Env. Sci. 4 (2011) 858–861. doi:10.1039/C0EE00313A.
[127] S.-Z. Huang, Y. Cai, J. Jin, Y. Li, X.-F. Zheng, H.-E. Wang, M. Wu, L.-H. Chen, B.-L. Su, Annealed vanadium oxide nanowires and nanotubes as high performance cathode materials for lithium ion batteries, J. Mater. Chem. A. 2 (2014) 14099. doi:10.1039/C4TA02339K.
[128] P. Kumar, F.-Y. Wu, T. Chou, L.-H. Hu, Chemically modified morphologies of vanadium pentoxide as superior cathode material for lithium ion battery, J. Alloys Compd. 632 (2015) 126–132. doi:10.1016/j.jallcom.2015.01.174.
[129] A.M. Glushenkov, M.F. Hassan, V.I. Stukachev, Z. Guo, H.K. Liu, G.G. Kuvshinov, Y. Chen, Growth of V2O5 nanorods from ball-milled powders and their performance in cathodes and anodes of lithium-ion batteries, J. Solid State Electrochem. 14 (2010) 1841–1846. doi:10.1007/s10008-010-1016-x.
[130] M. Przesniak-Welenc, J. Karczewski, J. Smalc-Koziorowska, M. Lapinski, W. Sadowski, B. Koscielska, The influence of nanostructure size on V2O5 electrochemical properties as cathode materials for lithium ion batteries, RSC Adv. 6 (2016) 55689–55697. doi:10.1039/C6RA05695D.
[131] C. Ban, M.S. Whittingham, Nanoscale single-crystal vanadium oxides with layered structure by electrospinning and hydrothermal methods, Solid State Ion. 179 (2008) 1721–1724. doi:10.1016/j.ssi.2008.01.037.
[132] Y.L. Cheah, N. Gupta, S.S. Pramana, V. Aravindan, G. Wee, M. Srinivasan, Morphology, structure and electrochemical properties of single phase electrospun vanadium pentoxide nanofibers for lithium ion batteries, J. Power Sources. 196 (2011) 6465–6472. doi:10.1016/j.jpowsour.2011.03.039.
[133] Z. Li, G. Liu, M. Guo, L.-X. Ding, S. Wang, H. Wang, Electrospun porous vanadium pentoxide nanotubes as a high-performance cathode material for lithium-ion batteries, Electrochimica Acta. 173 (2015) 131–138. doi:10.1016/j.electacta.2015.05.057.
[134] Y.L. Cheah, V. Aravindan, S. Madhavi, Improved Elevated Temperature Performance of Al-Intercalated V2O5 Electrospun Nanofibers for Lithium-Ion Batteries, ACS Appl. Mater. Interfaces. 4 (2012) 3270–3277. doi:10.1021/am300616k.
[135] L. Liang, M. Zhou, Y. Xie, Electrospun Hierarchical LiV3O8 Nanofibers Assembled from Nanosheets with Exposed 100 Facets and their Enhanced Performance in Aqueous Lithium-Ion Batteries, Chem. – Asian J. 7 (2012) 565–571. doi:10.1002/asia.201100757.
[136] Y. Wu, P. Zhu, X. Zhao, M.V. Reddy, S. Peng, B.V.R. Chowdari, S. Ramakrishna, Highly improved rechargeable stability for lithium/silver vanadium oxide battery induced viaelectrospinning technique, J Mater Chem A. 1 (2013) 852–859. doi:10.1039/C2TA00042C.
[137] D. Pham-Cong, K. Ahn, S.W. Hong, S.Y. Jeong, J.H. Choi, C.H. Doh, J.S. Jin, E.D. Jeong, C.R. Cho, Cathodic performance of V2O5 nanowires and reduced graphene oxide composites for lithium ion batteries, Curr. Appl. Phys. 14 (2014) 215–221. doi:10.1016/j.cap.2013.10.022.

[138] D. Kong, X. Li, Y. Zhang, X. Hai, B. Wang, X. Qiu, Q. Song, Q.-H. Yang, L. Zhi, Encapsulating V2O5 into carbon nanotubes enables the synthesis of flexible high-performance lithium ion batteries, Energy Env. Sci. 9 (2016) 906–911. doi:10.1039/C5EE03345D.
[139] C.. Xu, R. Inai, M. Kotaki, S. Ramakrishna, Aligned biodegradable nanofibrous structure: a potential scaffold for blood vessel engineering, Biomaterials. 25 (2004) 877–886. doi:10.1016/S0142-9612(03)00593-3.
[140] C.H. Lee, H.J. Shin, I.H. Cho, Y.-M. Kang, I.A. Kim, K.-D. Park, J.-W. Shin, Nanofiber alignment and direction of mechanical strain affect the ECM production of human ACL fibroblast, Biomaterials. 26 (2005) 1261–1270. doi:10.1016/j.biomaterials.2004.04.037.
[141] W.-E. Teo, W. He, S. Ramakrishna, Electrospun scaffold tailored for tissue-specific extracellular matrix, Biotechnol. J. 1 (2006) 918–929. doi:10.1002/biot.200600044.
[142] W.D. Callister, Materials Science and Engineering An Introduction, 7th ed., John Wiley & Sons, U.S.A., 2007.
[143] S. Sapra, D.D. Sarma, Simultaneous control of nanocrystal size and nanocrystal-nanocrystal separation in CdS nanocrystal assembly, Pramana. 65 (2005) 565–570. doi:10.1007/BF03010444.
[144] U. Holzwarth, N. Gibson, The Scherrer equation versus the “Debye-Scherrer equation,” Nat Nano. 6 (2011) 534–534. doi:10.1038/nnano.2011.145.
[145] W.H. Zachariasen, A General Theory of X-ray Diffraction in Crystal, Acta Crystallogr. 23 (n.d.) 558–564. doi:https://doi.org/10.1107/S0365110X67003202.
[146] L. Lutterotti, S. Matthies, H. Wenk, MAUD (Material Analysis Using Diffraction): a user friendly Java program for Rietveld Texture Analysis and more, Twelfth Int. Conf. Textures Mater. ICOTOM-12. 1599 (1999).
[147] X. Li, C. Liu, C. Zhang, H. Fu, X. Nan, W. Ma, Z. Li, K. Wang, H. Wu, G. Cao, Effects of Preinserted Na Ions on Li-Ion Electrochemical Intercalation Properties of V2O5, ACS Appl. Mater. Interfaces. 8 (2016) 24629–24637. doi:10.1021/acsami.6b08052.
[148] J.M. Hollander, W.L. Jolly, X-ray photoelectron spectroscopy, Acc. Chem. Res. 3 (1970) 193–200. doi:10.1021/ar50030a003.
[149] P. van der Heide, X-ray Photoelectron Spectroscopy: An introduction to Principles and Practices, John Wiley & Sons, 2011.
[150] J. Goldstein, D.E. Newbury, D.C. Joy, C.E. Lyman, P. Echlin, E. Lifshin, L. Sawyer, J.R. Michael, Scanning Electron Microscopy and X-ray Microanalysis, 3rd ed., Springer, U.S.A., n.d.
[151] D. Brandon, W.D. Kaplan, Microstructural Characterization of Materials, 2nd ed., John Wiley & Sons, 2008.
[152] J.B. Condon, Surface Area and Porosity Determinations by Physisorption, 1st ed., Elsevier, 2006.
[153] M.S. Islam, C.A.J. Fisher, Lithium and sodium battery cathode materials: computational insights into voltage, diffusion and nanostructural properties, Chem Soc Rev. 43 (2014) 185–204. doi:10.1039/C3CS60199D.
[154] C.R.A. Catlow, Computer Modelling in Inorganic Crystallography, Academic Press, San Diego, 1997.
[155] J.D. Gale, A.L. Rohl, The General Utility Lattice Program (GULP), Mol. Simul. 29 (2003) 291–341. doi:10.1080/0892702031000104887.
[156] J.D. Gale, GULP: A computer program for the symmetry-adapted simulation of solids, J. Chem. Soc. Faraday Trans. 93 (1997) 629–637. doi:10.1039/A606455H.
[157] B.W. Shore, Comparison of matrix methods applied to the radial Schrödinger eigenvalue equation: The Morse potential, J. Chem. Phys. 59 (1973) 6450–6463. doi:10.1063/1.1680025.

[158] P.M. Morse, Diatomic Molecules According to the Wave Mechanics. II. Vibrational Levels, Phys. Rev. 34 (1929) 57–64.
[159] C.L. Kong, Combining rules for intermolecular potential parameters. II. Rules for the Lennard –6 potential and the Morse potential, J. Chem. Phys. 59 (1973) 2464–2467. doi:10.1063/1.1680358.
[160] J.S. Braithwaite, C.R. a. Catlow, J.D. Gale, J.H. Harding, Lithium Intercalation into Vanadium Pentoxide : a Theoretical Study, Chem. Mater. 11 (1999) 1990–1998. doi:10.1021/cm980735r.
[161] T.S. Bush, J.D. Gale, C.R. a. Catlow, P.D. Battle, Self-consistent interatomic potentials for the simulation of binary and ternary oxides, J. Mater. Chem. 4 (1994) 831. doi:10.1039/jm9940400831.
[162] B.G. Dick, A.W. Overhauser, Theory of the Dielectric Constants of Alkali Halide Crystals, Phys. Rev. 112 (1958) 90–103. doi:10.1103/PhysRev.112.90.
[163] N.F. Littleton, M.J. Mott, Conduction in Polar Crystals. I. Electrlytic Conduction in Solid Salts, Trans Faraday Soc. (1938) 485–499.
[164] H. Shih, Electrochemical Impedance Spectroscopy for Battery Research and Development, Solartron Instruments, Hampshire, 1996.
[165] C. Gabrielli, Use and Application of Electrochemical Impedance Techniques, Solartron Instruments, Paris, 1997.
[166] M.V. Reddy, B. Pecquenard, P. Vinatier, A. Levasseur, Cyclic voltammetry and galvanostatic cycling characteristics of LiNiVO4 thin films during lithium insertion and re/de-insertion, Electrochem. Commun. 9 (2007) 409–415. doi:10.1016/j.elecom.2006.10.011.
[167] S. Zhang, W. Li, C. Li, J. Chen, Synthesis, Characterization, and Electrochemical Properties of Ag2V4O11 and AgVO3 1-D Nano/Microstructures, J. Phys. Chem. B. 110 (2006) 24855–24863. doi:10.1021/jp065478p.
[168] P. Suresh, A.. Shukla, S.. Shivashankar, N. Munichandraiah, Electrochemical behaviour of aluminium in non-aqueous electrolytes over a wide potential range, J. Power Sources. 110 (2002) 11–18. doi:10.1016/S0378-7753(02)00166-0.
[169] L. Noerochim, J.-Z. Wang, D. Wexler, Z. Chao, H.-K. Liu, Rapid synthesis of free-standing MoO3/Graphene films by the microwave hydrothermal method as cathode for bendable lithium batteries, J. Power Sources. 228 (2013) 198–205. doi:10.1016/j.jpowsour.2012.11.113.
[170] Y.L. Cheah, N. Gupta, S.S. Pramana, V. Aravindan, G. Wee, M. Srinivasan, Morphology, structure and electrochemical properties of single phase electrospun vanadium pentoxide nanofibers for lithium ion batteries, J. Power Sources. 196 (2011) 6465–6472. doi:10.1016/j.jpowsour.2011.03.039.
[171] A. Sakunthala, M.V. Reddy, S. Selvasekarapandian, B.V.R. Chowdari, P.C. Selvin, Energy storage studies of bare and doped vanadium pentoxide, (V1.95M0.05)O5, M = Nb, Ta, for lithium ion batteries, Energy Environ. Sci. 4 (2011) 1712–1725. doi:10.1039/C0EE00513D.
[172] V. Shklover, T. Haibach, R. Nespar, P. Novak, F. Reid, Crystal structure of the produce of Mg2+ insertion into V2O5 single crystals Locality: synthetic Sample:IIb, J. Solid State Chem. 123 (1996) 317–323.
[173] X. Zhou, C. Shang, L. Gu, S. Dong, X. Chen, P. Han, L. Li, J. Yao, Z. Liu, H. Xu, Y. Zhu, G. Cui, Mesoporous Coaxial Titanium Nitride-Vanadium Nitride Fibers of Core–shell Structures for High-Performance Supercapacitors, ACS Appl. Mater. Interfaces. 3 (2011) 3058–3063. doi:10.1021/am200564b.
[174] Yashima Masatomo, Ishimura Daiju, Ohoyama Kenji, Temperature Dependence of Lattice Parameters and Anisotropic Thermal Expansion of Bismuth Oxide, J. Am. Ceram. Soc. 88 (2005) 2332–2335. doi:10.1111/j.1551-2916.2005.00432.x.

[175] J.H. Kim, Lattice Parameter, Lattice Disorder and Resistivity of Carbohydrate Doped MgB2 and Their Correlation with the Transition Temperature, J. Nanosci. Nanotechnol. 9 (2009). doi:10.1166/jnn.2009.1761.
[176] J.D. Jorgensen, D.G. Hinks, S. Short, Lattice properties of MgB2 versus temperature and pressure, Phys. Rev. B. 63 (2001) 224522.
[177] Y. Zheng, H. Ding, M. Zhang, Preparation and electrochemical properties of nickel oxide as a supercapacitor electrode material, Mater. Res. Bull. 44 (2009) 403–407. doi:10.1016/j.materresbull.2008.05.002.
[178] S. Zhang, C. Peng, K.C. Ng, G.Z. Chen, Nanocomposites of manganese oxides and carbon nanotubes for aqueous supercapacitor stacks, Enhanc. Electrochem. Capacit. Pap. 1st Int. Symp. 55 (2010) 7447–7453. doi:10.1016/j.electacta.2010.01.078.
[179] H.-S. Nam, J.S. Kwon, K.M. Kim, J.M. Ko, J.-D. Kim, Supercapacitive properties of a nanowire-structured MnO2 electrode in the gel electrolyte containing silica, Enhanc. Electrochem. Capacit. Pap. 1st Int. Symp. 55 (2010) 7443–7446. doi:10.1016/j.electacta.2010.02.027.
[180] J. Kawakita, M. Majima, T. Miura, T. Kishi, Preparation and lithium insertion behaviour of oxygen-deficient Li1 + xV3O8 − δ, J. Power Sources. 66 (1997) 135–139. doi:10.1016/S0378-7753(96)02540-2.
[181] R. Baddour-Hadjean, A. Marzouk, J.P. Pereira-Ramos, Structural modifications of LixV2O5 in a composite cathode ($0 \leq x < 2$) investigated by Raman microspectrometry, J. Raman Spectrosc. 43 (2012) 153–160. doi:10.1002/jrs.2984.
[182] Y. Wei, C.-W. Ryu, K.-B. Kim, Improvement in electrochemical performance of V2O5 by Cu doping, J. Power Sources. 165 (2007) 386–392. doi:10.1016/j.jpowsour.2006.12.016.
[183] L. Mai, Q. An, Q. Wei, J. Fei, P. Zhang, X. Xu, Y. Zhao, M. Yan, W. Wen, L. Xu, Nanoflakes-Assembled Three-Dimensional Hollow-Porous $V_2O_5$ as Lithium Storage Cathodes with High-Rate Capacity, Small. 10 (2014) 3032–3037. doi:10.1002/smll.201302991.
[184] K. Takahashi, Y. Wang, K. Lee, G. Cao, Fabrication and Li+-intercalation properties of V2O5-TiO2 composite nanorod arrays, Appl. Phys. A. 82 (2006) 27–31. doi:10.1007/s00339-005-3375-1.
[185] O.B. Chae, J. Kim, I. Park, H. Jeong, J.H. Ku, J.H. Ryu, K. Kang, S.M. Oh, Reversible Lithium Storage at Highly Populated Vacant Sites in an Amorphous Vanadium Pentoxide Electrode, Chem. Mater. 26 (2014) 5874–5881. doi:10.1021/cm502268u.
[186] X. Liang, G. Gao, Y. Liu, T. Zhang, G. Wu, Synthesis and characterization of Fe-doped vanadium oxide nanorods and their electrochemical performance, J. Alloys Compd. 715 (2017) 374–383. doi:10.1016/j.jallcom.2017.04.242.
[187] Z. Li, C. Zhang, C. Liu, H. Fu, X. Nan, K. Wang, X. Li, W. Ma, X. Lu, G. Cao, Enhanced Electrochemical Properties of Sn-doped V2O5 as a Cathode Material for Lithium Ion Batteries, Electrochimica Acta. 222 (2016) 1831–1838. doi:10.1016/j.electacta.2016.11.174.
[188] G. Wee, H.Z. Soh, Y.L. Cheah, S.G. Mhaisalkar, M. Srinivasan, Synthesis and electrochemical properties of electrospun V2O5 nanofibers as supercapacitor electrodes, J. Mater. Chem. 20 (2010) 6720–6725. doi:10.1039/C0JM00059K.
[189] D. Li, Y. Xia, Electrospinning of Nanofibers: Reinventing the Wheel?, Adv. Mater. 16 (2004) 1151–1170. doi:10.1002/adma.200400719.
[190] D. Li, Y. Xia, Fabrication of Titania Nanofibers by Electrospinning, Nano Lett. 3 (2003) 555–560. doi:10.1021/nl034039o.
[191] M.G. McKee, G.L. Wilkes, R.H. Colby, T.E. Long, Correlations of Solution Rheology with Electrospun Fiber Formation of Linear and Branched Polyesters, Macromolecules. 37 (2004) 1760–1767. doi:10.1021/ma035689h.

[192] S.A. Theron, E. Zussman, A.L. Yarin, Experimental investigation of the governing parameters in the electrospinning of polymer solutions, Polymer. 45 (2004) 2017–2030. doi:10.1016/j.polymer.2004.01.024.
[193] W.K. Son, J.H. Youk, T.S. Lee, W.H. Park, The effects of solution properties and polyelectrolyte on electrospinning of ultrafine poly(ethylene oxide) fibers, Polymer. 45 (2004) 2959–2966. doi:10.1016/j.polymer.2004.03.006.
[194] M. Lubke, J. Shin, P. Marchand, D. Brett, P. Shearing, Z. Liu, J.A. Darr, Highly pseudocapacitive Nb-doped TiO2 high power anodes for lithium-ion batteries, J. Mater. Chem. A. 3 (2015) 22908–22914. doi:10.1039/C5TA07554H.
[195] H.-E. Wang, D.-S. Chen, Y. Cai, R.-L. Zhang, J.-M. Xu, Z. Deng, X.-F. Zheng, Y. Li, I. Bello, B.-L. Su, Facile synthesis of hierarchical and porous V2O5 microspheres as cathode materials for lithium ion batteries, J. Colloid Interface Sci. 418 (2014) 74–80. doi:10.1016/j.jcis.2013.12.011.
[196] Y. Liu, E. Uchaker, N. Zhou, J. Li, Q. Zhang, G. Cao, Facile synthesis of nanostructured vanadium oxide as cathode materials for efficient Li-ion batteries, J. Mater. Chem. 22 (2012) 24439–24445. doi:10.1039/C2JM34078J.
[197] C.F. Armer, M. Lübke, M.V. Reddy, J.A. Darr, X. Li, A. Lowe, Phase change effect on the structural and electrochemical behaviour of pure and doped vanadium pentoxide as positive electrodes for lithium ion batteries, J. Power Sources. 353 (2017) 40–50. doi:10.1016/j.jpowsour.2017.03.121.
[198] C. Zheng, L. Zeng, M. Wang, H. Zheng, M. Wei, Synthesis of hierarchical $ZnV_2O_4$ microspheres and its electrochemical properties, CrystEngComm. 16 (2014) 10309–10313. doi:10.1039/C4CE01445F.
[199] M.V. Reddy, S. Madhavi, G.V. Subba Rao, B.V.R. Chowdari, Metal oxyfluorides TiOF2 and NbO2F as anodes for Li-ion batteries, Spec. Issue Sel. Pap. Int. Power Sources Symp. 2005 Together Regul. Pap. 162 (2006) 1312–1321. doi:10.1016/j.jpowsour.2006.08.020.
[200] M.V. Reddy, G.V. Subba Rao, B.V.R. Chowdari, Preparation and Characterization of LiNi0.5Co0.5O2 and LiNi0.5Co0.4Al0.1O2 by Molten Salt Synthesis for Li Ion Batteries, J. Phys. Chem. C. 111 (2007) 11712–11720. doi:10.1021/jp0676890.
[201] I.D. Johnson, E. Blagovidova, P.A. Dingwall, D.J.L. Brett, P.R. Shearing, J.A. Darr, High power Nb-doped LiFePO4 Li-ion battery cathodes; pilot-scale synthesis and electrochemical properties, J. Power Sources. 326 (2016) 476–481. doi:10.1016/j.jpowsour.2016.06.128.
[202] S.-Y. Chung, J.T. Bloking, Y.-M. Chiang, Electronically conductive phospho-olivines as lithium storage electrodes, Nat Mater. 1 (2002) 123–128. doi:10.1038/nmat732.
[203] K. Hoang, M.D. Johannes, First-principles studies of the effects of impurities on the ionic and electronic conduction in LiFePO4, J. Power Sources. 206 (2012) 274–281. doi:10.1016/j.jpowsour.2012.01.126.
[204] C.H. Chen, J. Liu, M.E. Stoll, G. Henriksen, D.R. Vissers, K. Amine, Aluminum-doped lithium nickel cobalt oxide electrodes for high-power lithium-ion batteries, J. Power Sources. 128 (2004) 278–285. doi:10.1016/j.jpowsour.2003.10.009.
[205] P. Kalyani, N. Kalaiselvi, Various aspects of LiNiO2 chemistry: A review, Sci. Technol. Adv. Mater. 6 (2005) 689–703. doi:10.1016/j.stam.2005.06.001.
[206] S. Zhan, G. Chen, D. Liu, A. Li, C. Wang, Y. Wei, Effects of Cr doping on the structural and electrochemical properties of V2O5, J. Alloys Compd. 479 (2009) 652–656. doi:10.1016/j.jallcom.2009.01.023.
[207] F. Coustier, J. Hill, B.B. Owens, S. Passerini, W.H. Smyrl, Doped vanadium oxides as host materials for lithium intercalation, J. Electrochem. Soc. 146 (1999) 1355–1360.

[208] S. Zhan, Y. Wei, X. Bie, C. Wang, F. Du, G. Chen, F. Hu, Structural and electrochemical properties of Al3+ doped V2O5 nanoparticles prepared by an oxalic acid assisted soft-chemical method, J. Alloys Compd. 502 (2010) 92–96. doi:10.1016/j.jallcom.2010.03.133.
[209] S. Liang, J. Zhou, G. Fang, C. Zhang, J. Wu, Y. Tang, A. Pan, Synthesis of mesoporous β-Na0.33V2O5 with enhanced electrochemical performance for lithium ion batteries, Electrochimica Acta. 130 (2014) 119–126. doi:10.1016/j.electacta.2014.02.131.
[210] S.-R. Li, S.-Y. Ge, Y. Qiao, Y.-M. Chen, X.-Y. Feng, J.-F. Zhu, C.-H. Chen, Three-dimensional porous Fe0.1V2O5.15 thin film as a cathode material for lithium ion batteries, Electrochimica Acta. 64 (2012) 81–86. doi:10.1016/j.electacta.2011.12.131.
[211] P.H. Jampani, O. Velikokhatnyi, K. Kadakia, D.H. Hong, S.S. Damle, J.A. Poston, A. Manivannan, P.N. Kumta, High energy density titanium doped-vanadium oxide-vertically aligned CNT composite electrodes for supercapacitor applications, J Mater Chem A. 3 (2015) 8413–8432. doi:10.1039/C4TA06777K.
[212] P. Nithyadharseni, M.V. Reddy, K.I. Ozoemena, F.I. Ezema, R.G. Balakrishna, B.V.R. Chowdari, Electrochemical Performance of BaSnO3 Anode Material for Lithium-Ion Battery Prepared by Molten Salt Method, J. Electrochem. Soc. 163 (2016) A540–A545.
[213] N. Sharma, K.M. Shaju, G.V.S. Rao, B.V.R. Chowdari, Anodic behaviour and X-ray photoelectron spectroscopy of ternary tin oxides, J. Power Sources. 139 (2005) 250–260. doi:10.1016/j.jpowsour.2004.06.057.
[214] The structure of Ba3(VO4)2, Z. Für Krist. 131 (2010) 161. doi:10.1524/zkri.1970.131.1-6.161.
[215] J. Liu, W. Guo, F. Qu, C. Feng, C. Li, L. Zhu, J. Zhou, S. Ruan, W. Chen, V-doped In2O3 nanofibers for H2S detection at low temperature, Ceram. Int. 40 (2014) 6685–6689. doi:10.1016/j.ceramint.2013.11.129.
[216] H.X. Li, L.F. Jiao, H.T. Yuan, M. Zhao, M. Zhang, Y.M. Wang, High-performance Cu-doped vanadium oxide (CuxV2O5) prepared by rapid precipitation method for rechargeable batteries, Mater. Lett. 61 (2007) 101–104. doi:10.1016/j.matlet.2006.04.015.
[217] D. Zhu, H. Liu, L. Lv, Y.D. Yao, W.Z. Yang, Hollow microspheres of V2O5 and Cu-doped V2O5 as cathode materials for lithium-ion batteries, Scr. Mater. 59 (2008) 642–645. doi:10.1016/j.scriptamat.2008.05.020.
[218] S. De Vrieze, T. Van Camp, A. Nelvig, B. Hagström, P. Westbroek, K. De Clerck, The effect of temperature and humidity on electrospinning, J. Mater. Sci. 44 (2008) 1357. doi:10.1007/s10853-008-3010-6.
[219] A. Greiner, J.H. Wendorff, Electrospinning: A Fascinating Method for the Preparation of Ultrathin Fibers, Angew. Chem. Int. Ed. 46 (2007) 5670–5703. doi:10.1002/anie.200604646.
[220] Y. Ji, D. Fang, C. Wang, Z. Zhou, Z. Luo, J. Huang, J. Yi, Cobalt-doped V2O5 nanowire arrays on Ti foil for enhanced lithium-ion storage, J. Alloys Compd. 742 (2018) 567–576. doi:10.1016/j.jallcom.2018.01.293.
[221] M. Lübke, D. Howard, C.F. Armer, A.J. Gardecka, A. Lowe, M.V. Reddy, Z. Liu, J.A. Darr, High energy lithium ion battery electrode materials; enhanced charge storage via both alloying and insertion processes, Electrochimica Acta. 231 (2017) 247–254. doi:10.1016/j.electacta.2017.02.063.
[222] I.D. Johnson, M. Lübke, O.Y. Wu, N.M. Makwana, G.J. Smales, H.U. Islam, R.Y. Dedigama, R.I. Gruar, C.J. Tighe, D.O. Scanlon, F. Corà, D.J.L. Brett, P.R. Shearing, J.A. Darr, Pilot-scale continuous synthesis of a vanadium-doped LiFePO4/C nanocomposite high-rate cathodes for lithium-ion batteries, J. Power Sources. 302 (2016) 410–418. doi:10.1016/j.jpowsour.2015.10.068.
[223] J.F. Ni, H.H. Zhou, J.T. Chen, X.X. Zhang, LiFePO4 doped with ions prepared by co-precipitation method, Mater. Lett. 59 (2005) 2361–2365. doi:10.1016/j.matlet.2005.02.080.

[224] M. Ren, Z. Zhou, Y. Li, X.P. Gao, J. Yan, Preparation and electrochemical studies of Fe-doped Li3V2(PO4)3 cathode materials for lithium-ion batteries, Spec. Issue Sel. Pap. Int. Power Sources Symp. 2005 Together Regul. Pap. 162 (2006) 1357–1362. doi:10.1016/j.jpowsour.2006.08.008.
[225] D.M. Yu, S.T. Zhang, D.W. Liu, X.Y. Zhou, S.H. Xie, Q.F. Zhang, Y.Y. Liu, G.Z. Cao, Effect of manganese doping on Li-ion intercalation properties of V2O5 films, J. Mater. Chem. 20 (2010) 10841. doi:10.1039/c0jm01252a.
[226] W.J.H. Borghols, M. Wagemaker, U. Lafont, E.M. Kelder, F.M. Mulder, Impact of Nanosizing on Lithiated Rutile TiO2, Chem. Mater. 20 (2008) 2949–2955. doi:10.1021/cm703376e.
[227] J. Galy, Vanadium pentoxide and vanadium oxide bronzes—Structural chemistry of single (S) and double (D) layer MxV2O5 phases, J. Solid State Chem. 100 (1992) 229–245. doi:10.1016/0022-4596(92)90097-F.
[228] S. Zhan, Y. Wei, X. Bie, C. Wang, F. Du, G. Chen, F. Hu, Structural and electrochemical properties of Al3+ doped V2O5 nanoparticles prepared by an oxalic acid assisted soft-chemical method, J. Alloys Compd. 502 (2010) 92–96. doi:10.1016/j.jallcom.2010.03.133.
[229] M. Giorgetti, M. Berrettoni, W.H. Smyrl, Doped V2O5-Based Cathode Materials: Where Does the Doping Metal Go? An X-ray Absorption Spectroscopy Study, Chem. Mater. 19 (2007) 5991–6000. doi:10.1021/cm701910c.
[230] D. Sun, G. Jin, H. Wang, P. Liu, Y. Ren, Y. Jiang, Y. Tang, X. Huang, Aqueous rechargeable lithium batteries using NaV6O15 nanoflakes as high performance anodes, J. Mater. Chem. A. 2 (2014) 12999–13005. doi:10.1039/C4TA01675K.
[231] S. Nayak, B. Sahoo, T.K. Chaki, D. Khastgir, Facile preparation of uniform barium titanate ($BaTiO_3$) multipods with high permittivity: impedance and temperature dependent dielectric behavior, RSC Adv. 4 (2014) 1212–1224. doi:10.1039/C3RA44815K.
[232] J. Marsh, L. Minel, M.G. Barthes-Labrousee, D. Gorse, Interaction of epoxy model molecules with aluminium, anodised titanium and copper surfaces: an XPS study, Appl. Surf. Sci. 133 (1998) 270–286.
[233] F. Coustier, S. Passerini, W.H. Smyrl, Dip-coated silver-doped V2O5 xerogels as host materials for lithium intercalation, Solid State Ion. 100 (1997) 247–258. doi:10.1016/S0167-2738(97)00354-8.
[234] F. Hu, W. Jiang, Y. Dong, X. Lai, L. Xiao, X. Wu, Synthesis and electrochemical performance of NaV6O15 microflowers for lithium and sodium ion batteries, RSC Adv. 7 (2017) 29481–29488. doi:10.1039/C7RA04388K.
[235] N.A. Chernova, M. Roppolo, A.C. Dillon, M.S. Whittingham, Layered vanadium and molybdenum oxides: batteries and electrochromics, J Mater Chem. 19 (2009) 2526–2552. doi:10.1039/B819629J.
[236] M. Przesniak-Welenc, J. Karczewski, J. Smalc-Koziorowska, M. Lapinski, W. Sadowski, B. Koscielska, The influence of nanostructure size on V2O5 electrochemical properties as cathode materials for lithium ion batteries, RSC Adv. 6 (2016) 55689–55697. doi:10.1039/C6RA05695D.
[237] B.-H. Kim, K.S. Yang, D.J. Yang, Electrochemical behavior of activated carbon nanofiber-vanadium pentoxide composites for double-layer capacitors, Electrochimica Acta. 109 (2013) 859–865. doi:10.1016/j.electacta.2013.07.180.
[238] L. Mai, X. Xu, C. Han, Y. Luo, L. Xu, Y.A. Wu, Y. Zhao, Rational Synthesis of Silver Vanadium Oxides/Polyaniline Triaxial Nanowires with Enhanced Electrochemical Property, Nano Lett. 11 (2011) 4992–4996. doi:10.1021/nl202943b.
[239] H. Liu, Y. Wang, L. Li, K. Wang, E. Hosono, H. Zhou, Facile synthesis of NaV6O15 nanorods and its electrochemical behavior as cathode material in rechargeable lithium batteries, J. Mater. Chem. 19 (2009) 7885. doi:10.1039/b912906e.

[240] K. Zhu, H. Qiu, Y. Zhang, D. Zhang, G. Chen, Y. Wei, Synergetic Effects of Al3+ Doping and Graphene Modification on the Electrochemical Performance of V2O5 Cathode Materials, ChemSusChem. 8 (2015) 1017–1025. doi:10.1002/cssc.201500027.